University of Nottingham
UK | CHINA | MALAYSIA

STRUCTURAL EXPLORATION OF CANNABINOID RECEPTORS USING COMPUTATIONAL METHODS

LAHARI MURALI

BTech

School of Pharmacy
University of Nottingham Malaysia

Thesis submitted to the University of Nottingham for the degree of Doctor of Philosophy

November 2019

Acknowledgements

Firstly, I would like to express my sincere gratitude to **Dr Abigail Emtage**, **University of Nottingham (UNM)**, **Malaysia** for her valuable guidance, encouragement, and timely help. Her expertise helped me to a great extent.

I express my sincere thanks to **Dr Stephen Alexander**, **School of Pharmacy, University of Nottingham (UNUK), United Kingdom**, for hosting me in the UK campus and for the scholarly advice that was instrumental in the progress of my project.

I would also like to thank **Dr Jason Loo Siau Ee, Taylors University, Malaysia and Prof. Stephen Doughty** for their timely guidance and support through the years.

Special thanks to **Dr Wafa Hourani** and **Yousra Adel, School of Pharmacy, UNUK, United Kingdom** for helping me with the experimental sections of the work during my time in the UK. I would also like to especially thank **Dr Ian Withers, School of Pharmacy, UNUK,** for helping with all the IT and software related issues.

To my friends, former roommates and colleagues at UNM, I would like to express my gratitude for making the past four years a memorable experience.

Last, but not the least, my deepest thanks to my parents who stood by me through the entire journey as a strong pillar of support.

Abstract

Cannabinoid receptors (CB1 and CB2) are signalling proteins which belong to the largest family of transmembrane proteins called G protein-coupled receptors (GPCRs). Since their discovery, they have been widely studied for the notable pharmacological influences exerted by their interaction with cannabinoids and are hence viewed as druggable targets for a number of diseases. Along with their endogenous ligands and the metabolic enzymes that affect the bioavailability of endogenous cannabinoids, they form the endocannabinoid system. The discovery of crystal structures of CB1 and CB2 in recent years has relayed critical information regarding the conformation of the receptors in active and inactive states, and their binding pocket interactions. Though being invaluable sources of information, rigid crystal structures cannot completely rationalise structure-activity relationship for all classes of ligands that interact with the receptors. The work reported herein describes the exploration of the structures of CB1 and CB2 receptors via computational tools such as molecular modelling, docking, and molecular dynamics simulation. Accordingly, significant variations in the conformations of CB1 and CB2 in different states of activation were studied. It was observed that transmembrane helices 1,3,6 and 7 influence the structural features of both receptors at different states. In recent years, many ligands that are not classified as cannabinoids have been shown to influence the endocannabinoid system. In this regard, the work presented here also analyses the interaction of non-cannabinoid ligands at CB1 and CB2. In this regard, a select group of commonly used drugs were tested against CB1 and CB2 using [^{35}S]GTPγS binding assay for agonist activity. Furthermore, non-cannabinoids that have been reported to show activity at CB1 and CB2 were docked to models of the receptors to decipher their binding

mode. It was found that the binding mode depends on the binding pocket surface area and is stereoisomer specific. In general, the work documented herein provides an insight into the structural complexities of these receptors for the cannabinoid research community.

Related Publications

Loo, J. S. E.; Emtage, A. L.; Murali, L.; Lee, S. S.; Kueh, A. L. W.; Alexander, S. P. H. Ligand Discrimination during Virtual Screening of the CB1 Cannabinoid Receptor Crystal Structures Following Cross-Docking and Microsecond Molecular Dynamics Simulations. *RSC Adv.* **2019**, *9* (28), 15949–15956. https://doi.org/10.1039/C9RA01095E.

TABLE OF CONTENTS

Acknowledgements II
Abstract III
Related Publications V
Table of Figures X
Table of Tables XIV
Table of Abbreviations XV
1 Introduction 1
1.1 G protein-Coupled Receptors 1
1.1.1 Structure, Function and Classification 1
1.1.2 Numbering Systems for GPCRs 3
1.1.3 Residues and Motifs Involved in Activation of Class A GPCRs 4
1.1.4 Signal Transduction by GPCRs 7
1.1.5 Biased Agonism and Allosterism in GPCRs 10
1.1.6 Challenges Faced in GPCR Drug Discovery 12
1.2 The Endocannabinoid System and Cannabinoid Receptors 15
1.2.1 Cannabinoid Receptor 1 16
1.2.2 Cannabinoid Receptor 2 19
1.2.3 Cannabinoid Ligands 22
1.2.4 Other Members of the ECS 30
1.2.5 Pathophysiology Associated with Cannabinoid Receptors 31
1.3 Crystal Structures 36
1.4 Non-cannabinoid Ligands That Act on Cannabinoid Receptors 50
1.5 Computational Techniques 51
1.5.1 Molecular Modelling 51
1.5.2 Computational Molecular Docking 54
1.5.3 Molecular Dynamics (MD) Simulations 57
1.6 Aims and Objectives 60
2 Modelling Cannabinoid Receptors 64
2.1 Introduction 64
2.2 Aims 65

2.3 Structure Prediction of CB1 (Pre Crystal Structure) 66
2.3.1 Template Selection 66
2.3.2 Homology Modelling 68
2.4 Re-engineering CB1 and CB2 Models 73
2.4.1 Method 73
2.4.2 Qualitative Validation 75
2.5 Difference Between the Binding Modes in Pre-Crystal Structure and Post-Crystal Structure Models 79
2.5.1 Discussion 81
2.6 Identifying Binding Modes of Novel Cannabinoid Ligands with Opposing Functional Profiles at CB2 84
2.6.1 Method 84
2.6.2 Results 84
2.6.3 Discussion 85
2.7 Conclusion 86
3 Molecular Dynamics Simulations of Cannabinoid Receptor 1 88
3.1 Introduction 88
3.2 Aims 89
3.3 Methods 90
3.3.1 Preparation of CB1 Complexes 90
3.3.2 Embedding the Protein and Assembling the System 90
3.3.3 Running MD Simulations 91
3.3.4 Analysis 91
3.4 Results 92
3.4.1 Docking and Preparation of the Complex 92
3.4.2 RMSF Analysis 95
3.4.3 RMSD of Protein Structures 97
3.4.4 Ligand RMSD 101
3.4.5 Principal Component Analysis (PCA) 104
3.4.6 Conformation of Conserved Residues 113
3.4.7 Lipid Access Channel 117

3.5 Discussion 119
3.6 Conclusion 124
4 Molecular Dynamics Simulations of Cross Docked Cannabinoid Receptor 1 Activation States 125
4.1 Introduction 125
4.2 Aims 126
4.3 Methods 126
4.4 Results 127
4.4.1 Changes in Ligand Position 127
4.4.2 Principal Component Analysis (PCA) 129
4.4.3 Conformations of Conserved Residues 134
4.4.4 Pocket Volume 144
4.5 Discussion 146
4.6 Conclusion 148
5 Molecular Dynamics Simulations of Cannabinoid Receptor 2 150
5.1 Introduction 150
5.2 Aims 150
5.3 Methods 151
5.3.1 Preparation of CB2 Complexes 151
5.3.2 Assembling the System 151
5.3.3 Running MD Simulations 151
5.3.4 Analysis 152
5.4 Results 153
5.4.1 Docking and Preparation of the Complex 153
5.4.2 RMSF Analysis 156
5.4.3 RMSD of the Protein Structures 157
5.4.4 Ligand RMSD 158
5.4.5 Principal Component Analysis (PCA) 161
5.4.6 Conformation of Conserved Residues 167
5.4.7 Formation of Potential Lipid Access Channels 175
5.5 Discussion 177

5.6 Conclusion 182
6 Repurposing Non-Cannabinoid Ligands for Use at Cannabinoid Receptors 184
6.1 Introduction 184
6.2 Aims 185
6.3 Testing non-cannabinoid ligands at cannabinoid receptors 186
6.3.1 Selection of ligands to test 186
6.3.2 Working Mechanism of [^{35}S]GTPγS assay 187
6.3.3 Materials and Methods 189
6.3.4 Data Analysis 190
6.3.5 Results 191
6.3.6 Discussion 192
6.4 *In silico* docking studies of ligands that interact with CB1 and CB2 ... 193
6.4.1 Materials and Methods 193
6.4.2 Results 195
6.4.3 Discussion 204
6.5 Conclusion 207
7 Conclusions and Future Work 209
7.1 Conclusions 209
7.2 Future Work 214
8 References: 216
I Appendix 1 244
II Appendix 2 246
III Appendix 3 250
IV Appendix 4 251
V Appendix 5 252
VI Appendix 6 253

Table of Figures

Figure 1.1 General representation of GPCRs. 4
Figure 1.2 Major molecular switches commonly found in GPCRs that are involved in receptor activation. 5
Figure 1.3 Working mechanism of GPCRs. 9
Figure 1.4 Biased agonism in GPCRs 11
Figure 1.5 Number of GPCR crystal structures found in the PDB database per year 15
Figure 1.6 Pharmacological activity of different ligands 22
Figure 1.7 Endocannabinoids anandamide and 2-AG 24
Figure 1.8 Classical cannabinoids Δ^9-THC, HU-210, and JWH-133 25
Figure 1.9 Non-classical cannabinoids CP55940 and CP55244 26
Figure 1.10 Aminoalkylindoles WIN-55,212-2 and JWH-015 26
Figure 1.11 Arylpyrazoles SR141716, SR144528, and AM281 28
Figure 1.12 Cannabinoid ligands from other chemical classes 29
Figure 1.13 Allosteric modulators of cannabinoid receptors 30
Figure 1.14 Cognate ligands of CB1 and CB2 crystal structures 37
Figure 1.15 Comparison of binding pockets and toggle-switch residues - Superposition of inactive CB1 and active CB1 crystal structures. 41
Figure 1.16 Comparison of binding pockets and toggle-switch residues - Superposition of inactive CB1 and inactive CB2 crystal structures. 42
Figure 1.17 Overlay of cognate ligand binding modes of all lipid-binding receptors. 44
Figure 1.18 Potential lipid access channels found between TM1 and TM7 in inactive structures 46
Figure 1.19 Comparison of Ionic Lock and Tyr7.53 rotamer state between inactive CB1 and active CB1 crystal structures. 48
Figure 1.20 Comparison of Ionic Lock and Tyr7.53 rotamer state between of active CB1, active CB1 complexed with Gi, and inactive CB crystal structures. 49
Figure 1.21 Sample Ramachandran plot of bovine rhodopsin generated using PROCHECK 53
Figure 1.22 The operation mechanism of Glide. 56
Figure 1.23 The molecular mechanics potential energy function (U) comprising the non-bonded (van der Waals and coulombic interactions) and bonded interaction terms (bond length, angle bending, and dihedral energy) 58
Figure 2.1 Structure of COR167 and COR170 65
Figure 2.2 Local alignment of human CB1 receptor sequence with human LPA1 receptor sequence. 68
Figure 2.3 Homology models and their Ramachandran plots 70
Figure 2.4 Superposed CB1 models generated with LPA1 template 71
Figure 2.5 Plot of GlideScore versus experimental pKi values of energy-based model docked with agonists and antagonists. 72

Figure 2.6 Models with a complete ICL3 76
Figure 2.7 Models with a pseudo ICL3 76
Figure 2.8 Redocking cognate ligands into their respective template-based models. (a) MK0364 (19) in CB1-5U09 (b) AM10257 (23) in CB2-5ZTY. 78
Figure 2.9 Redocking cognate ligands into their respective template-based models. (a) AM6538 (18) in CB1-5TGZ (b) AM841 (21) in CB1-5XR8……..…….79

Figure 2.10 Docked pose of SR141716 in EB model of CB1 via SP – expanded sampling protocol. 80
Figure 2.11 Docked pose of SR141716 in CB1-5U09 model of CB1 via (a) SP and (b) XP protocol. 81
Figure 2.12 Docking COR167 (24) and COR170 (25) into CB2-5ZTY. 85
Figure 3.1 Ligands docked into inactive CB1 model (a) AM841 (21) and (b) AM6538 (18) 93
Figure 3.2 CB1-Apo protein post embedding into the system. 94
Figure 3.3 RMSF plots of CB1-Apo and CB1-AM841 systems 96
Figure 3.4 RMSF plot of the CB1-AM6538 system. 97
Figure 3.5 RMSD values of the CB1-Apo system against 5U09 and 5XR8 crystal structures. 98
Figure 3.6 RMSD values of CB1-AM841 system against 5U09 and 5XR8 crystal structures. 99
Figure 3.7 RMSD values of CB1-AM6538 system against 5U09 and 5XR8 crystal structures. 100
Figure 3.8 RMSD of ligand against its initial conformation in CB1-AM841 and CB1-AM6538 systems. 101
Figure 3.9 Positions of the ligand in CB1-AM841 in replicate 2. 103
Figure 3.10 Positions of the ligand in CB1-AM841 in replicate 3. 104
Figure 3.11 PCA plots of principal component 1 and 2 for transmembrane backbone atoms of CB1-Apo, CB1-AM841 and CB1-AM6538 systems. 105
Figure 3.12 Motions observed in PC1 of CB1 simulation systems. 107
Figure 3.13 Porcupine plot for PC1 of CB1-Apo system; Replicates 1 and 2. 108
Figure 3.14 Porcupine plot for PC1 of CB1-Apo system – Replicate 3. 109
Figure 3.15 Porcupine plot for PC1 of CB1-AM841 system replicates. 110
Figure 3.16 Porcupine plot for PC1 of CB1-AM6538 system. 112
Figure 3.17 Distance between the COM of carbon atoms comprising the aromatic rings of Phe200(3.36) and Trp6.48(356) of the CB1-Apo system. 113
Figure 3.18 Conformations of Phe200(3.36) and Trp6.48(356) in replicate 2 of CB1-Apo system. 114
Figure 3.19 Distance between Cζ and Cγ atoms in the residue pairs of Arg214(3.50)-Asp338(6.30) in all three systems considered in the study. 116

Figure 3.20 Distance between Cζ and Cγ atoms in the residue pairs of Arg214(3.50)-Asp(3.49) in all three systems considered in the study. 117
Figure 3.21 State of the lipid access channel found between TM1 and TM7 in replicate 3 of the CB1-Apo system at 35 ns and 40 ns. 118
Figure 4.1 Changes in ligand position in replicates 1 and 2 of CB1-AM11542 system. The initial position is shown in yellow and final position is shown in pink). The cartoon representation depicts the initial state of the receptor. 128
Figure 4.2 Changes in ligand position in replicates 1 and 2 of CB1*-MK0364 system. 129
Figure 4.3 PCA plots of principal component 1 and 2 for transmembrane backbone atoms of CB1-AM11542 and CB1*-MK0364 systems. 130
Figure 4.4 Porcupine plots for PC1 of CB1-AM11542 system. 131
Figure 4.5 Porcupine plots for PC1 of CB1*-MK0364 system. 133
Figure 4.6 Distance between the COM of carbon atoms comprising the aromatic rings of Phe200(3.36) and Trp356(6.48) in CB1-AM11542 and CB1*-MK0364 systems. 135
Figure 4.7 Changes in rotameric states of Phe200(3.36) and Trp356(6.48) in the replicate 2 of the CB1-AM11542 system. 136
Figure 4.8 Distances between the Cζ carbon of Arg214(3.50) and (a) Cγ of Asp338(6.30) and (b) Cγ of Asp213(3.49) in CB1-AM11542 system. 138
Figure 4.9 Initial and final conformations of residues involved in the arginine cage 'ionic lock' in the CB1-AM11542 system 139
Figure 4.10 Distances between the Cζ carbon of Arg214(3.50) and (a) Cγ of Asp338(6.30) and (b) Cγ of Asp213(3.49) in CB1*-MK0364 system. 141
Figure 4.11 Initial and final conformations of residues involved in the arginine cage 'ionic lock' in the CB1*-MK0364 system. 142
Figure 4.12 Changes conformation of Tyr7.35 in replicate 1 of CB1-AM11542 system. 143
Figure 4.13 Binding pocket volume calculated per 50 ns for CB1-AM11542 and CB1*-MK0364 systems. 145
Figure 5.1 Docked pose of CP55940 (6) into CB2. 153
Figure 5.2 Apo CB2 protein post embedding into the system. 154
Figure 5.3 (a)Position of ligand post equilibration of CB2-CP55940 system. 155
Figure 5.4 RMSF plots of CB2-Apo and CB2-CP55940 systems. 156
Figure 5.5 RMSD values of CB2-Apo and CB2-CP55940 systems against the crystal structure 5ZTY. 158
Figure 5.6 RMSD values of CP55940 (6) against its initial position throughout the trajectory of CB2-CP55940 system. 159
Figure 5.7 Changes in ligand position through replicate 1 of CB2-CP55940 system. 160
Figure 5.8 Changes in ligand position through replicate 2 of CB2-CP55940 system. 161
Figure 5.9 PCA plots of principal component 1 and 2 for transmembrane backbone atoms of CB2-Apo and CB2-CP55940 systems. 162

Figure 5.10 Porcupine plots for PC1 of CB2-Apo system..... 164
Figure 5.11 Porcupine plots for PC1 of CB2-CP55940 system..... 166
Figure 5.12 Distance between the COM of carbon atoms comprising the aromatic rings of Phe117(3.36) and Trp258(6.48) in CB2-Apo and CB2-CP55940 system..... 168
Figure 5.13 Changes in rotameric states of Phe117(3.36) and Trp258(6.48) in the replicate 3 of the CB2-Apo system..... 169
Figure 5.14 Distance between Cζ and Cγ atoms of Arg131(3.50)-Asp240(6.30) and Arg131(3.50)-Asp130(3.49) of the CB2-Apo system. 171
Figure 5.15 Initial and final conformations of residues involved in the 'ionic lock' in the CB2-Apo system..... 172
Figure 5.16 Distance between Cζ and Cγ atoms of Arg131(3.50)-Asp240(6.30) and Arg131(3.50)-Asp130(3.49) of the CB2-CP55940 system. 173
Figure 5.17 Initial and final conformations of residues involved in the 'ionic lock' in the CB2-CP55940 system..... 175
Figure 5.18 CB2-Apo model post equilibration 176
Figure 5.19 CB2-Apo model of replicate 3 after 500 ns simulation..... 176
Figure 6.1 Principle of [^{35}S]GTPγS Assay. 188
Figure 6.2 Effect of selected ligands on [^{35}S]GTPγS binding in CHO-CB1 and CHO-CB2 membranes 191
Figure 6.3 Binding modes of ligands docked to an inactive CB1 model. 197
Figure 6.4 Binding modes of ligands docked to CB1* model..... 200
Figure 6.5 Binding modes of ligands docked to CB2 model..... 203
Figure 6.6 Binding modes of fenofibrate (38) docked to the CB2 model. 204
Figure 7.1 Crystal Structure of 6KQI.. 210
Figure I.1 Sequences of CB1 and CB2 Receptors 244
Figure II.1 Ramachandran plots for re-engineered CB1 and CB2 models..... 246

Table of Tables

Table 1.1 List of cannabinoid drugs approved in various countries 32
Table 1.2 Summary of the cannabinoid crystal structures released to date. 38
Table 2.1 Percentage of sequence identity and gaps found in the local alignment of potential template sequences with CB1 sequence. 67
Table 2.2 Changes made in re-engineered models in comparison to their corresponding crystal structure templates..... 75
Table 6.1 Ligands tested against cannabinoid receptors..... 186
Table 6.2 Compounds with reported ability to bind to CB1 and CB2..... 194
Table I.1 Percentage identity and similarity of lipid binding GPCRs against CB1..... 245
Table I.2 Percentage identity and similarity of lipid binding GPCRs against CB1..... 245
Table II.1 Agonists used in docking evaluation of CB1 receptor homology model..... 247
Table II.2 Antagonists used in docking evaluation of CB1 receptor homology model.. 248
Table II.3 Binding pocket contact residues interacting with COR167 (24) and COR170 (25) docked to the inactive CB2 model and the predominant interaction type observed. 249
Table III.1 Motions of individual helices observed in PC1 analysis of CB1-Apo, CB1-AM841 and CB1-AM6538 systems..... 250
Table IV.1 Motions of individual helices observed in PC1 analysis of CB1-AM11542 and CB1*-MK0364 systems..... 251
Table V.1 Motions of individual helices observed in PC1 analysis of CB2-Apo Systems and CB2-CP55940 systems..... 252
Table VI.1 Details of ligands tested on CB1 and CB2 using [^{35}S]GTPγS 253
Table VI.2 Details of ligands selected for binding mode analysis by molecular docking 254
Table VI.3 Binding pocket contact residues interacting with non-cannabinoids docked to the inactive CB1 model and the predominant interaction type observed. 255
Table VI.4 Binding pocket contact residues interacting with non-cannabinoids docked to the active CB1 model and the predominant interaction type observed. 256
Table VI.5 Binding pocket contact residues interacting with non-cannabinoids docked to the inactive CB2 model and the predominant interaction type observed. 257

Table of Abbreviations

(arranged in alphabetical order)

2-AG	2-arachidonyl glycerol
A2AR	Adenosine 2Aα Receptor
AAI	Aminoalkylindoles
AC	Adenylyl Cyclase
AT1AR	Angiotensin II type 1A Receptor
β1AR	β1-Adrenergic Receptor
β2AR	β2-Adrenergic Receptor
BSA	Bovine Serum Albumin
BRIL	b_{562}RIL construct
cAMP	Cyclic Adenosine Monophosphate
CB1	Cannabinoid Receptor 1
CB2	Cannabinoid Receptor 2
CBD	Cannabidiol
COM	Centre of Mass
CPM	Counts Per Minute
D2	Dopamine D2 Receptor
E-4-OH-Tam	E-4-OH-tamoxifen
ECL	Extra-Cellular Loop
EC	Extra-Cellular Half of the Helix
ECS	Endocannabinoid System
E-End	E-endoxifen
ERK	Extracellular Signal-Regulated Kinase

E-Tam	E-tamoxifen
GDP	Guanosine 5'-diphosphate
GIRK	G protein-Coupled Inwardly Rectifying Potassium Channels
GnRH	Gonadotropin-releasing Hormone
GPCR	G protein-Coupled Receptor
GRK	G protein-Coupled Receptor Kinases
GTP	Guanosine-5'-triphosphate
H1	Histamine H1 Receptor
HBA	Hydrogen Bond Acceptor
HBD	Hydrogen Bond Donor
ICL	Intra-Cellular Loop
IC	Intra-Cellular Half of the Helix
IFD	Induced Fit Docking
LP	Lower Part of the Transmembrane Helix
LPA1	Lysophosphatidic Receptor 1
MAPK	Mitogen-Activated Protein Kinase (*formerly known as ERK*)
MD	Molecular Dynamics
MS	Multiple Sclerosis
MSA	Multiple Sequence Alignment
NAM	Negative Allosteric Modulator
NMR	Nuclear Magnetic Resonance
OPM	Orientation of Proteins in Membranes
PAM	Positive Allosteric Modulator
PCA	Principal Component Analysis
PDB	Protein Data Bank

PKA	Protein Kinase A
PLCβ	Phospholipase Cβ
POPC	1-palmitoyl-2-oleoyl-sn-glycero-3-phosphocholine
SERM	Selective Estrogen Receptor Modulators
S1P1	Sphingosine-1-Phosphate Receptor 1
Δ^9-THC	Δ^9-tetrahydrocannabinol
TM	Transmembrane Helix
WHO	World Health Organisation
XRD	X-ray Diffraction
Z-4-OH-Tam	Z-4-OH-tamoxifen
Z-End	Z-endoxifen
Z-Tam	Z-tamoxifen

1 Introduction

1.1 G protein-Coupled Receptors

1.1.1 Structure, Function and Classification

G protein-coupled receptors (GPCRs) are a family of transmembrane receptor proteins that are involved in signal transduction[1]. They are the largest family of membrane proteins constituting about 3% of genes in the human genome and with nearly 800 receptors being found in humans[1,2]. GPCRs are the target for a majority of drugs produced and are hence dubbed the most successful pharmaceutical targets[3]. As their name suggests, they transmit cell signals by interacting with G proteins which bind to the guanosine nucleotides, guanosine-5'-diphosphate (GDP) and guanosine-5'-triphosphate (GTP). Structurally, GPCRs are characterised by an extracellular amino-terminus (N-terminus), seven largely hydrophobic α-helical transmembrane (TM) domains linked by three intracellular (ICL) and three extracellular loops (ECL), and an intracellular carboxyl-terminus (C-terminus). An eighth α-helix may also be present in certain proteins in the intracellular portion preceding the C-terminus. Figure 1.1 shows a general representation of a GPCR. These receptors show the highest homology in the transmembrane helices and the most variations in the termini and ICL3 loop.

An early classification of GPCRs based on protein sequence homology led to six different classes; class A comprised of rhodopsin-like receptors, class B - secretin receptor family, class C - metabotropic glutamate receptors, class D - fungal mating pheromones, class E - cyclic AMP receptors, and class F - smoothened or frizzled receptors[4]. An

alternative classification scheme introduced later classifies the GPCRs found in only vertebrates into five families based on sequence similarity: Glutamate family (class C) – 22 members, Rhodopsin family (class A) – 719 members, Adhesion family (related to class B) – 33 members, Frizzled family (class F) - 11 members and Secretin family (class B) – 15 members. This scheme, known by the acronym GRAFS, does not include Class D and E receptors as they are not found in vertebrates[2,5]. The length of the N-terminus varies according to the class of the ligand that binds to the receptor– it is generally short for monoamine and peptide receptors (10-50 amino acids) and longer for glycoprotein hormone receptors and the glutamate family receptors. Adhesion receptors possess the longest N-terminus[6].

Around half of the GPCR proteins found in humans are involved in sensory functions such as taste, olfaction, light perception and pheromone signalling and about 350 of the non-sensory receptors are involved in intermediary signalling[2]. As of March 2019, for 62 unique GPCRs there exist a total of 321 crystal structures in the Protein Data Bank (PDB) database[7]; of these 7 are complexed with a G protein. Class A GPCRs constitute 88% of the total available structures out of which 24% are present in their active state[8]. 87 receptors of class A, 8 receptors of class C and 26 of adhesion GPCRs are classified as orphan i.e. those receptors for which the endogenous ligands are not known[2]. A study in 2013[9] reported that only 7% of drugs found in the DrugBank[10] database had a GPCR as the underlying target (109 targets were GPCRs out of 1479 underlying targets for 1663 drugs) while 26% of the 1663 drugs approved till 2013 were found to be linked with GPCR activity. This implies that the drugs exert their pharmacological effects via a small fraction

of the potential target receptors. Yet, this fraction is dominated solely by the aminergic receptors thus leaving a bigger population of potential targets untapped[9].

1.1.2 Numbering Systems for GPCRs

Special numbering systems are used to index residues in GPCRs for the purpose of comparing mutations, conserved residues and (or) or ligand interactions across proteins[11]. GPCR protein residues discussed herein are numbered according to the Ballesteros-Weinstein numbering scheme which is specific to class A GPCRs[12]. According to this system, a residue is marked by its TM helix number followed by a locant. The locants are conferred depending on their location with respect to the most conserved residue in the TM helix. The most conserved residue within each TM helix, across all class A GPCRs, is assigned the locant 50; those residues succeeding it (in the direction of the C-terminus) are assigned locants greater than 50 while those preceding it (in the direction of the N-terminus) are assigned locants lesser than 50, in a linear order. E.g. 6.48 denotes a residue in TM6 two residues before the most conserved in that helix: Pro6.50. The most conserved residues in each helix along with their degree of conservation across class A is: **Asn1.50**: 98%, **Asp2.50**: 90%, **Arg3.50**: 95%, **Trp4.50**: 97%, **Pro5.50**: 78%, **Pro6.50**: 99%, **Pro7.50**: 88% [8]. Residues located within the ECL and ICL are numbered using their global position within the protein amino acid sequence.

Alternative numbering schemes for class A GPCRs include those by Oliveira[13] and Baldwin-Schwartz[14,15] where the residue positions are numbered from helix extracellular ends. The objective is to assign the same numbers to the residues located at the same depth in the membrane. E.g. 6.13, 5.13 (Oliveira) or V-13, V1-13 (Baldwin-Schwartz). Class B

(both Adhesion and Secretin), Class C, and Class F use Wootten[16], Pin[17], and Wang[18] systems respectively.

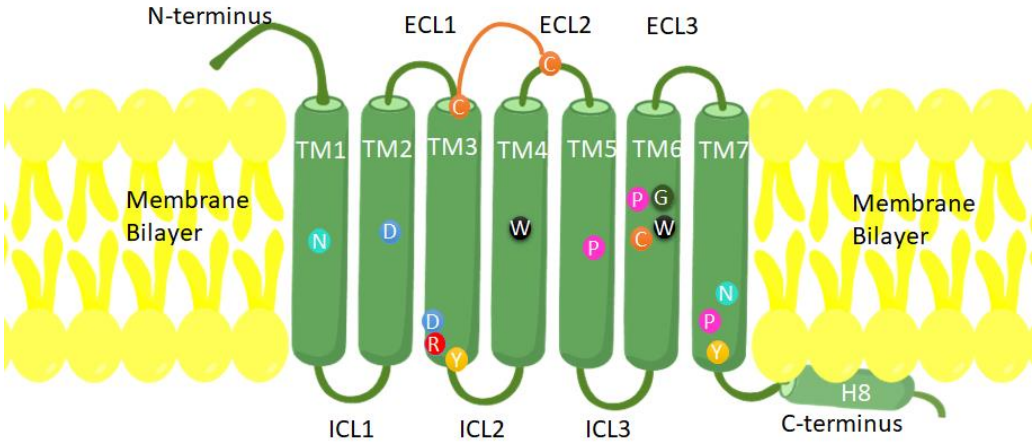

Figure 1.1 General representation of GPCRs. *Conserved residues Asn1.50, Asp2.50, Arg3.50, Trp4.50, Pro5.50, Pro6.50, Pro7.50 are given in their one-letter code form in each transmembrane helix. Cysteine disulphide bridge commonly found in class A GPCRs is shown in orange, connecting TM3 and ECL2. Motifs shown: TM3 – DRY, TM6 – CWGP, and TM7-NPXXY(only NPY shown)*

1.1.3 Residues and Motifs Involved in Activation of Class A GPCRs

Interaction with a ligand provokes a structural rearrangement in GPCRs – agonists, in particular, trigger changes that enable the binding of the G protein heterotrimeric complex to the cytosolic side of a receptor. Almost all class A GPCRs have a similar activation mechanism[19]. One of the common conformational changes observed during activation is the outward swing of the lower half of TM6 in tandem with changes in TM5. The swing has been likened to that of a vertical seesaw with the lower half of TM6 moving away from the orthosteric binding pocket to accommodate the G protein and upper half moving towards the binding pocket. Pro6.50 creates a kink in TM6 around which this swing is centred – thus functioning as a 'hinge'[19]. This residue forms a part of the highly

conserved CWXP motif in class A GPCRs. TM7 experiences a rearrangement primarily in the intracellular part. These rearrangements observed in the TM helices create or break inter-helical bonds which function as 'microswitches'. A switch can be considered as a rotamer change in the side chain of a conserved residue[20]. Some of the well-known GPCR microswitches are shown in Figure 1.2 for chemokine receptor 4, rhodopsin, the β2-adrenoreceptor (β2AR) and Adenosine 2A receptor (A2AR).

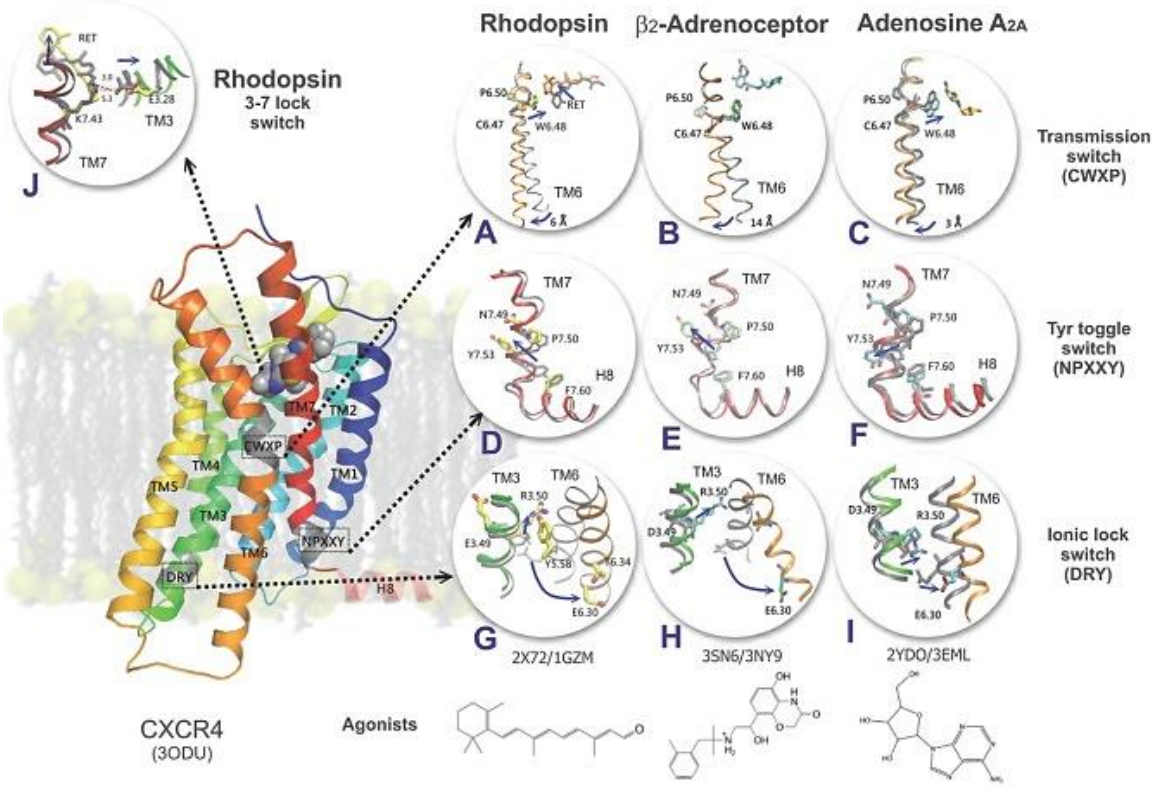

Figure 1.2 Major molecular switches commonly found in GPCRs that are involved in receptor activation. *Source: Trzaskowski et al.19. The images in circles show the superposition of inactive vs active state of the labelled proteins. Their PDB IDs are given below the superpositions (active/inactive). The agonists of the active state structure for each protein is given at the bottom of the image.*

1. **Ionic lock of TM3:** Arg3.50 forms an interhelical salt bridge interaction with Asp/Glu6.30 and Asp3.49 in the inactive state[21,22]. This was first studied in the inactive state crystal structure of bovine rhodopsin and gonadotropin-releasing hormone receptors (GnRH) respectively[23]. Upon activation, the swing of the lower half of TM6 away from the orthosteric binding pocket breaks the salt bridge interaction between Arg3.50 and Asp6.30 in TM3 and TM6. This breakage has been suggested to be a trigger for activation in certain GPCRs [19]. Similarly, the weakening of the Arg3.50-Asp3.49 bond has been proven to favour activation in GnRH[21]. However, an acidic residue at position 6.30 is only 30% conserved which means that many receptors do not exhibit this salt bridge. In these cases other interactions may occur; for example, the histamine H1 receptor exhibits a hydrogen bond between Tyr3.60 and His6.31[19]. Regardless of whether the salt bridge is formed or not, in GPCRs, the residues around Arg3.50 are said to form an 'arginine cage' whereby the rotameric state of the residue is constrained[24].
2. **NPXXYX(5,6)F motif:** This is a highly conserved motif located at the intracellular end of TM7. Like Pro6.50 in TM6, Pro7.50 creates a kink around the motif in TM7. In the inactive conformers of rhodopsin and serotonin 2C receptors, Tyr7.53 interacts with the Phe7.60 residue on H8 as if to 'lockdown' on H8[25,26]; in an active receptor, state Tyr7.53 participates in a hydrophobic cluster between TM6 and TM7. In an intermediate state, as seen in β2AR and A2AR, the tyrosine side chain changes its rotamer conformation and points upwards, towards the centre of the receptor. In this rotamer state, it is involved

in a hydrogen bond network with structural water molecules[25]. The Tyr7.53-Phe7.60 interaction is not observed in β2AR and A2AR in both their active and inactive state crystal structures[19].

3. **Rotamer Toggle Switch:** This switch involves a shift in the rotamer of Trp6.48 of the CWXP motif. In the crystal structure of muscarinic M2 and M3 receptors, it was found that the rotamer state of Trp6.48 did not influence the functional state of the receptor[27,28]. However, in rhodopsin and the A2AR receptor, a shift in the rotamer state was observed[29] on comparing active and inactive states. Here, the rotamer shift and the TM6 swing were observed to be stabilised by the cognate ligand through steric interactions[24,30,31]. In serotonin 2A receptor, the aromatic interaction between serotonin and Phe6.52 serves as a trigger for the conformational shift in Trp6.48. In β1 adrenergic receptor (β1AR) and β2AR, the ligand does not directly interact with Trp6.48; the TM6 swing is instead mediated through the movement of TM5. Thus, the role of Trp6.48 in receptor activation is quite case-specific and nearly 30% of GPCRs have a different residue at 6.48[20]. The switch has hence been renamed as a 'transmission switch'[32].

Rhodopsin also contains 3-7 lock switch (as seen in Figure 1.2) between TM3 and TM7. Further information regarding this switch can be found in the review by Trzaskowski *et al.*[19].

1.1.4 Signal Transduction by GPCRs

Guanine nucleotide-binding proteins or G proteins are heterotrimeric proteins with three subunits: α, β and γ. G_α and G_γ are attached to the plasma membrane by lipid anchors.

In an inactive G protein, the G_α subunit is bound to GDP. The binding of an agonist to a GPCR induces a structural re-arrangement in the inactive receptor. This is followed by the intracellular G protein preferentially coupling to the active receptor and forming a GPCR-G protein dimer. Among class A GPCRs, residues in cytoplasmic ends of TM2, TM3, TM5, TM6 and TM7, and also ICL2, ICL3 and H8 are in contact with G_α, and residues in the cytoplasmic ends of TM1, ICL1 and H8 are in contact with G_β[33]. The coupling leads the α-subunit to undergo a conformational change; GDP is subsequently released due to the disruption of its binding site and is replaced by GTP. G_α dissociates from the trimeric complex and the subunits go on to activate their respective effector proteins and secondary messengers. For instance, $G_{\alpha s}$ can activate adenylyl cyclase (AC), resulting in increased cyclic adenosine monophosphate (cAMP) levels. This, in turn, can induce protein kinase A (PKA) activation. PKA is a serine-threonine kinase that phosphorylates transcription factors, other kinases, and GPCRs[34]. Activation terminates when GTP hydrolyses to GDP and the G protein trimer is re-formed (Figure 1.3).

Broadly classifying, there are 4 types of G_α subunits with different roles in signal transduction :

1. $G_{\alpha s}$ is involved in the stimulation of AC
2. $G_{\alpha i/o}$ functions in the inhibition of AC, activation of extracellular signal-regulated kinase-mitogen-activated protein kinase (ERK/MAPK), downregulation of Ca^{2+} channels, and the activation of GIRK (G protein-coupled inwardly rectifying potassium) channels.
3. $G_{\alpha q/11}$ is responsible for activating phospholipase Cβ (PLCβ) and upregulating K^+ channels.

4. $G_{\alpha 12/13}$ activates phospholipase Cε, phospholipase D, the Rho guanidine nucleotide exchange factors, and upregulates E-cadherin mediated cell adhesion[35].

G_β and G_γ activate PLCβs, phosphatidyl inositol-3 kinases, c-Jun N-terminal kinase, and GIRK channels and also downregulate Ca^{2+} channels. With the aid of genomic analysis currently, 16 G_α, 5 G_β and 12 G_γ subunits have been cloned and sequenced[36].

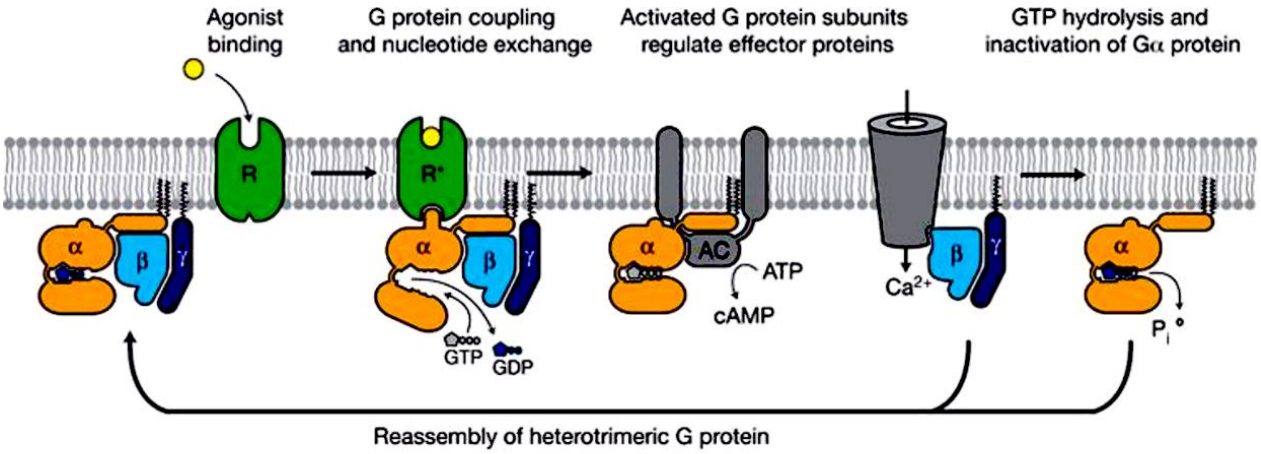

Figure 1.3 Working mechanism of GPCRs. *Source: Rasmussen et al.[37]. Agonist molecule binding to a receptor at its basal state (R) transforms it into the active state (R*). This leads to the heterotrimeric (αβγ) GDP-bound G protein complex to couple to the active receptor. Upon coupling, GDP, is released and GTP takes its place, and the GTP bound Gα subunit dissociates from the trimer. The GTP-Gα and Gβγ subunits regulate the adenylyl cyclase (AC) and calcium channels (Ca2+) respectively. Post-hydrolysis of GTP, the heterotrimeric unit reassembles.*

When β-arrestin binds to a GPCR, it leads to desensitisation and inhibits interaction with G proteins. There are four known arrestins: visual arrestin and cone arrestin which are present in the retina, β-arrestin-1, and β-arrestin-2[38]. These proteins are thought to reduce G protein signalling by creating a steric hindrance and thus preventing the G protein's

interaction with the respective GPCR at ICL2 and ICL3[39,40]. This uncouples GPCRs from the signal transduction leading to desensitisation of the secondary messenger pathway[41]. This manner of desensitisation requires a co-ordinated response by G protein receptor couples kinases (GRK) and β-arrestins[42]. Apart from these kinases and arrestins, desensitisation can also occur via protein kinase C or PKA mediated phosphorylation of the GPCR, receptor degradation (in lysosomes) and regulation of gene transcription or translation[34].

1.1.5 Biased Agonism and Allosterism in GPCRs

GPCRs are known to exhibit biased signalling and pleiotropy[43]. Certain GPCRs can bind to more than one kind of G protein or β-arrestin to activate heterogeneous signalling pathways that elicit different functional responses in a cell. For example, when angiotensin binds to the Angiotensin II type 1A (AT1AR) receptor, $G_{\alpha q}$ proteins are recruited leading to inositol triphosphate production which results in vasoconstriction and fluid retention. The activation process also recruits β-arrestins leading to a G protein independent signalling which gives out a positive ionotropic and cardioprotective response[44]. This is an example of unbiased or canonical signalling. On the contrary, when the angiotensin II analogue SII binds to AT1AR, only β-arrestin dependent MAPK pathway is activated without any G protein coupling. This is an example of biased signalling or in this case biased agonism[45](Figure 1.4). Biased signalling can be highly useful to develop drugs with high specificity. Carvedilol, a β-adrenergic agonist, has been shown to stimulate β-arrestin mediated cell survival signalling pathways and inhibit the G protein-mediated toxic effect of catecholamines. It is suggested that carvedilol might significantly improve survival in patients with heart failure compared with other unbiased beta blockers[46]. Sometimes biased

ligands can also help counteract the adverse effects caused by activation of a receptor. Nicotinic acid, the agonist of niacin receptor GPR109A, decreases serum-free fatty acids through the G protein-signalling but causes cutaneous flushing due to activation of the β-arrestin pathway. The biased ligand MK-0354 being G protein biased does not invoke the flushing, thus posing as an ideal candidate for hyperlipidaemia[47].

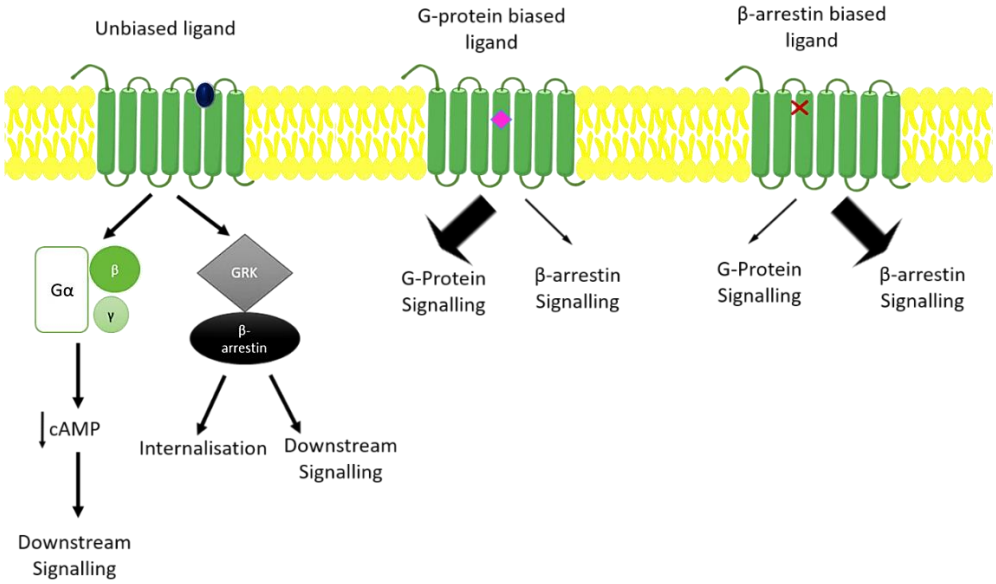

Figure 1.4 Biased agonism in GPCRs. *An unbiased ligand potentially recruits both G protein and β-arrestin for downstream signalling. Contrarily, a biased ligand preferentially activates either G protein signalling or β-arrestin signalling over the other.*

Allosterism is a commonly observed feature in GPCRs. An allosteric site on a receptor is a binding site other than the designated orthosteric binding site[48]. An allosteric ligand (or a modulator) upon binding to the allosteric site causes a conformational change in the protein such that the receptor's interaction with other molecules (such as ligands) or proteins is altered. Generally, modulators are of two types: a positive allosteric modulator (PAM) promotes binding of an orthosteric ligand by increasing receptor's affinity towards

the ligand, while a negative allosteric modulator (NAM) decreases the affinity and inhibits binding of an orthosteric ligand[49]. Alternatively, allosteric modulators can either increase or inhibit the receptor signalling. The NAM or PAM activity shown by an allosteric ligand may sometimes be probe dependent, i.e. the activity could vary according to the bound orthosteric ligand. Some of the GPCRs that are reported to show allosterism include muscarinic, dopaminergic, α-adrenergic, chemokine, serotonin, adenosine and cannabinoid receptors with gallamine, zinc, amiloride, I-TAC, oleamide, PD 81,723 and ORG27569 (Section 1.2.3.2, Figure 1.13, Ligand (16)) respectively acting as modulators[50–52]. Indeed the binding of a G protein to the GPCR itself is seen as an example for allosterism[50]. Some of the common allosteric locations for GPCRs include the crevices or channels between TM helices, the extracellular loops and N-terminus, the GPCR-G protein interface, the intracellular region near the G protein coupling site, extracellular sites on the outer sides of the TM bundle or ion modulation (at various locations, including inter-membrane TM regions)[50,53].

1.1.6 Challenges Faced in GPCR Drug Discovery

Despite the varied functionality of GPCRs and their prolific potential as targets, drug discovery for pathophysiological conditions mediated by these receptors still proves to be quite challenging. This is due to the inherently complex nature of GPCRs, which in turn can be attributed to their plasticity and ability to exhibit biased signalling. As biased signalling demonstrates, ligands of diverse chemical classes have the potential to activate relatively hidden pathways that the corresponding receptor initiates. In this direction, Kobilka and Granier suggest the crystallisation of receptors at different states of activation and de-sensitisation – bound to different G proteins, β-arrestins and GRKs, (as GRKs

phosphorylate the intracellular loop and C-terminus in a ligand-dependent manner like the former two) can reveal the finer details as to how the bound ligand or ligands initiate activation or stabilise the inactive state[54]. Indeed, a time-resolved mass spectrometry study and a crystal structure of a GPCR-G protein assembly of β2AR showed that the amino acids involved in the initial interaction between the GPCRs and their G proteins might be different from the ones seen in their nucleotide-free GPCR-G protein models[55,56]. Similarly, GPCR dimer crystal structures can help us understand the physical aspects of the crosstalk between two GPCRs and provide insights into signalling and allosteric modulation[57,58].

Given the importance of high-quality GPCR structures to furthering our understanding, the dearth of structural information available for many GPCRs is a significant reason as to why drug discovery in this area is still a formidable challenge. Initial studies on GPCR structure mainly relied on 2D crystals, with bacteriorhodopsin being the earliest one to be crystallised[59]. Although the rhodopsin protein had been discovered in frogs as early as 1977[60], it was only in the year 2000 that the 3D crystal structure of ground state bovine rhodopsin was released through X-ray diffraction (XRD)[23]. Low-level expression of receptors, instability in detergent, proteolysis of loop membranes and/or low yield of the functional protein during purification, poor thermodynamic stability and difficulty in obtaining crystals of size and quality apt for XRD analysis are some factors that contribute to the hurdles faced in GPCR crystallisation [61–63]. To counteract this, GPCRs are often engineered to promote stability by:

1. co-crystallising with high-affinity ligands,
2. introducing thermostabilising mutations,

3. truncating disordered regions, termini and (or) or lengthy extracellular domains,
4. fusing receptors with soluble proteins such as T4- lysozyme or cytochrome, b_{562}RIL (BRIL) in place of intracellular loops or N-terminal regions,
5. complexing the receptor with mini-G proteins to study the active state of the receptor, as well as receptor antibody Fab fragment complex formation[37,62,64–66].

These modifications are made either independently or in combination with other techniques such as usage of a synchrotron microfocus beam suitable for the protein crystal size, lipidic cubic phase for crystallization, novel detergents for protein extraction and purification, and high-level recombinant expression systems for better protein expression[61]. Nuclear Magnetic Resonance (NMR) spectroscopy is also used to determine protein structure in a liquid phase. Indeed the amount of GPCRs deposited per year is on the rise; in 2018 alone, 72 new GPCR crystal structures were deposited (Figure 1.5). However, artefacts due to crystal packing and crystal structure imperfections, and costs involved in structure elucidation are yet to be overcome. That said, experimental methods are not the only means by which protein structures can be studied: computational or *in silico* studies can provide a fast, cost-effective alternative means to predict, refine and analyse GPCRs. Indeed, computational methods specific to GPCRs study are being continually developed and assessed[66–70]. More about some of these computational methods will be discussed in the forthcoming sections and chapters.

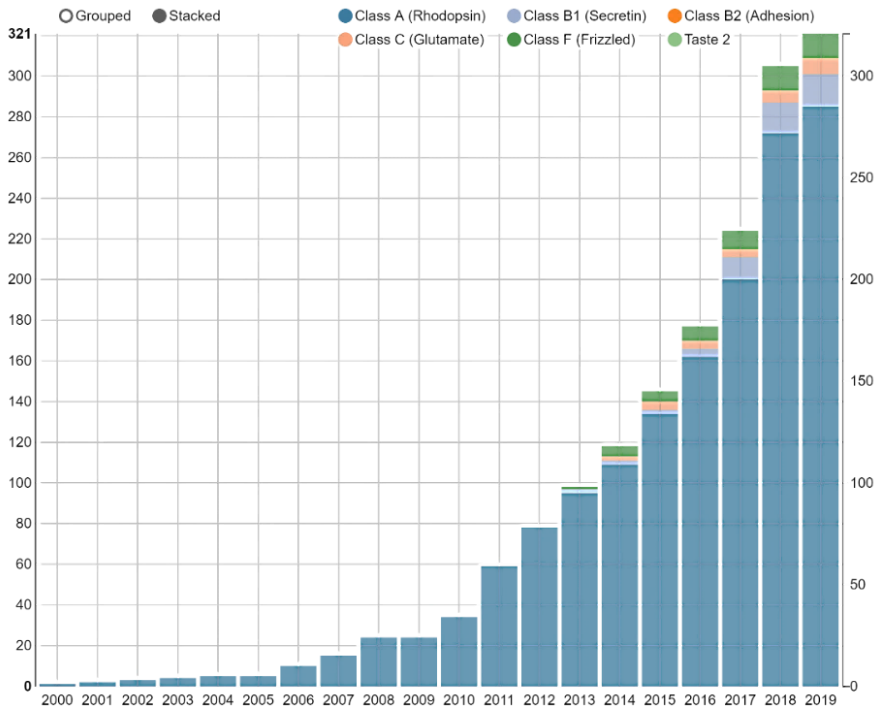

Figure 1.5 Number of GPCR crystal structures found in the PDB database per year *(until March 2019) Source: GPCRdb*[8].

1.2 The Endocannabinoid System and Cannabinoid Receptors

Lu and Mackie describe the endocannabinoid system (ECS) as a widespread neuromodulatory system that influences the development of the central nervous system and its responses to endogenous and environmental stimuli. It comprises the cannabinoid receptors, CB1 and CB2, the endogenous cannabinoids (endocannabinoids), and the enzymes responsible for the synthesis and degradation of the endocannabinoids[71].

The cannabinoid receptors, Cannabinoid Receptor 1 (CB1) and Cannabinoid Receptor 2 (CB2) belong to the α-subgroup of class A of GPCRs. Frederiksson *et al.* classified them under the MECA receptor cluster of the α-subgroup which also consists of melanocortin receptors, endothelial differentiation G coupled receptors (lysophosphatidic

and sphingosine-1 phosphate receptors), adenosine binding receptors, and three orphan GPCRs (GPR-3, -6, and -12)[5].

1.2.1 Cannabinoid Receptor 1

Prior to the discovery of CB1, cannabinoids were thought to exert their effects by interacting with the plasma membrane as these compounds are lipophilic in nature[72]. The discovery and structure elucidation of Δ^9-tetrahydrocannabinol (Δ^9-THC) (3) (Section 1.2.3.1.1, Figure 1.8, Ligand (3)), the primary component of the cannabis plant, by Raphael Mechoulam and Yechiel Gaoni in 1964 led to speculation that a distinct receptor must exist on which the compound would act[73,74]. This receptor was subsequently discovered when Devane *et al.* studied the binding of [^{3}H]CP55940 (6) (Section 1.2.3.1.1, Figure 1.9, Ligand (6)) in the brains of mice. It was reported that the bound protein has a high affinity for cannabinoids, is stereoselective, and pharmacologically distinct[75]; this receptor was designated as CB1. The human CB1 gene is present on chromosome 6q14-q15 and encoded by the gene CNR1. Interestingly, the coding region of CNR1 has no introns but just a single exon sequence which is touted to accelerate the protein expression process[76,77].

CB1 receptors are present in abundance in the brain cortex of humans, specifically within the association and limbic cortices, and in lower levels in the motor and primary sensory regions[78]. They have also been found to be located presynaptically in γ-aminobutyric acid-nergic neurons and also in the hippocampus. CB1 has been shown to form both homo- and heterodimers (with dopamine D2 receptor and opioid receptors)[79]. Generally found in mammals and a few other vertebrates, the human CB1 is 472 amino acid residues in length while that found in other mammals has 473 residues. It also shows high conservation across species. The human CB1 has 97% sequence identity with rat and

mouse CB1, while rat CB1 has 100% amino acid sequence identity and 95% nucleic acid sequence identity with mouse[77]. The receptor possesses a long N-terminus of approximately 112 residues and a C-terminus of about 57 residues.

CB1 possesses almost all of the most conserved residues of class A GPCRs (Asn134(1.50), Asp163(2.50), Arg214(3.50), Trp241(4.50), Pro358(6.50) and Pro394(7.50)) except in TM5 where Leu286(5.50) is present in place of the most conserved proline. The lack of proline makes TM5 in CB1 more rigid compared to that of other receptors where Pro5.50 creates a bulge and promotes unwinding of residues from 5.45 to 5.48 to relieve geometric clashes and aid in orienting ligand interactions[80]. Pro5.50 is also touted to be essential for activating in other class A receptors while in CB1, a Leu5.50Pro mutation disrupted signalling[81,82]. Due to the absence of a conserved residue, for sequence comparison studies or alignment with other class A GPCRs, Tyr294(5.58) in TM5 of CB1 is aligned with the second most conserved residue (Tyr5.58 for class A) of the other receptor to maintain the end-to-end alignment of helix sequences[83]. CB1 also has other standard motifs of class A such as DRY in TM3, CWXP (present as CWGP) in TM6 and NPXXY (present as NPIIY). However, instead of the characteristic disulphide bridge between TM3 and ECL2 of class A GPCRs, CB1 receptor has a disulphide bridge within ECL2 formed between Cys256 and Cys264 (amino acid sequence of CB1 is given in Appendix 1, Figure I.1).

1.2.1.1 Signalling in CB1

CB1 signals primarily via $G_{\alpha i}$ and $G_{\alpha o}$[84] and exhibits high affinity for both G protein subtypes[85]. CB1 also favours $G_{\alpha s}$ dependent-signalling in specific cell types, under certain conditions, such as when $G_{\alpha i}$ activation is limited, on simultaneous activation with other

$G_{\alpha i}$ linked GPCRs, or based on the type of agonist bound to it[86,87]. Cannabinoid agonists WIN55,212-2 (8) (Section 1.2.3.1.1, Figure 1.10, Ligand (8)) and N-arachidonoyl dopamine have also been shown to activate $G_{\alpha q}$ signalling when bound to CB1[88,89]. The functional selectivity of cannabinoids also allows certain ligands to function as agonists in some pathways and antagonists in others. A 2005 study compared the influence of structurally distinct cannabinoid ligands on $G_{\alpha i}$ protein coupling and found that desacetyllevonantradol acted as an agonist for $G_{\alpha i1}$ and $G_{\alpha i2}$ but acted as an inverse agonist for $G_{\alpha i3}$. (R)-methanandamide, on the contrary, acted as an inverse agonist for $G_{\alpha i1}$ and $G_{\alpha i2}$ and as an agonist for $G_{\alpha i3}$[90].

1.2.1.2 History of CB1 Structure Prediction

In 1995, Bramblett *et al.* published a putative model of CB1 using a variety of methods to determine helix length; hydrophobic and variability moment vectors were used to identify the transmembrane helix ends and delineate the orientation of each helix within the lipid membrane. This work also described a tentative helical bundle based on a possible helical arrangement of the rhodopsin molecule[83]. Later, a CB1 model with the transmembrane helices based on the electron density map of bacteriorhodopsin was constructed and possible binding sites for Δ^9-THC (3) were analysed[91]. After the publication of the crystal structure of bovine rhodopsin in 2000, Shim *et al.* studied the binding of non-classical cannabinoid agonists on a homology model built with a bovine rhodopsin template using a combination of Monte Carlo and Molecular Dynamics (MD) simulations[92]. Since then there have been many reports of CB1 receptor homology models constructed using different templates, namely rhodopsin, the β2AR and A2AR; these models (in conjunction with mutation studies) have shed light on structural information

such as the identification of residues that form the orthosteric binding pocket, the toggle switches that activate the receptor, the role of loops in respect to ligand binding and maintaining structural stability, to mention a few[92–101]. In the year 2016, the very first crystal structure of inactive human CB1 receptor bound to the antagonist AM6538 (18) (Section 1.3, Figure 1.14 and Table 1.2), was released[102]. This was followed by the release of another inactive crystal and three active crystal structures, one of which is complexed with a $G_{\alpha i}$ protein[103–105]. The crystal structures will be discussed in detail in forthcoming sections of this report (see Section 1.3 and Table 1.2).

1.2.2 Cannabinoid Receptor 2

In 1993, a peripheral cannabinoid receptor was discovered in a study that attempted to explain certain pharmacological properties of Δ^9-THC (3) such as immunosuppression, anticonvulsive effects and attenuation of vomiting; this was designated the CB2 receptor[106]. Human CB1 and CB2 receptors have a sequence identity of 44% overall, and 68% between their TM helices. In contrast to the high homology observed in CB1 across vertebrates, cloned mouse CB2 receptor shows only 82% and 93% sequence identity with the human and rat CB2 receptors respectively. The human CB2 gene is present on the chromosome 1p36.11 and encoded by the gene CNR2[77].

CB2 receptors are localised in sites of immune regulation (the spleen, tonsils and thymus) and expressed in all the haematopoietic stem cells such as lymphocytes, natural killer cells, macrophages, mast cells and neutrophils[107]. Initially thought to be expressed only in the peripheral tissues, they were later found in the microglia[108] and very small amounts in the brainstem[109]. They also protect the brain microglia from neurotoxicity by modulating the release of anti- or pro-inflammatory cytokines[110]. CB2 has also been

suggested to form homo- and heterodimers like CB1, but CB2 dimerization has not yet been explored in depth[111].

The human CB2 receptor consists of 360 amino acid residues. In addition to the DRY motif characteristic of class A, the CWXP motif is present as CWFP and the NPXXY motif is present as NPVIY. The presence of glycine in CWXP of CB1 (Section 1.2.1) renders TM6 of CB1 more flexible than that of CB2[112]. Similar to CB1, CB2 also has a disulphide bond formed within ECL2 between Cys174 and Cys179, thus deviating from the characteristic of class A. It also lacks a proline at position 5.50 and has a leucine instead. Hence, for sequence comparison studies or alignment with other GPCRs the residue Tyr210(5.58) of CB2 is aligned with Tyr5.58 of most other GPCRs[112] (amino acid sequence of CB2 is given in Appendix 1, Figure I.1).

1.2.2.1 Signalling in CB2

Similar to CB1, CB2 signals mainly via $G_{\alpha i}$ and $G_{\alpha o}$[84] proteins; however, CB2 shows notably lower affinity for $G_{\alpha o}$ in comparison to $G_{\alpha i}$[85]. CB2 binds poorly with $G_{\alpha s}$ owing to the rigidity of its TM6. It has been postulated that even for CB1 (with its comparative flexibility of TM6) to bind to $G_{\alpha s}$, the TM6 should move further away than that seen in its crystal complex with $G_{\alpha i}$[104]. As established earlier, the CWFP motif restricts the movement of TM6 and impedes the complexing with $G_{\alpha s}$. Cannabinoid ligands also exhibit functional bias at CB2. Screening cannabinoid ligands at AC inhibition and ERK-MAPK activation pathway assays revealed the variations in ligand concentration required for each cannabinoid to successfully inhibit or stimulate the respective pathways[113]. Studies have also shown the bias exhibited by prominent cannabinoid agonists with respect to receptor internalisation, trafficking and signalling[114–116].

1.2.2.2 History of CB2 structure prediction

The very first 3D model of CB2 in its inactive form was built by Song *et al.*[97]. In order to determine the helical ends, the periodicity in hydrophobicity and variability of the sequence were analysed through Fourier-transform analysis. Cysteine scanning accessibility mutagenesis was used to test the receptor bundle, and relative helix heights were adjusted to data from GPCR mutation studies. The aim of developing the CB2 model was to provide a structural explanation for the selectivity of CB2 or CB1 by WIN-55,212-2 (8)[97]. Following this, Gouldson *et al.* generated a CB2 model based on rat β2AR to study the binding of cannabinoid antagonist SR144528 (11) (Section 1.2.3.1.2, Figure 1.11, Ligand (11))[117]. Following the release of the crystal structure for bovine rhodopsin, Xie *et al.* published a homology model for CB2 using rhodopsin as the template for transmembrane regions[118]. 10 protein sequences were utilised to identify helical regions via multiple sequence alignment and loops were built using protein backbones identified from the PDB. Helix tilt and packing properties, inter-helix hydrogen bonding interactions, potential disulphide bridges and conserved residues were some of the aspects analysed in the study. Many studies followed suit using rhodopsin proteins, human sphingosine-1 phosphate receptor 1 (S1P1), human β1AR and β2AR, and human A2AR as templates for modelling to study potential binding sites and motifs on CB2, CB1 or CB2 selectivity among cannabinoid ligands and virtual screening for rational drug design[97,119–126]. In the year 2019, a crystal structure for the inactive form of CB2 co-crystallised with the antagonist AM10257 (23) (Section 1.3, Figure 1.14 and Table 1.2) was released[127]. Details regarding the crystal structure will be discussed in detail in the forthcoming sections (Section 1.3 and Table 1.2).

1.2.3 Cannabinoid Ligands

Generally, the ligands of GPCRs can be classified into full agonists, partial agonists, neutral antagonists (antagonists) and inverse agonists depending on their activity (Figure 1.6).

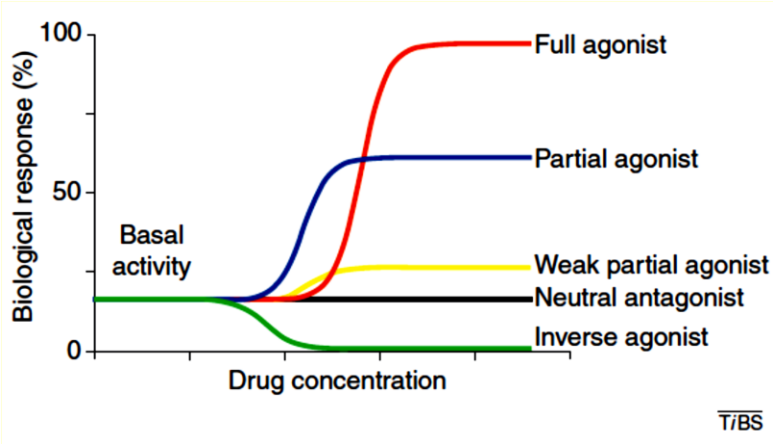

Figure 1.6 Pharmacological activity of different ligands. *Source: Tate, 2012*[128]

An agonist is a drug molecule which, upon binding to the receptor, pushes it towards an active state. Those agonists with an intermediate efficacy, which even when bound to all available receptors elicit only a submaximal tissue response, are called partial agonists. Full agonists, on the contrary, can produce the maximal response at a sufficient efficacy. An antagonist upon binding does not activate the receptor nor inhibits the basal activity. Inverse agonists bind to constitutively active receptors and suppress the basal signalling i.e. they have a negative efficacy[48,128]. The activity of a ligand at a GPCR can be identified using several different biological assays, of which [^{35}S]GTPγS binding assay is one[129]. This assay measures the level of G protein activation following agonist occupation

of a GPCR. The assay is suggested to suit $G_{\alpha i/o}$ coupled receptors due to their higher rate of nucleotide exchange[129].

Δ^9-THC (3) was the first cannabinoid to be discovered when Gaoni and Mechoulam isolated it as an oily, viscous liquid from *Cannabis sativa* preparation[73]. The discovery of cannabinoid receptors led on to the discovery of endogenous cannabinoids or 'endo'cannabinoids. In 1992, Devane *et al.* isolated and characterised N-arachidonoylethanolamine, commonly called anandamide (1), from porcine brain[130]. Anandamide (1) is the first known endocannabinoid and derives its name from Sanskrit whereby "Ananda" means pure bliss. Since then many more phytocannabinoids and endocannabinoids have been discovered consequently paving the way for a whole new generation of synthetic cannabinoids. Irrespective of the chemical class, whether a cannabinoid favourably binds to CB1 or CB2 depends on its selectivity towards that particular receptor. This section of the chapter briefly looks at the significant classes of cannabinoids known today.

1.2.3.1 Orthosteric Ligands

1.2.3.1.1 Agonists

(a) Endocannabinoids

Endocannabinoids are eicosanoids that are 20:4,n-6 series of fatty acid amides. The other endocannabinoids that were discovered following anandamide (1), are homo-r-linolenoylethanolamide, docosatetraenoylethanolamide, 2-arachidonyl glycerol (2-AG) (2), and noladine ether[131,132]. However, anandamide (1) and 2-AG (2) are the most studied endocannabinoids to date (Figure 1.7). Anandamide (1) is an ethanolamide and acts as a partial agonist at CB1 and CB2. 2-AG (2) was first isolated from canine intestine[133] and is

a monoglyceride. Unlike anandamide (1), it acts as a full agonist at CB1[84]. In terms of their selectivity, however, both the endocannabinoids are slightly selective towards CB1 over CB2. As they belong to different chemical classes, both ligands follow different biosynthetic and biodegradative pathways[134,135]. Based on anandamide (1), first-generation CB1 selective agonists have also been developed; these include R-(+)-methanandamide, arachidonyl-2`-chloroethylamide, arachidonylcyclopropylamide and O-1812[84].

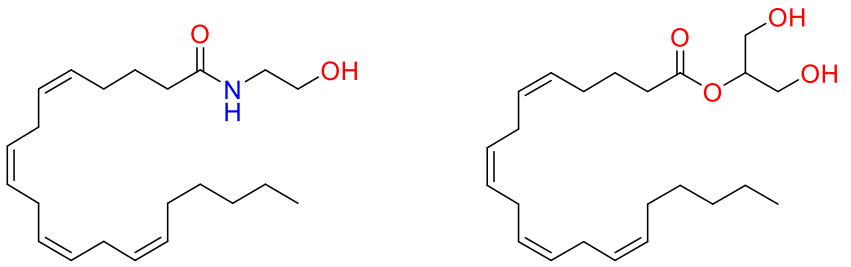

(1) Anandamide (2) 2-AG

Figure 1.7 Endocannabinoids anandamide and 2-AG

(b) Classical Cannabinoids

The classical cannabinoid ligands are characterised by an ABC-tricyclic benzopyran ring. They include the phytocannabinoids Δ^9-THC (3) and cannabinol, as well their synthetic analogues HU-210 (4) and JWH-133 (5) (Figure 1.8). Δ^9-THC (3), the popular psychoactive component of *C. sativa*, is a partial agonist at CB1. Certain studies have also reported Δ^9-THC (3) to exhibit antagonistic activity towards CB1 and CB2[84]. Δ^8-THC, another constituent of *C. sativa* and an isomer of Δ^9-THC (3), also shows partial agonist activity at CB1. In contrast, the synthetic analogue of this compound, HU-210 (4) is a full agonist at CB1[136]. JWH-133 (5), JWH-139, and HU-308 are first-generation CB2 selective agonists derived from the THC molecule[137,138].

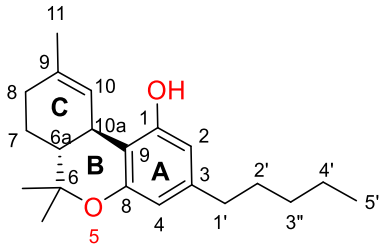

(3) Δ^9-THC

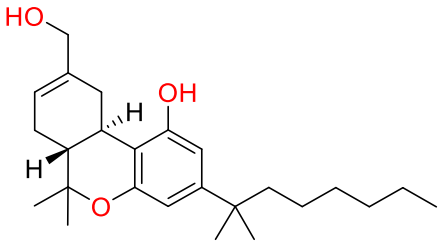

(4) HU-210

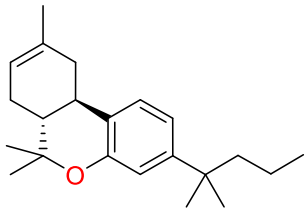

(5) JWH-133

Figure 1.8 Classical cannabinoids Δ^9-THC, HU-210, and JWH-133

(c) Non-classical Cannabinoids

These compounds were first synthesised by Pfizer in 1984 as analogues of classical cannabinoids but excluding the dihydropyran ring of Δ^8-THC[139]. This family consists of AC-bicyclic and ACD-tricyclic analogues. CP55940 (6) is one of the most important ligands in this series (Figure 1.9); as a radiolabelled ligand [^{3}H]CP55940 (6) has made possible the characterisation of CB1 and is still widely used in ligand binding studies[75]. It acts as a full agonist at both CB1 and CB2 and is 10-50 times more potent than Δ^9-THC (3) in mouse models[125–127]; however, it has the same selectivity towards CB1 and CB2. CP55244 (7) (Figure 1. 9) is an example of ACD tricyclic analogue; it is suggested to have a higher affinity and relative intrinsic activity at CB1 than CP55940 (6)[126,].

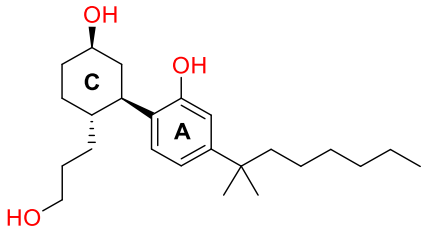

(6) CP55940

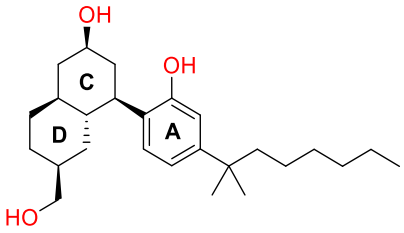

(7) CP55244

Figure 1.9 Non-classical cannabinoids CP55940 and CP55244

(d) Aminoalkylindoles

In the 1900s, researchers from Sterling Winthrop reported a new family of cannabimimetic compounds, derived from pravadoline[143]. These aminoalkylindoles (AAIs) have reduced ability to behave as non-steroidal anti-inflammatory drugs but show increased affinity towards cannabinoid receptors[144]. R-(+)-WIN55212, also known as WIN55,212-2 (8), is the most studied compound of this series (Figure 1.10). It is an AAI with a slightly higher selectivity for CB2, though shows high affinity for both CB1 and CB2[145]. The tritiated form of this compound has been used to characterize and map cannabinoid receptors in rat brain[146,147].

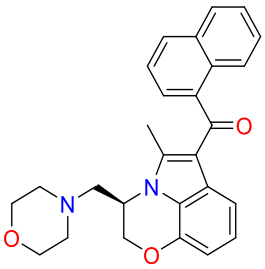

(8) WIN-55,212-2

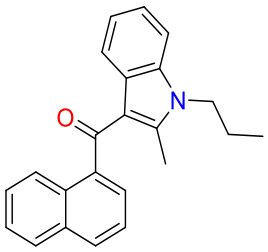

(9) JWH-015

Figure 1.10 Aminoalkylindoles WIN-55,212-2 and JWH-015

The S-(-)-enantiomer named WIN55,212-3, however, lacks any activity at the cannabinoid receptors both *in vivo* and *in vitro*[84]. A later study, however, reported that at low micromolar concentrations in *in vitro* tests this enantiomer behaved as a partial inverse agonist at CB1 and as a neutral antagonist at CB2[148]. Newer AAIs have since been developed whereby the indole nucleus of WIN55,212-2 (8) has been replaced with a pyrrole ring or an indene ring, or where the aminoalkyl substituent is replaced with a simple alkane. JWH-015 (9), a CB2 selective agonist, is one such example of a new AAI[149] (Figure 1.10).

(e) Novel agonists

In addition to the above-mentioned classes of agonists, a few novel agonists have also been developed. Bayer synthesised an agonist, BAY38-7271 that has CB1 selective properties and was shown to exhibit neuroprotective properties in rat trauma models[150]. Similarly, Abbot laboratories developed a CB2 selective agonist A-796260 which showed analgesic and anti-inflammatory activities *in vivo* in rodent pain models[151].

1.2.3.1.2 Antagonists or Inverse Agonists

(a) Dialkylpyridoles

The prototypical members of this series include the Sanofi-developed compounds SR141716 (10), a potent CB1-selective ligand, and SR144528 (11) (Figure 1.11), a potent CB2-selective ligand[152,153]. It has been reported that both the compounds exhibit inverse agonist activity[153–155] at CB1 and CB2 receptors respectively. SR141716 (10) was marketed as an anti-obesity drug under the generic name rimonabant (brand names Acomplia, Zimuli) but was banned later by the U.S. Food and Drug Administration due to the psychiatric adverse events observed in clinical trials[156]. Two analogues, AM251 and

AM281 (12) (Figure 1.11), were then developed based on SR141716 (10)[157]. AM281 (12) has nearly 350 times greater affinity for the CB1 receptor than its parent compound. Indeed, many antagonists co-crystallised with CB1 and CB2 in the inactive crystal structures are either derivatives or analogues of SR141716 (10).

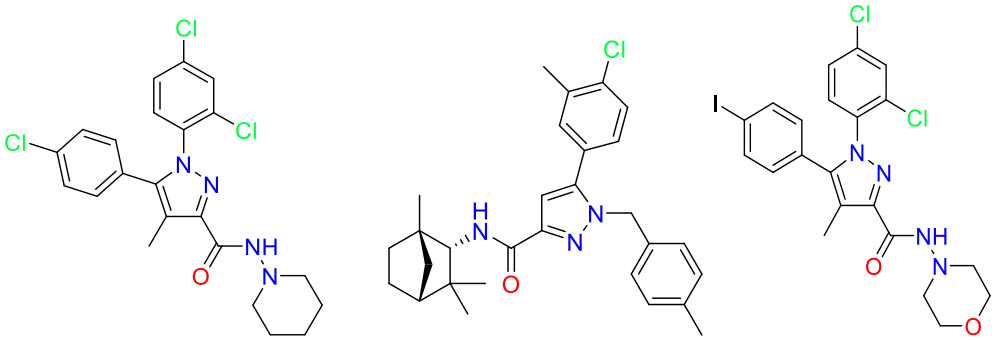

(10) SR141716 (11) SR144528 (12) AM281

Figure 1.11 Arylpyrazoles SR141716, SR144528, and AM281

(b) Other Chemical Classes

In addition to diarylpyrazoles, antagonists or inverse agonists of other chemical classes that show high selectivity for either CB1 or CB2 have been developed. For example, LY320135 (13) (Figure 1.12) is an antagonist developed by Eli Lily and has more than 70 fold selectivity for CB1 over CB2. However, its affinity for the receptor is much lower than that of SR141716 (10)[158]. AM630 (14) (Figure 1.12), a pravadoline derivative, is a CB2 selective antagonist or inverse agonist[159]. Several studies have shown that AM630 (14) has mixed agonist and antagonist properties towards CB1 in that it is a low-affinity partial CB1 agonist[154,160,161]. JTE907 (15) (Figure 1.12) is also an example of a novel CB2

receptor inverse agonist; it has been shown to produce anti-inflammatory effects in *in vivo* studies[162].

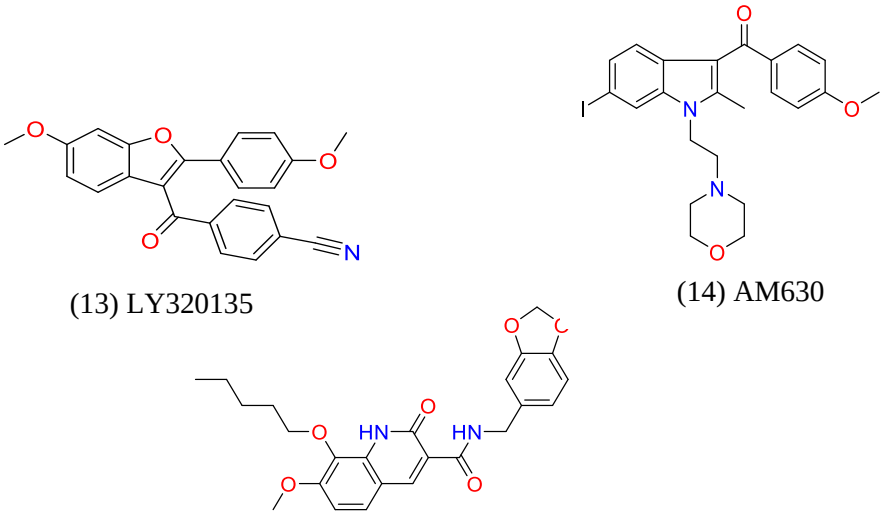

(13) LY320135 (14) AM630

(15) JTE907

Figure 1.12 Cannabinoid ligands from other chemical classes

1.2.3.2 Allosteric Ligands

The first allosteric site on CB1 was reported in 2005 by a pharmacological study on three novel compounds from Organon: ORG27569 (16), ORG27759, and ORG29647[163] (Figure 1.13). ORG27569 (16) acts as a PAM to CP55940 (6) but as a NAM to SR141716 (10). Some of the other popular allosteric ligands of CB1 include PSNCBAM-1, GAT100 (17), and the endogenous pepcans and lipoxin A4. Pepcan-12 acts as a PAM at CB2 but as a NAM at CB1[164]. The first synthetic allosteric modulator for CB2 was designed by the structural modification of 2-oxopyridine-3-carboxamide derivatives that have been shown to be orthosteric cannabinoid ligands. It acts as a PAM at CB2 and exhibited anti-nociceptive activity in an *in vivo* rat neuropathic pain model[165].

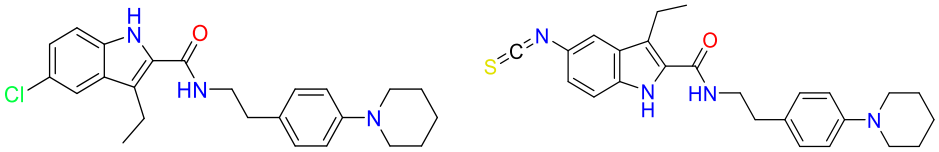

(16) ORG27569 (17) GAT100

Figure 1.13 Allosteric modulators of cannabinoid receptors

1.2.4 Other Members of the ECS

As seen earlier, the ECS is also composed of enzymes that metabolise endogenous ligands of CB1 and CB2. These enzymes, fatty acid amide hydrolase (FAAH) and monoacylglycerol lipase (MAGL), regulate the level of endocannabinoids, thereby influencing their bioavailability at CB1 and CB2[166,167]. FAAH is a membrane protein belonging to the amidase family[168]. The primary function of FAAH is the catalysis of anandamide (1) resulting in its degradation to ethanolamine and arachidonic acid, and oleamide to oleic acid. MAGL is a serine hydrolase[168]. MAGL catalyses the degradation of 2-AG (2) to arachidonic acid and glycerol. In the amygdala, it co-localises with FAAH and the CB1 receptor[167]. Cannabinoid ligands were also found to bind with certain GPCRs which are not canonical cannabinoid receptors. These are called the non-cannabinoid or novel cannabinoid receptors and include GPR18, GPR55, and GPR119. Though these receptors interact with cannabinoids, they do not necessarily share many structural features with CB1 or CB2. Further information regarding these receptors can be found in Pertwee *et al.*[169].

1.2.5 Pathophysiology Associated with Cannabinoid Receptors

Several studies in recent years have shown that the ECS, the cannabinoid receptors in particular, potentially mediate a number of physiological and psychological conditions[170,171]. This versatility with respect to pharmacology has garnered an interest around CB1 and CB2 being potential targets to develop drugs for various conditions. Cannabinoids have already been or are used in the traditional medicine practice of many cultures. Usage of cannabinoids to relieve pain has been documented in ancient China, India, Greece and Israel[170]. Jamaican fishermen use cannabis to increase their ability to see during night fishing excursions to enabling them to catch more fish[172]. The drugs which are already in the market of various countries can be found in Table 1.1. The following section briefly looks at some of the conditions where cannabinoid receptors are seen as promising targets.

Analgesia and motor function: The ECS is autoprotective by nature and exhibits anti-nociceptive properties via activation of CB1 or inhibiting FAAH through drugs such as OL-135, URB597, and *N*-arachidonoylglycine[167,173]. CB1 receptors are highly expressed in the areas that correlate with pain in the central nervous system and peripheral afferent neurons, and areas of motor control such as substantia nigrum and the cerebellum[174]. Endocannabinoids are also abundant in these regions. Phytocannabinoids have been shown to exhibit inhibitory activity on motor effects, and accordingly Δ^9-THC (3) or Cannabidiol (CBD)-containing formulations have shown to provide analgesia[171]. The CB2 receptor, too, has been implicated in modulating acute pain, chronic inflammatory pain, post-surgical pain, cancer pain, and pain associated with nerve injury[107]. CB2 selective agonists

such as HU308, GW405833, and AM1241 have shown antinociceptive activity in various pain models[167].

S. No	Brand Name	Active Component	Indications	Marketed Countries
1	Sativex®	Nabiximols (*Cannabis sativa* extracts including mainly Δ^9-THC (3) and CBD at a ratio of 1:1)	MS spasticity, symptomatic relief of neuropathic pain in MS	Canada, Mexico and several European countries
2	Cesamet®	Nabilone (Δ^9-THC (3) analogue)	Nausea and vomiting induced by chemotherapy	UK, Ireland, USA, Canada
3	Canemes®	Nabilone	Nausea and vomiting induced by chemotherapy	Germany, Austria
4	Marinol®	Dronabinol ((-)-trans-Δ^9-THC)	Nausea and vomiting induced by chemotherapy. Anorexia related to weight loss in patients with AIDS	UK, Ireland, USA, Canada
5	Syndros®	Dronabinol	Nausea and vomiting induced by chemotherapy. Anorexia related to weight loss in patients with AIDS	USA
6	Epidiolex®	Pure plant-derived CBD	Dravet syndrome and Lennox–Gastaut syndrome	USA
7	Cannabis extracts (e.g. Tilray)	Δ^9-THC (3) and CBD at different ratios	Various conditions	Canada, South America, Australia, New Zealand and Europe
8	Dried flowers (Bedrocan®)	Δ^9-THC (3) and CBD at different ratios	Various conditions	Europe

Table 1.1 List of cannabinoid drugs approved in various countries. *Source: Fraguas-Sanchéz and Torres-Suaréz[171].*

Cancer: Both CB1 and CB2 are found to be overexpressed in glioblastomas, prostate cancer and hepatocarcinomas[171], and high expression is actually associated with better disease-free survival rate. About 90% of HER-2 positive tumours overexpress CB2; while some consider this a sign of poor prognosis, other studies associate the CB2 receptor overexpression with major recurrence-free survival in patients with both estrogen-receptor-positive and negative mammary tumours[175]. Both CBD and Δ^9-THC (3), administered alone or in combination, have displayed an anti-proliferative effect on several glioma cell lines by inducing apoptosis, with the participation of CB2 receptor[176,177]. Δ^9-THC (3), JWH-015 (9), and WIN-55,21-2 (8) show cytotoxic activity towards hepatocarcinoma via CB2 mediation[178]. Δ^9-THC (3), JWH-015 (9), and WIN-55,21-2 (8), CBD and anandamide (1) exhibit antiproliferative activity on breast cancer cells in a cannabinoid receptor-dependent manner[179–181]; a newly proposed treatment strategy for breast cancer involves combining cannabinoids with existing anti-tumour drugs such as cisplatin or tamoxifen[182].

Brain and breast cancers are the most studied carcinomas for treatment with cannabinoids and show promising results. However, much clarity is required in terms of usage of cannabinoids for chemotherapy and it depends on the type of carcinoma to be treated. As of present, Δ^9-THC (3) and CBD appear to be likely treatment strategies for hepatic, glial and breast carcinomas[171].

Energy metabolism: Evidence from many scientific studies suggest that the ECS, in particular, the activation of CB1 receptors, favours weight gain by promoting food intake, controlling GI motility, and inflammation, and also by tuning down processes such as energy expenditure, brown adipose tissue thermogenesis, white adipose tissue lipolysis, and increasing lipogenesis in the liver[183–185]. Piazza *et al.* suggest that an increased level of

endocannabinoids and the over-expression of CB1 is a hallmark of obesity – two things that help in the development as well as the maintenance of the condition[184]. This makes CB1 antagonists a potential instrument to tackle obesity[186]. However, some drugs have the ability to cross the blood-brain barrier and cause psychiatric side effects as seen in the case of SR141716 (Section 1.2.3.1.2(a)). Hence, it is important to design pharmacophores that exclusively target peripheral CB1 receptors. Alternatively, this exostatic nature of CB1 receptors can be harnessed for better use such as in the treatment of anorexia and cachexia. Indeed, treatment with Δ^9-THC (3) has been shown to stimulate appetite and weight gain in patients with cancer and AIDS extensively[187,188].

Neurological disorders: The level of cannabinoid receptor expression in the central nervous system varies with the associated neurological disorder. With regards to multiple sclerosis (MS), the expression of cannabinoid receptors is speculated to vary with disease progression. Studies on post-mortem brain tissue samples revealed that both CB1 and CB2 were over-expressed[189] in MS. However, another study on plasma samples from patients with different subtypes of MS showed an increased CB1 and CB2 mRNA levels in only primary-progressive type[171]. Several clinical studies have been conducted to test the efficiency of cannabinoids in treating MS but with contradictory results[171]. However, the Δ^9-THC or CBD oromucosal spray has proven to be beneficial with no severe adverse effects; in fact, it has been approved in many countries for treatment (Table 1.1).

In the case of epilepsy, the ECS (specifically CB1) has shown to exhibit neuroprotective effects against excitotoxic events[190–192]. Several clinical studies of administering CBD rich extracts without Δ^9-THC have shown positive results in treating epilepsy, especially amongst children[171]. Dravet and Lennox-Gastaut syndromes, in

particular, show high response rates with CBD administration, and a drug Epidolex has been approved for treatment (Table 1.1)[171].

The effects of the ECS on Parkinson's disease, however, are detrimental. The activation of the ECS in basal ganglia has a negative impact by impairing motor movement[193]. The expression of CB1 was found to be uneven in post-mortem brain samples; the expression was low in certain parts of basal ganglia but unchanged at other areas[194]. Cannabinoid antagonists were suggested to exhibit anti-parkinsonian activity in rat models but failed to be effective in clinical trials[171].

Other conditions: Apart from the above-stated conditions, cannabinoid receptors are alluded to intervene in other disorders - such as those related to the cardiovascular system, type II diabetes mellitus, renal disorders, retinal problems (specifically glaucoma), emesis, alcohol and opioid addiction, reproductive, and psychiatric disorders - either in an autoprotective or a pathological manner. They are also suggested to be involved in Alzheimer's and Huntington's in an autoprotective manner[171]. Detailed information regarding the influence of the ECS on human physiology and psychology can be found in the works of Pacher (2006)[170], Pertwee (2008)[167], Piazza *et al.*, (2017)[184], Fraguas-Sánchez and Torres-Suárez (2018)[171], and Gonçalves and Dutra (2019)[195]. Clinical studies show that Δ^9-THC (3) and CBD appear to be beneficial to treat a host of conditions. Cannabis extract in various forms is popularly used by the general public to treat post-traumatic stress disorder, Tourette syndrome and anxiety. However, more research is required in this area as conflicting evidence exists regarding the impact by Δ^9-THC (3) and other CB1 agonists on cognition and memory[196,197].

1.3 Crystal Structures

As mentioned in Sections 1.2.1.2 and 1.2.2.2, there are currently five crystal structures for human CB1 and one for human CB2 available in PDB[102–105,127]. The crystal cognate ligands are shown in Figure 1.14. The general aspects of the six crystal structures (excepting thermostabilising mutations) are summarised in Table 1.2. Due to the nature of ligands they interact with, CB1 and CB2 are often categorised as lipid-binding receptors along with lysophosphatidic receptor 1 (LPA1), S1P1 (both are in the MECA subgroup), free fatty acid, leukotriene, prostanoid, platelet-activating factor receptors and three orphan receptors (GPR18, GPR119, and GPR55)[198]. This section compares the existing crystal structures of cannabinoid receptors and the similarities they share with LPA1 and S1P1. Both receptors have higher sequence identity to CB1 and CB2 in comparison to other lipid-binding receptors (Appendix 1) as well as compared to members of the α-subgroup.

LPA1 and S1P1, are available as crystal structures with PDB IDs 4Z34 and 3V2Y respectively[200,201]. 4Z34 is co-crystallised with the antagonist ONO9780307 and 3V2Y with its antagonist ML056. The corresponding crystal structure papers were used as sources for comparing crystal structures unless specified.

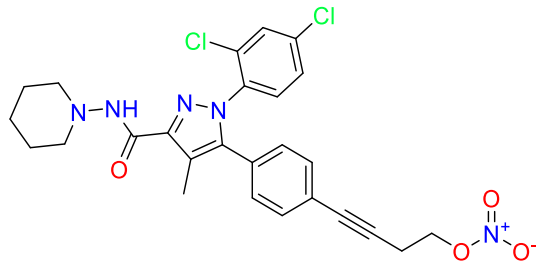

(18) AM6538

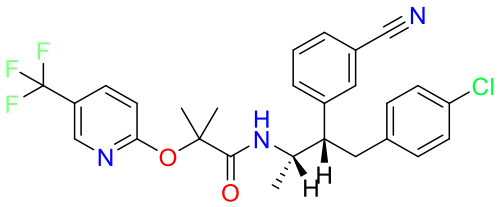

(19) MK0364

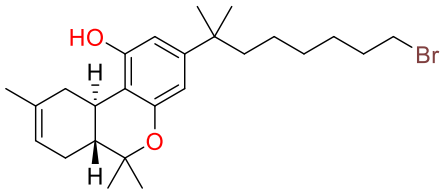

(20) AM11542

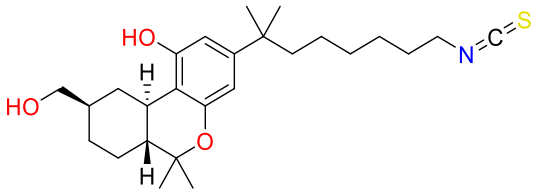

(21) AM841

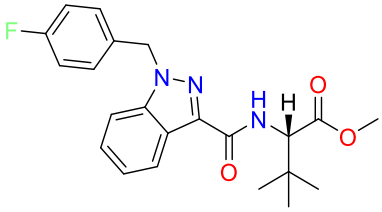

(22) MDMB-Fubinaca

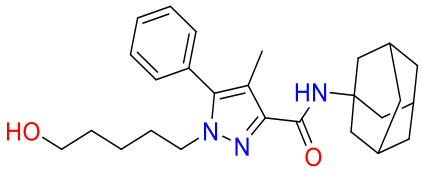

(23) AM10257

Figure 1.14 Cognate ligands of CB1 and CB2 crystal structures

Protein	PDB ID	State	Ligand bound	Resolution	Type of construct replacing ICL3	Truncation of N and C terminals	Binding Pocket Volume (Å^3)
CB1	5TGZ	Inactive	AM6538 (AM251 derivative)	2.8Å	Flavodoxin (Val306 to Pro332)	1-98 and 434-472	833
CB1	5U09	Inactive	MK0364 (Taranabant)	2.6Å	PGS domain (His302 to Pro332)	1-89 and 421-472	564[a]
CB1	5XRA	Active	AM11542 (tetrahydrocannabinol)	2.8Å	Flavodoxin (Arg307-Arg331)	1-98 and 415-472	384
CB1	5XR8	Active	AM841 (hexahydrocannabinol)	2.95Å	Flavodoxin (Arg307-Arg331)	1-98 and 415-472	387[a]
CB1	6N4B	Active (Coupled to $G_{\alpha i}$)	MDMB-Fubinaca (MDMB-Fub)	3.0Å	Complexed to $G_{\alpha i}$-G_{β}-G_{γ} heterotrimer. Also complexed to scFv16 (Gln 314 – Gln 334)	1-108 and 412-472	NA
CB2	5ZTY	Inactive	AM10257 (SR141716 derivative)	2.8Å	T4-lysozyme (Ser 222 – Ala 235)	1-20 and 326-360	447

Table 1.2 Summary of the cannabinoid crystal structures released to date. *Calculated using SiteMap*[199]**.** NA-Not available

Transmembrane bundle:

1. A stark contrast between the active and inactive structures is the arrangement of TM helices. In 5TGZ and 5U09, the helices are arranged such that the orthosteric binding pocket and the extracellular region spans a greater surface area as compared to the intracellular area. This has been attributed to the movement of TM1 and TM2 away from the orthosteric binding pocket. TM1 and TM2 of 5TGZ have been reported to show a 7 Å and 2 Å shift respectively when superposed with the helix bundle of LPA1 or S1P1.
2. In 5XRA, 5XR8 and 6N4B, the helix arrangement is inverse to that of inactive structures. The orthosteric pocket volume shrinks in size while intracellular side expands, for G protein binding. The reduction in pocket volume for 5XRA and 5XR8 was calculated to be 53% of that of 5TGZ. The inward movement of residues Phe170(2.57) and Phe174(2.64) influenced the conformational re-arrangement TM1 and TM2, pulling them closer to the pocket. Al-Zoubi *et al.* suggested that due to crystal packing in 5XRA and 5XR8, the TM2 hinges at Gly166(2.53) and Ser167(2.54), causing the helix to intrude into the binding pocket[202].
3. 5ZTY shows a unique helix arrangement; the intracellular portion adopts a conformation similar to that of inactive CB1 structures, while the extracellular portion is similar to that of 5XR8. This is quite evident from the binding pocket volume, which is much closer to 5XR8 than to 5TGZ or 5U09, and the conformation of TM1 and TM2.

N-terminus:

1. The N-termini in 5TGZ and 5U09 are V-shaped loops which interact with the bound antagonists, and they act like a plug to the orthosteric binding pocket (Figure 1.15). This intrusion of the N-terminus is a likely factor for TM1 moving away from the binding pocket. It has also been suggested that the top-to-top crystallisation in 5TGZ and the contact of adjacent bundles in 5U09 has created crystal artefacts by affecting the arrangement of the extracellular loops and the N-terminus packing[202].
2. 5XRA, 5XR8 and 6N4B have their N-terminus residing over the binding pocket without any direct involvement in ligand binding. In all three structures, the N-terminus has a single helix turn. It is suggested that the N-terminal displacement is necessary to accommodate the agonist due to possible steric clashes with the tert-butyl moiety in FUB or the benzopyran scaffold in AM11542 (20) and AM841 (21) if the N-terminus was present inside the binding pocket. Such steric clashes are not observed with the N-terminus loop and the cognate ligand in 5TGZ or 5U09 (Figure1.15).

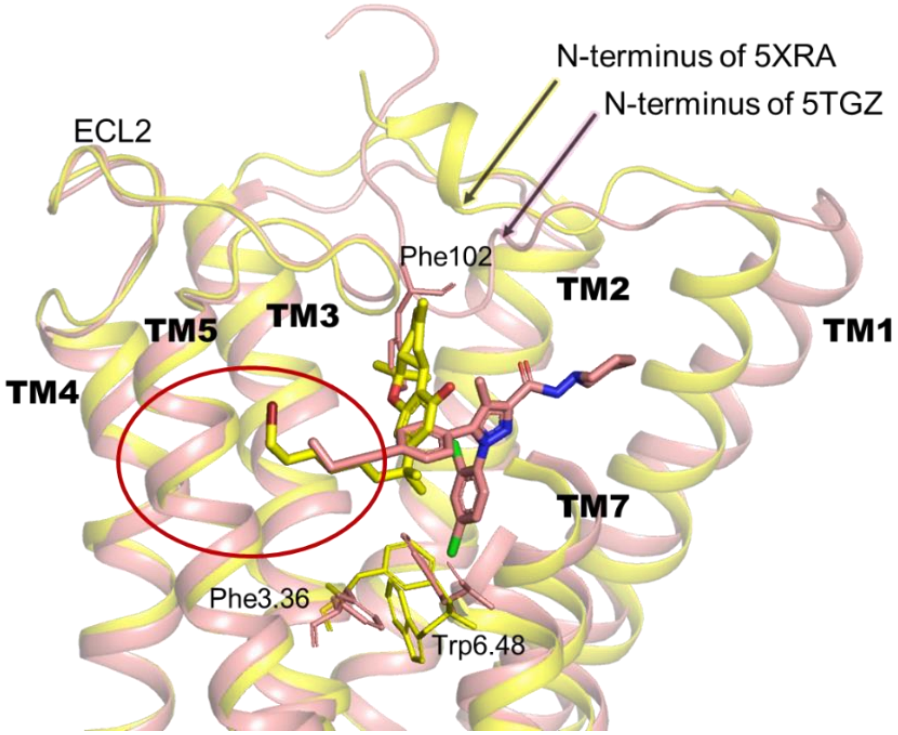

Figure 1.15 Comparison of binding pockets and toggle-switch residues - Superposition of inactive CB1 (5TGZ: pink) and active CB1 (5XRA: yellow) crystal structures. *The extended binding conformation of AM6538 (18) in inactive structure pushes TM1 away; this gives the N-terminus space to intrude into the binding pocket and expand it further. If the N-terminus were to enter the binding pocket in the active structure in a similar way, steric interactions with Phe102 would have been observed. In the inactive structure, Phe200(3.36) and Trp356(6.48) are engaged in a face-face aromatic stacking interaction with no ligand intervention. In the active structure, the twisting of TM6 has led to Trp356(6.48) moving away from the binding pocket. This allows Phe200(3.36) to be free and change its rotameric state in the direction of the binding pocket. The ligands are represented as sticks and residues as thin tubes. TM6 has been fully truncated and TM7 is half truncated for image clarity. The encircled area represents the long channel described in the main text.*

3. 5ZTY also has an N-terminal loop similar to the active structures of CB1 with a single turn above the orthosteric binding pocket. Similarly, the cognate ligand within the

binding pocket is positioned such that if the N-terminus loop resided in the pocket, steric clashes would have been observed (Figure1.16).

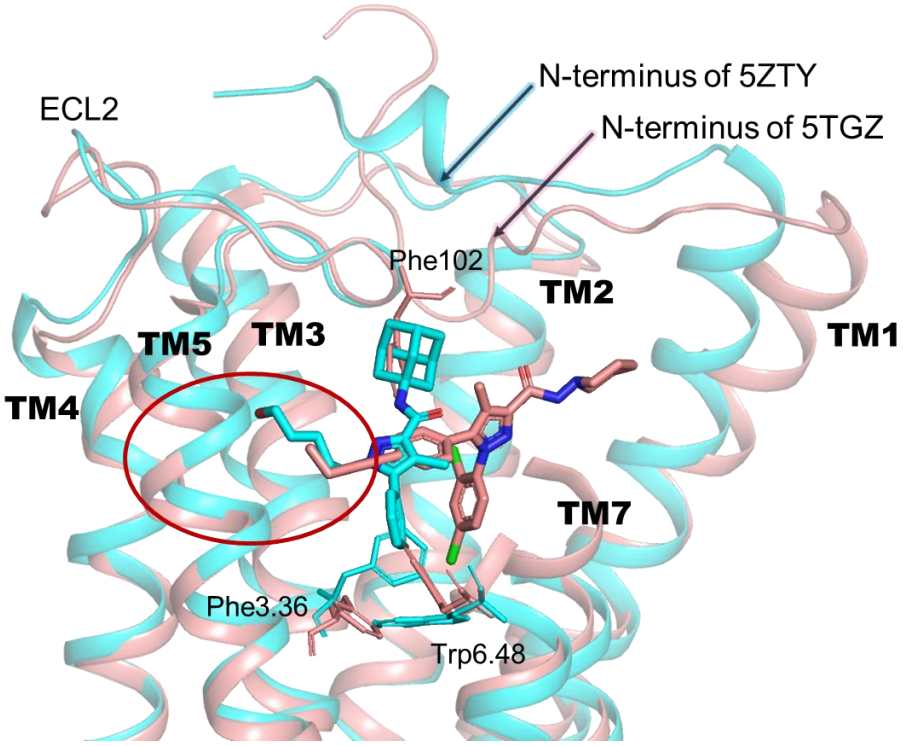

Figure 1.16 Comparison of binding pockets and toggle-switch residues - Superposition of inactive CB1 (5TGZ: pink) and inactive CB2 (5ZTY: cyan) crystal structures. *N-terminus of CB2 stays above the binding pocket unlike that of inactive CB1. If the N-terminus were to intrude the binding pocket in inactive CB2, steric clashes with Phe102 would have been observed. The aromatic interaction between toggle switch residues is interrupted by the phenyl moiety of the cognate ligand. Phe200(3.36) flips into the binding pocket and Trp356(6.48) bends by almost 90° to interact with the ligand. The ligands are represented as sticks and residues as thin tubes. TM6 has been fully truncated and TM7 has been half truncated for image clarity. The encircled area represents the long channel.*

4. Crystal structures of LPA1 and S1P1 have a much more pronounced helical loop in their N terminus, compared to the ones observed in CB1 or CB2. Similar to active CB1 structures and CB2, they do not intrude into the binding pocket.

It must be highlighted that the wildtype N-terminus is truncated in all the crystal structures and is of the order of a few amino acid residues. Hence, the influence of crystal structure packing on N-terminal packing cannot be ruled out. There also exists the possibility that the full-length N-terminus might assume an entirely different conformation from that seen in the currently available crystal structures.

Orientation of the cognate ligand:

1. Cognate ligands of both inactive structures bind deep in the orthosteric pocket in a perpendicular manner. AM6538 (18) binds deeper into the pocket of 5TGZ than the antagonists of S1P1 and LPA1. The cyclohexane arm of AM6538 (18) pushes TM1 and TM2 away from the binding pocket; this provides more space for the re-entrant N-terminus and further expands the pocket. MK0364 (19) binds to CB1 in a quite unusual position between TM1 and TM7 in comparison to inhibitors of other class A GPCRs; the trifluoromethylpyridine projects out of the gap between TM1 and TM7, and the cyanophenyl moiety buries deep into the binding pocket.
2. In active structures, all three agonists (AM11542 (20), AM841 (21), and MDMB-Fub (22)) adopt a folded conformation and fold into a V-shape. AM11542 (20) and AM841 (21) bind in the region between TM3, ECL2, TM5, TM6, and TM7; their aliphatic tails occupy the region between TM3, TM5, and TM6 and their aromatic head groups face TM1 (Figure 1.15). MDMB-Fub (22), despite being structurally dissimilar from AM11542 (20) and AM841 (21), has an overlapping binding pocket with other agonist structures (Figure 1.17). The p-fluorobenzyl moiety of Fub occupies the region between TM3, TM5, and TM6, similar to the alkyl chains of the AM-derivatives.

3. The binding pocket of inactive CB2 crystal structure overlaps that of CB1 agonist crystal structures, S1P1 and LPA1. The cognate ligand assumes a folded V-shape as seen in active CB1 structure cognate ligands. This is unlike the extended conformation seen in the inactive CB1 structures (Figures 1.15 and 1.17).

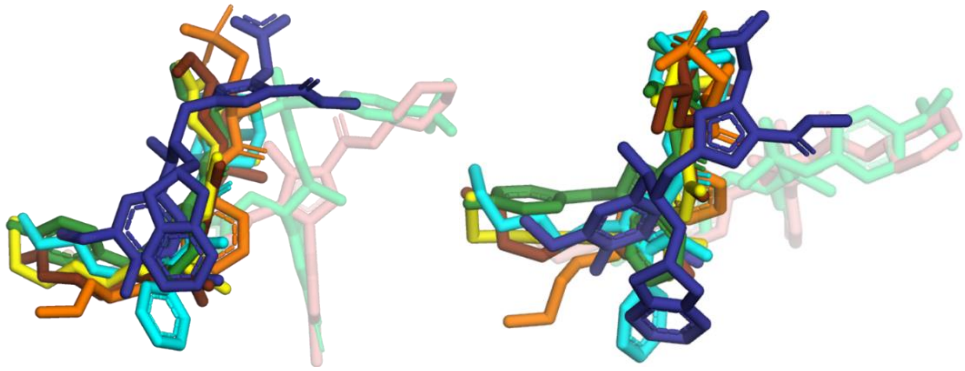

Figure 1.17 Overlay of cognate ligand binding modes of all lipid-binding receptors. *(a) Side view (b) Top view. Cognate ligands of inactive CB1 structures are rendered transparent [AM6538 (18) (5TGZ) – pink; MK0364 (19)(5U09) – green]. Other ligands included are : AM11542 (20) (5XRA:yellow), AM841 (21) (5XR8:brown), MDMB-Fub (22) (6N4B:deep green), AM10257 (23)(5ZTY:cyan), ML065 (3V2Y:orange), and ONO9780307 (4Z34:violet). Cognate ligands of inactive structure bind in an extended conformation. Other cognate ligands show a folded conformation and their binding sites of ligands coincide with each other. ONO9780307, however, doesn't exhibit the C-shape fold commonly seen in that binding pocket.*

Long channel: In all three types of crystal structures discussed in this section, the region of binding pocket between TM 3, 5 and 6 has been dubbed the 'long channel'. This region is occupied by alkyl chains in almost all receptors (Figures 1.15 and 1.16), viz

1. Nitroalkyl chain of AM6538 (18) – 5TGZ
2. Aliphatic tails of AM-derivatives.
3. Alkyl chain of AM10257 (23)– 5ZTY

MDMB-Fub (22) does not have an alkyl chain, but its chlorophenyl group sits in the equivalent area of the binding pocket. MK0364 (19) in 5U09, does not have an alkyl chain and also binds far from this pocket. The alkyl chain of ML056 in S1P1 receptor also occupies the long channel region. This has led to speculation that the long channel could be a conserved binding region for alkyl chains in the lipid-binding receptors.

Lipid access channel:

1. The gap between TM1 and TM7 has been considered to be an alternative ligand access pathway in both S1P1 and LPA1 structures to receive ligands via the plasma membrane. As mentioned previously, the wide opening between TM1 and TM7 of 5TGZ implies that a possible pathway could exist in CB1. This channel was also proposed in the resolution of 5U09, where a 'lipid access channel' was identified lined by the residues Asp104, Ser123(1.39), and Ser383(7.39) (Figure1.18).
2. Although no channels were detected in the active structures due to the inward movement of TM1 and TM2 towards the pocket, MD simulations of 6N4B hinted at a possible pathway. In four of six simulations run by the authors, TM1 was found to move outward creating a gap between TM1 and TM7. The authors also found that the event coincided with the binding of a 1-palmitoyl-2-oleoyl-sn-glycero-3-phosphocholine (POPC) molecule and stabilization of the position of the N terminus in relation to the extracellular surface of the receptor[104].
3. As 5ZTY has an extracellular portion similar to agonist bound CB1 structures, no channel pathway is seen in the crystal structure.

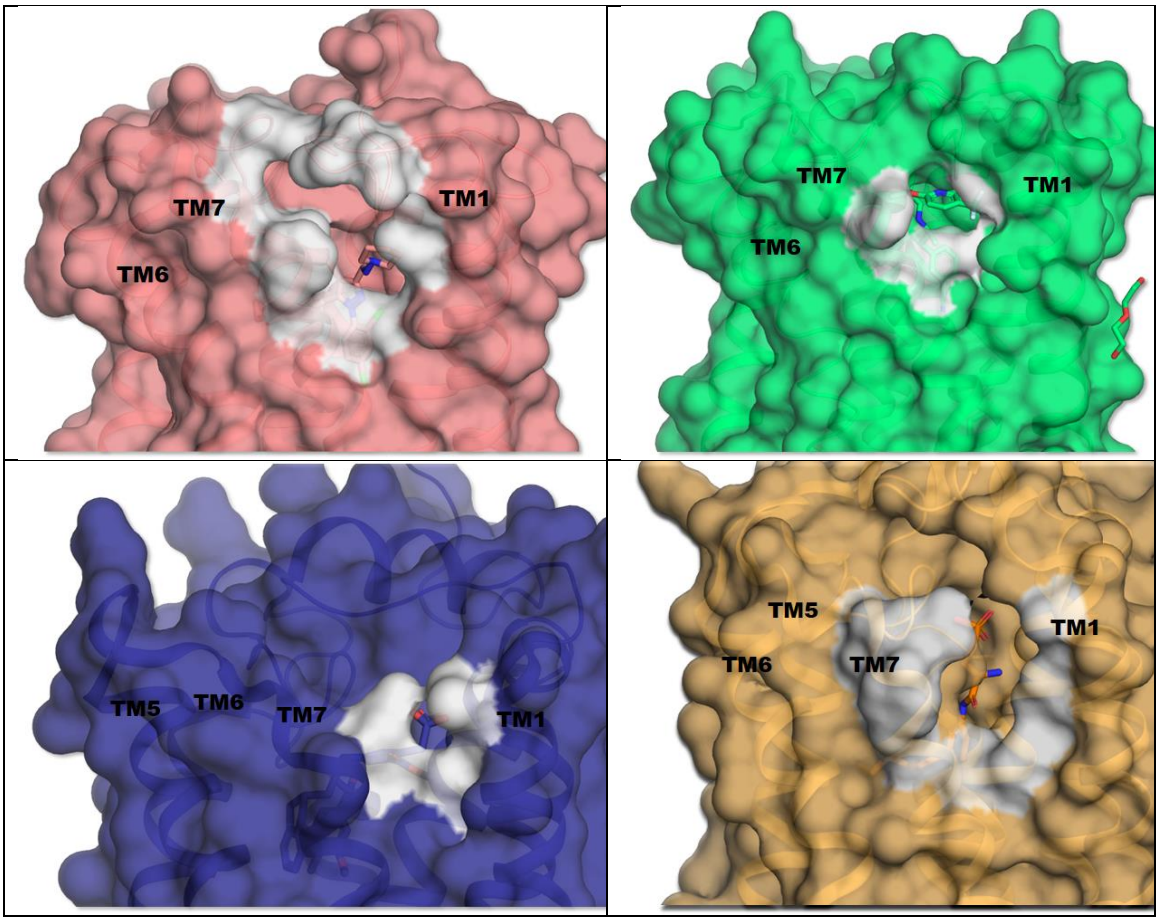

Figure 1.18 Potential lipid access channels found between TM1 and TM7 in inactive structures *- 5TGZ (pink) and 5U09 (green), LPA1 (violet) and S1P1 (light orange). The entry path is highlighted in white.*

Twin toggle switch:

1. In 5TGZ and 5U09, the residues Phe200(3.36) and Trp356(6.48) exhibit aromatic stacking with each other, consistent with previous data (Section 1.1.3) (Figure 1.15).
2. In 5XRA and 5XR8, a synergistic conformational change of the residues has been observed[127]. Li *et al.* reported that the rotation of TM3 and side-chain flip of Phe200(3.36) towards the ligand occurred simultaneously with the rotation of TM6 and side-chain movement of Trp356(6.48) away from TM3 (Figure 1.15). This movement

broke the aromatic stacking interaction observed in the inactive state crystal structures. The authors also speculate that this ‘twin toggle switch', plays a role in the activation of the receptor as a previous study has already shown[93].

3. In 64NB, Phe200(3.36) repositions itself and interacts with the indazole ring of FUB in a manner similar to that seen in other agonist structures. The repositioning allows Trp356(6.48) to be free and rotate inward, thus relaxing the kink in TM6 and it straightens up. Consequently, the intracellular end moves outward in a ‘seesaw’ manner to create space for G protein coupling. The twin toggle switch hence appears to be a critical part of CB1 activation, although having an ambiguous role in other class A GPCRs (Section 1.1.3).
4. In 5ZTY, the cognate ligand forms a stacking interaction with Trp258(6.48) and restrains its rotamer state, unlike inactive CB1 structures where Phe117(3.36) interacts with Trp258(6.48) to latch its conformation (Figure 1.16).

Ionic Lock :

1. In 5TGZ and 5U09, Arg214(3.50) forms salt bridge interactions with both Asp213(3.49) and Asp338(6.30) – thereby creating the ‘ionic lock’ described in Section 1.1.3 (Figure 1.19). In contrast, both LPA1 and S1P1 inactive structures do not possess the above-mentioned salt bridge interactions due to (a) the DRY motif present as ERH for both the LAP1 and S1P1 receptors, (b) Asp6.30 facing away from the binding pocket in LPA1, and (c) the lack of Asp residue at the position 6.30 in S1P1.

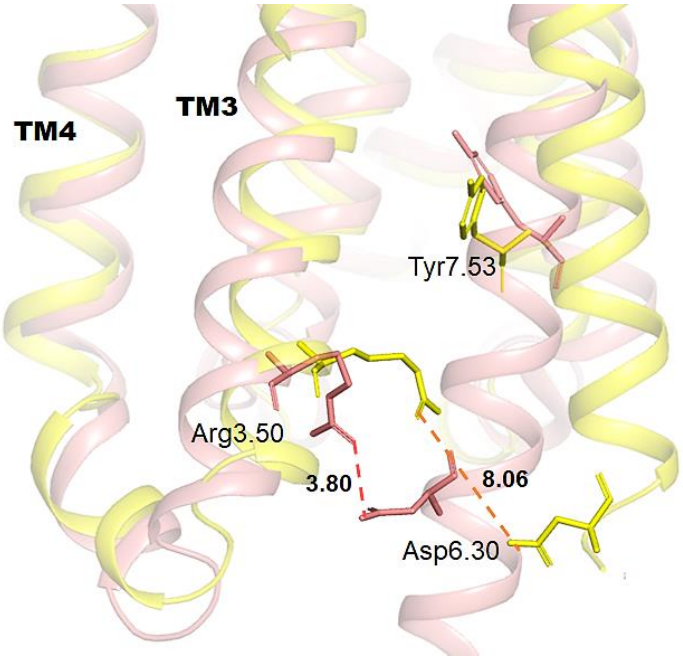

Figure 1.19 Comparison of Ionic Lock and Tyr7.53 rotamer state between inactive CB1(5TGZ: pink) and active CB1(5XRA: yellow) crystal structures. *In the inactive state, Arg214(3.50) is in close contact with Asp338(6.30) (pink dashed lines). Asp338(6.30) of the active structure moves away from the binding pocket due to the seesaw movement of TM6; this breaks the ionic interaction with Arg214(3.50), which points downwards. Tyr397(7.53) of inactive CB1 points up towards the centre of the receptor while that of the active structure is turned towards TM6. Interacting atoms are connected by dashed lines. The distance of separation (in Angstroms) between interacting atoms given near dashed lines.*

2. The active structures 5XRA and 5XR8 do not show any salt bridge interactions for Arg214(3.50) as the residue turns away from Asp213(3.49) and points downward. In 6N4B, Arg214(3.50) points in towards TM7 (Figure 1.20).
3. In 5ZTY, Arg131(3.50) forms salt bridge interactions with both Asp130(3.49) and Asp241(6.30) in similar to inactive structures of CB1 (Figure 1.20).

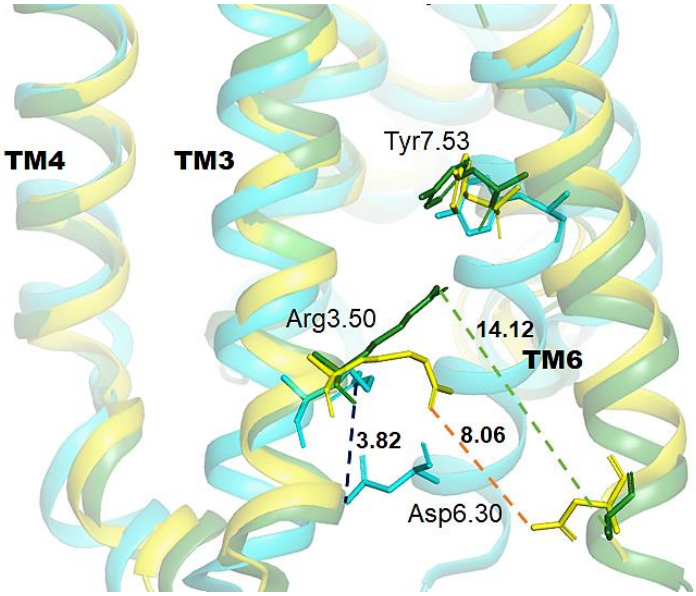

Figure 1.20 Comparison of Ionic Lock and Tyr7.53 rotamer state between of active CB1 (5XRA: yellow), active CB1 complexed with Gi (6N4B: dark green), and inactive CB2 (5ZTY: cyan) crystal structures. *Similar to inactive CB1, inactive CB2 exhibits ionic interaction between TM3 and 6. Asp6.30 of both active structures assume a similar conformation. Arg131(3.50) of active CB1 in 5XRA, while it points towards TM7 in 6N4B. Compared to 5XRA, Tyr397(7.53) of 6N4B is tilted by 45° and points towards the long channel. Tyr299(7.53) of 5ZTY also points towards the long channel differing from CB1 inactive structure. In both images, TM7 is hidden from view by TM6 and TM5 has been removed for image clarity. Residues are shown as thin tubes. Interacting atoms connected by dashed lines. The distance of separation (in Angstroms) between interacting atoms given near dashed lines.*

NPXXY motif:

1. Similar to the rotamer conformation seen in other inactive structures, namely β2AR and A2AR (Section 1.1.3), the Tyr397(7.53) residue in 5TGZ and 5U09 points upward towards the centre of the receptor. Inactive LPA1 and S1P1 also exhibit a similar rotamer state for Tyr397(7.53) (Figure 1.19).
2. Tyr397(7.53) of 5XRA and 5XR8 points upwards in the direction of TM6 and forms a π-π edge-face interaction with Phe2.42. In 64NB, however, Tyr397(7.53) points

sideways towards the proposed 'long channel' region; no π-π interactions are seen with Phe2.42 here (Figures 1.19 and 1.20).

3. Tyr299(7.53) of 5ZTY also assumes a conformation quite similar to the one seen in 6N4B and points sideways in the direction of the 'long channel' region (Figure 1.20).

1.4 Non-cannabinoid Ligands That Act on Cannabinoid Receptors

In Section 1.2.4, it was seen that cannabinoid ligands act on receptors that are not canonical cannabinoid receptors. Likewise, many studies have found that certain drugs, apart from those designated as cannabinoid receptor agonists and antagonists or FAAH and MAGL inhibitors, influence the ECS on an observable if not equal measure. Some examples include propofol, a popular anaesthetic and flurbiprofen that increase the level of anandamide (1) by inhibiting FAAH[203–205]. Ethanol, too, was shown to influence emotion and cognition by indirectly influencing the endocannabinoid system (Section 1.2.5)[206].

In this regard, selective estrogen receptor modulators (SERMs) have been identified to act on both CB1 and CB2. SERMs act on estrogen receptors by mimicking estrogen in some tissues and by blocking estrogen activity at others. In breast tissues, SERMS have an anti-estrogenic effect and inhibit the proliferative effects of estrogen-mediated through the estrogen receptor[207]. Hence, SERMS are generally used to reduce the risk of breast cancer in high-risk and average-risk women. The most popular in present-day clinical usage SERM is tamoxifen. Though being effective in treating breast carcinomas, SERMs are often accompanied with the risk of causing ovarian cancer and produce cytotoxicity in cancers which are devoid of estrogen receptors[208]. By chemical class, SERMs can be divided as triphenylethylenes (which comprise tamoxifen, its

derivatives, and its metabolites), benzothiaphenes, indoles, tetrahydronaphthalenes, and benzopyran.

At CB1 and CB2, they show selectivity and with a moderate to high affinity in an isostereomer dependent manner; they mostly act as inverse agonists at the receptor but also show insurmountable or surmountable antagonism in an isostereomer dependent manner[209]. Therefore, it is speculated that SERM action on cannabinoid receptor may represent an estrogen receptor-independent pathway by which these drugs exhibit cytotoxicity. As cannabinoids and SERMS exhibit overlapping anti-proliferative, anti-angiogenic and pro-apoptotic actions, developing novel cannabinoid scaffolds based on tamoxifen has been suggested for future drug development purposes[208].

1.5 Computational Techniques

As discussed in **S**ection 1.1.6, drug discovery in GPCRs is largely impeded by the challenges in obtaining high-quality experimental structures. *In silico* methods provide a faster and more cost-effective alternative to explore targets for which structural information is not available, or to utilise and improve the structures solved by crystallisation.

1.5.1 Molecular Modelling

In the phraseology of computational modelling, the protein whose structure is to be predicted is often called the query protein. Modelling methodologies can be generally classified into three branches: *ab initio*, fold recognition (also known as threading), and comparative modelling (better known as homology modelling)[210]. In *ab initio*, the native structure of the query protein is predicted using only its amino acid sequence[211]. Fold recognition techniques find a relationship between sequence and fold similarity[210]. Homology modelling is the method of constructing *in silico* protein models using the

structural and conformational information obtained from the protein whose sequence is homologous to that of the protein whose structure is to be built, for accurate prediction of the target structure. Homology models can be built either using a single template or multiple templates. It is generally considered that to generate models of good quality, the sequence identity between the query and the template sequence should be more than 30%[212]. Evolutionary relationships between protein molecules, advances in structural genomics, and the increasing number of protein structures being solved make homology modelling a reliable method for structure prediction[212].

The general steps involved in homology modelling are[210]:

1. Template recognition and initial alignment
2. Alignment correction
3. Backbone generation
4. Loop modelling
5. Side-chain modelling
6. Model optimization
7. Model validation.

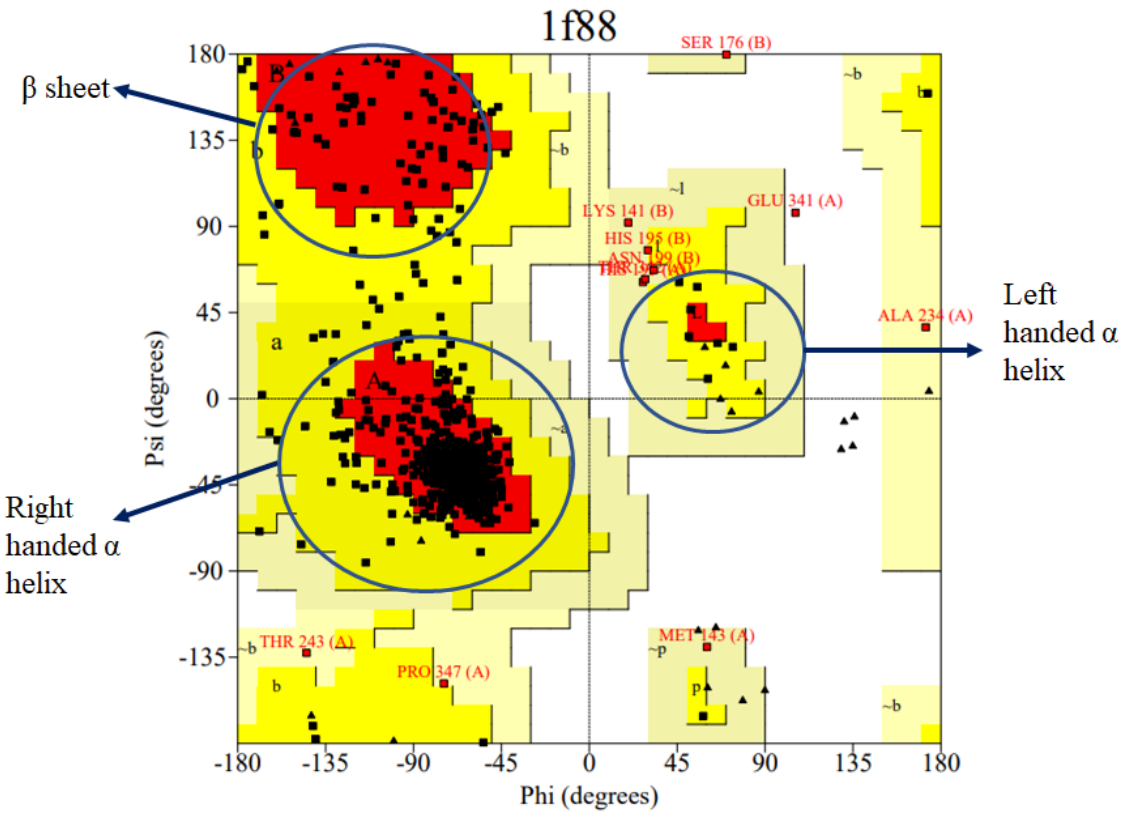

Figure 1.21 Sample Ramachandran plot of bovine rhodopsin (PDB ID 1F88[23]) generated using PROCHECK[213]. *The red denotes most favoured regions, yellow denotes additionally allowed regions, ivory denotes generously allowed regions, and white denotes disallowed regions. Residues with steric clashes are named and represented as red squares, glycine residues as black triangles and other residues as black squares. Regions representing residues of specific secondary structures are marked in the figure.*

For the qualitative evaluation of protein models, a Ramachandran plot is often used. It is a plot of φ versus ψ dihedral angles that map the conformational space of a polypeptide (protein). It was developed on the basis of sterically allowed dihedral angles and hence can be used to identify 'allowed' or 'disallowed' regions in a protein[214]. A sample plot is shown in Figure 1.21.

Prime from the Schrodinger Software Suite is one of the many homology modelling tools available in the present day[215]. Prime incorporates both homology modelling and

fold recognition in a single program for accurate structure prediction[215]. In a comparative study of modelling software in predicting the secondary structure for a range of proteins, it was observed that Prime performed better when target-template sequence identity was as low as 19 %[216]. Model building in Prime has two modes : (1) 'Knowledge-based modelling' which builds insertions and closes gaps using segments from known structures, and (2) 'Energy-based modelling' which builds a physically reasonable loop for missing residues from scratch on the basis of energy, not based on a template.

1.5.2 Computational Molecular Docking

Computational docking in drug design, in general, involves two molecules: a ligand, which is a molecule that binds to or interacts with another molecule through non-covalent interactions without any chemical bond formation, and a receptor (or a target protein) which is generally the larger of the two species. The ligand is flexible to change its conformation while the protein may be rendered rigid or some parts of it allowed to be flexible. The three main functions of any computational docking program are (a) characterising the binding site on the target, (b) positioning the ligand into the binding site (sampling) and (c) evaluating the strength of interaction for that specific ligand-receptor pose (scoring)[217]. Stochastic methods are one type of sampling algorithm known. Stochastic methods search the conformational space by modifying the ligand conformation in a random manner[218]**.** Genetic algorithm and Monte Carlo are two well-known stochastic methods. Genetic algorithm is based on Darwin's theory of evolution whereby the program carries over the high-scoring conformational features from the current to the next generation of ligand conformers. Subsets of conformation can be exchanged via crossovers as well new conformers be introduced by random mutations[217]. In Monte Carlo searches,

the ligand conformations are generated by randomly rotating or translating it about a bond. The energy of that random conformation is then calculated and compared against a standard Metropolis criterion, based on which the conformation may be either accepted or rejected[217].

According to Meng *et al.*, the purpose of a scoring function is to demarcate the correct poses form the incorrect poses, or rather the binding compounds from inactive ones within a reasonable computation time[218]. The empirical function, a type of scoring function, decomposes the binding energy into different components such as hydrogen bonds, lipophilicity, ionic interactions and entropy penalties; each component is then multiplied with a co-efficient obtained from regression analysis of ligand-protein complexes with known binding affinities and then finally summed up to give a final score [218,219].

Glide[220] from Schrodinger Inc. is one of the popular tools used for docking experiments. The operation mechanism of Glide can be best described as a funnel with a series of hierarchical filters that select for the best ligand pose at each stage (Figure 1.22). Glide has been suggested to provide accurate docking results in a number of studies comparing docking results[221–223]. Ligand poses are first selected by initial screens over the entire phase space of the ligand. Selected poses are then minimised in the field of the receptor using an OPLS-AA force field in conjunction with a distance-dependent dielectric model. The lowest energy poses hence obtained are then examined for the nearest torsion minima by Monte Carlo[220].

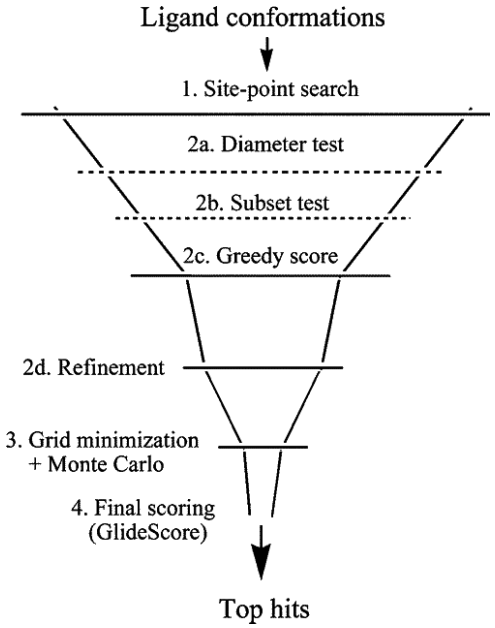

Figure 1.22 The operation mechanism of Glide. *Source: Friesner et al.*[220]

Glide uses GlideScore[220], a modified version of the empirical ChemScore, and is calculated as:

GlideScore = (0.05 * van der Waals energy) + (0.15 * coulombic energy) + rewards for favourable lipophilic bonds + rewards for hydrogen bond + rewards for metal binding interactions + rewards and penalties for additional terms such as amide twists, buried polar groups etc. + penalty for freezing rotatable bonds + rewards for polar interactions.

Glide has two docking modes: Standard Precision (SP) and Extra Precision (XP)[220]. While SP mode acts as a softer version allowing ligands with a reasonable propensity to bind, XP exerts severe penalties on poses that contravene established laws of physical chemistry. Both modes offer an expanded sampling setting that allows more poses to pass through the pose filters in Glide. Schrodinger also offers an induced fit docking (IFD)[224] tool, whereby the protein residues can additionally be defined as flexible. It operates by

first generating an ensemble of poses for each ligand using Glide. For each pose, the receptor side chains near the ligand are re-oriented using Prime. After energy minimisation of those re-oriented receptors, each ligand is then re-docked into the low energy receptors and the complex is assigned a GlideScore[224].

1.5.3 Molecular Dynamics (MD) Simulations

Proteins, though being structurally stable machinery, are at often times quite flexible even at their native state. Signalling proteins like GPCRs are required to exhibit this flexibility when shifting from inactive to active state and returning to the basal state. A structure obtained via NMR, XRD, or homology modelling gives only a snapshot of the state of the protein at a particular instant of activation or basal state[225]. While computational docking predicts the energetically favourable pose for a ligand in a protein, it does not provide information as to how that pose affects that protein's conformation - as the protein is not fully flexible. In this regard, MD simulations can predict the movement of individual components of a system with respect to time in an environment where the interatomic interactions are governed by the general laws of physics [226].

A classical MD simulation uses Newton's equations of motions to predict the spatial position of each atom as a function of time. First, the force on each atom is calculated which is then used to predict the position and velocity of an atom at a particular time. This process is then repeated on a successive number of timesteps[225], the repetition being large enough to capture structural changes of biological importance. The timestep in most cases in maintained in the order of a few femtoseconds to ensure numerical stability [226]. The resulting trajectory is hence like a three-dimensional movie of a few nano or

microseconds with each frame representing the position and velocity of the system at each timestep.

The forces in an MD simulation are calculated with the help of a force field. A force field can be defined as a mathematical expression that comprises the functional form of potential energy, including the bonded and non-bonded interaction terms between the atoms in the system[227] as in Figure 1.23.

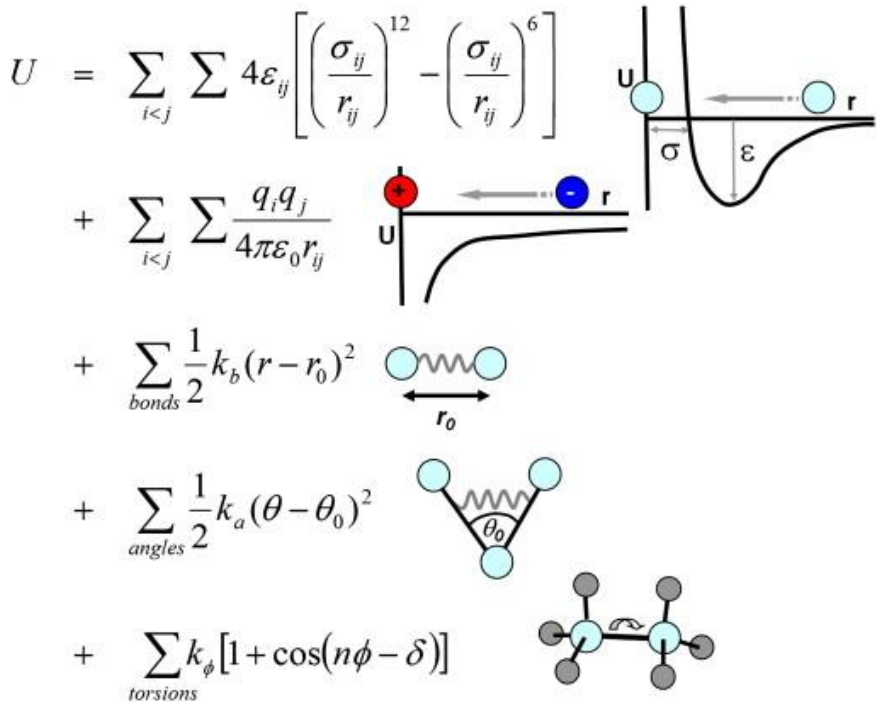

Figure 1.23 The molecular mechanics potential energy function (U) comprising the non-bonded(van der Waals and coulombic interactions) and bonded interaction terms (bond length, angle bending, and dihedral energy). *Source: Anwar and Zahn*[228]

Bonds stretches and angles in a force field are expressed as harmonic functions and dihedral angles as a cosine function; indeed, in a classic MD simulation, the atoms can be likened to spheres and the bonds that connect them as springs[226,227]. Hence, the atoms are

allowed to move only within a certain distance of each other, in a spring-like manner. The non-bonded terms such as electrostatic and van der Waal interactions are modelled using Coulomb's law and Lennard-Jones potential respectively. For long-range electrostatic interactions, particle mesh Ewald method under periodic boundary conditions is normally used. Some of the common force fields used presently are AMBER, GROMOS, and CHARMM[229–231].

1.5.3.1 Principal Component Analysis

One of the analysis techniques used in the work reported to study the major motions of a protein in the simulation trajectories is called Principal Component Analysis (PCA). PCA is a multivariate statistical analysis technique that reduces the number of dimensions required to describe the protein dynamics[232]. In general mathematics, it is used to identify correlation in large data sets.

According to Amedei *et al.*, dividing configurational space in a dynamics trajectory can be into two types: (1) essential subspace – that contains very few degrees of freedom and comprises most of the positional motions (2) remaining space – where the motions are constrained. They discovered that a simple linear transformation of the Cartesian co-ordinate deviation allows to differentiate the two subspaces in a trajectory[233]. Hence, the application of PCA to MD trajectories is also called 'essential dynamics'.

In an MD context, a PCA calculation involves setting up a covariance matrix (or variance-covariance matrix) of the atomic coordinates of the protein that make up the system trajectory. Eigenvalue decomposition of this matrix gives eigenvectors and their associated eigenvalues. The eigenvectors represent a correlated displacement of groups of atoms in the system (i.e. their direction) while the eigenvalues describe the magnitude of

displacement (or the variance of motions). The higher eigenvalues represent the motions on a larger scale i.e. the essential motions. The corresponding eigenvalue-eigenvector pair is called the principal component of a trajectory. Displacement along a principal component can be visualised by projecting the trajectory i.e. the original co-ordinate data onto the respective eigenvector[232].

1.6 Aims and Objectives

As seen in sections 1.2.1.2, 1.2.2.2, and 1.3, there are already 5 crystal structures solved for CB1 and one crystal structure solved for CB2. Crystal structures, however, do not represent the proteins in their native state due to addition of thermostabilising mutations, constructs, and truncation of residues for structure stabilisation (Section 1.1.6), aside from artefacts such as missing residues and atoms. In addition, PDB structures do not contain hydrogen atoms as they are not well detected in x-ray crystallography experiments. As mentioned in Section 1.5.3, crystal structures are rigid and cannot convey all the structural features of a protein. Especially for GPCRs, where structural plasticity is often exhibited, crystal structures are not enough to understand the conformational landscape of a receptor. Studying the conformational landscape, in turn, can aid in understanding complex characteristics such as biased signalling and allosterism that GPCRs exhibit. GPCRs at their resting state will be in an apo form i.e. without any ligand bound. Apo form is regarded as an intermediate state between active and inactive states. This is because the apo receptors can exhibit active-conformation like features through which they emit a minimal degree of signalling (basal activity)[234]. It must be noted that none of the available CB1 or CB2 crystal structures is in an apo state, thus making structural studies of the

receptors the primary aim of the work reported herein. Given that MD simulations offer an easy way to study molecular motions, the work reported herein will predominantly use unbiased MD.

1. The first step involves re-engineering the receptors to remove crystal structure imperfections. Due to efficiency and precedence of use in re-engineering, homology modelling will be used to refine existing crystal structures[235–238]. Using the inactive state model of CB2 hence generated, the binding mode of novel cannabinoid ligands shall also be predicted.
2. To investigate the possible conformation that an apo CB1 receptor might assume, MD simulations will be performed on a re-engineered inactive state CB1 receptor model. In addition, two holo CB1 models will be subject to simulations as well (i) an agonist bound CB1 model - to investigate if a chosen position of agonist is favourable for activation of CB1. (ii) an antagonist bound CB1 model - to serve as control and to analyse the variations in the response of the receptor towards an agonist and antagonist.
3. In a separate study, the transition of an inactive CB1 model to an active state and vice versa will be analysed. This will be investigated via a cross-docking study of CB1 active and inactive structures wherein the cognate ligand of their template crystal structure is docked into their opposing state model. These two cross-docked models will then be subject to MD simulations. In both CB1 studies, the direction of the conformational change observed in the protein molecule of each system will be analysed using common structural analysis methods such as root mean square fluctuation

(RMSF), root mean square deviation (RMSD), and PCA to assess whether ligand bias can be reversed and important conformational changes that makeup activation and inactivation can be observed and further quantified.

4. Similar to CB1, CB2 lacks a crystal structure in the apo form. As of yet, CB2 also does not have a solved active state crystal structure as well. To investigate the potential conformations that the apo state and an agonist bound state of CB2 might assume, MD simulations will be performed on a generated model of inactive CB2 in both the apo state as well an agonist docked holo state. Similar to the simulations of CB1, the direction of the conformational change observed in the protein molecule will be observed using tools such as RMSD, RMSF, and PCA.

As already described in Section 1.4, certain non-cannabinoid ligands also interact with CB1 and CB2. These ligands are potentially reusable to treat a different condition other than the one they are intended for. With the aim of drug repurposing, the interaction of non-cannabinoid ligands at CB1 and CB2 will also be studied. This work will utilise two different approaches. Firstly, a set of drugs currently used for known indications will be tested against CB1 and CB2 for agonist activity using [^{35}S]GTPγS binding assay, a commonly used method to compare agonist potency and efficacy of ligands at GPCRs (Section 1.2.3). Secondly, non-cannabinoid ligands that have been reported to show activity at CB1 and CB2 will be docked to the receptor models generate; the binding mode and ligand-receptor interactions will be analysed. Through the analysis, the study hopes to gain data required for further scaffold designs.

It is to be noted that the CB1 and CB2 receptor models generated and studied, and all the protein sequences and structures used for those studies pertain to the human species only, unless otherwise stated.

2 Modelling Cannabinoid Receptors

2.1 Introduction

Though CB1 has been studied since 1988, it was only in October of 2016 that its first crystal structure was released (Section 1.2.2.1)[102]. Hence, to predict the structure of CB1 before this period, different modelling techniques were used, of which homology modelling was the most preferred due to its reliability (Section 1.5.1). Accordingly, different class A GPCRs such as rhodopsin, A2AR and β2AR for which crystal structures were already available were used as templates to build homology models for CB1 (Section 1.2.2.1). Even for proteins with a known crystal structure, homology modelling is still applicable in the form of re-modelling or re-engineering the protein with the crystal structure as a template (re-engineering here refers to the creation of a model of a receptor using its crystal structure as the template and its wild type amino acid sequence as the query). This is because the crystal structures contain artefacts and additional modifications that aid in crystallisation (Section 1.1.6). CB1 models re-engineered from the original structure are being used in the present for structural studies such as docking, as well as for virtual screening and MD simulations (Section 1.4.1)[235,236,239,240].

The study presented herein was started in early 2016 when the crystal structure for CB1 was not available. Therefore, the initial aim was to predict the structure of CB1 and validate the resulting model. However, after the release of crystal structures, CB1 and CB2 were re-engineered using the available crystal co-ordinates as templates. Hence, the first section of this chapter details the homology modelling and validation of CB1 models generated before the release of the first inactive crystal structure. The second section of the chapter includes the re-engineering of crystal structures of CB1 and CB2. The differences

in the binding mode of CB1 homology models versus CB1 re-engineered models are then compared and contrasted.

The third section deals with identifying the binding mode of two novel CB2 selective ligands. COR167 (SER601) (24) and COR170 (25) are 6-substituted 4-quinolone-3-carboxylic acid-based CB2 selective ligands. Though structurally analogous to each other (Figure 2.1), the ligands show varying functional profiles at the CB2 receptor. While COR167 (24) shows agonist properties at CB2[241,242], COR170 (25) shows inverse agonist properties at the same[241,243]. This part of the chapter aims at predicting the binding mode by which the ligands effect this opposing functional profile on CB2 using molecular docking.

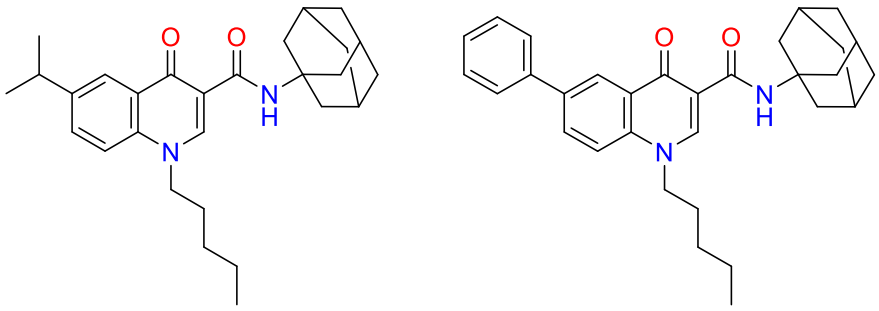

(24) COR167 (25) COR170

Figure 2.1 Structure of COR167 and COR170

2.2 Aims

1. To generate and re-engineer models of CB1 and CB2 using homology modelling
2. To validate the models and compare them
3. To identify the binding mode of two novel cannabinoid ligands

2.3 Structure Prediction of CB1 (Pre Crystal Structure)

2.3.1 Template Selection

The amino acid sequence of the human CB1 receptor was retrieved from the UniProt Knowledgebase[244] (accession number P21554). A BLAST search was performed against PDB using default parameters on the NCBI BLAST server[245] to identify the GPCRs with known structures that are homologous to CB1. The top four results from the BLAST search (Table 2.1) were taken forward for local alignment to select a suitable template. The amino acid sequences of the potential templates were also retrieved from the UniProt Knowledgebase. Human A2AR, which was used as a template in previous cannabinoid receptor modelling work within this research group, was also considered for local alignment. The alignment was done using the EMBOSS Water tool hosted by the European Bioinformatics Institute server[246]. The default parameters (BLOSUM62 matrix, gap penalty 10.0 and extension penalty 0.5) were maintained. Sequence alignment was done over the entire protein sequence, as extracellular loops too play an important role in ligand binding[98,99,247]. The alignment file was checked for proper alignment of the conserved residues, motifs (mentioned in Section 1.1.2 and 1.1.3) and TM sequences, as well as sequence identity and gaps, to allow selection of the most suitable template. The results of the local alignment using the WATER tool are as given in Table 2.1.

GPCRs with known crystal structures (UniProt accession numbers given in brackets)	% identity with CB1 receptor protein sequence	% gaps found in alignment
Human LPA1 (Q92633)	27.9	11.2
Human S1P1 (P21453)	27.6	21.8
Turkey β1AR (P07700)	25.1	29.1
Squid rhodopsin (P31356)	23.5	12.5
Human A2AR (P29274)	28.0	21.7

Table 2.1 Percentage of sequence identity and gaps found in the local alignment of potential template sequences with CB1 sequence.

As per Table 2.1, the percentage of sequence identity falls below 30% for all receptors considered, making them apparently unqualified to be used as templates for homology modelling (Section 1.5.1). However, it is to be noted that in the case of GPCRs, the overall sequence identity is often compensated with a high level of conserved residues and motifs within the TM regions, as the loops tend to show most variation between different classes and families of receptors[248] (Section 1.1.1). Human A2AR appears to be the best candidate as a template in terms of the sequence identity. However, the percentage of gaps is higher than seen in other candidates.

Human LPA1 appears to be the next best option in terms of both percentage sequence identity and percentage of gaps. As seen before, LPA1 and CB1 are both lipid binding receptors with comparable structural features and ligand binding modes (Sections 1.2 and 1.3). Furthermore, a tryptophan residue at position 5.43 is unique to only the cannabinoid and lysophosphatidic acid receptors. A metabolite of 2-AG (2), 2-arachidonic

phosphatidic acid, and phosphorylated anandamide (1) have been shown to bind to LPA1 with relative ease. All these factors make human LPA1 a suitable template to model CB1[200]. The local alignment of human CB1 sequence with human LPA1 sequence using WATER is depicted in Figure 2.2.

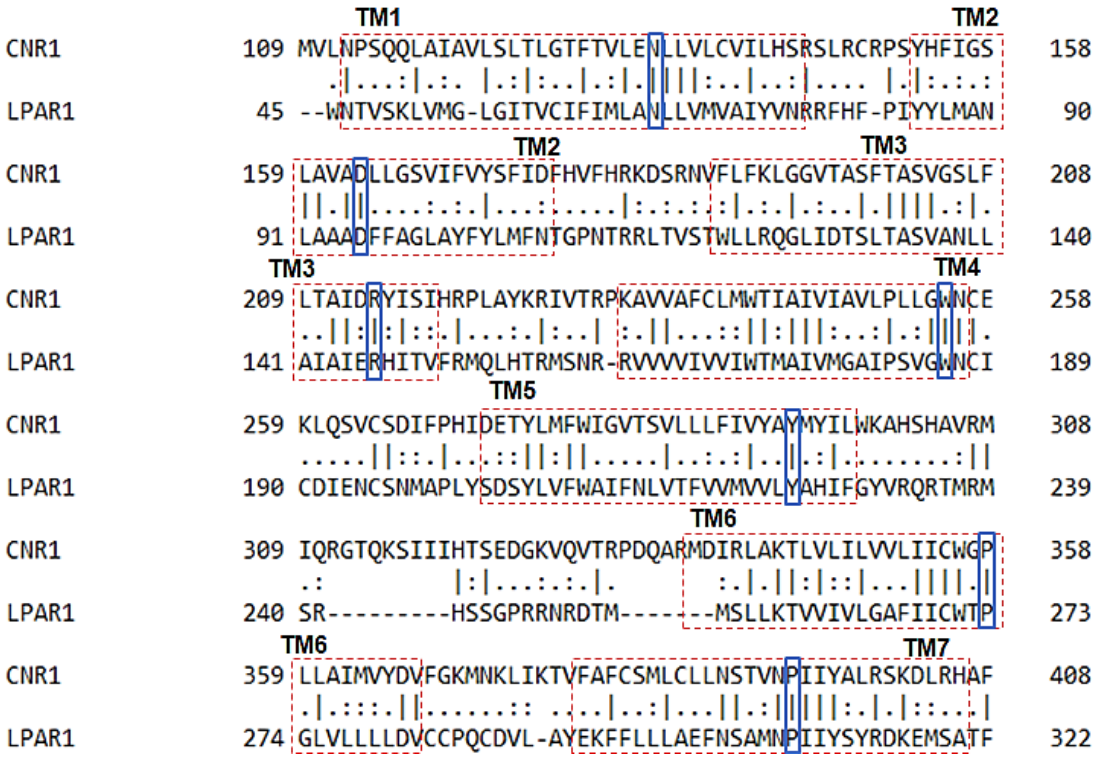

Figure 2.2 Local alignment of human CB1 receptor sequence with human LPA1 receptor sequence. *The red dashed boxes represent the TM regions. Residues in blue rectangles represent the most conserved residues in the TM helix (refer to Section 1.1.2 and 1.2.1). CNR1 represents human CB1 receptor sequence and LPAR1 represents human LPA1 receptor sequence.*

2.3.2 Homology Modelling

2.3.2.1 Method

PDB repository has three inactive crystal structures for LPA1. For modelling purposes, the crystal structure with the least number of missing residues and mutations

(PDB ID: 4Z34) was chosen as the template[200]. The crystal structure is of 3.0 Å resolution; it starts from Asn20 at the N-terminal and ends at Gly327 in the C-terminal. It contains a non-native BRIL construct inserted within ICL3 from Arg233 and Arg247. The construct, cognate ligand, and water molecules were removed prior to homology modelling.

Molecular modelling was performed with the structure prediction wizard of Prime tool of the Schrödinger, Inc. 2015 Suite[215]. The alignment between the two sequences was modified to minimise the gaps and ensure that the conserved residues and motifs common to both template and query proteins (Sections 1.1.2 and 1.2.1), and TM helix ends were accordingly aligned. Models were built using both 'knowledge-based' and 'energy-based' method settings that Prime offers (Section 1.5.2). 40 models were built using the knowledge-based method, and only one was built using the energy-based method since 'one' is the maximum output for this setting (this model is henceforth referred to as EB). The N-terminus, ICL3, and C-terminus were truncated in the construction of the models to reduce computational cost since the focus is on the ligand-binding pocket (ICL3 of CB1 is 36 residues long and is lengthier compared to ICL1 and ICL2). A disulphide bridge was set to be built between Cys257-Cys264 using proximity constraints option. The best model among the knowledge-based homology structures was chosen on the basis of their Ramachandran plots, which were generated using the PROCHECK tool of PDBsum server[213]. The best model was named as KB_best.

2.3.2.2 Qualitative Validation

The models start from Gln115 in the N-terminus up until Pro298 in the C-terminus, with a gap for ICL3 that starts from Glu309 to Leu341. The best models obtained using each method and their Ramachandran plots are as shown in Figure 2.3. The KB_best model

has 91.8% of residues in the most favoured regions while 0.6% of the total residues are in the disallowed regions. For the EB model, 91.0% of the total residues are in the favoured regions while 1.6% of the total residues are in the disallowed regions.

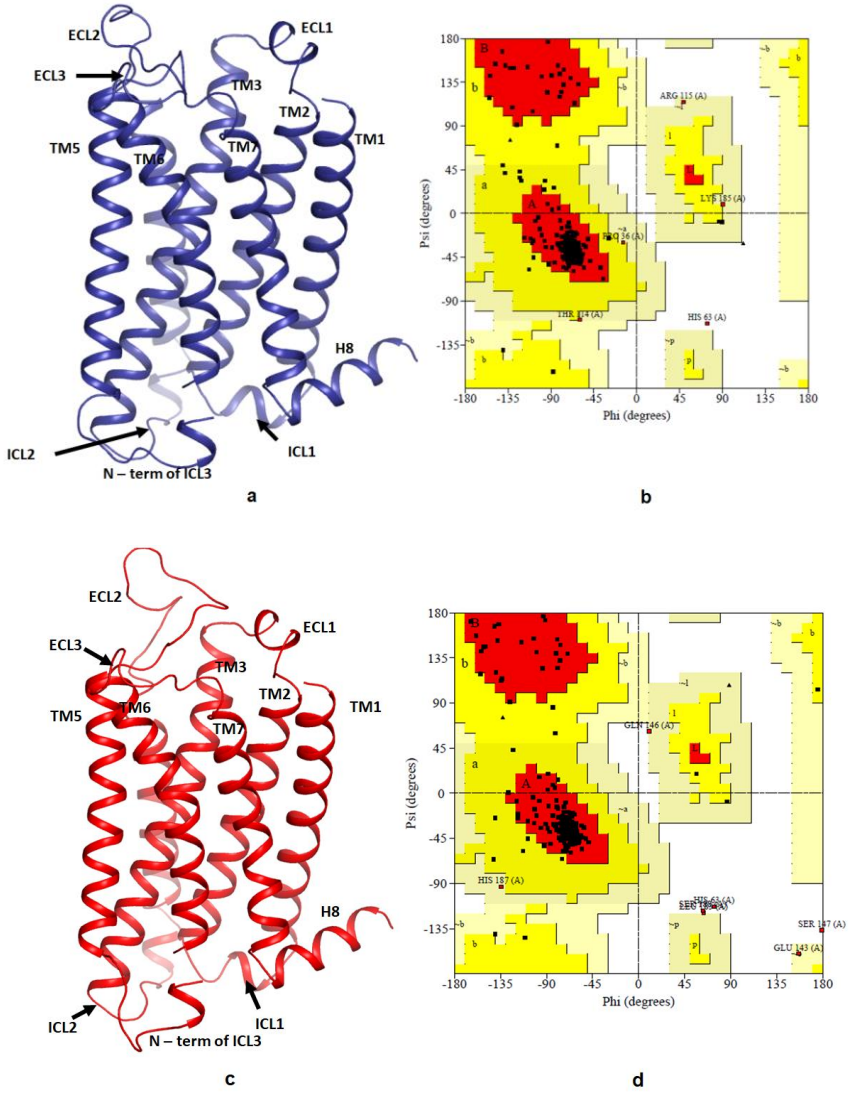

Figure 2.3 Homology models and their Ramachandran plots. *(a) The best homology model built using the Prime-knowledge-based method (KB_best) and (b) its Ramachandran plot. (c) Homology model built using Prime-energy based method (EB) and (d) its Ramachandran plot. The plot notations are given in Section 1.5.1. In (a) and (c), TM4 is hidden behind TM6.*

The KB_best and EB model have an RMSD of 3.5 Å between their backbone atoms. The helical bundle in both models are similar to each other since the same template was used to build both. The TM helices 2, 3, 5, 6 and 7 form the binding core in the models. Helix length of TM4 is longer in both than predicted by Bramblett et al.[83]. ECL2 is toward the binding pocket in KB_best and away in the EB model as if to suggest a 'closed' and 'open' state respectively (Figure 2.4). Both models were then taken forward for quantitative validation.

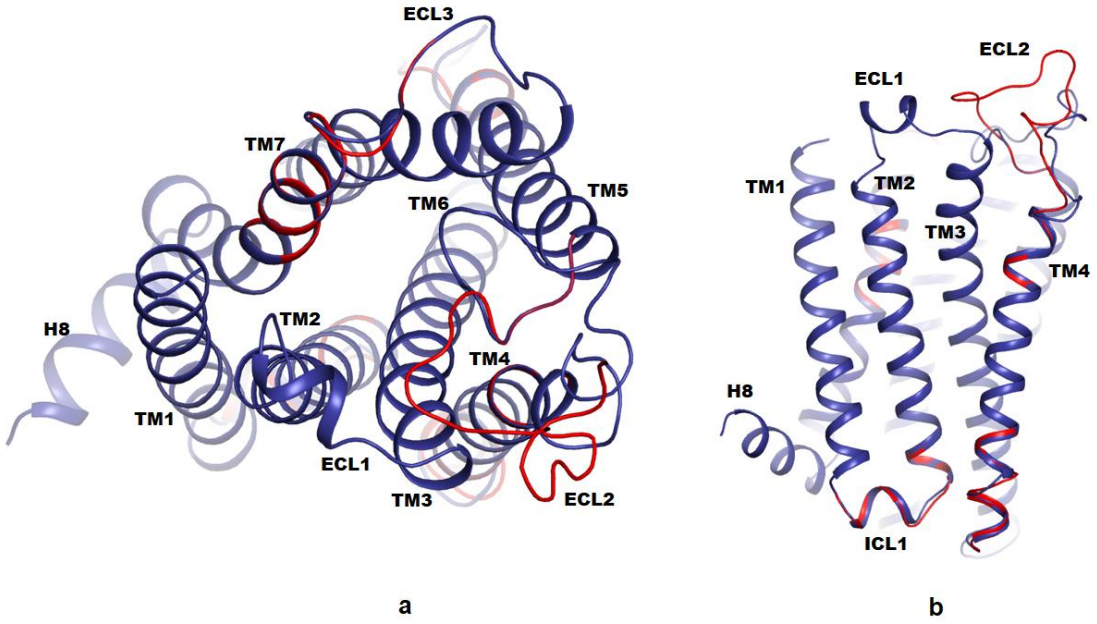

Figure 2.4 Superposed CB1 models generated with LPA1 template *– KB_best (blue) and EB (red) using Knowledge-based and Energy-based methods in Prime. (a) Top view (b) Side view*

2.3.2.3 Quantitative Validation - Computational Docking Evaluation

2.3.2.3.1 Method

The software Glide from Schrodinger Inc.,[220] was used for ligand docking purposes. Protein files were prepared using the Protein Preparation Wizard[249]. Existing hydrogen

atoms were deleted, and new hydrogen atoms were added. The termini were capped with ACE and NMA groups, and the hydrogens atoms were subject to restrained minimisation. The p*Ka* and other parameters were maintained at default. A test set of agonists and antagonists (given in Appendix 2, Table II.1 and Table II.2) of CB1 with established *Ki* values, compiled in a previous cannabinoid receptor modelling work within this research group, was used for validation. The ligands were retrieved from PubChem database[250] and those that were unavailable in PubChem were drawn using Maestro[251] from Schrödinger, Inc. The ligands were finally prepared using the LigPrep tool[252]. Possible protonation states at pH 7.0+/-2.0 were generated. The grid generated for docking was a 34 Å box, containing an internal 10 Å box, through which the centre of each docked ligand would be required to pass. Glide docking was done in two modes – SP and XP. 10 conformations per ligand were generated in each docking combination.

2.3.2.3.2 Results

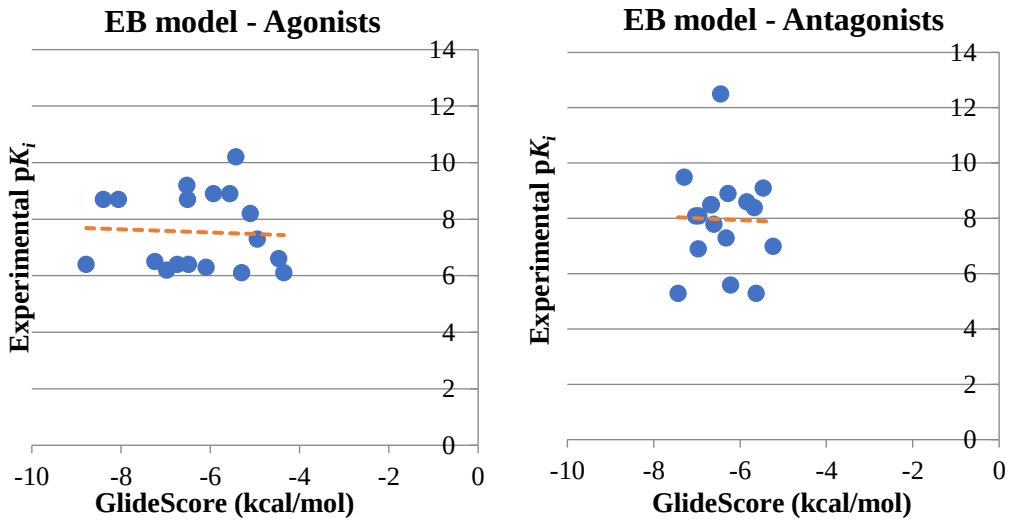

Figure 2.5 Plot of GlideScore versus experimental pKi values of energy-based model docked with agonists and antagonists. *The trendline is shown as an orange dashed line in both graphs.*

The GlideScore, an approximation of binding affinity, was considered as a criterion for selection of the best-docked structure. The top GlideScore that best reflected realistic binding was then plotted against the experimental K_i values, and the Spearman's rank correlation coefficient (ρ) and coefficient of determination (R^2) were calculated. The R^2 and ρ values calculated from the plot of GlideScore vs experimental pK_i (Figure 2.5) for agonist and antagonist docking were not statistically significant and do not show any correlation; however, the correlation scores for the EB model were better in comparison to the same obtained for the KB_best model. The protocol that yielded the best values for the EB model was SP with expanded sampling option. For agonists the $R^2 = 0.0028$ and $\rho = -0.0531$, and for antagonists $R^2 = 0.0007$, $\rho = -0.0264$ (Figure 2.5).

2.4 Re-engineering CB1 and CB2 Models

2.4.1 Method

Similar to the method explained in Section 2.3.2.1, CB1 and CB2 crystals were remodelled using Prime. Models were generated for crystal structures 5TGZ (CB1 inactive), 5U09 (CB1 inactive), 5XR8 (CB1 active), and 5ZTY (CB2 inactive). The complete ICL3 was generated for models based on 5U09 (35 residues long) and 5ZTY (17 residues long), as they were later used for MD simulation studies (Chapter 3 and Chapter 5). On the contrary, ICL3 was truncated for models based on 5TGZ and 5XR8 to minimise computational expenditure as these models were used predominantly in docking-based studies (Chapter 6). To re-engineer models with a complete ICL3,

1. An energy-based model including the ICL3 with the crystal co-ordinates as template was first built. This was done to get an energetically favourable conformation of ICL3 (Section 1.5.2).

2. Then, using the energy-based model as the template for ICL3 and crystal structure coordinates as the template for the rest of the receptor, the knowledge-based method was employed to build the required receptor models.
3. The resulting model was then subjected to loop refinement on residues that were marked as residing in unfavourable regions on their Ramachandran plots (Appendix 2, Figure II.1). The plots were generated using PROCHECK[213]. The loop refinement wizard of Prime under default settings was used for this purpose.

For models with truncated ICL3, the knowledge-based method was used to build a model with crystal structure template (Step 2). A short pseudo loop was generated as a replacement for ICL3. The omitted residues are given in Table 2.2. In the case of CB1-5TGZ, loop refinement was not considered to be necessary, as the outlier residues are located on the pseudo-loop and C-terminus. Docking studies reported herein pertain only to the canonical binding pocket seen in class A GPCRs; hence CB1-5TGZ was not subjected to refinement. CB1-5XR8 model did not have any outliers and hence was also not refined. The details of each model generated are given in Table 2.2

Model	PDB ID of template	N- and C-terminal residues omitted	ICL3 residues omitted	Residues with missing atoms corrected	Mutations re-built
Inactive CB1	5TGZ	Met1-Cys98 and Pro413-Leu472	Arg307-Arg331	Met109,Gln115, Leu117,Gln261, Lys370	Thr210Ala, Glu273Lys, Thr283Val, Arg340Glu
Inactive CB1	5U09	Met1-Gly99 and Pro413-Leu472	None	Arg145,Arg182, Gln261,Lys370, Phe412	Thr210Ala
Active CB1	5XR8	Met1-Met103 and Cys414-Leu472	Arg307-Arg336	Lys183,Lys232, Met337,Arg400	Thr210Ala, Glu273Lys, Thr283Val
Inactive CB2	5ZTY	Met1Asp18 and Cys320-Cys360	None	Lys33,Arg66,Leu144, Leu145	Thr127Ala, Thr153Leu, Arg242Glu, Gly304Glu

Table 2.2 Changes made in re-engineered models in comparison to their corresponding crystal structure templates.

2.4.2 Qualitative Validation

The generated models with full ICL3 and pseudo ICL3 are given in Figures 2.6 and 2.7 respectively.

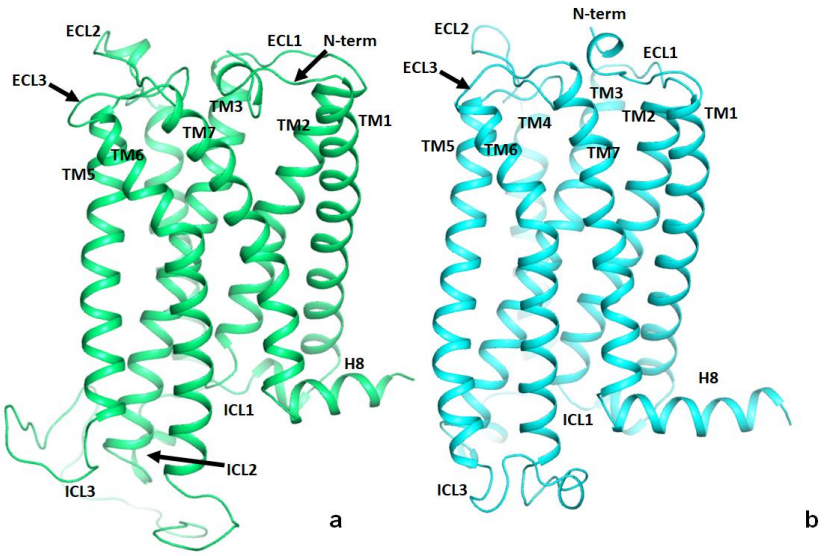

Figure 2.6 Models with a complete ICL3 *(a) CB1 based on 5U09; TM4 is hidden behind TM6. (b) CB2 based on 5ZTY. The segments of N-terminus and C-terminus omitted are given in Table 2.2*

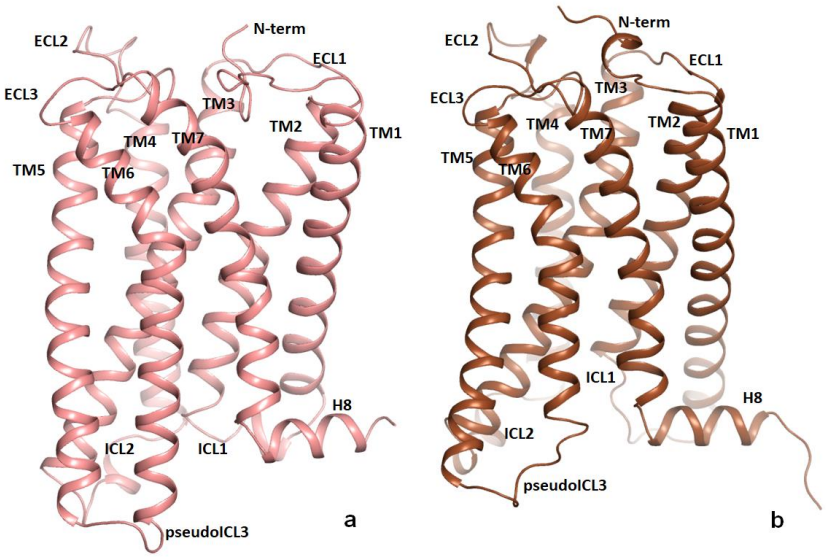

Figure 2.7 Models with a pseudo ICL3 *(a) CB1 based on 5TGZ (b) CB1 based on 5XR8. The segments of N-terminus and C-terminus omitted are given in Table 2.2*

CB1 has a larger ICL3 loop than CB2. Accordingly, ICL3 of CB1-5U09 (Figure 2.6(a)) has a rather expanded ICL3 as compared to CB2-5ZTY. However, the loops in both models are well contained in the region of the protein which is near the intracellular face

of the lipid bilayer. RMSD value of the generated models against their respective template crystal structures was measured without fitting (for all regions except the full or pseudo ICL3). The backbone Cα, C and N atoms were used for calculations. CB1-5U09 has an RMSD value of 0.249 Å against its crystal structure, and CB2-5ZTY has a value of 0.973 Å against its crystal structure. CB1-5TGZ shows the highest RMSD value of 1.363 Å while CB1-5XR8 shows a very low value of 0.01 Å.

2.4.2.1 Re-docking cognate crystal ligand

As a means of validating the correctness of the binding pocket, the crystal cognate ligands were re-drawn and re-docked into the binding site. A grid of an appropriate size (24 Å, internal box 10Å) was constructed for each model with the cognate ligand of its template crystal structure as its centre. SP mode in Glide was used for docking cognate ligands.

Models with complete ICL3

As seen in Figure 2.8, the cyanophenyl and dichlorophenyl groups in MK0364 (19) are aligned well with the crystal cognate ligand in 5U09 (in green). However, the trifluoromethylpyridine ring is faced upward in the redocked ligand (in grey) rather than pointing at TM1, as in the crystal structure. In CB2-5ZTY, the redocked AM10257 (23) (in grey) occupies the same position as the cognate ligand in the crystal structure (in cyan). Minimal changes are seen with respect to the orientation of the aliphatic chain and the rotamer angle of the benzene facing down into the binding pocket. RMSD value (for common atoms) between the crystal and re-docked ligand for 5U09 is 4.426 Å and for 5ZTY is 0.764 Å.

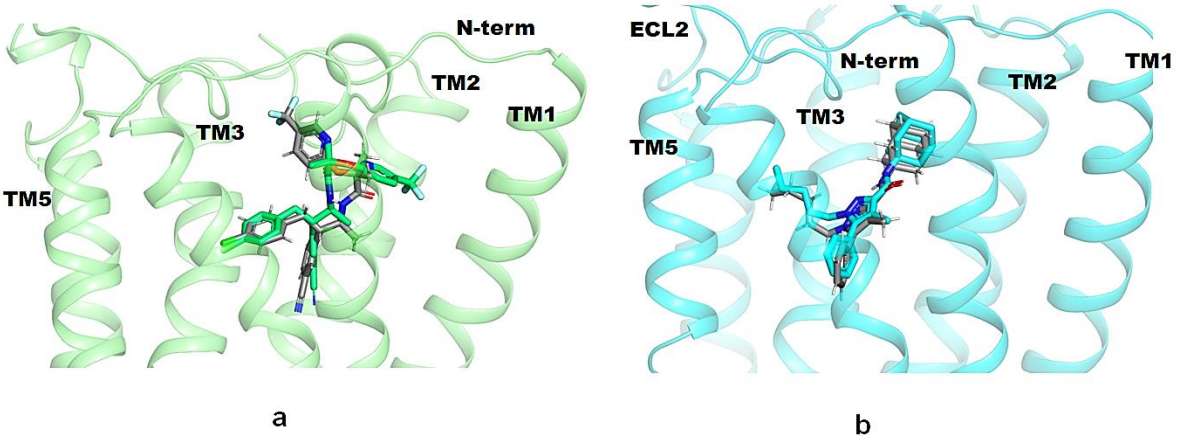

Figure 2.8 Redocking cognate ligands into their respective template-based models. (a) MK0364 (19) in CB1-5U09. *TM6 and 7 are in the foreground, and TM4 is hidden behind TM5.* ***(b) AM10257 (23) in CB2-5ZTY.*** *In both images TM6 and 7 are in the foreground; the redrawn-redocked ligand is shown in grey. N-term refers to N-terminus loop.*

Models with truncated ICL3

From Figure 2.9, it can be seen that the re-docked ligand (in grey) occupies the same position as the cognate ligand in the crystal structure in both the inactive (in pink) and active (in brown) CB1 models with truncated loops. There are slight variations between the pose of the crystal cognate ligand and redrawn cognate ligand. In 5TGZ, the aminoalkyl group of AM6538 (18) was not fully resolved during crystallisation process[102]. The redrawn (and redocked) AM6538 (18) containing the nitro group shows a possible orientation of the same group. It extends towards TM5 and forms a π-cation interaction with Trp279(5.43) and a hydrogen bond with Thr197(3.33). Apart from that, only minimal variation with respect to the ligand substituent group position is seen. RMSD value between the crystal and re-docked ligand (for the common atoms) is 0.421 Å.

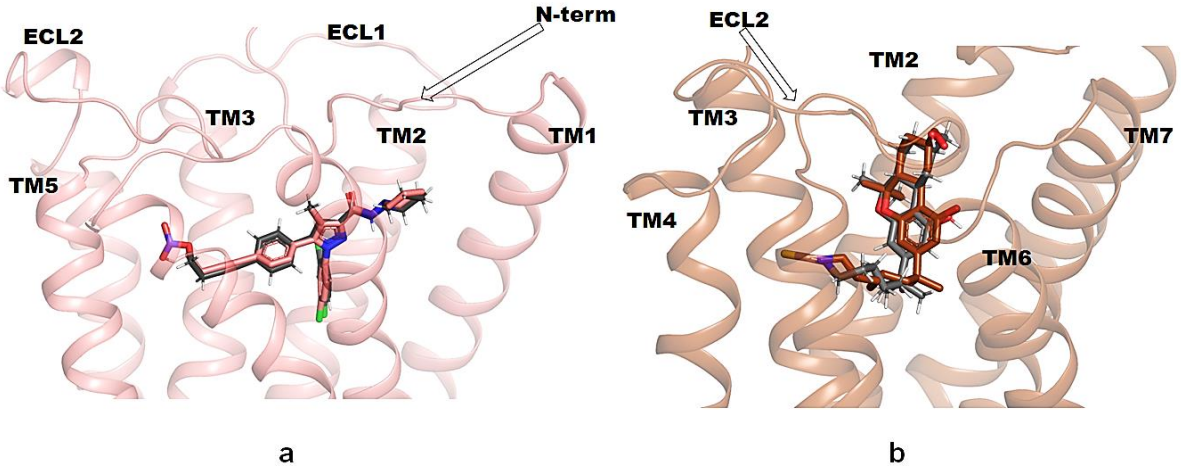

Figure 2.9 Redocking cognate ligands into their respective template-based models. (a) AM6538 (18) in CB1-5TGZ *(both ligand and receptor in pink). TM6 and 7 are in the foreground, and TM4 is hidden behind TM5.* ***(b) AM841 (21) in CB1- 5XR8*** *(both ligand and receptor in brown). TM5 is in the foreground. TM1 is hidden behind TM7. In both images, the redrawn-redocked ligand is shown in grey. N-term refers to N-terminus loop.*

In the case of CB1-5XR8, the aromatic head group of crystal cognate ligand and re-docked ligand coincide well with one another in the binding pocket. Similar to AM6538 (18) in 5TGZ, AM841 (21) in 5XR8 is missing the thiocyanate group at the end of its aliphatic tail. The redrawn (and redocked) ligand shows a possible orientation of the same group in the active structure. The group extends in the direction of TM3 and TM4, and away from TM5. RMSD value between the crystal and re-docked ligand is 0.825 Å (for the common atoms).

2.5 Difference Between the Binding Modes in Pre-Crystal Structure and Post-Crystal Structure Models

To illustrate how the ligand binding mode varies with change in the template, the antagonist SR141716 (10) was docked to the EB model (generated from LPA1 template)

and CB1-5U09. For the EB model, SP with expanded sampling was used, as that particular setting of docking gave better correlation scores than the rest (Section 2.3.2.3.2) in quantitative evaluation. The ligand, here, shows an extended conformation whereby, the dichlorophenyl arm points towards TM1 and piperidine arm points in the direction of TM5. The chlorophenyl arm points down into the binding pocket (Figure 2.10). A chlorine atom of the dichlorophenyl arm interacts with Lys192(3.28) via a halogen bond with a hydrogen attached to the side chain nitrogen atom. The central pyridazine ring interacts forms a stacking interaction with Phe379(7.35). It does not interact with the toggle switch residues – instead Phe200(3.36) and Trp356(6.48) are facing each other and are engaged in a face-face stacking interaction. Even after subjecting the ligand to IFD, the same orientation was obtained.

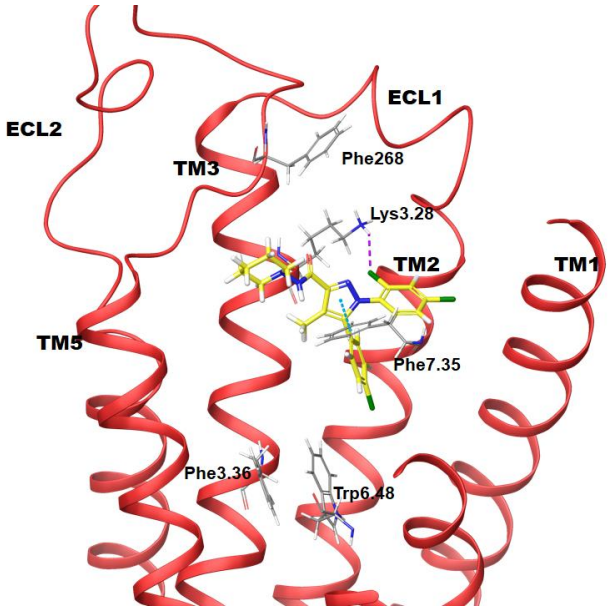

Figure 2.10 Docked pose of SR141716 in EB model of CB1 via SP – expanded sampling protocol. *Phe7.35 is in the foreground. TM6 and 7 have been removed for picture clarity.*

In the case of CB1-5U09, SP docking was used to identify the binding mode of SR141716 (10) (Figure 2.11). As observed, the ligand displays an extended conformation in CB1-5U09 as well. However, the dichlorophenyl arm and piperidine arm have switched places. Furthermore, the piperidine arm is pointing upward. Subjecting the same complex to XP docking results in a conformation quite similar to the one described in the docking of SR141716 (10) to 5TGZ[102] and 5U09[105]. It also assumes an extended conformation, but the piperidine arm is pointing towards TM1 as seen in the studies mentioned afore.

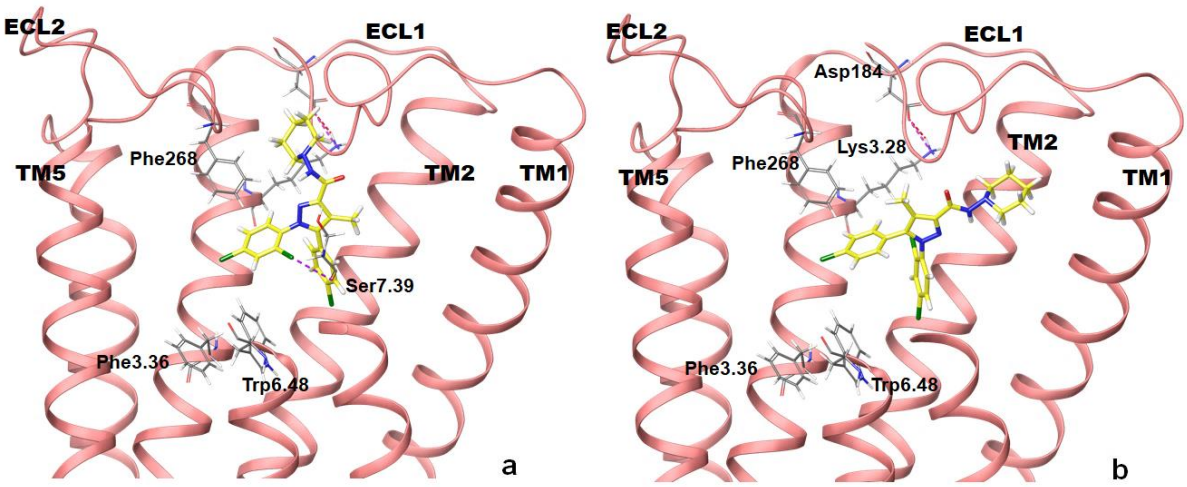

Figure 2.11 Docked pose of SR141716 in CB1-5U09 model of CB1 via (a) SP and (b) XP protocol. *In (a) Ser7.39 is in the foreground. TM6 and 7 have been removed for picture clarity.*

2.5.1 Discussion

As mentioned in Section 2.1, the initial aim of the study was to identify a protocol that is best suited to model the CB1 receptor from a known template and validate such a model. After amino acid sequence analysis, LPA1 was found to be a suitable template to

model CB1, due to the reasons mentioned in Section 2.3.1. Duly, crystal structure with PDB ID 4Z34, an inactive structure of LPA1, was chosen as the template. Upon validating the models hence generated, it was found that the correlation scores (for a plot of experimental pKi vs Glide Score) were very low.

By the end of 2016, the first inactive crystal structure of CB1 was released followed by many more structures (Section 1.3), relaying critical information regarding the nature of CB1 binding pocket. Prior to the release of cannabinoid crystal structures, it was suggested that Lys3.28 played an important role in the binding of endogenous, classical and non-classical cannabinoids. Mutagenesis experiments have demonstrated the importance of this residue in the binding of SR141716 (10) and deem it to be responsible for the inverse agonistic activity of biarylpyrazoles[112]. SR141716 (10) was speculated to bind in the 3-4-5-6 TM region of CB1. Its carboxamide oxygen was said to interact with the inactive receptor via a hydrogen bond with Lys3.28. It was also suggested that when SR141716 (10) binds to the inactive receptor, the dichlorophenyl ring forms an aromatic stacking interaction with Phe3.36, which in turn stacks with Trp6.48. In this docking position, SR141716 would block any movement of the Phe3.36 or Trp6.48 toggle switch[93,95].

An analysis of the CB1 crystal structures reveals that Lys192(3.28) does not interact with the cognate ligand in the inactive as well as the active states. This is true for the CB2 crystal structure as well[127]. The side chain of Lys3.28 is oriented parallel to the binding pocket pointing towards TM2. The side-chain nitrogen atom of the Lys forms a hydrogen bond with Asp184(ECL1). Hence, it is possible that Lys3.28 is involved in maintaining structural stability for cannabinoid receptors.

At this juncture, the aim of the study was diverted towards understanding the structural facets of cannabinoid receptors not conveyed by crystal structures; for this, models of CB1 and CB2 were re-engineered from the available crystal structures (Section 2.4). From the 'open' ECL2 conformation in EB model (Figure 2.3), it appears that energy-based method may not be suitable for re-engineering; neither the active nor inactive crystal structures of CB1 or CB2 released till date have such an ECL2 orientation. Hence, the knowledge-based method was used to obtain a good replicate of the template (Section 1.5.1). Save alone CB1-5TGZ model, other models generated (CB1-5U09, CB1-5XR8, and CB2-5ZTY) show RMSD less than 1 Å against the backbone atoms of their respective crystal structures (excluding ICL3 loops). Due to their closeness with their templates, the binding pocket of the models was validated by their ability to dock the crystal cognate ligands in the orientation seen in the crystal structures. Except for the docking of MK-0364 in CB1-5U09, all other redocked cognate ligands have RMSD less than 1 Å – indicative of a good redocked pose.

To understand how the binding pockets of LPA1-based and CB1 crystal structure-based inactive models vary, the antagonist SR141716 (10) was docked to EB model (LPA1 based model which had slightly better correlation value over KB_best model). The binding mode of SR141716 at CB1-5U09 is similar to that observed in the docking of the same to the crystal structures of 5U09[105] (as reported by Shao *et al.*; image not shown here). As reported in Section 2.5, the dichlorophenyl arm and cyclohexane arm of SR141716 occupy opposing positions when docked to the EB model. Even after the application of IFD, which is rather sophisticated than SP docking[224] (Section 1.5.2), the EB model did not change its binding conformation. Furthermore, in the CB1 models generated with LPA1 as the

template, the Lys192(3.28) was indeed facing into the binding pocket and interacting with the ligand. As to whether that conformation of Lys192(3.28) solely influenced the binding conformation however requires an in-depth study of the binding pockets of LPA1 and CB1.

Though XP docking shows a better binding mode for SR141716 (10) (in CB1-5U09) from crystal redocking experiments (Section 2.4.2.1), it can be seen that SP docking too produces acceptable results. Furthermore, it has been reported in certain docking software comparison studies that SP gave better results than XP docking[223,253,254]. Hence, as in the case of Section 2.4, future docking experiments will use SP docking to avoid any bias in results.

2.6 Identifying Binding Modes of Novel Cannabinoid Ligands with Opposing Functional Profiles at CB2

2.6.1 Method

The CB2-5ZTY model was used for this study. A grid of an appropriate size to encompass the orthosteric binding pocket was generated using Schrodinger's Grid Generation tool (version 2019.1). Ligands were docked onto CB2-5ZTY using Glide (version 2019.1) in SP mode[255] with default values. 20 poses per ligand were produced and the top-scoring pose in terms of GlideScore was selected for analysis.

2.6.2 Results

COR167 (24) and COR170 (25) adopt a conformation resembling AM10257 (23) (Figure 2.12). The adamantyl group points towards the extracellular pocket mouth and the propyl group is oriented towards TM4. The substituent groups point into the pocket. COR167 (24) forms an edge-face π-π stacking interaction with Phe183(ECL2) and a face-face stacking interaction with Phe117(3.36). COR170 (25) forms a π-π stacking interaction

with and Trp258(6.48). In both cases, Phe87(2.57) (hydrogen bond donor (HBD)) forms an aromatic hydrogen bond with the oxygen atom (acceptor (HBA)) of the heterocyclic ring core of the ligands.

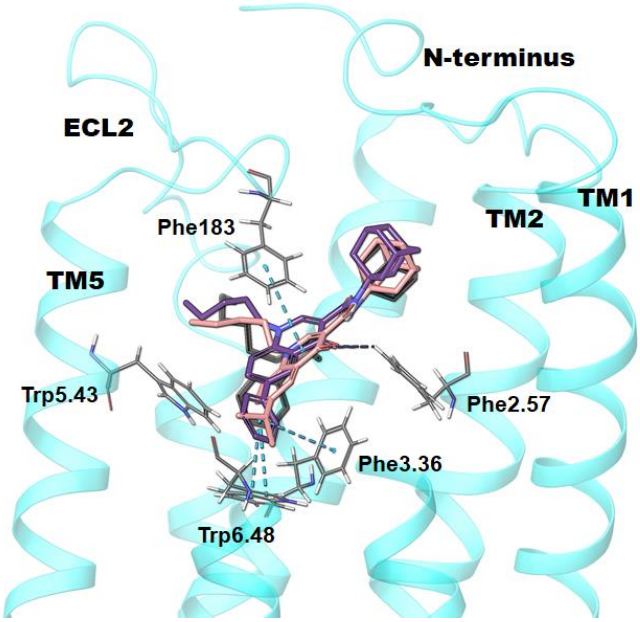

Figure 2.12 Docking COR167 (24) (pink) and COR170 (25) (purple) into CB2-5ZTY. *The cognate ligand, AM10257 (23), of the 5ZTY is depicted in black tracing. Residues are depicted as thin sticks. TM6 and 7 have been truncated for purposes of picture clarity. Blue and black dotted lines represent π-π and aromatic hydrogen bonds respectively.*

A full list of the contact residues that COR167 (24) and COR170 (25) interact with the inactive CB2 model (within a cut-off radius of 4 Å) and the predominant interaction type observed is given in Appendix 2 (Table II.3).

2.6.3 Discussion

Docking of COR167 (24) and COR170 (25) in CB2 showed that both ligands coincide well with the binding mode of AM10257 (23). One potential reason is that the presence of the adamantyl moiety in AM10257 (23) as well as COR167 (24) and COR170

(25) helps in orienting the latter two in the binding pocket. Hence, it can be suggested that the adamantyl moiety potentially influences the orientation of a ligand in both CB1 and CB2.

Another feature observed is the aromatic stacking between toggle switch residues Phe117(3.36) and Trp258(6.48) and the ligands phenyl group in the docking of COR170 (25). This is also seen in the interaction of the cognate ligand AM10257 (23) with CB2 in 5ZTY. When MRI2594 and MRI2687, two novel ligands that differ by a phenyl group, were tested on CB2 via β-arrestin2 recruitment assay, it was found that they act as an agonist and inverse agonist respectively[127]. Subsequent docking studies revealed that much similar to COR170 (25), MRI2687 interacted with Trp258(6.48) via its phenyl group. MRI2594, though occupying the same binding pocket, did not interact with Trp258(6.48). As mentioned earlier (Section 1.3), change in the rotamer position of Trp6.48 is a key component in the activation of CB1[93,94,103]. From the above results and studies, it can be suggested that Trp6.48 interaction is responsible for imparting COR170 (25) its inverse agonist properties at CB2, though it is an analogue of a CB2 agonist (COR167(24)).

2.7 Conclusion

In this chapter, the homology modelling and re-engineering of CB1 and CB2 models were reported. Pre-crystal structure release, an inactive state LPA1 was used as the template for homology modelling. For re-engineering, the respective crystal structures were used to develop inactive state CB1 and CB2 and inactive state CB2. Subsequent validation and binding mode comparison indicated that the re-engineered models offer reliable binding modes compared to LPA1 based models. Furthermore, standard precision (SP) in Glide was identified as a suitable option for further docking experiments. This chapter also

reports the identification of the binding mode of two novel analogous novel cannabinoids, COR167 (24) and COR 170 (25) that show opposing functional responses at CB2. Both ligands assumed an orientation overlapping that of AM10257 (23), the cognate ligand of 5ZTY. It was also proposed that stacking interaction of COR170 (25) with Trp6.48 residue and the lack of one in the case of COR167 (24) could be responsible for imparting COR170 (25) its inverse agonist properties at CB2.

3 Molecular Dynamics Simulations of Cannabinoid Receptor 1

3.1 Introduction

As mentioned in Section 1.3, five crystal structures of CB1 are available at present: two inactive structures and three active structures, with one active structure complexed with $G_{\alpha i}$ protein. Though crystal structures provide indispensable information regarding the conformation of active and inactive states of a receptor, they represent the conformation of the receptor at only one instant of time. Proteins, specifically membrane proteins, are highly flexible and upon ligand binding go through several conformational changes before arriving at the state seen in the crystal structure. If the ultimate aim of studying protein structures is to aid structure-based drug design, then the knowledge of how the protein responds to a ligand (and vice versa) is essential. As explained in Section 1.5.3, molecular dynamics simulations offer an effective way to study such a response by predicting the motions of a protein.

In this chapter, molecular dynamics simulations carried out on an inactive CB1 model are reported. Three systems were simulated using inactive CB1 as the starting structure: CB1-Apo, CB1 bound to an agonist, and CB1 bound to an antagonist. The inactive model generated using crystal structure with PDB ID 5U09 as the template (Section 2.4.1) was used for the study, owing to its high resolution[105]. As mentioned in Section 1.6, apo states can function as an intermediate state between antagonist-bound inactive and agonist-bound active states. [234]. Despite the availability of several inactive and active crystal structures (Section 1.3), CB1 does not have an apo crystal structure solved

yet. Therefore, to identify the architectural changes in the transition of an antagonist-bound inactive CB1 to an apo form, the CB1-Apo system was simulated. In other words, the aim was to observe how the absence of a ligand affects an inactive CB1 structure. The CB1-agonist simulation was done to observe if the presence of an agonist in a particular binding mode directs an inactive model towards an active state. AM841 (21), the cognate ligand of an active CB1 crystal structure (Section 1.3), was the agonist chosen for the study. It is a hexahydrocannabinol. Under *in vitro* conditions, AM841 (21) has been shown to reduce gastrointestinal motility by acting on intestinal CB1 receptors in normal and stressed mice[256]. CB1-antagonist simulations were performed to serve as control and to analyse the variations in the response of the receptor towards an agonist and an antagonist. The antagonist chosen was AM6538 (18), the cognate ligand for inactive crystal structure 5TGZ (Section 1.3). It is a derivative of AM251, which in turn is an analogue of SR141716 (10). AM6538 (18) has a higher affinity for CB1 than MK0364 (19), the cognate ligand of 5U09[102].

3.2 Aims

1. To run molecular dynamics simulation on three CB1 systems namely, CB1-Apo, CB1-AM841, and CB1-AM6538 with an inactive CB1 model as the starting structure.
2. To identify the direction of the conformational change observed in the receptor of each system using RMSF, RMSD, and PCA.
3. To investigate if the chosen initial position of the agonist is favourable for activation of CB1.

3.3 Methods

3.3.1 Preparation of CB1 Complexes

The inactive CB1 model for simulation using crystal structure 5U09 was generated as described in Section 2.4.1. Preparation of ligands, AM841 (21) and AM6538 (18), and its docking into the CB1 model was done using SP mode in Glide[257] as described in Section 2.4.2.1. The chirality of the ligands was retained; no ionised states were generated. All other parameters were set to default.

3.3.2 Embedding the Protein and Assembling the System

The processed protein was embedded into an all-atom POPC bilayer using the webserver CHARMM-GUI[258]. CHARMM-GUI uses data from the Orientation of Proteins in Membranes (OPM) database to aid in embedding the model[259]. A rectangular box type was chosen. The system was built using the replacement method where the protein is first surrounded by lipid-like spheres whose positions are subsequently used to place lipid molecules from the library of CHARMM-GUI. The bilayer consisted of 240 POPC molecules. The protein-membrane system was solvated with TIP3P[260] water and 11 chloride ions were added for neutralisation. The initial positions of the ions were obtained after 2000 steps of Monte Carlo simulations performed by the server outside the membrane region. The box sizes for CB1-Apo, CB1-AM841 and CB1-AM6538 systems were 97.59 x 97.59 x 103.57 Å, 97.65 x 97.65 x 103.57 Å and 97.65 x 97.65 x 103.57 Å respectively. The centre of the system was set to Z = 0. The lipid molecules were distributed equally on both sides of the membrane. The system was checked for penetration of lipid tail into protein surfaces and no such interferences were found. The force field parameters for ligands were generated using the CGenFF program built-into the same server[261].

3.3.3 Running MD Simulations

The CHARMM 36 force field was used in GROMACS 2016.4 to perform MD simulations[230]. The system was energy minimised using the steepest descent algorithm. NVT equilibration was run for 100 ps. NPT equilibration was run in four steps: 10 ns of restrained dynamics, 5 ns with only backbone atoms restrained, 5 ns with only sidechain atoms restrained and 50 ns of unrestrained simulations. Restraint force used was 1000 kJ/mol. For production runs, the Nose-Hoover thermostat[262] and Parrinello-Rahman barostat[263] were used for temperature and pressure coupling respectively; velocity rescale[264] was used for temperature coupling in equilibration runs. A temperature of 310 K was maintained throughout the simulation. 2 fs was used as the time step. All bonds involving hydrogen atoms were constrained using the LINCS algorithm[265]. The production simulations were run in triplicate for 250 ns each for CB1-Apo simulations and ligand-CB1 complexes. Cut-offs of 12 Å were applied for short-range van der Waals and electrostatic interactions, while long-range electrostatic interactions were calculated using particle mesh Ewald[266]. Each replicate had a different initial velocity; a random generator was used to generate velocities.

3.3.4 Analysis

RMSF and RMSD calculations were performed using GROMACS tools. PCA was performed using pyPcazip[267] and GROMACS tools. Trajectories were visualised using VMD 1.9.2 software[268]. Gnuplot 4.6 was used for plotting all graphs[269].

3.4 Results

3.4.1 Docking and Preparation of the Complex

The inactive CB1 protein docked with agonist AM841 (21) and antagonist AM6538 (18) is shown in Figure 3.1. The orientation of the agonist partly coincides with the binding position of the cognate ligand (shown in green in Figure3.1(a)). The agonist ligand here binds near the proposed lipid access channel area between TM7 and TM1 (discussed in Section 1.3), at a position far removed from its binding site in the active crystal structure[103].

As shown by the 2D interaction plot generated using LigPlot[270] (Figure 3.1(c)), the A, B, and C rings (as designated in Section 1.2.3.1.1 for classical cannabinoids) form the aromatic head group. AM841 (21) shows predominantly hydrophobic interactions with residues in the N-terminus, TM1, and TM7. With the sulphur atom of Met384(7.40) (acceptor), the phenol in the A ring of the aromatic head group of the ligand (donor) forms a hydrogen bond.

This binding site is also different from that proposed by Picone *et al*.[271] AM841 (21) was predicted to bind vertically, with the aromatic headgroups occupying the region between TM2, TM3, and TM7 and the N=C=S moiety forming a thiocarbamate interaction with Cys386(7.42). It has, however, been postulated that classical and endocannabinoids enter CB1 and CB2 through the lipid membrane rather than passing through the aqueous layer[272]. AM841 (21), in particular, has been proposed to prefer the lipid route[121] in interacting with CB2. Furthermore, it has been suggested that classical cannabinoids preferentially adopt an orientation where the aliphatic tails are parallel to the phospholipid components of the membrane bilayer, while the tricyclic ring orients perpendicular to the membrane surface and the phenolic hydroxyl near the bilayer interface[273].

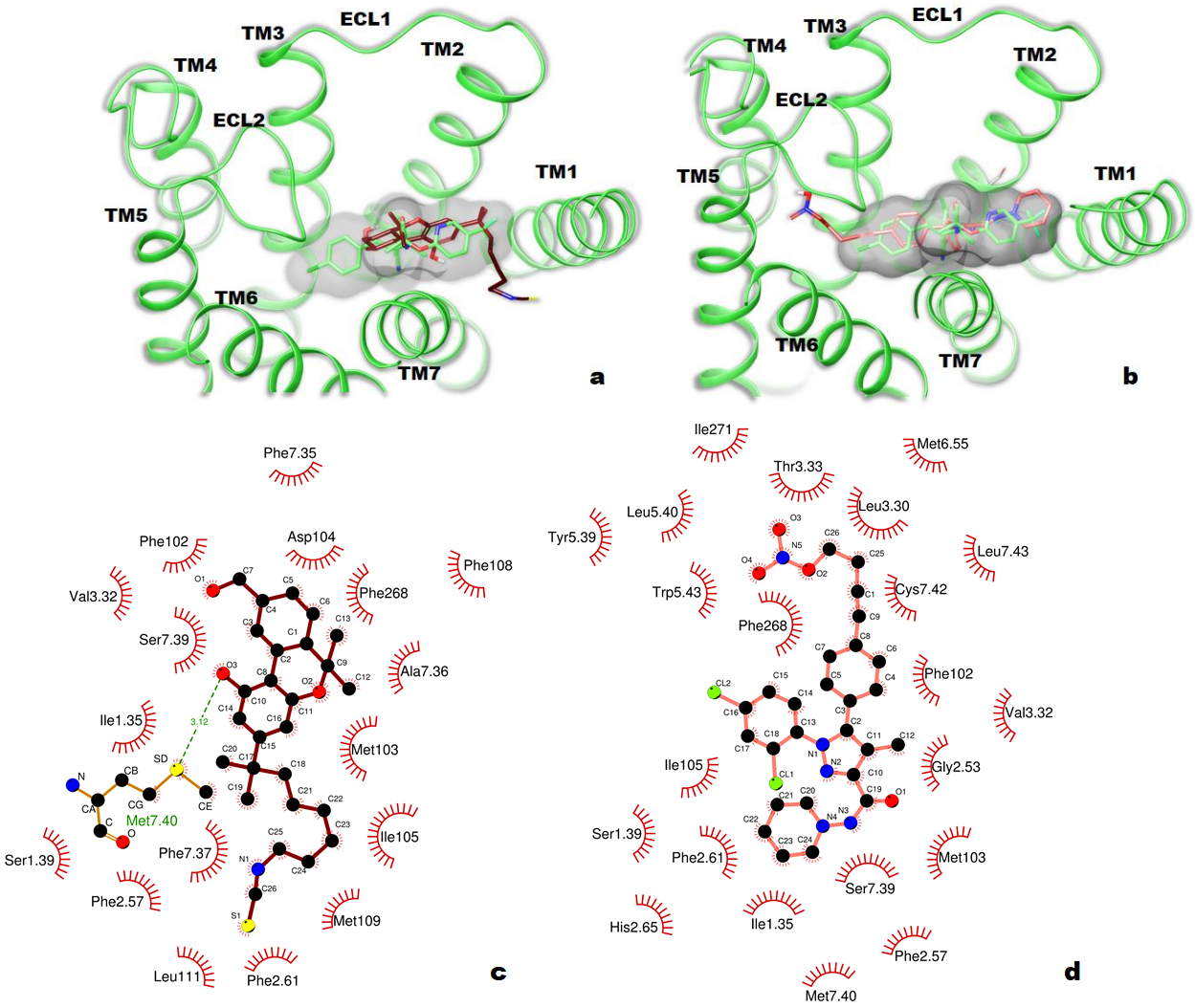

Figure 3.1 Ligands docked into inactive CB1 model (a) AM841 (21) (brown) and (b)AM6538 (18) (pink). *In (a) and (b) the grey surface shows the binding pocket of the cognate ligand. Cognate ligand MK0364 (19) is shown in green.* ***(c) 2D ligand interaction diagram of AM841 (21) with CB1. (d) 2D ligand interaction diagram of AM6538 (18) with CB1.*** *The ligand atoms are coloured as per ASL rules. Red curves represent hydrophobic residues. The green dotted line represents a hydrogen bond. In (a) and (b) only polar hydrogen are shown; in (c) and (d) no hydrogens are shown. 2D ligand diagrams generated using LigPlot*[270].

As the docked orientation of AM841 (21) in CB1 bears resemblance to the above description, the complex seen in Figures 3.1 (a) and (c) was taken forward for MD simulations to investigate the further course of the ligand.

The orientation of the antagonist coincides well with the binding position of the cognate ligand (shown in green in Figure 3.1 (b)). AM6538 (18) docks to the same binding site as in its crystal structure, 5TGZ (Figure 3.1 (b) and (d)). The dichlorophenol moiety of the ligand form an edge-face π-π interaction with Phe170(2.57) and an aromatic hydrogen bond with the backbone oxygen atom of Ser383(7.39) (acceptor) (not shown in the figure). The nitrate group also forms aromatic hydrogen bonds with Trp279(5.43) (donor) and Tyr275(5.39) (not shown in the figure). Post embedding into the membrane bilayer, the CB1-Apo system looks as shown in Figure 3.2.

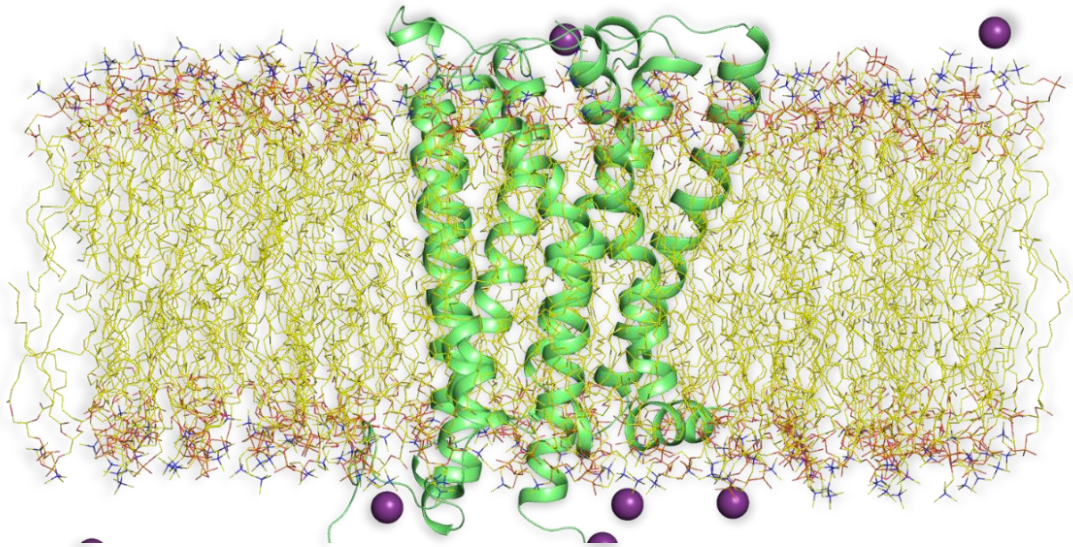

Figure 3.2 CB1-Apo protein (in green) post embedding into the system. *Water molecules are not displayed in the image. Chlorine atoms are shown as spheres (in purple) and phospholipid molecules are shown as sticks (yellow).*

3.4.1.1 Post Equilibration Structural Changes

Following the unrestrained NPT equilibration, the position and orientation of the ligands in CB1-AM841 and CB1-AM6538 systems changed by the order of 1 – 1.5 Å RMSD. Upon viewing the complexes, it was observed that the changes are not significant.

Similarly, the conformation of the rotamers certain residues – most notably the toggle switch residues Phe200(3.36) and Trp356(6.48) – was also observed to have changed from their crystal structure conformations in all three systems. The change, however, is rather insignificant and the shift in angle magnitude is too small to be quantified. This post equilibration state before productions runs is referred to as the initial conformation or initial state in the current chapter.

3.4.2 RMSF Analysis

Figures 3.3 and 3.4 show the RMSF calculation for backbone atoms in all three systems. The loop regions fluctuate more than the transmembrane regions (indicated by the curly braces in Figures 3.3 and 3.4). ICL3, in particular, fluctuates the most. Among all three systems, CB1-AM6538 exhibits the least fluctuation for ICL3. The C-terminus (including H8) shows the second-highest fluctuation, with CB1-Apo showing the most and CB1-AM6538 the least. Other loops show considerable stability in all systems.

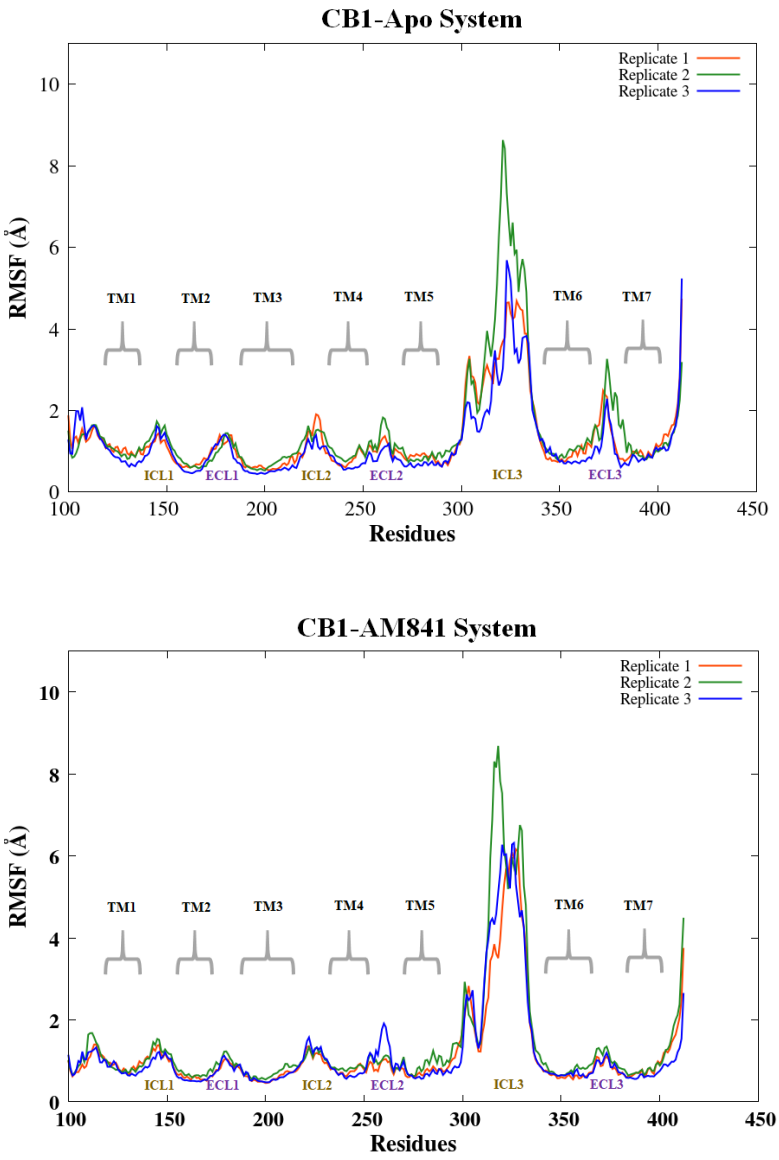

Figure 3.3 RMSF plots of CB1-Apo and CB1-AM841 systems. *Replicates 1, 2, and 3 of each system are represented by colours orange, green, and blue. Curly braces represent the TM regions. ECL and ICL regions are marked under the respective plot areas.*

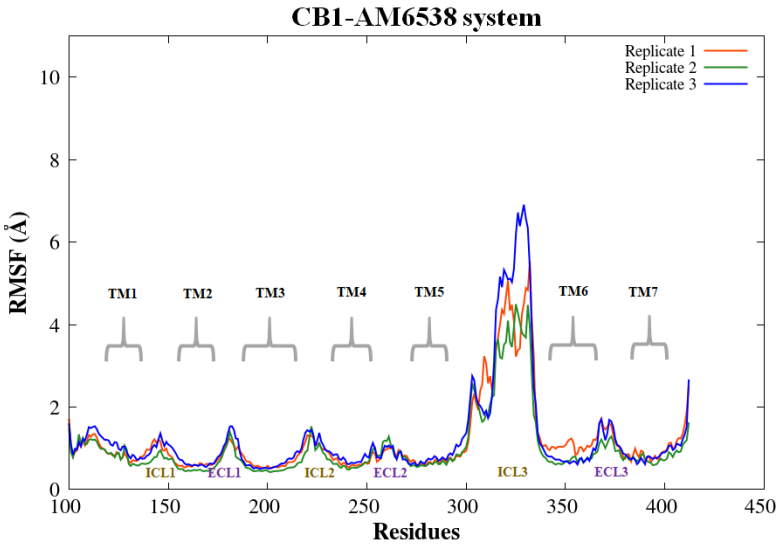

Figure 3.4 RMSF plot of the CB1-AM6538 system. *Replicates 1, 2, and 3 of each system are represented by colours orange, green, and blue. Curly braces represent the TM regions. ECL and ICL regions are marked under the respective plot areas.*

3.4.3 RMSD of Protein Structures

RMSD for the protein transmembrane backbone (TM-BB) atoms was calculated for all the systems against crystal structures 5U09 and 5XR8. As seen in the case of RMSF results (Section 3.4.2), loop regions show highly fluctuating movement, which would increase the RMSD value and mask the value of TM helix movement. Crystal structures, as mentioned earlier, have missing atoms in the sidechains. Hence, loops and side chains were eliminated from RMSD calculation and only TM-BB atoms were considered.

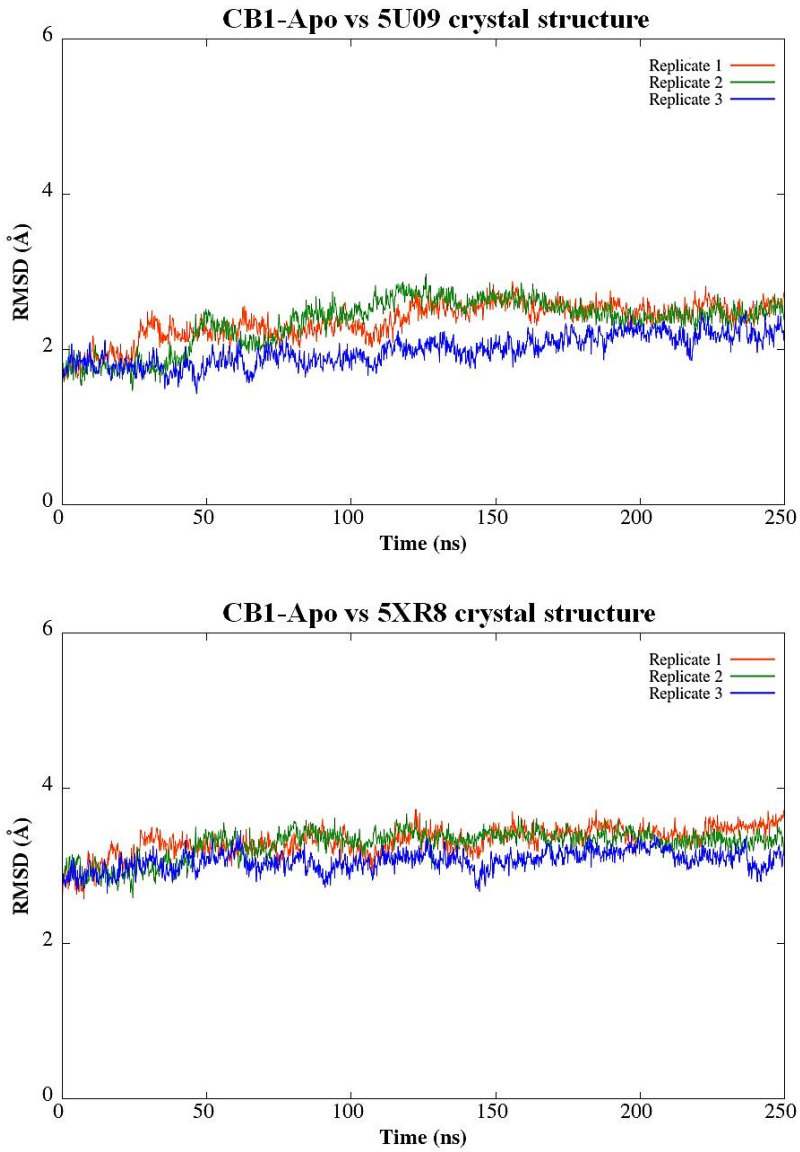

Figure 3.5 RMSD values of the CB1-Apo system against 5U09 and 5XR8 crystal structures. *Replicates 1, 2, and 3 are represented by colours orange, green, and blue.*

The RMSD for the replicates of the CB1-Apo system against the crystal structure 5U09 (Figure 3.5) is slightly lower than 2 Å at the start of the simulation. With time, the deviation increases in all three replicates. Replicates 1 and 2 show an increase in the value by approximately 1 Å at 25 ns and 50 ns respectively while replicate 3 shows a gradual

increase of about 0.4 Å. For the same system against active crystal structure i.e. PDB ID: 5XR8, a steady rise in RMSD is seen across all three replicates (Figure 3.5).

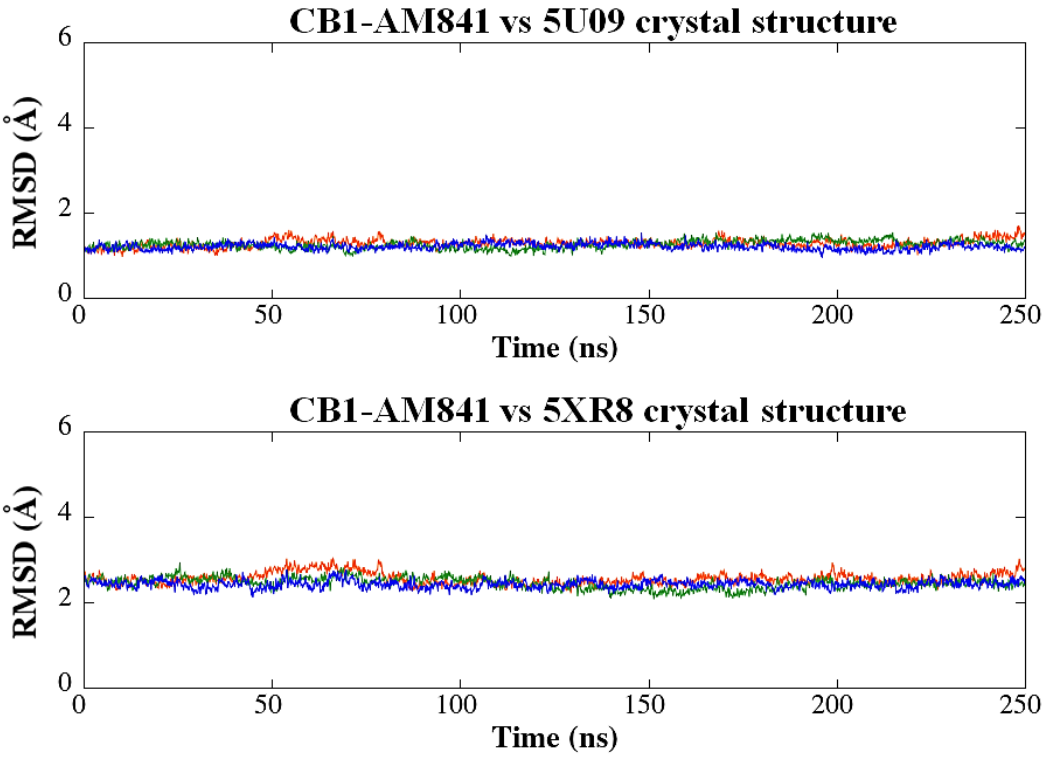

Figure 3.6 RMSD values of CB1-AM841 system against 5U09 and 5XR8 crystal structures. *Replicates 1, 2, and 3 are represented by colours orange, green, and blue.*

The RMSD for the replicates of the CB1-AM841 system calculated against 5U09 (Figure 3.6) remains stable through the entire trajectory within an order of 1-2 Å in all three replicates. Against 5XR8 (Figure 3.6), the system shows RMSD in the range of 2-3 Å. These values too remain stable in all three replicates.

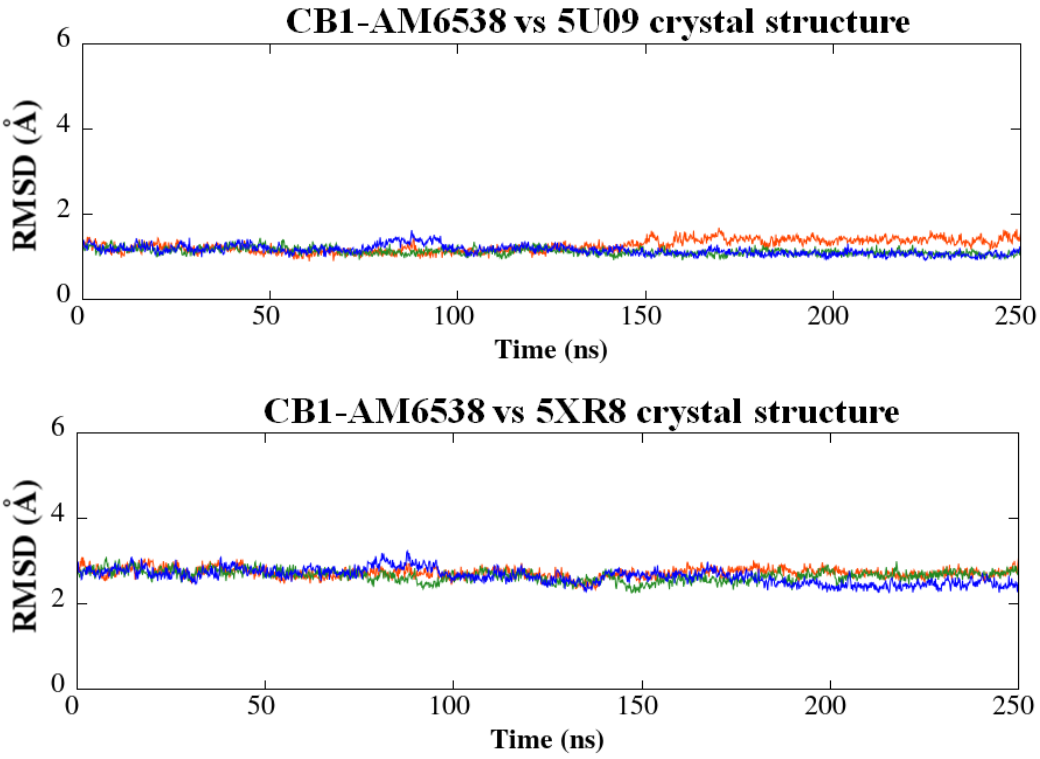

Figure 3.7 RMSD values of CB1-AM6538 system against 5U09 and 5XR8 crystal structures. *Replicates 1, 2, and 3 are represented by colours orange, green, and blue.*

Considering the CB1-AM6538 system, RMSD against both inactive and active crystal structures (Figure 3.7) remains within a narrow range (1-1.9 Å against 5U09; 2.5-3.0 Å against 5XR8), thus indicating a very stable protein-ligand complex.

3.4.4 Ligand RMSD

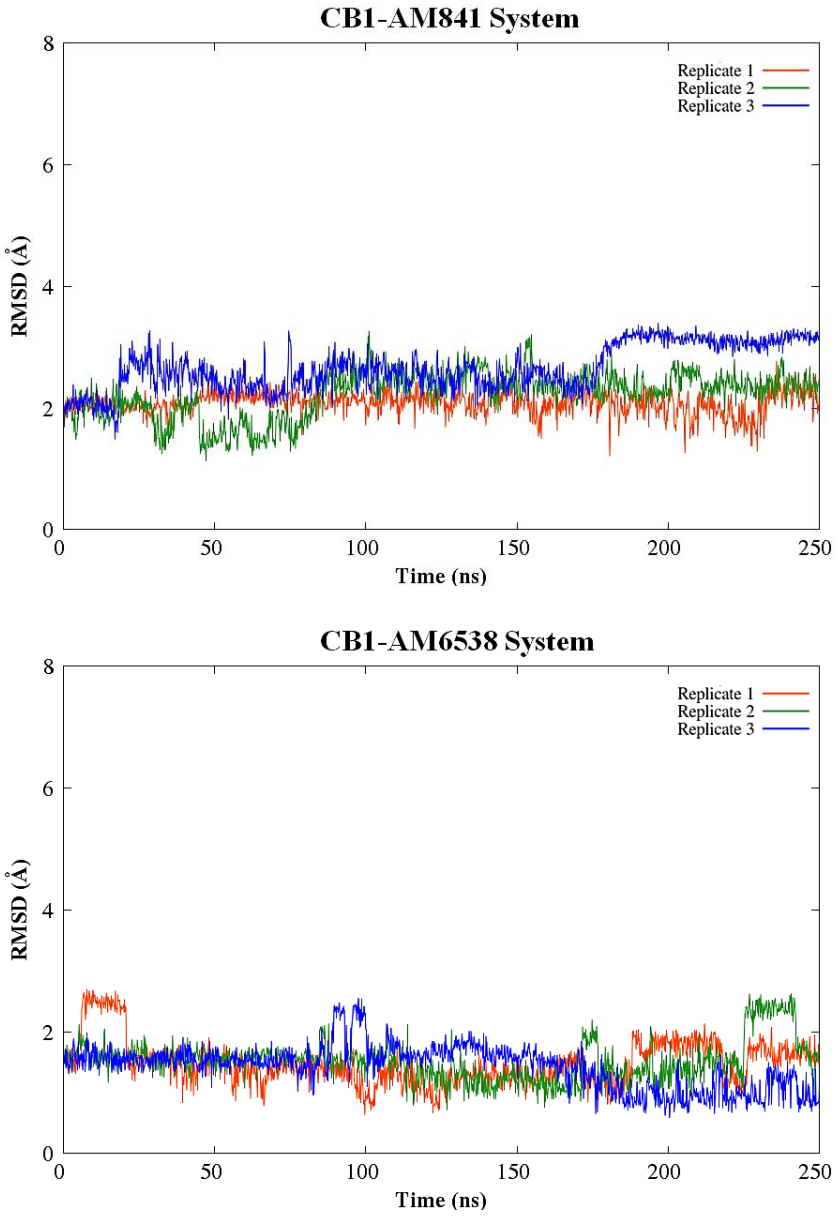

Figure 3.8 RMSD of ligand against its initial conformation in CB1-AM841 and CB1-AM6538 systems. *Replicates 1, 2, and 3 are represented by colours orange, green, and blue.*

The RMSD of the ligand molecules in the CB1-AM841 and CB1-AM6538 system was calculated with the initial state of the ligand as the reference structure (Figure 3.8).

RMSD of AM841 (21) in replicate 1 of CB1-AM841 system does not show much change throughout the run. However, in replicates 2 and 3 the RMSD value fluctuates between the range of 1.5-3.7 Å. At about 50 ns, the RMSD value drops in replicate 2, but then shows an increase from 60ns. The value stabilises at around 100ns and shows minor fluctuations beyond that. Figure 3.9 shows the various position of the ligand through the run. At 83 ns (ligand in green) when the RMSD steadily rises, the ligand is entering into the TM bundle. At 95 ns (ligand in blue), it goes in further into the binding pocket – however, at 100ns (ligand in yellow), it shifts from its position. At 154 ns (ligand in pink), it again goes back into the pocket. At 200ns (cyan) and 250 ns (orange), the ligand appears to have only slightly shifted from its position seen at 154 ns. In replicate 3, an increase in value is observed at about 20ns into the simulation (Figure 3.8). The RMSD fluctuates after that but stays well above 2 Å. Between 165-190 ns, a steady increase in RMSD is observed which then remains stable until the end of the run. Upon investigating the corresponding ligand positions (Figure 3.10), it was observed that at 20 ns, the aliphatic tail of AM841 (21) has entered fully into the orthosteric binding pocket and the aromatic head group is entering deep into the binding pocket (ligand in green). At 170 ns the tail moves closer to TM1 (ligand in yellow). At 180 ns the tail moves further into the binding pocket and the head group is pushed furthermore into the binding pocket (in pink). At 220 ns, a similar conformation is seen (in light pink), which sustains all through the trajectory. In both replicates, hydrogen bonds are being formed and broken with the binding pocket residues (predominantly serine residues) shown in Figure 3.1 (c) and Gly166(2.53).

The RMSD of the replicate 1 of CB1-AM6538 (Figure 3.8) system ranges within 0.5-2.3 Å, with random fluctuations. The most stable time interval lasts from 25-90 ns. The

ligand RMSD value for AM6538 (18) in replicate 2 is between 1.6 – 2 Å up until 110 ns, after which a slight decline in values is seen. However, post-175 ns the RMSD climbs up with heavy fluctuations. From about 140 ns, replicate 3 shows a steady decline in RMSD value which stops at about 190 ns beyond which only minor fluctuations are observed. On investigating the ligand position for replicate 3, no overall change was observed in the position of the ligand. Rather, slight changes in the position of cyclohexane and nitro alkyl groups were observed.

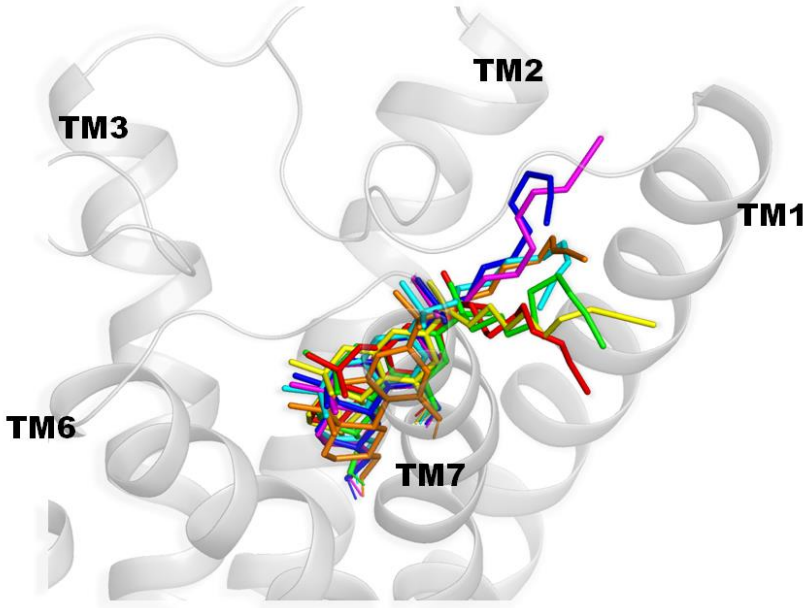

Figure 3.9 Positions of the ligand in CB1-AM841 in replicate 2. *The initial position is given in red. The positions at 83 ns, 95 ns, 100 ns, 154 ns, 200 ns and 250 ns are represented in colours green, blue, yellow, pink, cyan and orange respectively.*

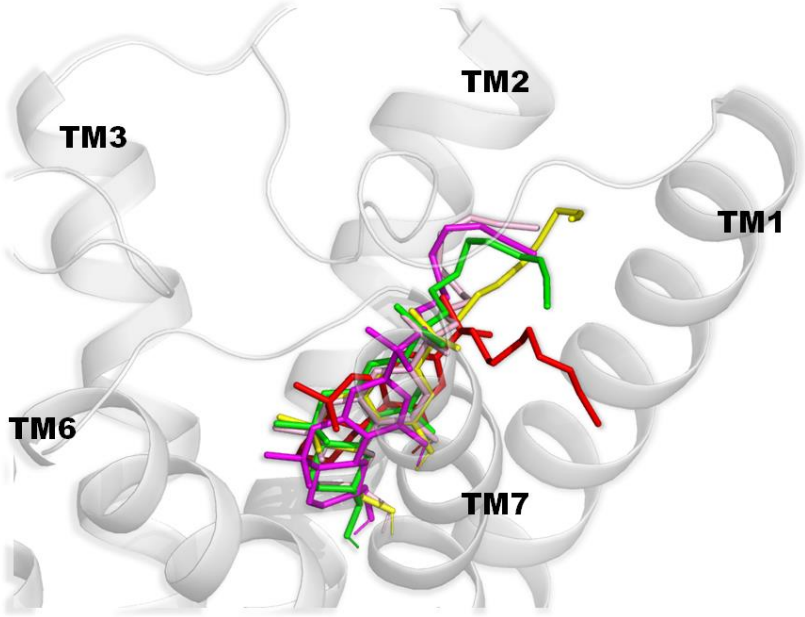

Figure 3.10 Positions of the ligand in CB1-AM841 in replicate 3. *The initial position is given in red. The positions at 20 ns, 170 ns, 180 ns, and 250 ns are represented in colours green, yellow, pink, and light pink respectively.*

3.4.5 Principal Component Analysis (PCA)

As mentioned in Section 1.5.3.1, PCA reduces the number of dimensions required to describe the dynamics of a protein. The trajectory that has undergone PCA describes these 'essential' motions in the essential subspace of the protein which show the most variation. In this section, PCA performed on TM-BB atoms of the protein molecule for every replicate in each system are reported. As the primary aim of the PCA in this study is to identify the TM helix motion, loop regions and side chains have been eliminated from the analysis. Furthermore, only principal components 1 and 2 were considered as they have the eigenvalues higher than the rest and hence represent the majority of intermolecular movement (scree plot not shown here; as mentioned in Section 1.5.3.1 the highest eigenvalues represent the essential motions)[274]. The projection of eigenvector 1 on

eigenvector 2 for all three replicates of a system plotted onto a common subspace is shown in Figure 3.11.

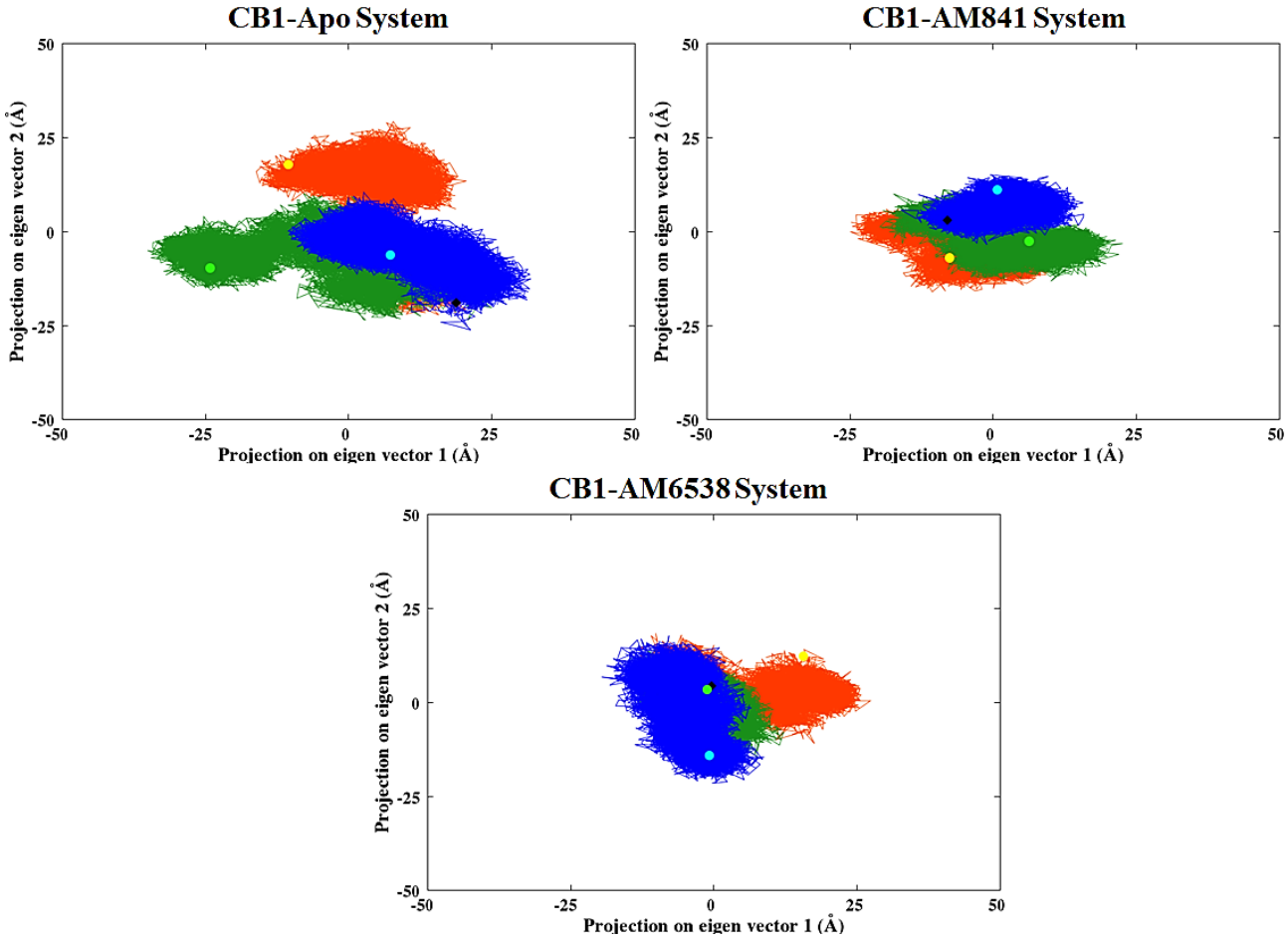

Figure 3.11 PCA plots of principal component 1 and 2 for transmembrane backbone atoms of CB1-Apo, CB1-AM841 and CB1-AM6538 systems. *The replicates 1, 2, and 3 are represented by colours orange, green, and blue respectively. Black diamond denotes the initial position of the protein. The yellow, green, and cyan dots represent the final position of the proteins in replicates 1, 2, and 3 respectively.*

In the 2D plots, each point represents a structure; the closer two points are to each other, the more similar are the structures represented by the points. Points far off from each other represent structures that are dissimilar to each other[275]. From the area spanned by

each replicate in the plots (Figure 3.11), it can be observed that the helices of the CB1-Apo system explore more conformations than those complexed with a ligand. Though an overlap is seen in the helical movement of CB1-Apo system trajectories, from the final position (indicated by the dots) it can be seen that the motions are quite distinct from one another. In contrast, in the CB1-AM6538 system (Figure 3.11) the final position of replicate 2 is much closer to the initial position. Replicate 3 overlaps with replicate 2 but has its final position far from the initial position unlike replicate 3. Replicate 1 occupies a different area of the subspace indicating its opposing motions to that seen in replicates 2 and 3. The replicates of CB1-AM841 system (Figure 3.11) overlap one another and span a much lesser area compared to CB1-Apo and CB1-AM6538 systems. But similar to CB1-AM6538 system, the final position indicated by the PC is closer to the initial position.

The PCA plots provide an insight into the extent of conformational sampling by the receptor in a replicate. In order to identify which part of TM-BB shows the most movement and the direction of that movement, porcupine plots for PC1 were generated using PyMol[276]. The plots for each system along PC1 are given in Figures 3.13 – 3.16. A guide for the terms used to describe the motions is given in Figure 3.12.

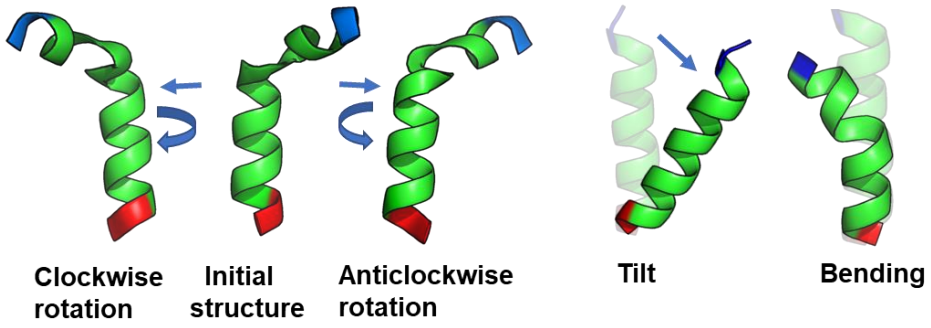

Figure 3.12 Motions observed in PC1 of CB1 simulation systems. *Anticlockwise and clockwise twists were defined as such when observing the protein from the extracellular side (top-down viewpoint).*

3.4.5.1 CB1-Apo System

For the CB1-Apo system, TM4 shows the least movement of all helices in all three replicates. Its movement mainly consists of the helix tilting sideways. The upper half (EC) (i.e. that half of the helix near the extracellular region) of TM1 moves laterally away from the binding pocket in all three replicates, albeit in different directions (Figure 3.13 and 3.14). The EC end of TM3 in replicate 1, bends towards TM5. In replicates 2 and 3, it bends slightly away from the binding pocket and towards the direction of TM4. The lower portion (IC) (i.e. the half of the helix near the intracellular region) remains fairly stable, with a mild rotatory movement in clockwise and anticlockwise directions respectively. The motions seen in TM2 and TM5 are described in Appendix 3.

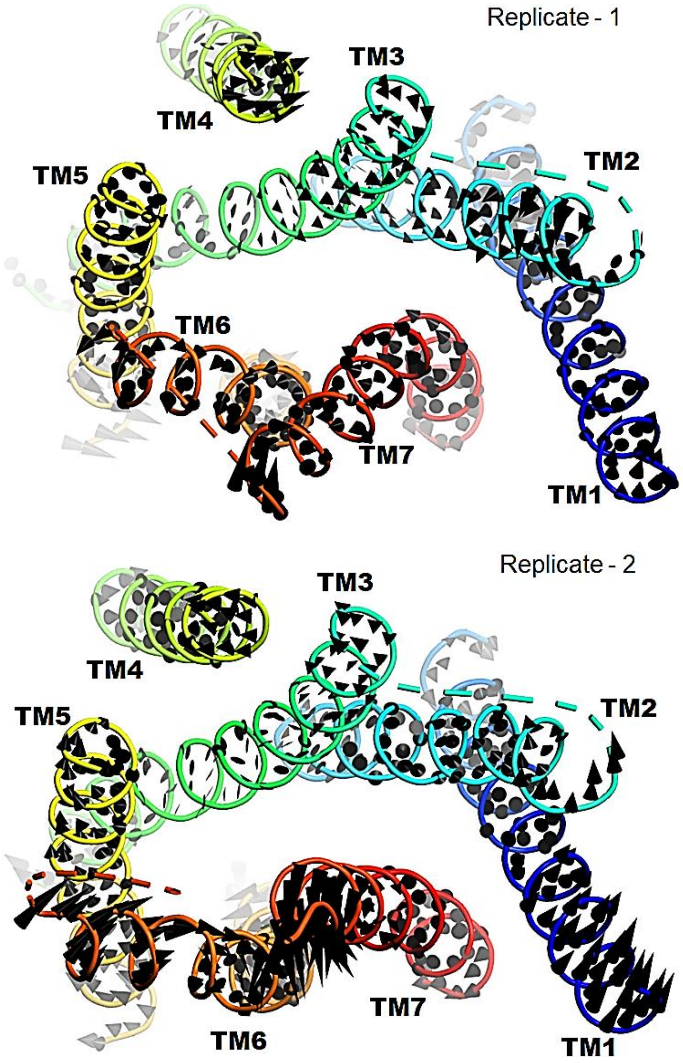

Figure 3.13 Porcupine plot for PC1 of CB1-Apo system; Replicates 1 and 2. *The transmembrane regions are coloured in the direction of blue to red from TM1 to TM7. Black arrows denote the direction of movement.*

In TM6, the proline kink separates the EC and IC halves of the helix. IC half in replicate 1 moves into the binding pocket, while the EC end rotates upward in an anticlockwise direction. In replicate 2, EC end bends down towards TM7 while IC end bends away from TM7 and in the direction of TM5. The IC half in replicate 3 also moves away from TM7, but the EC end rotates down in a clockwise fashion. TM7 shows the most

flexibility of all the helices. In replicate 1, the IC half bends into the binding pocket while the EC end bends up straightening the proline kink. Conversely, in replicate 2 the EC end bends downwards in a direction away from the binding pocket and the IC half shows a downward clockwise rotation. In replicate 3, downward clockwise rotation of the helix rotation is seen with the N-terminus of the helix (near ICL3) bending towards TM6.

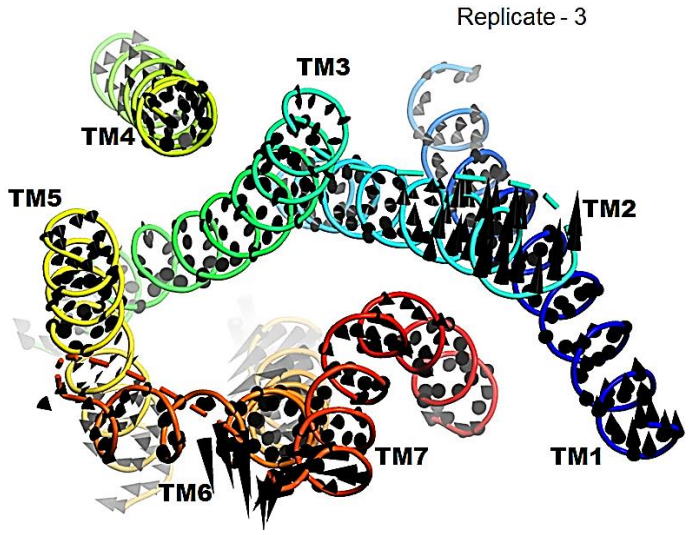

Figure 3.14 Porcupine plot for PC1 of CB1-Apo system – Replicate 3. *The transmembrane regions are coloured in the direction of blue to red from TM1 to TM7. Black arrows denote the direction of movement.*

3.4.5.2 CB1-AM841 System

Figure 3.15 shows the movement of helices for CB1-AM841 system along PC1 for all replicates. TM1 in replicate 1 shows a lateral tilting of its EC and IC halves in opposing directions. In replicates 2 and 3 the IC half bends towards TM2. The EC end, however, shows rotatory motion in anticlockwise and clockwise directions respectively. The IC of TM3 shows more movement than the EC end. In replicate 1, it bends away from TM5

while in replicates 2 and 3 it bends towards TM5 and the binding pocket. In replicate 3, the EC end shows considerable movement by bending away from the binding pocket.

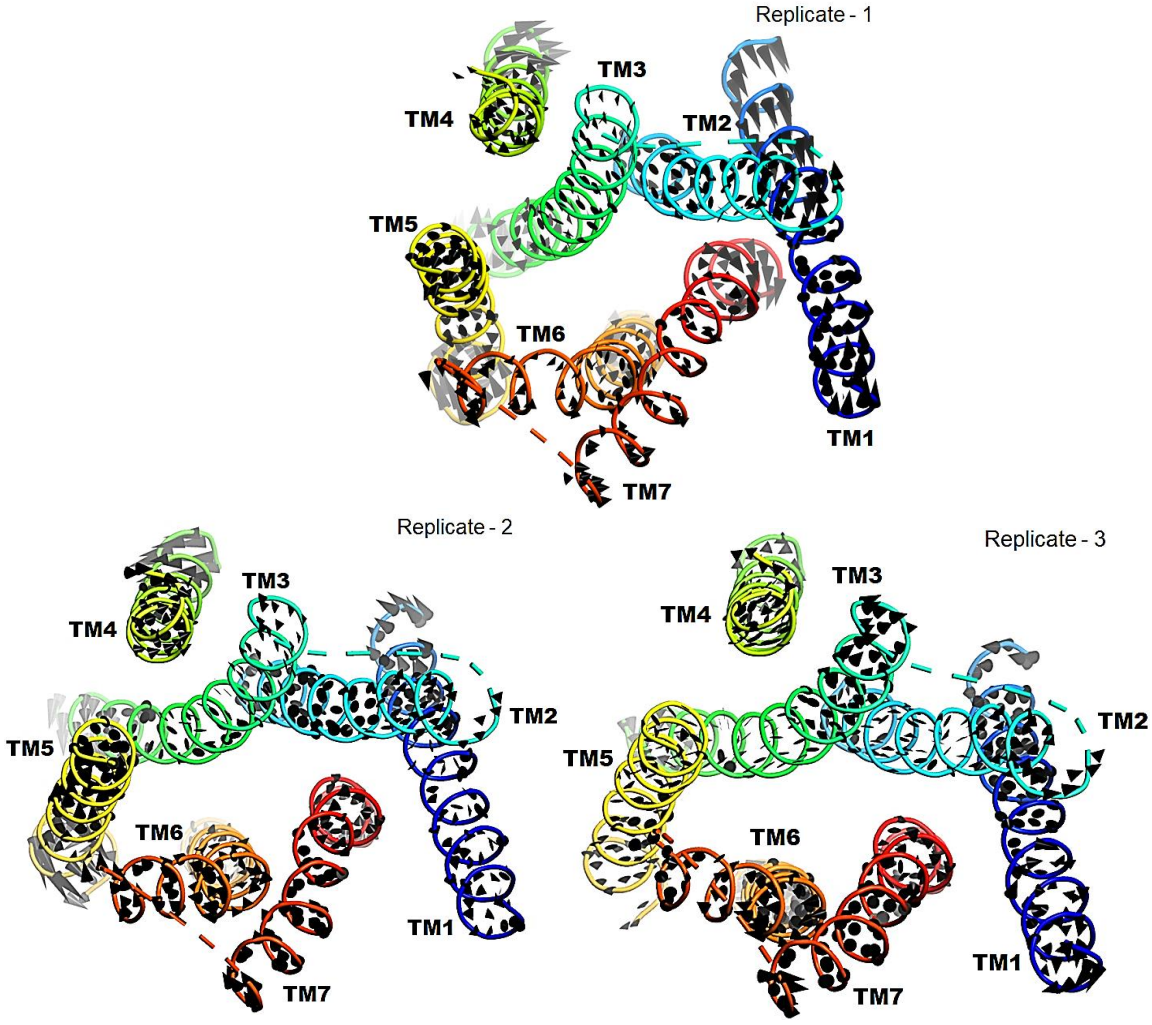

Figure 3.15 Porcupine plot for PC1 of CB1-AM841 system replicates. *The transmembrane regions are coloured in the direction of blue to red from TM1 to TM7. Black arrows denote the direction of movement.*

TM6 in replicate 1 shows the EC end bending away from TM5 while the IC rotates downward in an anticlockwise manner. In replicate 2, EC end bends towards TM5, and IC shows rotation in the clockwise direction. In replicate 3, however, EC end tries to

straighten the kink while IC bends towards TM7. EC end of TM7 bends towards TM1 in replicate 1, while IC bends out the binding pocket. In replicates 2 and 3, the IC end moves into the binding pocket while EC end shows varied motions such as bending towards TM6 and rotating downwards in the clockwise direction. The motions seen in TM2, TM4 and TM5 are described in Appendix 3.

3.4.5.3 CB1-AM6538 System

Figure 3.16 shows the movement of helices for CB1-AM6538 system along PC1 for all replicates. IC of TM3 bends towards TM5 in replicate 1 while EC end bends out of binding pocket. In replicate 2, the inverse is observed with the IC bending away from the pocket. In replicate 3, the helix tilts away from the binding pocket.

In the case of TM6, the EC end shows a bend towards TM5 (replicate 1) or straightening of the helix bending away from TM5 (replicates 2 and 3). IC tilts down in the direction of TM7 in replicate 1, tilts toward TM5 in replicate 2, and move in a direction opposite to the binding pocket in replicate 3. The EC region of TM7 bends towards TM6 in replicate 1, while bending away from it in replicates 2 and 3. The IC portion does not show much motion in replicate 1 but rotates upward and downwards in replicates 2 and 3. The motions seen in TM1, TM2, TM4 and TM5 are described in Appendix 3.

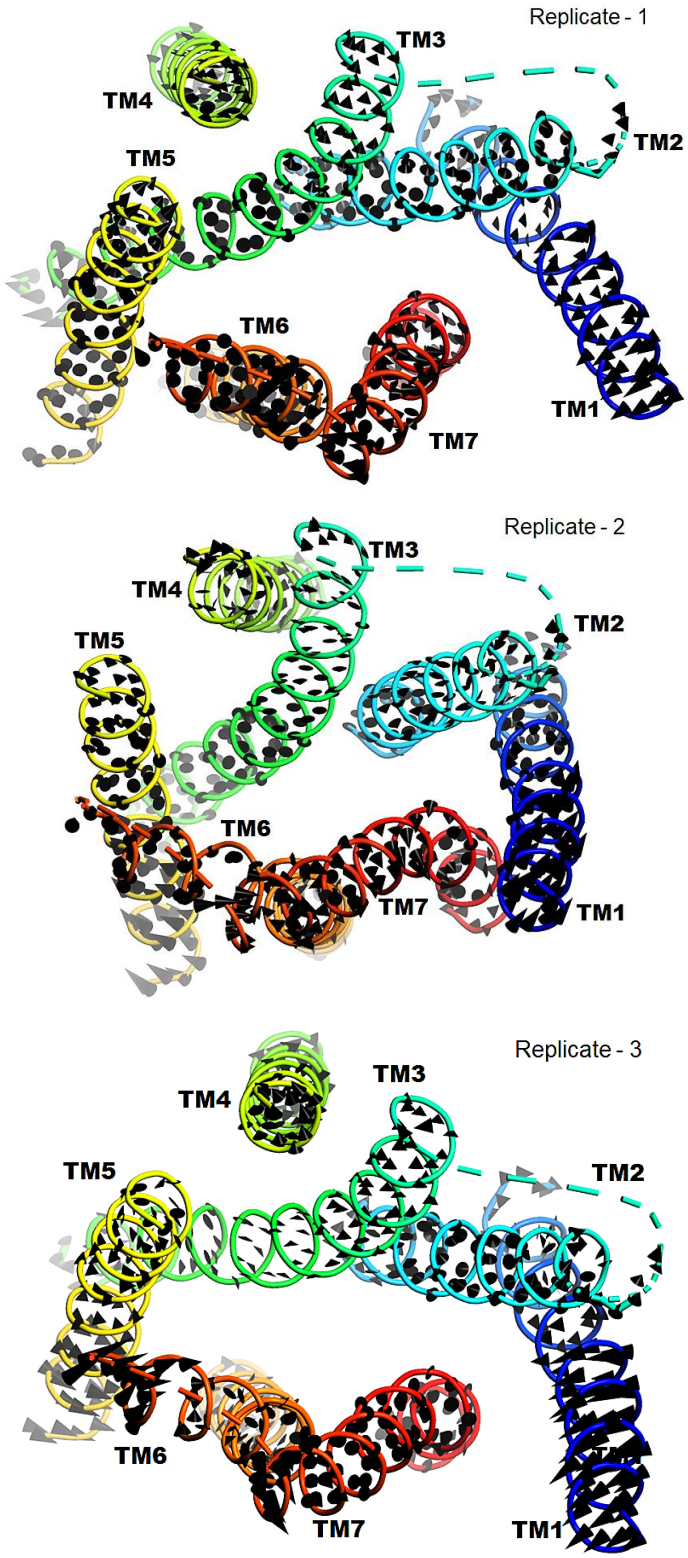

Figure 3.16 Porcupine plot for PC1 of CB1-AM6538 system. *The transmembrane regions are coloured in the direction of blue to red from TM1 to TM7. Black arrows denote the direction of movement.*

3.4.6 Conformation of Conserved Residues

3.4.6.1 Twin Toggle Switch

As seen in Sections 1.1.3 and 1.3, the rotameric change and a break in the interaction between Phe200(3.36) and Trp6.48(356) is essential in the transition from inactive to active structures of cannabinoid receptors. In 5U09 (the template crystal structure) both residues are in a face-face π-π stacking interaction with each other. To identify how different conditions (such as apo or ligand-bound) affect this interaction, the distance between Phe200(3.36) and Trp6.48(356) was monitored through each trajectory. As only the side chain rings are involved in the stacking, the distance between the centre of mass (COM) of the carbon atoms comprising the aromatic rings of both residues was considered.

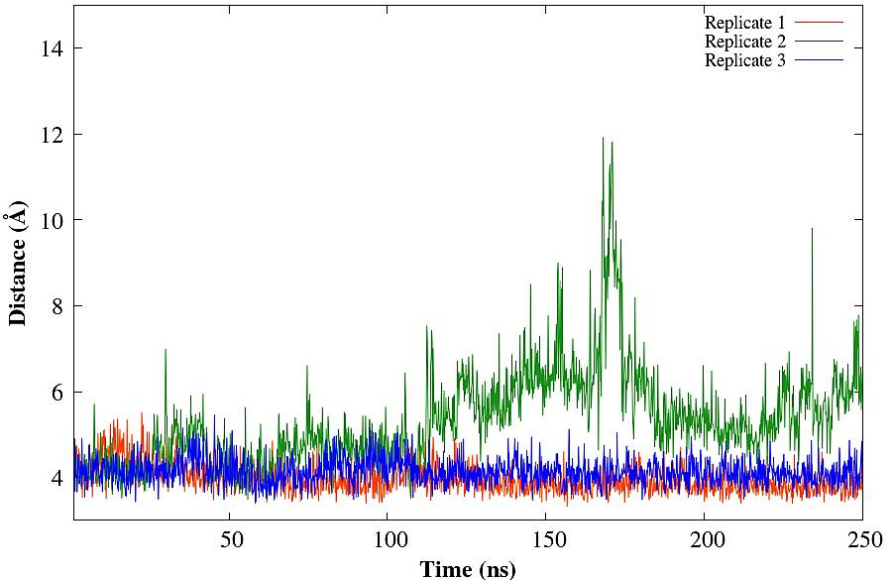

Figure 3.17 Distance between the COM of carbon atoms comprising the aromatic rings of Phe200(3.36) and Trp6.48(356) of the CB1-Apo system. *Replicates 1, 2, and 3 are represented by colours orange, green, and blue.*

In the CB1-Apo system (Figure 3.17), replicates 1 and 3 show almost no change in the distance. In replicate 2, however, an increase in the distance between the residues is observed until about 180 ns, beyond which it decreases and shows minor fluctuations. Upon viewing trajectories, it was confirmed that the largest difference in distance occurs at about 168 ns (Figure 3.18 shown in green) when Trp356(6.48) turns away from Phe200(3.36) and away from the binding pocket. Phe200(3.36), on the other hand, turns away from TM6 and looks into the binding pocket. The figure also shows the positions of the two residues (in blue) at 175 ns whereby Phe200(3.36) resets back to its position at 125 ns (in red). Trp6.48(356), though not back at its original position, is still nearer to Phe200(3.36) than its position at 168 ns.

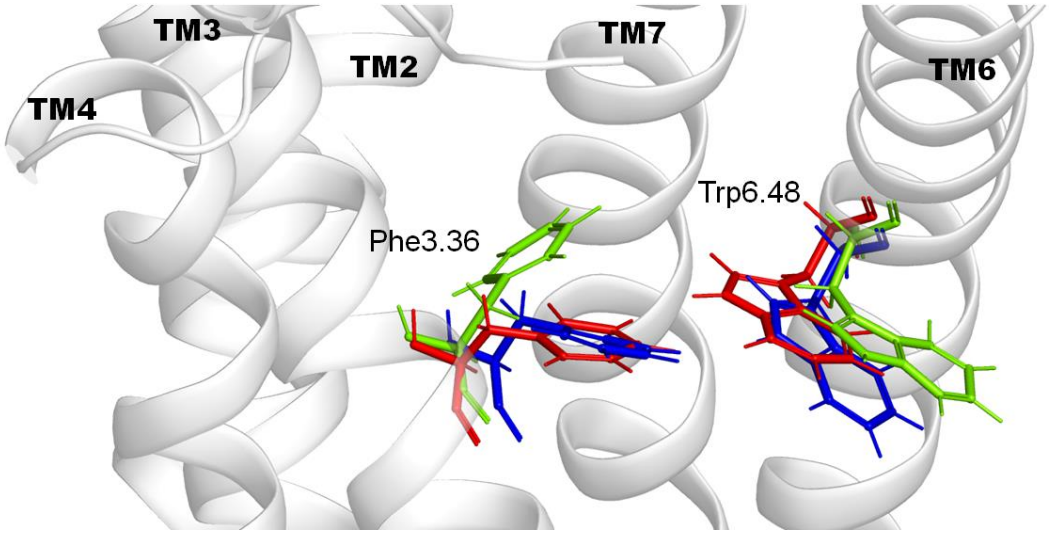

Figure 3.18 Conformations of Phe200(3.36) and Trp6.48(356) in replicate 2 of CB1-Apo system. *Red, green, and blue represent conformations at 125 ns, 168.20 ns and 175 ns respectively.*

In both CB1-ligand complex systems, the distance between the increased or decreased by only 0.5-1 Å (graphs not shown). Upon visualisation, it was observed that these changes did not cause any significant change in the interaction.

3.4.6.2 Arginine Cage Ionic Lock

As seen in Sections 1.1.3 and 1.3, the breakage in the ionic lock between Arg131(3.50)-Asp130(3.49) and Arg131(3.50)-Asp240(6.30) is a hallmark of GPCR activation. In this regard, the distance between side chains of residue pairs of Arg131(3.50)-Asp130(3.49) and Arg131(3.50)-Asp240(6.30) was monitored throughout the trajectory. Aspartic acid has a carboxylic side chain capable of switching the extra pair of electrons via resonance. Hence, instead of measuring the distance between basic nitrogen to acidic OH the distance between the immediately preceding carbon atoms of either residue in both pairs was calculated. In Arg131(3.50), this corresponds to the Cζ atom and in both aspartic acid residues, this corresponds to the Cγ atom.

In all three systems considered, the distance between the side chains of Arg214(3.50)-Asp338(6.30) (Figure 3.19) fluctuates within a range of 4 – 10 Å. Replicate 1 of the CB1-Apo systems exhibit the highest distance of sidechain separation between Arg214(3.50)-Asp338(6.30). In replicates 2 and 3 of CB1-Apo system, the fluctuation subsides at certain intervals where a minimum distance between the two side chains is reached. In contrast, both ligand complexed systems of CB1 show the same level of fluctuation across their replicates.

In the case of CB1-Apo and CB1-AM6538 systems, the distance between Arg214(3.50)-Asp213(3.49) remains fairly constant (Figure 3.20), with random spikes in values. CB1-AM841 system, however, shows almost the same level of fluctuation in the sidechain distance between Arg214(3.50)-Asp213(3.49) as that observed between Arg214(3.50)-Asp338(6.30). This implies that while distance fluctuations between Arg214(3.50)-Asp338(6.30) in CB1-Apo and CB1-AM6538 systems were influenced

predominantly by the helical movement, the same in CB1-AM841 system was additionally affected by the conformational changes in Arg214(3.50) as well. This was further confirmed upon visualising trajectories.

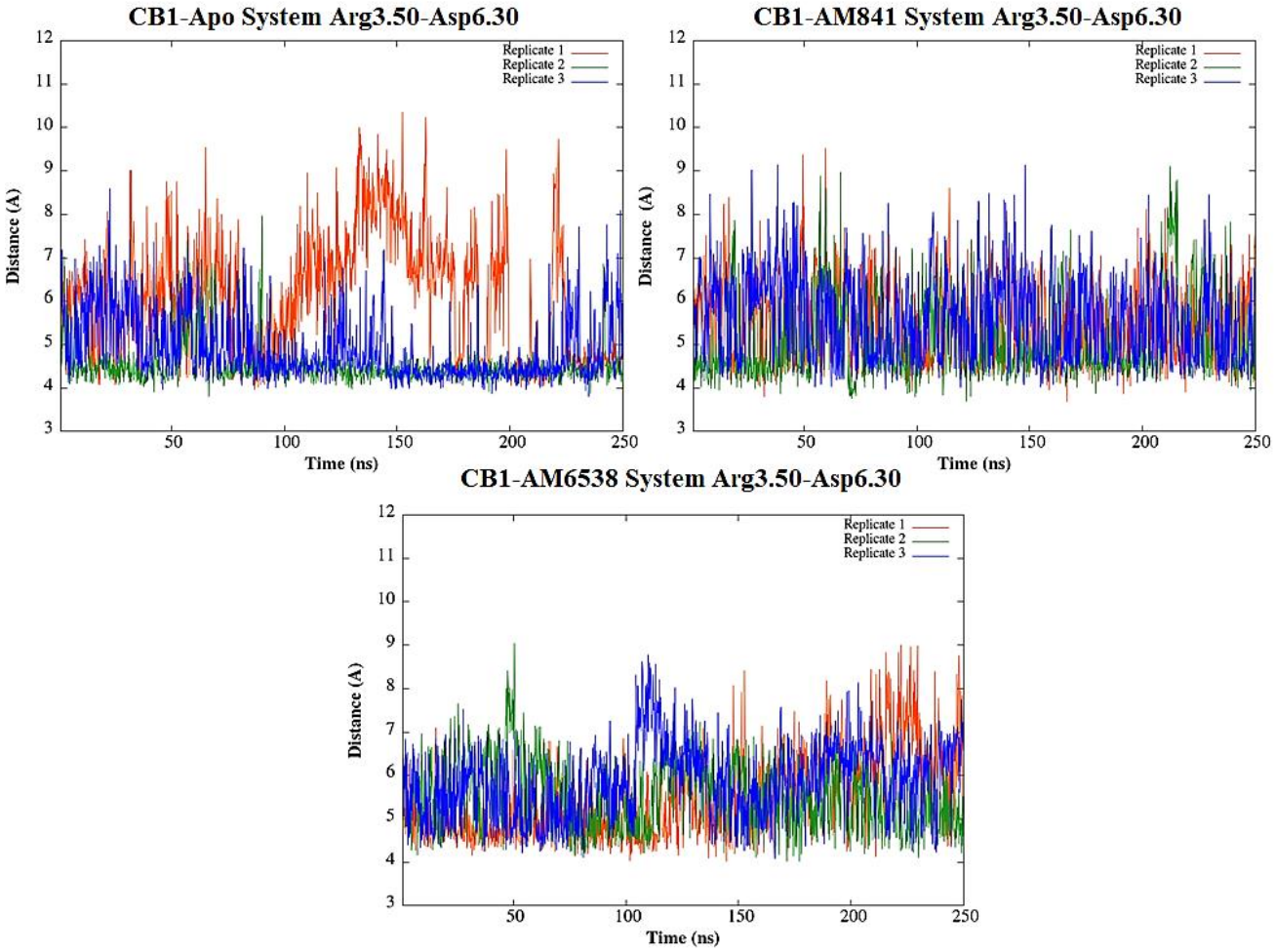

Figure 3.19 Distance between Cζ and Cγ atoms in the residue pairs of Arg214(3.50)-Asp338(6.30) in all three systems considered in the study. *Replicates 1, 2, and 3 are represented by colours orange, green, and blue.*

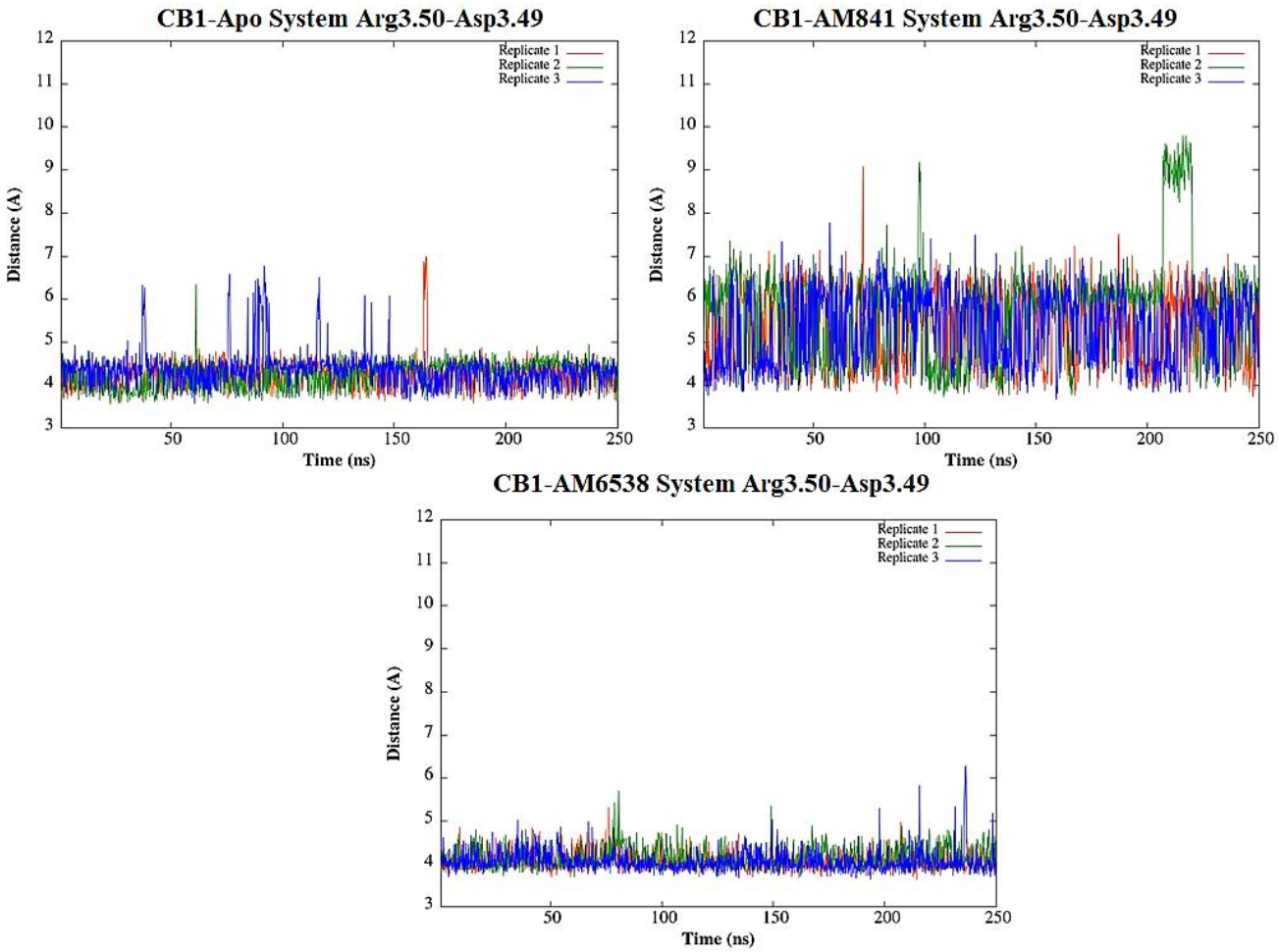

Figure 3.20 Distance between Cζ and Cγ atoms in the residue pairs of Arg214(3.50)-Asp(3.49) in all three systems considered in the study. *Replicates 1, 2, and 3 are represented by colours orange, green, and blue.*

3.4.7 Lipid Access Channel

It has been mentioned in Section 1.3 that LPA1, S1P1, and CB1 inactive crystal structures all possess an access channel between TM1 and TM7 that could function as an entry point for both lipids and ligands[104,277,278]. In that regard, the access channel between TM1 and TM7 was monitored for the receptor in the CB1-Apo system. As observed in the analysis of PC1 for CB1-Apo systems, TM1 shows movement in a direction lateral to the binding pocket. This movement disrupts the potential entry pathway in CB1-Apo

conformation. The channel in 5U09 is surrounded by the residues Ile119(1.35), Phe381(7.37), and Met384(7.40)[105]. In the CB1-Apo simulation, the position and the conformation of the residues change as per the movement of their respective TM helices and the pocket closes. The closing of the channel occurs between 35-40 ns in replicates 1 and 3, and between 70-75 ns in replicate 2. In Figure 3.21, the changes in the channel in replicate 3 between 35-40 ns is shown. In all replicates, the pathway between the orthosteric pocket and the opening constricts with time until it is reduced to a minimum. Within the next 5 ns, the pathway closes, and the opening is rendered as an outer surface pocket.

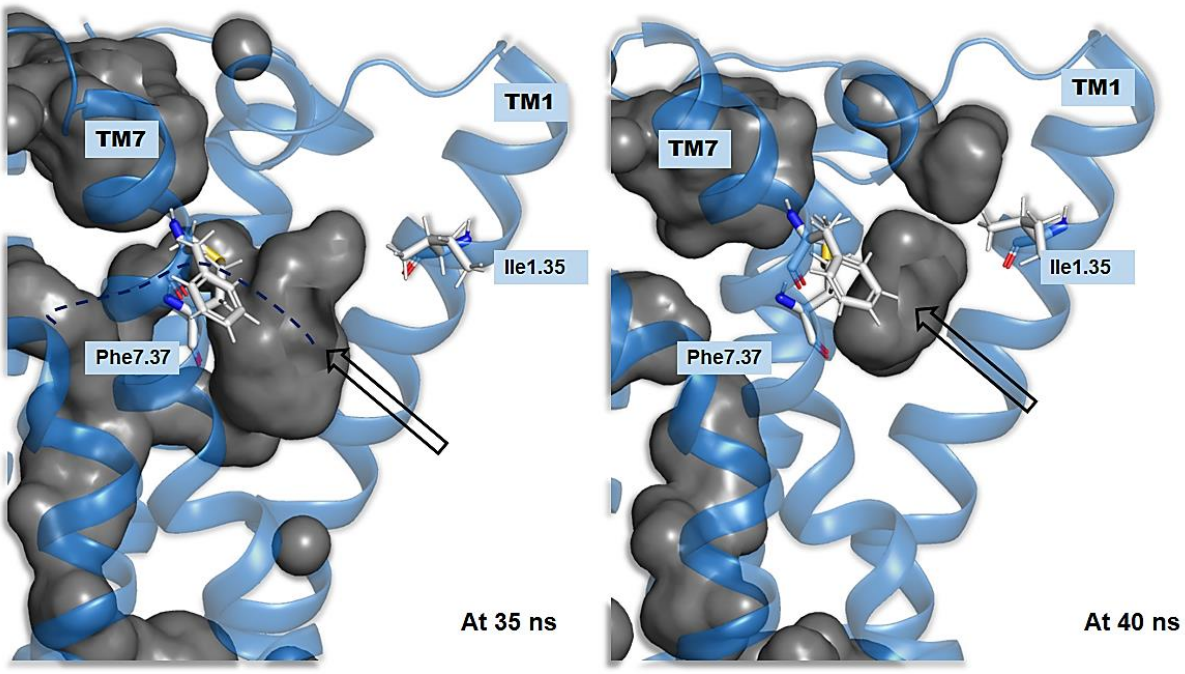

Figure 3.21 State of the lipid access channel found between TM1 and TM7 in replicate 3 of the CB1-Apo system at 35 ns and 40 ns. *Residues flanking the channel are represented as sticks (in white). Voids and pockets are represented as surfaces (in grey). The entrance of the channel is marked by the black arrow. Blue dashed lines indicate the connection between the orthosteric pocket and channel opening.*

3.5 Discussion

From the RMSF calculations, the most fluctuating regions of the receptor constructs were identified. As expected, the ICL3 loops showed the most fluctuation in all three systems as it is often the longest loop in class A GPCRs (barring the termini loops). From the subsequent RMSD calculations on the TM-BB atoms, a general direction of the transmembrane bundle conformation was identified. The CB1-Apo system showed an increase in values when RMSD was calculated against 5U09 (inactive crystal structure) and 5XR8 (active crystal structure), implying that the receptor is progressing towards a conformation unlike that seen in 5U09 or 5XR8. For CB1-AM841 and CB1-AM6538 systems, however, the RMSD values showed very small deviations, indicating stable protein backbones.

Analysis of PC1 showed that a majority of helix motions are shared across all systems. It must be noted here that the starting structure in all the systems was the same, hence, it can be asserted that the ligands (or lack of ligand) are responsible for precipitating any changes. The PCA of TM-BB of all replicates in each system in a common subspace revealed the variation in motions exhibited by the protein helices. From the visual analysis as well as porcupine plots generated of PC1, it was observed that TM4 shows the least motion in all three systems. In comparison to other TMs, TM4 also has very few residues participating in the binding pocket as observed from crystal structures as well as the docking studies conducted in the present work (Sections 2.4.2, 2.5, 2.6, and 3.4.1). TM4 is suggested to be involved in dimerization in certain class A GPCRs[279] and hence might be required to be structurally stable. The study of CB1 dimerization, however, goes beyond the scope of this study. From the porcupine plots, it can be seen that TM1 predominantly

shows a tilt towards TM7 or away from TM7. This may be critical in shaping the conformation of the helical bundle, as evidenced in inactive and active CB1 crystal structures (Section 1.3). Notwithstanding the general conformation, the movement of TM1 could also be important in instances of ligand entry via the access channel. Observing the access channel in CB1-Apo simulations, it was realised that the outward movement of TM1 reshapes the channel which completely disappears within 100 ns of the run. In the CB1-AM841 complex, PC1 of TM1 shows a tilt towards TM7 in replicates 2 and 3, thus allowing the ligand to further into the binding pocket.*

The most variation in movement, however, is shown by TM6 and TM7. From the analysis of PC1 of TM6 in the three systems, it can be concluded that TM6 predominantly exhibits bending, centred around the Pro kink. Indeed, it has been recently reported that TM6 of CB1 shows the largest helix bending among all agonist-bound GPCRs, irrespective of the presence or absence of G protein mimics[103]. The presence of Gly355(6.49) in the CWGP motif allows for such flexibility (Section 1.2.2) and less steric clashes. TM7, too, exhibits helical bending predominantly in the EC end where a synergistic motion with TM6 is observed in all replicates due to the linkage via ECL3. From the porcupine plots of PC1, it can be seen that the IC of TM7 is comparatively more flexible than that of other helices in CB1-Apo and CB1-AM841 systems. It has also been reported that in the agonist crystal structure the TM7 hinge region exhibits a partial unwinding centred on the residue Tyr397(7.53) of the NPXXY motif[103]. In the CB1-AM6538 system, TM7 exhibits fewer variations in motion (Section 3.4.5.3), as compared to the apo and agonist bound systems. This apparent lack of flexibility is rather expected as AM6538 (18) is an antagonist.

In the crystal structures 5U09 and 5XR8, the distance between the carbons(Cζ and Cε) which are the closest to the atoms involved in the salt bridge between Arg 214(3.50) – Asp338(6.30) is 4.5 Å and 12.4 Å, respectively; similarly, that between Cε and Cζ of Asp213(3.49) - Arg 214(3.50) is 4.3 Å (5U09) and 7.3 Å (5XR8). In the three CB1 systems simulated herein, the distance between the same carbon atoms of Arg 214(3.50) – Asp338(6.30) and Asp213(3.49) - Arg 214(3.50) salt bridges range closer to the values mentioned above (4 – 10 Å, as seen in Section 3.4.6.2). It has already been mentioned in Section 3.4.6.2 that the separation between Arg 214(3.50) – Asp338(6.30) in CB1-Apo system is primarily influenced by the movement of helices as Arg214(3.50) is in close contact with Arg213(3.49). Observing Figure 3.11, it can also be seen that the ionic lock breaks and reforms at different intervals for different replicates. This 'arginine cage' region adopts a conformation that is unlike of active or inactive crystal structures and this can be attributed to the flexibility of the apo state. MD simulations of apo M2 receptor and apo β2AR have reported breakage and reformation of the ionic lock leading to three different types of Arg3.50-Asp6.30 interactions: closed, semi-open, and fully open[280,281]. The authors credit these variations to the ability of apo state receptor to sample different conformations. In a study involving apo CB1 simulations (starting from an inactive state), Diaz *et al.* too have suggested flexibility to be the causative factor in the separation of the ionic lock[235].

In CB1-AM841, both helical movements and conformational changes in Arg214(3.50) influence the separation between residues in the arginine cage region (Section 3.4.6.2). From the plots of CB1-AM841 system in Figures 3.19 and Figure 3.20, it can be seen that Arg214(3.50) is away from Asp213(3.49) as much as it is removed from

Asp338(6.30). In an active receptor, both salt bridge interactions involving Arg214(3.50) are broken and the arginine extends out into the G protein binding region. While a fully open state has not been achieved in the reported simulations (due to rigidity of the docked complex), the findings do imply that Arg214(3.50) has started its separation away from Asp213(3.49). Considering the CB1-AM6538 system, much like CB1-Apo, the distance between the side chains of Asp213(3.49) and Arg 214(3.50) is below 5 Å with few sporadic increases. Yet, unlike CB1-Apo, the fluctuation in distance is equal across all replicates. The distance between Arg214(3.50) and Asp338(6.30), however, is the same as that of the agonist (CB1-AM841) system. It must be noted that Asp338(6.50) is proximal to ICL3 – the most flexible loop in CB1; therefore, the IC terminal of TM6 may be affected by the loop's fluctuations. There exists a possibility of water network maintaining these interactions transforming the closed state to a semi-open one[280]. However, analysis of water networks is out of scope for the work reported herein.

Despite the high variations in motions of TM3 and TM6, the interaction between toggle switch residues is stable in all three systems (Section 3.4.6.1), except for replicate 2 of the CB1-Apo system where a temporary break in the interaction was observed. Diaz *et al.* in their simulation of apo CB1, observed such a breakage of the interaction leading to an intermediate conformation (without progressing to an active state conformation)[235]. Li *et al.* also observed three different conformations of Trp6.48 for active, inactive, and apo states of in their simulations of A2AR[282]. Indeed, the flexibility seen in the 'ionic lock' residues also applies to Trp6.48 in apo simulations. Simulations involving M2 and S1P1 receptors have revealed that Trp6.48 assumes a variety of conformations in the apo state in comparison to the ligand bound one[277,280]. Hence, from the analysis of conserved residues

in all three systems, it can be deciphered that CB1-Apo is progressing towards an intermediate conformation that resembles neither active nor inactive state completely.

This chapter also investigated if a head group first entry of a classic cannabinoid would be favourable to activate the receptor. A change in the ligand orientation was seen in replicates 1 and 2; however, the ligand did not progress towards the conformation seen in 5XR8. After 250 ns of simulation, no evidence regarding the transformation of the receptor into an active state was found. A head group-first entry into the receptor via access channel, hence, may take time to orient itself in the binding pocket and trigger activation. In 2016, a steered MD study to identify the potential pathways for entry of Δ^9-THC into CB1 was conducted on a CB1 model generated using the LPA1 receptor as template[278]. It was recognised that to pull Δ^9-THC (3) into the binding pocket, the path that required the least application of force was through the gap between TM7-TM1 or TM2 gateway, with the ligand entering aliphatic tail-first into the receptor. Upon carrying out triplicates of supervised MD on the fully entered ligand, it was observed that Δ^9-THC (3) did not venture any further into the binding pocket but rather remained in the region between TM7, TM1, and TM2. Activation of the receptor, however, was observed in one MD replicate[278]. In replicates 1 and 2 of the simulations reported herein, the agonist AM841 (21) remained in the binding pocket region between TM7, TM1 and TM2, resembling the position of Δ^9-THC (3) in the above-mentioned study. In a study by Picone *et al.*,[271] the N=C=S tail of AM841 was suggested to interact with Cys355(6.47) of CB1; their mutagenesis experiments also revealed Cys355(6.47) to be important in the binding of AM841. and subsequent activation of the receptor. The formation of a thiocarbamate was not observed in the crystal structure[103] but could be an important factor in the activation of the receptor

upon initial binding. This interaction between Cys335(6.47) and AM841 (21) was also not observed in the study reported here; with a headfirst entry, such an interaction might take a longer time than a tail-first entry. Given that biological functions occur in the timescale of milliseconds, it can be said that the length of simulations is not sufficient enough to observe the agonist entry into the receptor and subsequent activation. A longer simulation time, specifically for the CB1-Apo and CB1-Agonist complexes will help explore the further conformations that the receptor would assume.

3.6 Conclusion

In this chapter, the molecular dynamics simulations of inactive CB1 in three different modes namely CB1-Apo, CB1-agonist complex, and CB1-antagonist complex have been described, and the findings reported. Through RMSD analysis and PCA, it was found that the CB1-Apo structure was moving neither towards an active or an inactive conformation as seen in the crystal structures. It was also observed that in the CB1-Apo structure, the proposed ligand access channel gets closed due to changes in the TM helical bundle. The CB1-antagonist complex was observed to maintain the inactive state of the receptor, throughout the trajectory in the majority of replicates. The CB1-agonist complex exhibited conformational changes indicative of breaking away from an inactive state, with regards to the ionic lock. Scrutinizing the molecular motions to the level of inter-atomic distances between key residue-residue interactions of agonist complex revealed that the receptor had not yet completely transformed to an active state. This implies that the chosen initial position of headfirst entry of the ligand into the binding pocket may either delay activation or not be favourable for activation at all. It was hence concluded that longer simulation times would be required to confirm the speculations.

4 Molecular Dynamics Simulations of Cross Docked Cannabinoid Receptor 1 Activation States

4.1 Introduction

In chapter 3, the changes in the architecture of an inactive state CB1 receptor under different conditions were investigated and compared via unbiased MD simulations. The ability of a chosen ligand pose to trigger receptor activation was also studied. This chapter aims to understand and compare the transitions in an inactive state receptor when approaching an active state and vice versa. To study such transitions, unbiased simulations of an inactive state model and an active state model cross-docked with the cognate ligand of the opposing functional state crystal structure were run. In other words, CB1, based on PDB ID 5U09, was complexed with AM11542 (20) (cognate ligand of PDB ID 5XRA) whilst CB1*, based on 5XRA, was complexed with MK0364 (19) (cognate ligand of 5U09). This helps to observe if CB1 activation and inactivation process exhibit directly opposing structural motions in the receptor. Furthermore, it was noted in Chapter 3 that the length of the simulation to be a limitation (Section 3.6). In that regard, these cross-docked motions were conducted for a microsecond. The trajectories of the systems analysed herein were taken from the unbiased MD simulation studies described in the study reported by Loo *et al*[240]. Certain aspects of the analyses reported in this chapter have been published in the same study.

4.2 Aims

1. To analyse the conformational changes of the receptor in an unbiased molecular dynamics simulations of an inactive state CB1 docked to an agonist and an active state CB1 docked to an antagonist.
2. To identify the course of the receptor conformational changes using PCA, monitoring conserved motifs involved in CB1 activation, and monitoring the pocket volume.
3. To identify the positional changes of the docked agonist and antagonist after the simulation.

4.3 Methods

The cross-docking of ligands, MD simulations of the cross-docked complexes and subsequent RMSD analysis on protein and ligand structures were supplied by the lead investigator, Dr Jason Loo Siau Ee, as mentioned in Loo *et al.*[240]. Simulations were conducted using GROMACS 2018[283] using the Amber ff99SB-ILDN* force field, supplemented with Slipids parameters for lipids and the General Amber Force Field for ligand parameters[284–286]. Ligand topologies were generated using Acpype and partial charges were calculated using AM1-BCC method[287]. The complexes were embedded into a pre-equilibrated POPC membrane bilayer and were aligned as per the OPM database[259]. TIP3P[260] water was used to solvate the system and 0.15 M NaCl was added to neutralise the system. 100 ns equilibration was conducted using NPT ensemble. The temperature was maintained at 300 K using Berendsen thermostat[288] and pressure at 1 atm using semi-isotropic Parinello–Rahman barostat[263]. Position restraints were applied to the complexes with a force constant of 1000 kJ/(mol nm^2). Cut-offs of 10 Å were applied for short-range

van der Waals and electrostatic interactions, while long-range electrostatic interactions were calculated using particle mesh Ewald[266]. All bonds involving hydrogen atoms were constrained using the LINCS algorithm[265]. Unrestrained production simulations were then run at 300 K and 1 atm with the Nose Hoover thermostat[262] and Parinello–Rahman barostat for 1000 ns (1 μs). A time step of 2 fs was used.

Residue-residue distance measurements in conserved motifs (such as twin toggle switch and arginine cage ionic lock seen earlier in Sections 3.4.6) were performed using GROMACS 2018[283]. PCA analysis was performed using pyPcazip and PyMol. The volume of the binding pocket was calculated for every 25 ns of the trajectory using SiteMap[289]. Trajectories were visualized using VMD[268]. The conformation of the protein and ligand at the start of the production simulation (i.e. post-equilibrium structure) is referred to as initial state or initial conformation in this chapter.

4.4 Results

4.4.1 Changes in Ligand Position

The RMSD of the ligands against their conformations in their respective crystal structures (i.e. 5U09 for MK0364 (19) and 5XRA for AM11542 (20)) calculated by Loo *et al*. revealed that the ligand conformation is relatively stable throughout the simulation for both the ligands[240] with fluctuations in the range of 2 Å. However, comparing positions of ligand at the start of the simulation and after 1 μs shows certain significant changes in the orientation of ligands in both CB1-AM11542 and CB1*-MK0364 systems. AM11542 (20) adopts an orientation in the inactive model quite similar to that observed in 5XRA. The V-shape of AM11542 (20) is much more pronounced after 1 μs in comparison to its initial state (Figure 4.1), due to the aliphatic tail being almost perpendicular to the aromatic head

group (the A, B and C rings, as designated in Figure 1.8, Section 1.2.3.1.1, form the aromatic head group for AM11542 (20)). Loo *et al.* reported that the lowest RMSD between cross-docked AM11542 (20) and cognate AM11542 (20) of 5XRA was 1.44 Å, whereby the cross-docked ligand almost replicated the cognate ligand orientation[240]. The RMSDs of initial vs final position of AM11542 (20) in replicates 1, 2, and 3 are 2.56 Å, 3.18 Å, and 2.69 Å respectively.

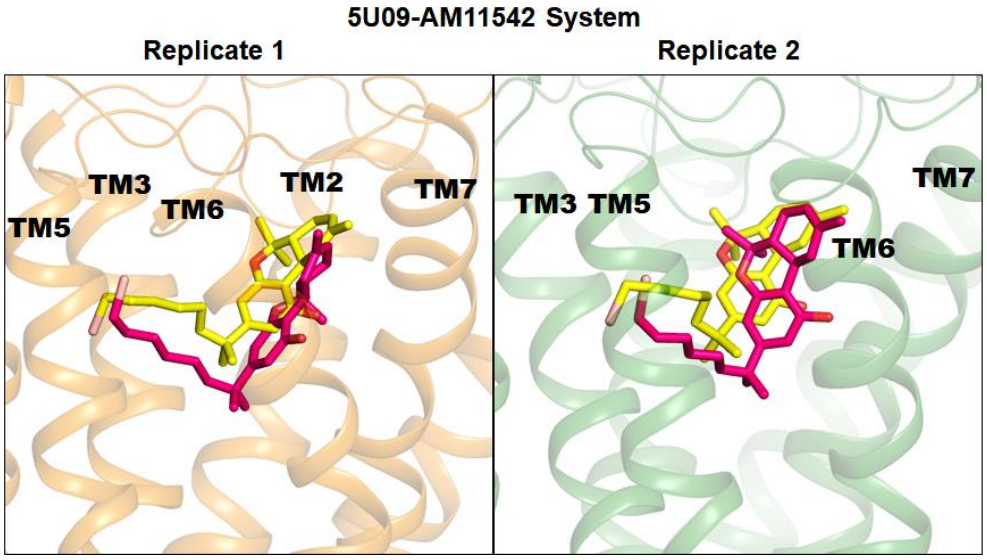

Figure 4.1 Changes in ligand position in replicates 1 and 2 of CB1-AM11542 system. *The initial position is shown in yellow and final position is shown in pink). The cartoon representation depicts the initial state of the receptor.*

Such replication of the cognate conformation by the cross-docked ligand, however, was not observed in the case of CB1*-MK0364 complex[240]. The lowest RMSD value achieved against crystallographic MK0364 (19) was 5.76 Å. Yet, comparing the pre- and post-MD orientations it can be seen that MK0364 (19) has gone from a folded to a slightly extended conformation, observed specifically in the trifluoromethylpyridine arm in replicate 3. In replicates 1 and 3, the ligand binds much deeper than the initial orientation.

Replicate 2 also shows a deeper binding but not to the extent observed in other replicates (Figure 4.2). The RMSDs of initial versus final position of MK0364 (19) in replicates 1, 2, and 3 are 3.22, 2.45, and 2.76 Å respectively.

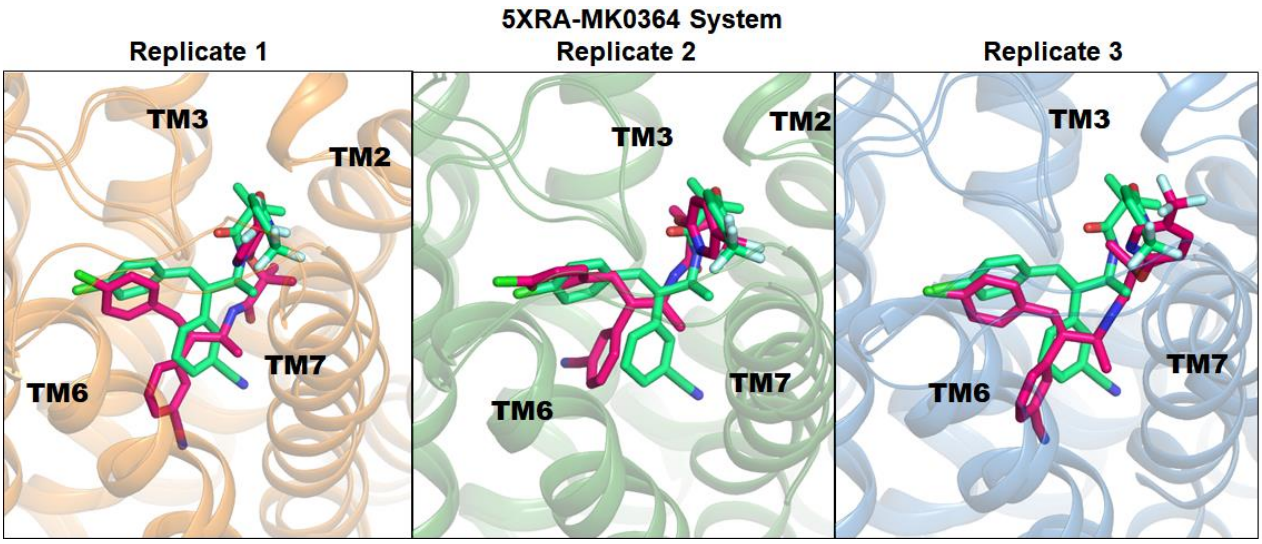

Figure 4.2 Changes in ligand position in replicates 1 and 2 of CB1*-MK0364 system. *The initial position is shown in green and final position is shown in pink.*

4.4.2 Principal Component Analysis (PCA)

As mentioned in Section 1.5.3.1, PCA reduces the number of dimensions required to describe the dynamics of a protein and helps identify essential motions in a trajectory. In this regard, PCA on TM-BB atoms of the proteins in both systems was performed in the same manner as mentioned in Section 3.4.5 for CB1 models. In CB1*-MK0364 system (Figure 4.3), from the projection of PC1 on PC2, it can be seen that the replicates diverge from their starting point and occupy different regions on the subspace. Replicate 2 shows more variance than replicates 1 and 3. CB1-AM11542 is rather similar to the 5XRA system in terms of the replicates. The replicates diverge in distinct directions from their starting point and occupy different regions on the subspace.

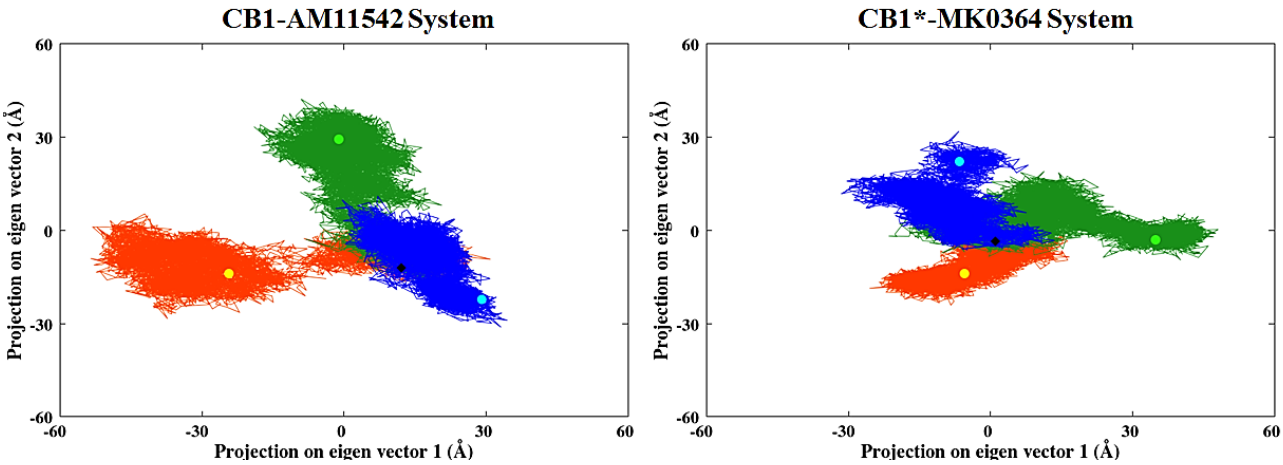

Figure 4.3 PCA plots of principal component 1 and 2 for transmembrane backbone atoms of CB1-AM11542 and CB1*-MK0364 systems. *The replicates 1, 2, and 3 are represented by colours orange, green, and blue respectively. The black dot denotes the initial position of the protein. The yellow, green, and cyan dots represent the final position of the proteins in replicates 1, 2, and 3 respectively.*

To identify which part of each helix shows the most movement and the direction of that movement, porcupine plots for PC1 of the TM-BB atoms of each replicate in each system were generated using PyMol[276]. The plots for each system along PC1 are given in Figures 4.4 and 4.5. A guide for the terms used to describe the motions has already been provided in Figure 3.8.

4.4.2.1 CB1-AM11542 system

The motions observed in TM3 can be best described by dividing the helix into two halves as seen in PCA analysis in Section 3.4.– the helix which is nearer to the extracellular surface (EC) and lower half (IC) which is nearer to the intracellular surface. Though exhibiting minimal displacement, the EC and IC ends of TM3 show distinguishable motion in all three replicates. In replicate 1, the EC end bends towards TM2 while the IC end bends towards the binding pocket. In replicate 2, EC end bends away from the binding pocket

while the IC end bends towards TM6. Finally, in replicate 3, EC end bends away towards TM4 and away from TM2; the IC end bends away from TM5 and towards TM2.

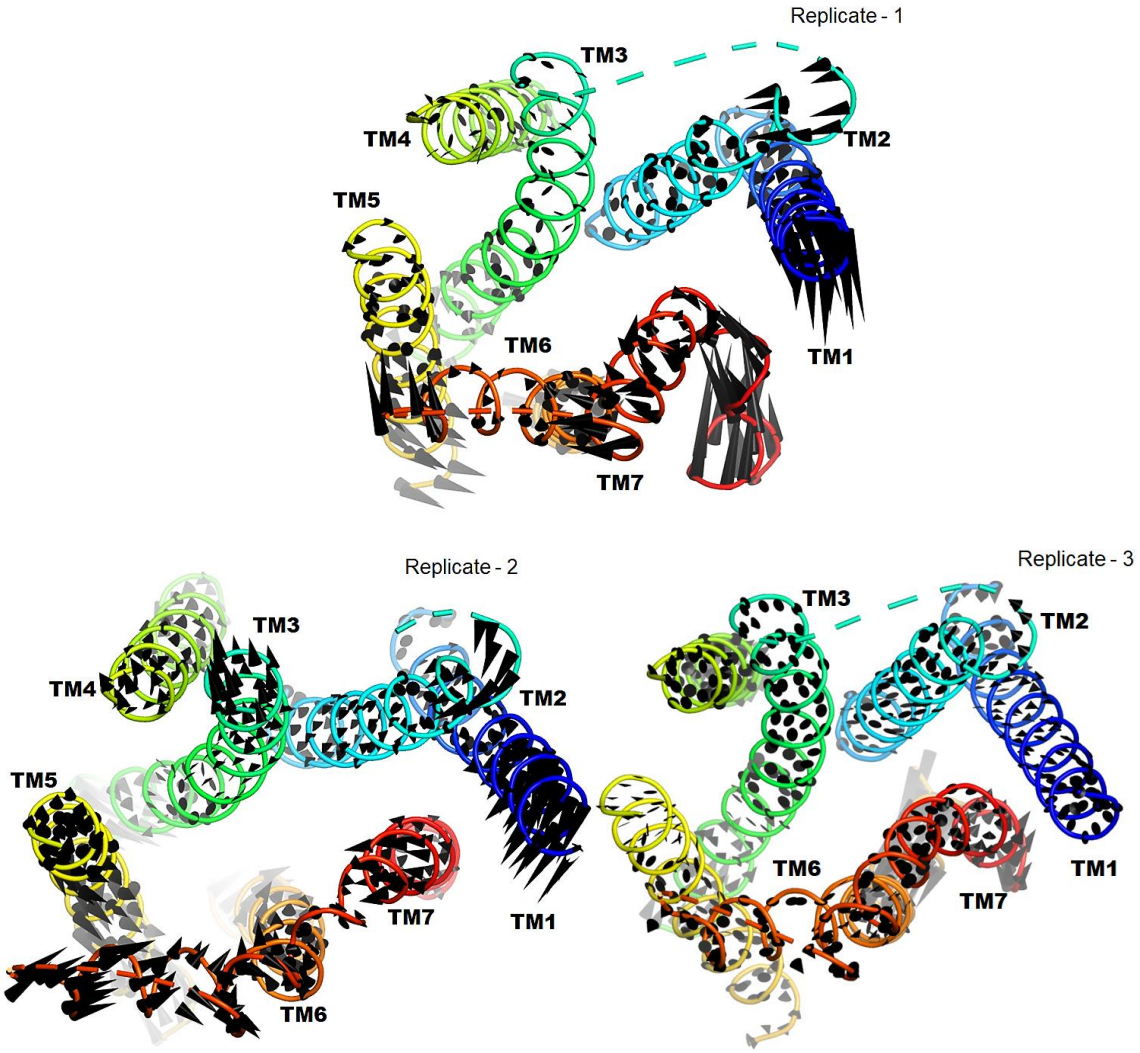

Figure 4.4 Porcupine plots for PC1 of CB1-AM11542 system. *The transmembrane regions are coloured in the direction of blue to red from TM1 to TM7. Black arrows denote the direction of movement.*

The motions in TM5, similar to that in TM3, can be best described by dividing the helix into two halves. In replicate 1, the EC end tilts towards TM3, and the IC end bends away from the binding pocket. In replicate 2, the EC end bends in a direction out of the

binding pocket and the IC end moves towards the binding pocket. In replicate 3, minimal movement is seen with the EC end bending away from TM3 and the IC end bending towards TM3.

In TM6, the proline kink is used to distinguish the EC and IC halves of the helix. In replicate 1, the EC end elongates, and the IC end bends towards TM7. In replicate 2, both halves bend towards TM7 – straightening the proline kink. In replicate 3, both halves bend away from TM7 and the binding pocket.

Considering TM7, replicate 1 shows noticeable helix unwinding near the NPXXY motif, causing the C-terminus connected to H8 to move into the binding pocket. The rest of the helix moves upward causing helix elongation in the mid-portion. Motions in replicate 2 are threefold: N-terminus of the helix connected to ECL3 bends away from the binding pocket, the mid-portion of the helix moves closer to that of TM6 (and moves into the binding pocket as well), and the C-terminus bends away from TM6. TM7 of replicate 3 shows minimal motion compared to replicate 1 and 2. EC end bends away from the binding pocket in a downward direction, while the IC end bends towards TM1 (and the binding pocket).

The motions observed in TM1, TM2, and TM4 are given in Appendix 4.

4.4.2.2 CB1*-MK0364 system

TM1 shows different types of motions in all three replicates. In replicate 1, the middle portion of the helix bends towards the binding pocket, while that near to ICL1 shows bending in a direction lateral to the binding pocket. In replicate 2, TM1 again shows tilting movement (in its IC end) in a direction lateral to the binding pocket. In replicate 3

however, the EC end of TM1 bends away from the binding pocket, causing a slight expansion in the mid part of the helix.

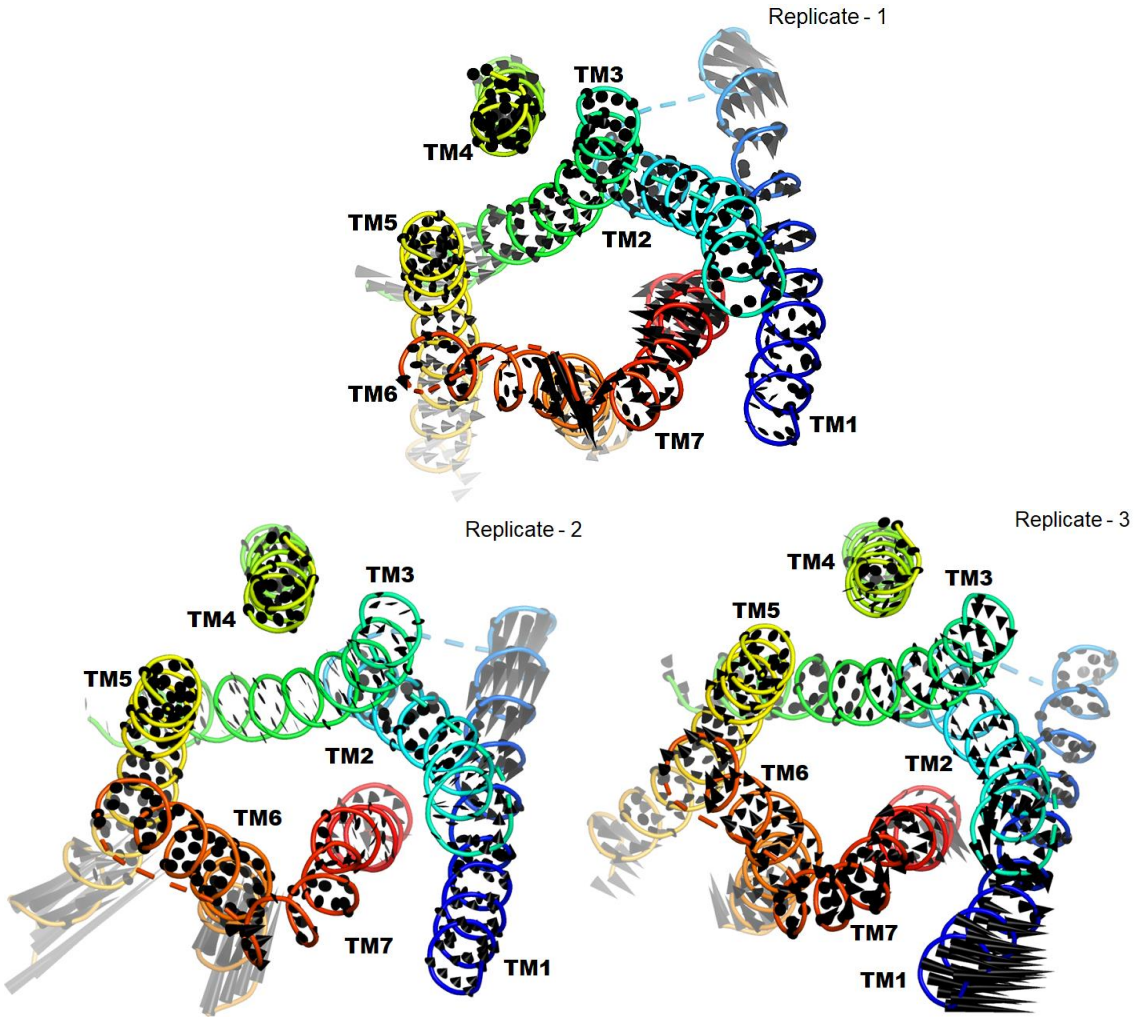

Figure 4.5 Porcupine plots for PC1 of CB1*-MK0364 system. *The transmembrane regions are coloured in the direction of blue to red from TM1 to TM7.* ***Black*** *arrows denote the direction of movement.*

For TM5, the C-terminus connected to ICL3 in all three replicates shows movement towards the binding pocket. The rest of the helix shows an outward movement with varying magnitudes of displacement across the replicates.

In the case of TM6, very faint bending motions towards TM7 are observed in the EC end of replicates 1 and 2, while in replicate 3 a very notable tilt out of the binding pocket is observed. The IC end of replicate 1 bends outward to the binding pocket, whereas in replicates 2 and 3 it moves towards the binding pocket, as seen for TM5.

TM7, too, exhibits different types of motions in all three replicates. In replicate 1, the N-terminus of TM7 near ECL3 shows an outward bend away from the binding pocket while the rest of the helix bends into the binding pocket. TM7 in replicate 2, however, shows very faint motions with the bending of the N-terminus away from TM6 being the only notable movement. In replicate 3, TM7 shows an upward movement causing the mid-portion of the helix to elongate. C-terminus near H8, however, shows bending in a direction away from the binding pocket.

The motions observed in TM2, TM3, and TM4 are given in Appendix 4.

4.4.3 Conformations of Conserved Residues

4.4.3.1 Twin Toggle Switch

Owing to the role of the aromatic toggle switch residues in CB1 activation (Section 1.1.3 and 1.3), the conformation of and the distance between the residues Phe200(3.36) and Trp356(6.48) was monitored throughout the trajectory for each system (Figure 4.6), similar to that seen in CB1 and CB2 simulations (Sections 3.4.6.1).

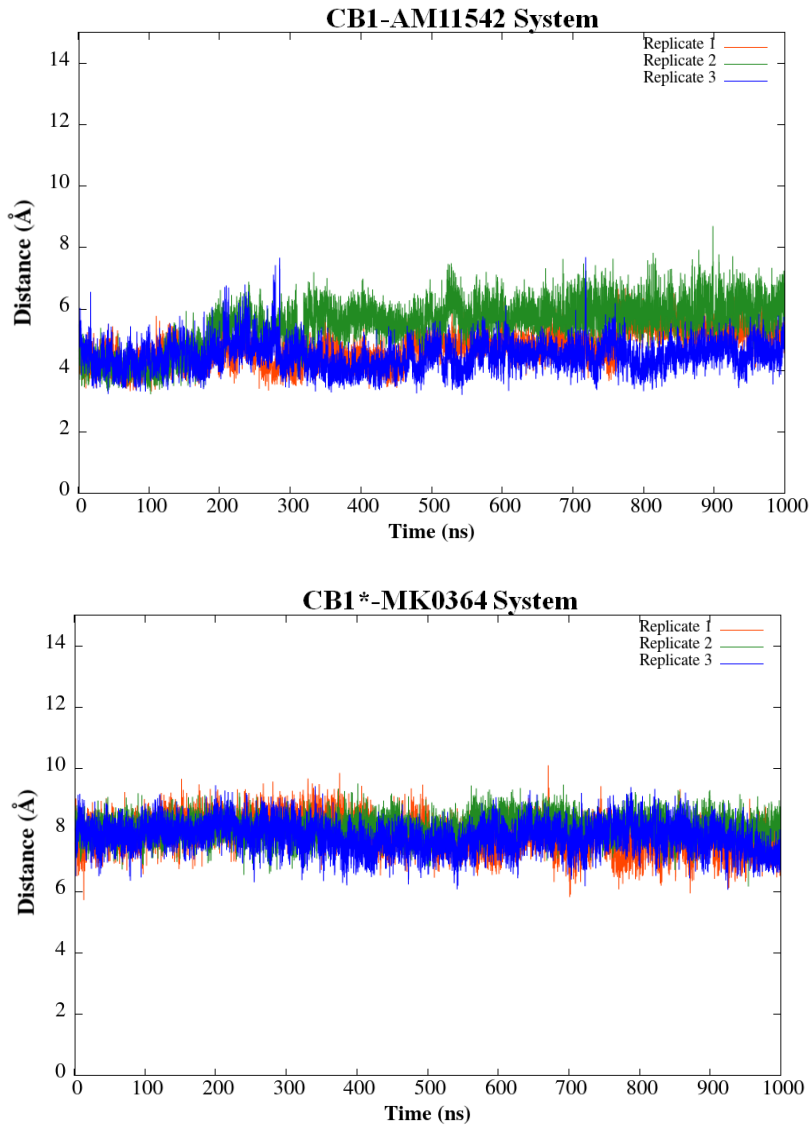

Figure 4.6 Distance between the COM of carbon atoms comprising the aromatic rings of Phe200(3.36) and Trp356(6.48) in CB1-AM11542 and CB1*-MK0364 systems. *Replicates 1,2, and 3 of each system are represented by colours orange, green, and blue respectively.*

In both CB1-AM11542 and CB1*-MK0364 systems, the distance between residues constituting the aromatic toggle switch – Phe200(3.36) and Trp356(6.48) – is almost constant throughout the entire trajectory in all replicates. Inspecting the trajectories, it was observed that in replicates 1 and 2 of the CB1-AM11542 system, the rings of both residues

are almost parallel to each other for a period of time. Between 775-800 ns and 175-200 ns of replicates 1 and 2 (Figure 4.7), the plane of the ring of Phe200(3.36) becomes perpendicular to that of Trp356(6.48). In replicate 3 of the same system, the ring planes of both residues are parallel to each other for most of the trajectory. However, on two separate time intervals, the rings of Phe200(3.36) and Trp356(6.48) flips such that the rotamer angles of the rings change, but the residues are still parallel to each other. In the case of CB1*-MK0364 system, the rotamer angles of both residues do not show a significant change and are almost consistent throughout the run.

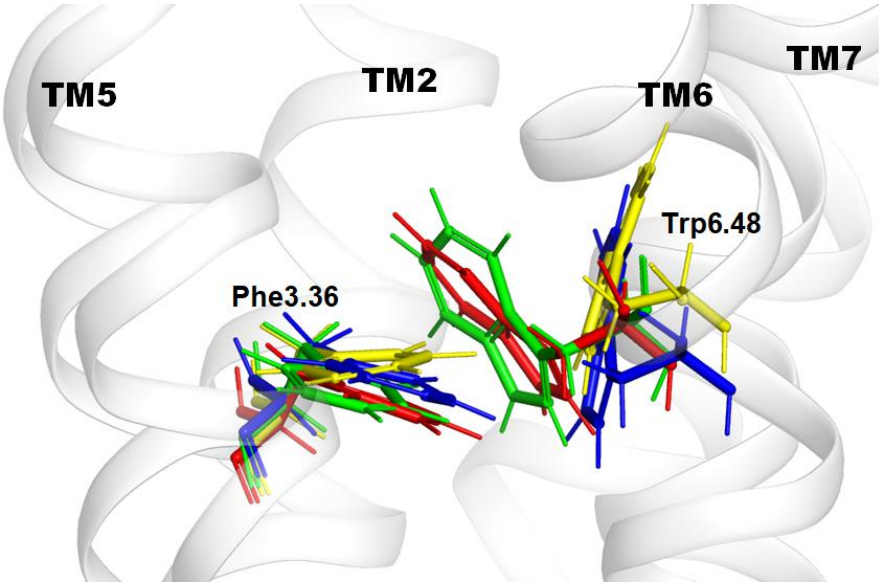

Figure 4.7 Changes in rotameric states of Phe200(3.36) and Trp356(6.48) in the replicate 2 of the CB1-AM11542 system. *The colours representing the time points are: Red – initial position; Green – 175 ns; Blue – 200 ns; Yellow – 1000 ns.*

4.4.3.2 Arginine Cage Ionic Lock

As discussed previously (in Sections 1.1.3, 1.3, and 3.4.6.2), that the breakage in the ionic lock between Arg214(3.50)-Asp213(3.49) and Arg214(3.50)-Asp338(6.30) is a key event in the activation of GPCRs. Therefore, as seen in Section 3.4.6.2, to monitor the side chains that form an ionic lock between TM3 and TM6 in CB1, the distances between the Cζ carbon of Arg214(3.50) and Cγ of Asp213(3.49) and Cγ of Asp338(6.30) atoms were calculated. The distances are given in Figures 4.8 and 4.10.

In the CB1-AM11542 system, the distance between the side chains of Arg214(3.50) and Asp338(6.30) is almost constant around the value of 5 Å in replicates 1 and 2 (Figure 4.8). In replicate 3, however, the distance of separation increases from about 600 ns onwards. It reaches a maximum around 762 ns, after which the value remains in the range of 10 Å until the end of the run. The distance between the side chains of Arg214(3.50) and Asp213(3.49) is well below 5 ns for the entire trajectory in all three replicates (Figure 4.8). From the trend in the distance between the side chains, it can be suggested that in the CB1-AM11542 system the conformation of Arg214(3.50) remains the same. The increase in distance between Arg214(3.50) and Asp338(6.30) is due to the movement of TM6 away from TM3, and not solely due to a conformation change in Arg214(3.50). This was confirmed upon visualising the trajectories (Figure 4.9).

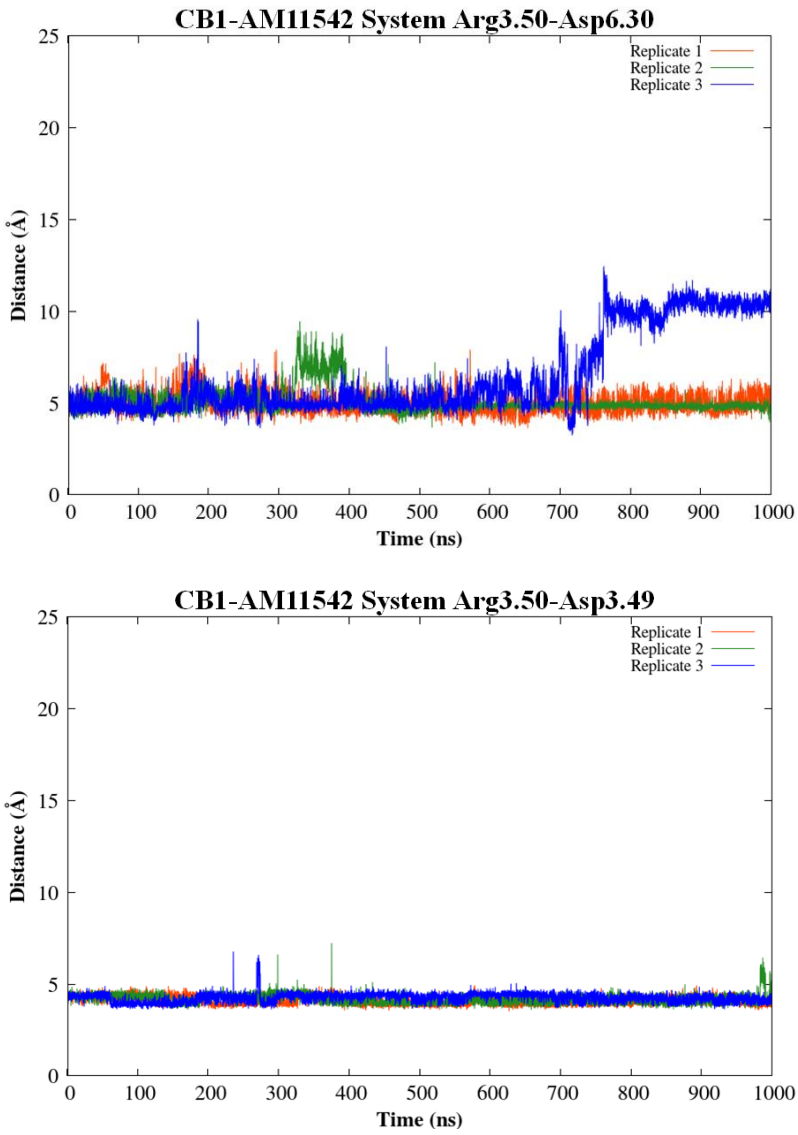

Figure 4.8 Distances between the Cζ carbon of Arg214(3.50) and (a) Cγ of Asp338(6.30) and (b) Cγ of Asp213(3.49) in CB1-AM11542 system. *Orange, blue and green represent replicates 1, 2, and 3 respectively.*

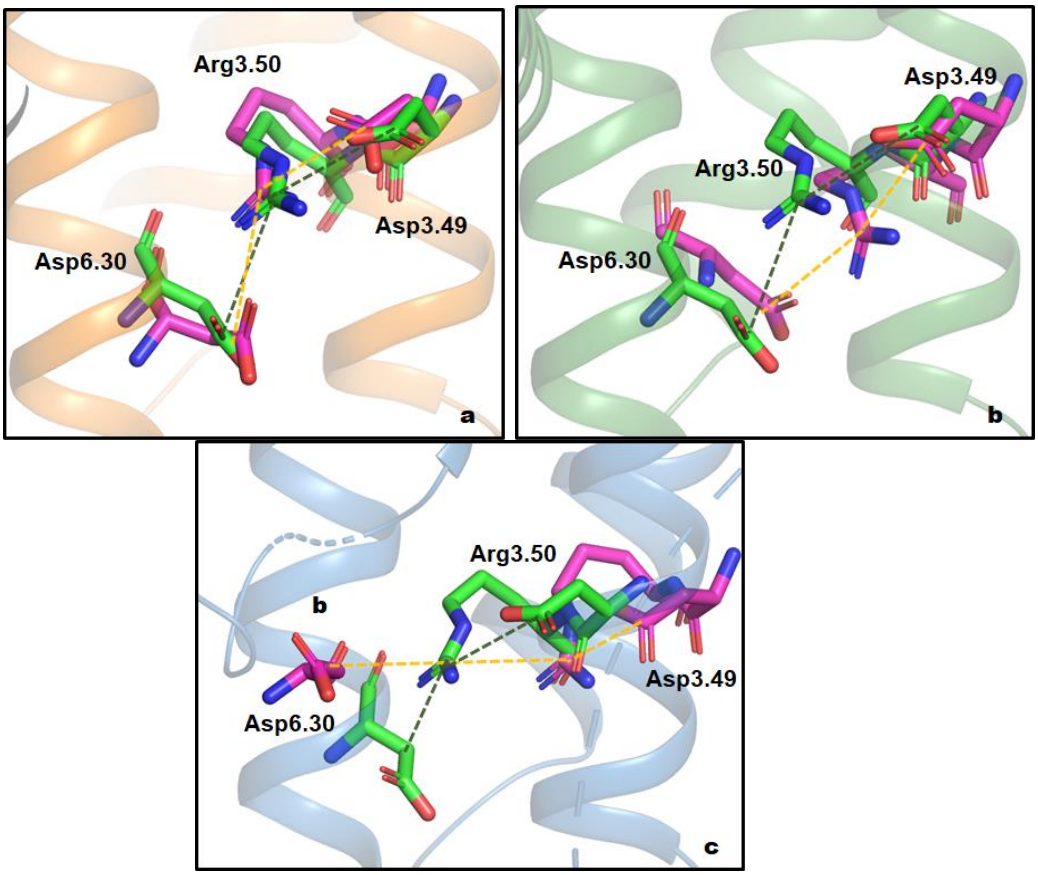

Figure 4.9 Initial (green) and final (pink) conformations of residues involved in the arginine cage 'ionic lock' in the CB1-AM11542 system. *(a) Replicate 1 (b) Replicate 2 (c) Replicate 3. Dotted lines link the carbon atoms of residues between which the distances were measured (green – initial state; orange – final state). The cartoon representation depicts the initial state of the receptor.*

In replicate 1 of the CB1*-MK0364 system, the distance between the side chains of Arg214(3.50) and Asp338(6.30) ranges from 10-15 Å, throughout the trajectory (Figure 4.10). Visualising the trajectories and comparing the initial and final state (Figure 4.11 (a))s, it could be seen that the difference in the distance between the two residues is rather small. In replicate 2, the separation reaches a maximum at around 600 ns, after which the distance steadily drops and reaches a minimum around 800ns. The distance again starts increasing after 850 ns but is still under the initial value. This was confirmed upon visualising the trajectories and comparing the initial and final position states of the two residues (Figure 4.11 (b)).

In replicate 3, the separation increases with fluctuation. After 400 ns, the residues come closer, but the separation increases again around 600 ns. Post 800 ns, the distance between is rather stable and ranges between 10-15 Å, as in replicate 1 (Figure 4.11 (c)). The distance between the side chains of Arg214(3.50) and Asp213(3.49) is below 5 Å for most of the simulation in all replicates. However, sporadic fluctuations are seen all along the trajectory at various intervals. The separation between side chains ranges from 5-10 Å during such fluctuations (Figure 4.10).

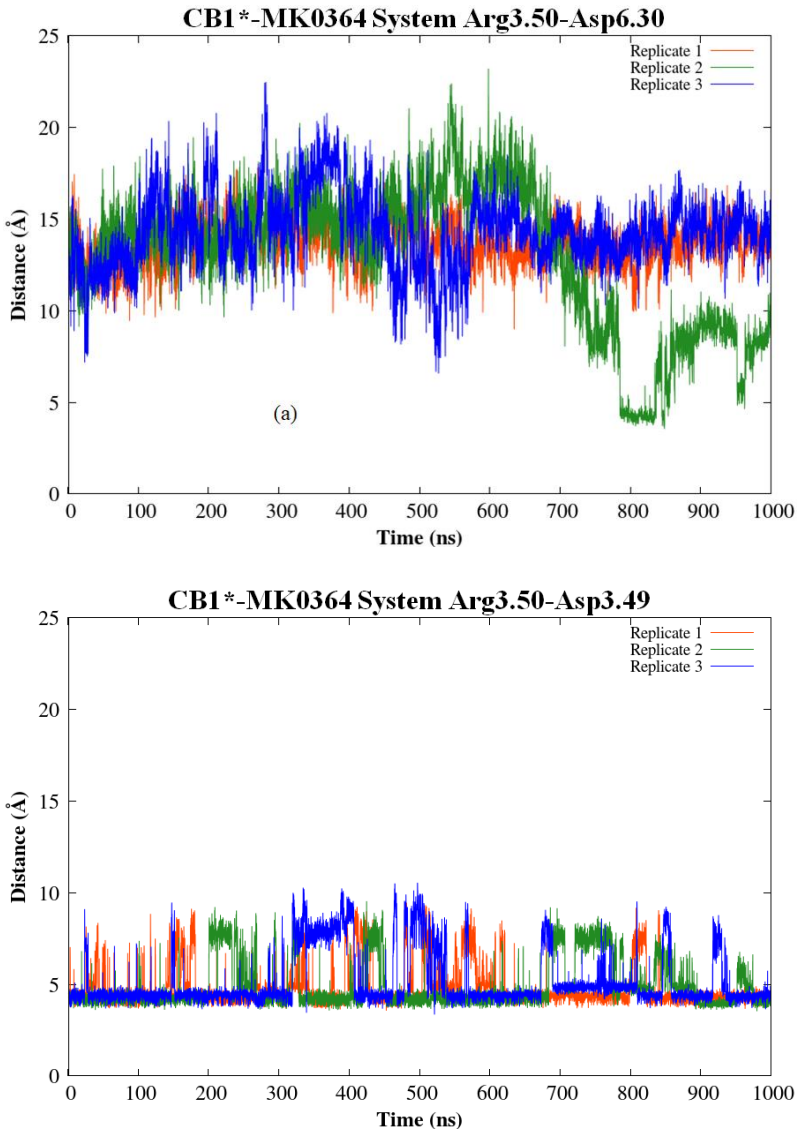

Figure 4.10 Distances between the Cζ carbon of Arg214(3.50) and (a) Cγ of Asp338(6.30) and (b) Cγ of Asp213(3.49) in CB1*-MK0364 system. *Orange, blue and green represent replicates 1, 2, and 3 respectively.*

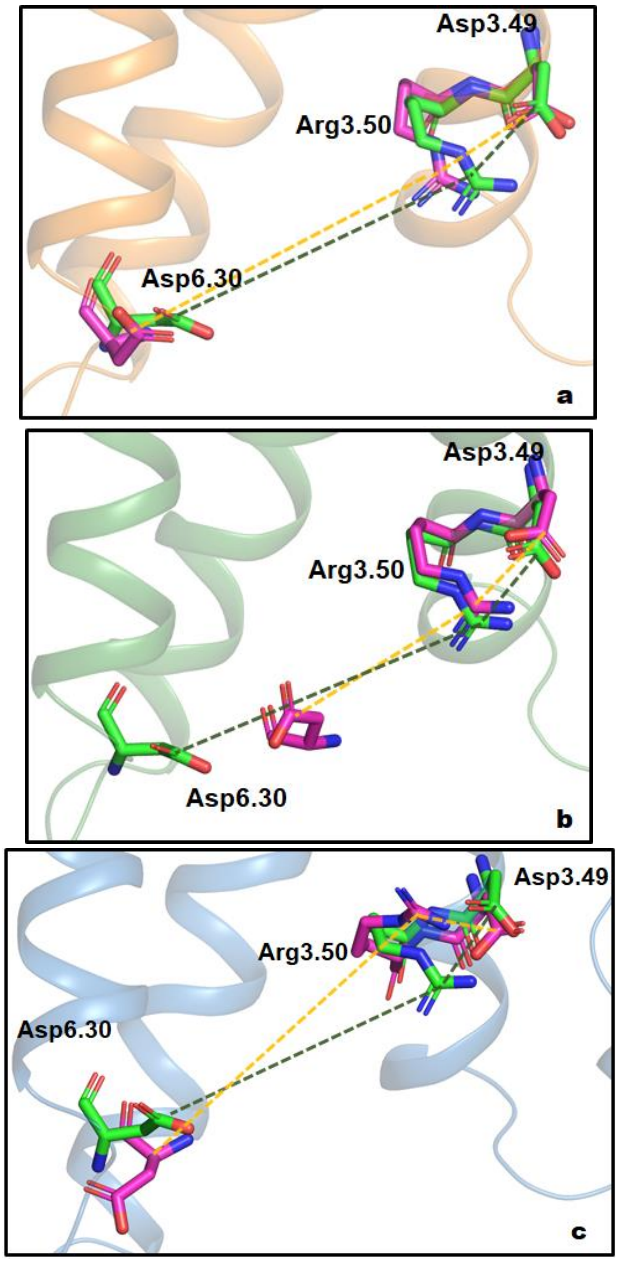

Figure 4.11 Initial (green) and final (pink) conformations of residues involved in the arginine cage 'ionic lock' in the CB1*-MK0364 system. *(a) Replicate 1 (b) Replicate 2 (c) Replicate 3. Dotted lines link the carbon atoms of residues between which the distances were measured (green – initial state; orange – final state). The cartoon representation depicts the initial state of the receptor.*

4.4.3.3 Conformation of Tyr7.53 Residue

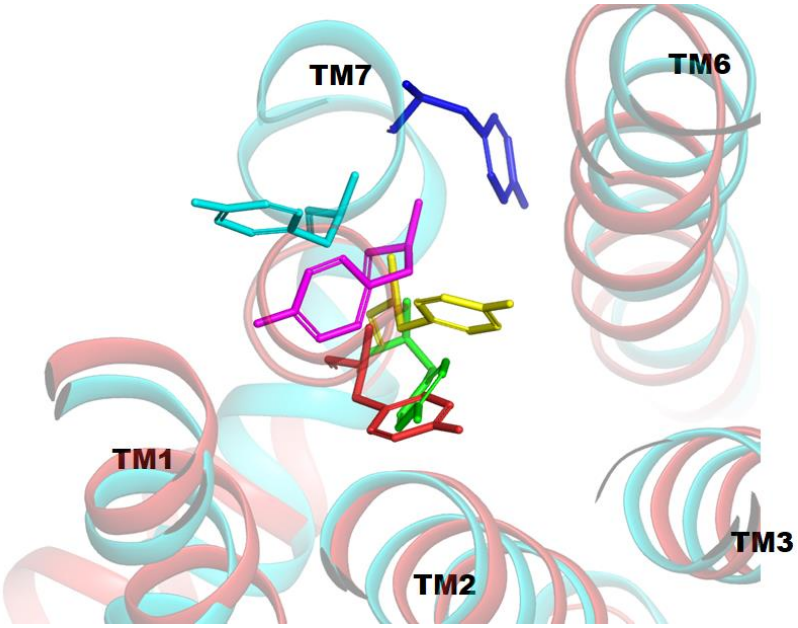

Figure 4.12 Changes conformation of Tyr7.35 in replicate 1 of CB1-AM11542 system. *The colours representing the time points are: Red – initial position; Green – 325 ns; Blue – 800 ns; Yellow – 850 ns; Pink – 150ns; Cyan – 975 ns; Orange – 1000ns (final position). Hydrogens are hidden. Red and cyan cartoons represent the initial and final conformations of the protein.*

In Section 1.1.3, the role of Tyr7.53 in the activation of GPCRs was discussed and in Section 1.3, the differences in the conformation of Tyr7.53 in active and inactive crystal structures of CB1 were reviewed. In that regard, the conformation of Tyr397(7.53) was monitored through the trajectory. Tyr397(7.53) shows very few changes in almost all replicates of both systems and the conformation maintained as seen in the crystal structure template of the respective systems. However, in replicate 1 of CB1-AM11542 system, Tyr397(7.53) adopts differential conformations due to the extensive helix unwinding of the NPXXY motif (Figure 4.5). As shown in Figure 4.12, around 325 ns (in green), a minor change in ring conformation as compared to the initial structure (in red) is seen. At 800 ns,

the residue faces downward parallel to the binding pocket (in blue) but at 850 ns (in yellow), it adopts a conformation similar to that of the active structure – pointing towards TM6. By about 975 ns, however, the residue has flipped its rotamer and points outside of the 7TM helical bundle, in the direction of H8 (in pink). By the end of the run, the tyrosine is fully pointing out of the protein (in cyan).

4.4.4 Pocket Volume

One of the notable differences between active and inactive state CB1 is their binding pocket volume (Section 1.3, Table 1.2). CB1 (i.e. 5U09) measures a volume of 564 $Å^3$ while CB1* (i.e. 5XRA) has a pocket volume of 384 $Å^3$. In this regard, to observe the influence of cross-docking on the binding pocket shape, the volume of the pocket was monitored through the trajectories and recorded for every 50 ns. The position of the ligand in each frame was used to define the pocket. The default value of 6 Å was used to set a margin around the ligand within which volume was to be calculated. In both cases, the pocket volume is within a range of 300-800 $Å^3$. From the graphs in Figure 4.13, it can be seen that the volumes are rather fluctuating and no explicit trend in volume change is seen. For the CB1-AM11542 system, the volume in replicate 1 and 3 shows a decreasing trendline. Replicate 2, on the other hand, follows a slightly increasing trendline. In the case of CB1*-MK0364 complexes, the trendline is increasing for replicate 1, almost constant for replicate 2 and decreasing for replicate 3; however, the changes are very minimal.

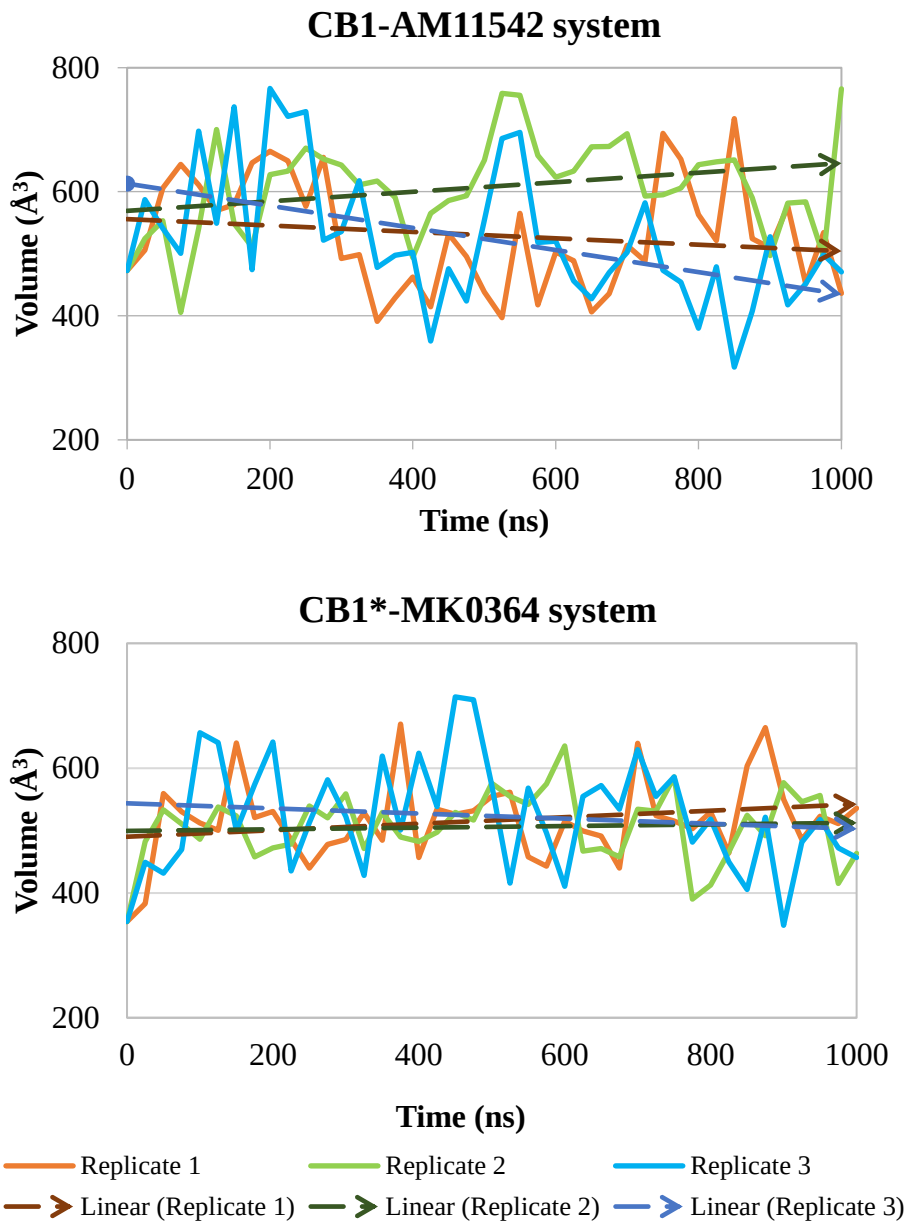

Figure 4.13 Binding pocket volume calculated per 50 ns for CB1-AM11542 and CB1*-MK0364 systems. *The linear trendlines are represented as dashed arrows. The points represent the binding pocket volume per 25 ns of the trajectory. The colours that represent each replicate is as given in the legend below the plots.*

4.5 Discussion

From the analysis of the trajectories, it is evident that the receptor in both CB1-AM11542 and CB1*-MK0364 systems show a minimal conformational change in transitioning towards the opposite activation state. In the PCA of CB1-AM11542 system, a few notable motions resembling the active state structure were observed i.e. the intracellular ends of TM5 and TM6 moving out of the binding pocket in replicate 1 and replicate 3, respectively. Indeed, in replicate 3, Arg214(3.50) and Asp338(6.30) are progressively separated from one another (Figure 4.9(c)). The bending of intracellular end of TM3 moving away from TM5 (as seen in PCA of CB1-AM11542 system) though not observed in the 5XRA crystal structure could have in addition affected the proximity of Arg214(3.50) and Asp338(6.30). However, Arg214(3.50) does not extend into the G protein binding area as seen in 5XRA (or other CB1 active structures seen in Section 1.3); it still points towards Asp213(3.49).

In the case of toggle switch residues in the aromatic network, the swing of Phe200(3.36) towards and Trp356(6.48) away from the binding pocket (which is considered to trigger activation in cannabinoid receptors, as seen in Section 1.3) were not observed. At the end of the simulation, the ring plane of both residues become perpendicular to each other in replicates 1 and 2. It can be said that face-face π-π interaction has been disturbed from the change in the conformation of Trp356(6.48). Thus, any stacking interaction, if formed, may be edge-faced. This conformation is unlike that seen in either CB1 active or inactive systems (Section 1.3, Figure 1.15). The residues are parallel to each other in the inactive CB2 structure (Section 1.3, Figure 1.16), but it is Trp258(6.48) which assumes a horizontal position not Phe200(3.36) as observed in CB1-AM11542.

According to the RMSD analysis of CB1-AM11542 system described in Loo *et al.*, it was found that the RMSD value of the protein in CB1-AM11542 system against both crystal structure templates (5XRA and 5U09) steadily increased with time. It was hence implied that the protein could be exploring conformations unlike either of the activation states[240]. In this regard, it could be suggested that the toggle switch conformation could be due to or causing such a conformational deviation.

Considering the conserved residue Tyr7.53, the changes in its conformation in replicate 1 of CB1-AM11542 (as observed in Section 4.4.3.3), can be attributed to the extensive unwinding of the NPXXY motif. At 975 ns, Tyr7.53 points in the direction of H8 and in its final conformation Tyr397(7.53) faces completely out of the helical bundle (Figure 4.12), breaking the hydrophobic interaction with residues of TM6. This conformation has not been observed in any of the CB1 crystal structures released till date. In the 5U09 crystal structure, the tyrosine points upward into the binding pocket while in 5XRA crystal structure it points in the direction of TM6 and forms a π-π edge-face interaction with Phe155(2.42) (Section1.3). Changes in the conformation of this conserved tyrosine residue support the idea that the protein could be exploring conformations unlike either of the activation states, as seen earlier in the discussion. However, further studies are required to determine if the changes in the conformation of Tyr397(7.53) is associated with the activation state of CB1 or solely a result of the flexibility of the NPXXY motif.

In replicates 2 and 3 of CB1*-MK0364 system, the RMSD against 5XRA was found to steadily increase while the values against 5U09 correspondingly decreased[240]. Loo *et al.* attributed this trend in RMSD to the inward movement (with respect to the binding pocket) of the intracellular end of TM6 in replicate 2 and outward movement (with respect

to the binding pocket) of extracellular end of $TM1^{240}$ – two notable helical changes observed in inactive structures (Section 1.3). These changes were also observed in the PC1 analysis (Section 4.4.2.2). Accordingly, in replicate 2, the inward movement of TM6 brings Asp338(6.30) closer to TM3. It was also seen in the PC1 analysis that the TM5 in all replicates showed the inward movement of its intracellular ends and outward movements of its extracellular ends, with respect to the binding pocket. Observing the conformation of the twin toggle switch residues, no significant changes were observed with respect to the CB1*-MK0364 system (Section 4.4.3.1).

Though significant changes in RMSD were observed in both systems[240], the volume of the binding pocket does not show explicit changes. Analysing the trendline of the change in volume, replicates 1 and 3 of CB1-AM11542 system show a decreasing trend. This is in agreement with the observed literature, as 5XRA (for which AM11542 is the cognate ligand) has a smaller pocket volume than that of 5U09 (on which CB1 is based) (Section 1.3, Table 1.2). The changes in the trendline for the binding pocket volume of CB1*-MK0364 system, are very minimal.

4.6 Conclusion

Thus, the positional changes of ligands and the conformational changes of receptors in the unbiased simulation of an inactive and an active state CB1 cross-docked with the cognate ligand of their template-crystal structure were analysed. Comparing the position of ligands before and after simulation, the docked agonist (AM11542 in CB1) and antagonist (MK0364 in CB1*) were found to bind deeper in the binding pockets than their initial position. PCA, conserved residue conformation analysis, and calculation of binding pocket volume show that the receptors in neither of the systems analysed have fully

attained its opposing activation state within the considered 1 μs. Either a different receptor conformation was being explored (in the case of CB1-AM11542) or partial changes towards the intended state were observed (in the case of CB1*-MK0364). It has been suggested that the partial change could be due to system finding itself in a local minimum[240]. Hence, the active state structures could be subjected to an apo state simulation and ligands of different chemical classes could be used to explore possible conformations in their transition to an inactive or resting state.

5 Molecular Dynamics Simulations of Cannabinoid Receptor 2

5.1 Introduction

As seen in Section 1.3, the crystal structure of inactive CB2 has a conformation unlike that seen in inactive CB1 structures, but rather it is much closer to active CB1 structures. This leaves much room to speculate about the conformation of an active CB2 crystal structure. At the time of writing this study, no active or agonist bound crystal structure for CB2 is available. Much like CB1, there is no crystal structure available for the apo state of CB2 either. As mentioned for CB1 in Section 3.1, to investigate the potential conformations that the apo state and an agonist bound state CB2 might assume, molecular dynamics simulations were performed on a model generated from the existing inactive crystal structure for CB2 (PDB ID 5ZTY) in both the apo state as well as docked to the CB2 agonist CP55940 (6). Given the absence of any other CB2 crystal ligand, the non-selective CP55940 (6) was chosen to be docked to CB2. CP55940 (6) is a well-established cannabinoid ligand which has played a critical role in the characterisation of CB1 and CB2 (as described in Section 1.2.3.1.1).

5.2 Aims

1. To run molecular dynamics simulations on two CB2 systems namely, CB2-Apo and CB2-CP55940 with an inactive CB2 model as the starting structure.
2. To identify the direction of the conformational change observed in the protein molecule of each system using RMSF, RMSD, and PCA.

3. To identify conformational changes in the ligand.

5.3 Methods

5.3.1 Preparation of CB2 Complexes

The inactive CB2 model for simulation using crystal structure 5ZTY was generated as described in Section 2.4.1. Preparation of the ligand CP55940 (6) and its docking into the CB2 model was carried out as per the methods described in Section 2.4.2.1. The chirality of the ligand was retained; no ionised states were generated. All other parameters were set to default.

5.3.2 Assembling the System

Both the CB2-Apo model and the CB2-CP55940 docked complex were embedded into two separate POPC bilayer systems using CHARMM-GUI web server[258] as mentioned in Section 3.3.2. The bilayer consists of 242 POPC molecules and 13 Chlorine ions were added for neutralisation; the ions were added using Monte Carlo simulations performed by the server. The system was solvated with TIP3P[260] water. The centre of the system was set to Z = 0. The box sizes for apo and ligand-bound systems are 97.28 x 97.28 x 112.4 Å and 97.31 x 97.31 x 112.4 Å respectively. The parameters for ligands were generated using the CGenFF program built into the CHARMM-GUI server.

5.3.3 Running MD Simulations

The CHARMM 36 force field[230] was used in GROMACS 2019.2 to perform MD simulations[290]. The system was energy minimised using the steepest descent algorithm. NVT equilibration was run for 100 ps. NPT equilibration was run in four steps: 10 ns of restrained dynamics, 5 ns with only backbone atoms restrained, 5 ns with only sidechain

atoms restrained and 50 ns of unrestrained simulations. Restraint force used was 1000 kJ/mol. In production runs, the Nose-Hoover thermostat[262] and Parrinello-Rahman barostat[263] were used for temperature and pressure coupling respectively; velocity rescale was used for temperature coupling in equilibration runs. The simulations were conducted at a temperature of 310 K. The time step used was 2 fs. All bonds involving hydrogen atoms were constrained using the LINCS algorithm[265]. Cut-offs of 12 Å were applied for short-range van der Waals and electrostatic interactions, while long-range electrostatic interactions were calculated using particle mesh Ewald[266]. The production runs were run in triplicate for 500 ns each for both CB2-Apo and CB2-CP55940 systems. Each replicate had a different initial velocity; a random generator was used to generate velocities.

5.3.4 Analysis

PCA analysis was performed using pyPcazip tools[267]. The individual PCs were analysed using PyMol[276]. RMSF, RMSD and other residue-residue distance calculations were performed using GROMACS tools. RMSF values were calculated using the initial structure as the reference. The RMSDs for transmembrane backbone atoms were calculated for both apo and ligand complexed model using the co-ordinates of 5ZTY as the reference structure. Gnuplot 4.6 was used for plotting all graphs[269]. Trajectories were visualised using VMD 1.9.2[268].

5.4 Results

5.4.1 Docking and Preparation of the Complex

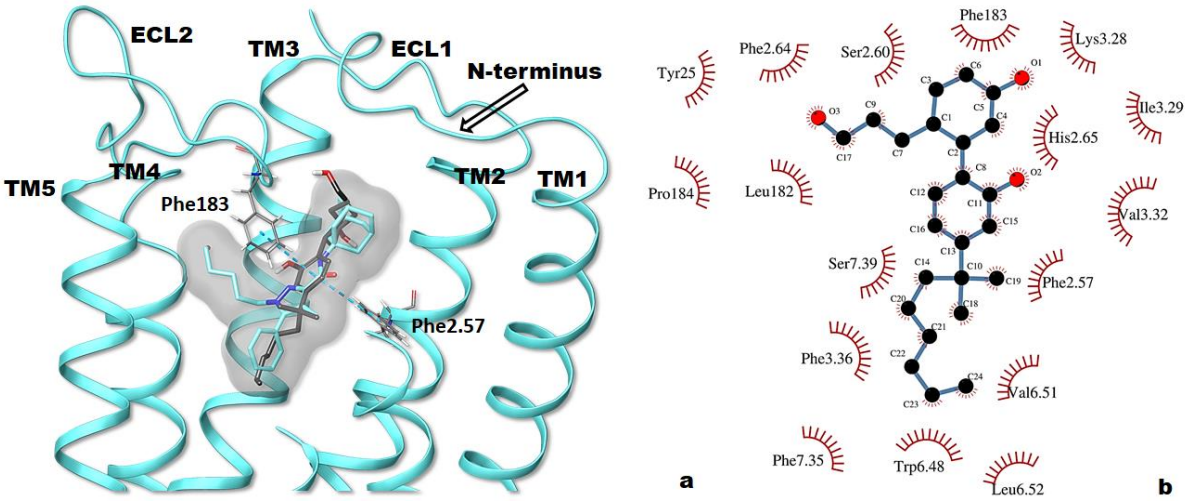

Figure 5.1 (a) Docked pose of CP55940 (6) into CB2. *CP55940 (6) is shown in grey and the cognate ligand AM10257 (23) is shown in cyan as sticks. Residues are shown as thin tubes in grey. The binding pocket of the cognate ligand is shown as a grey surface. Blue dotted lines indicate π-π interactions. Only polar hydrogens are shown for both ligands. TM6 and TM7 were removed for purposes of image clarity.* ***(b) 2D Ligand interaction diagram of CP55940 (6) with CB2*** *–residues within 3.9 Å displayed. Image generated using LigPlot*[270].

Figure 5.1 (a) shows the pose of the ligand CP55940 (6) docked into the generated CB2 model. As seen in the figure, the docked ligand overlaps well with the binding pocket of the cognate ligand of 5ZTY (AM10257 (23)). The central phenyl ring (A ring, as designated in Section 1.2.3.1.1) forms edge-face π-π interactions with Phe87(2.57) and Phe183(ECL2). The aliphatic tail points down into the pocket and forms hydrophobic interactions with surrounding residues (Figure 5.1 (b)) including the toggle switch residues, Phe117(3.36) and Trp258(6.48). The cyclohexanol ring (C ring, as designated in Section 1.2.3.1.1) is inclined towards TM2 and TM3. The ligand is aligned along the aromatic portions of the cognate ligand and assumes an almost linear conformation. This pose is

different from that seen in the docking studies of CP55940 (6) with 5ZTY crystal structure conducted by Li *et al.* in the crystal structure study[127]. In their study, CP55940 (6) assumed a bent V-shape as in the case of CB1 crystal structure agonists[103] (Section 1.3). The aliphatic tail of CP55940 (6) coincided with the aliphatic portion of the AM10257 (23) and no hydrophobic contacts with the toggle switch residues was observed.

The embedded complex is shown in Figure 5.2

5.4.1.1 Post Equilibration Structure

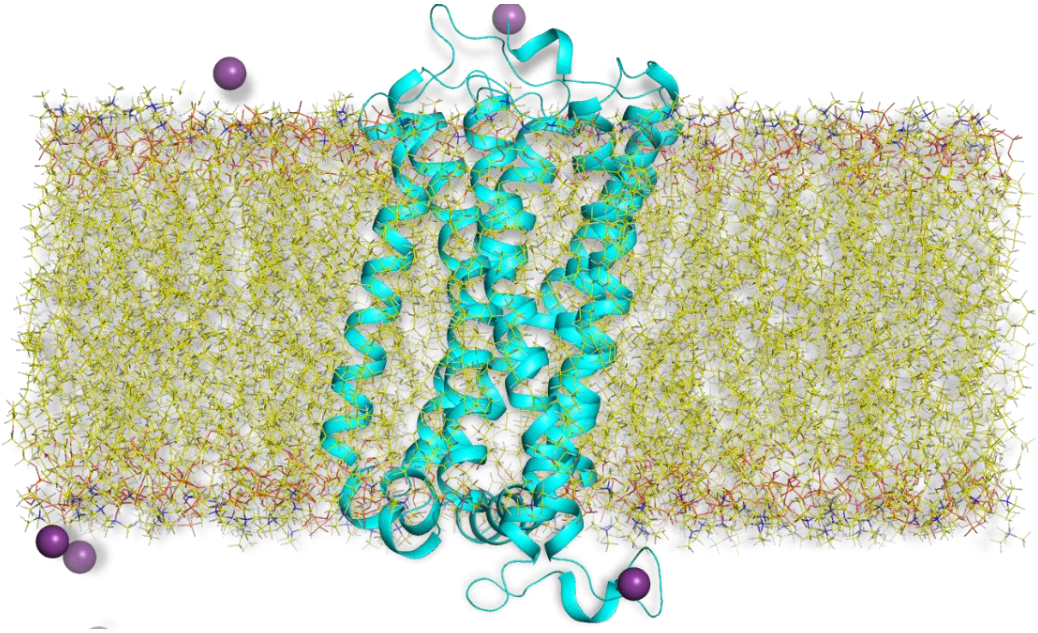

Figure 5.2 Apo CB2 protein (in cyan) post embedding into the system. Water molecules are not displayed in the image. *Chlorine atoms are shown as spheres (in purple) and phospholipid molecules are shown as sticks (yellow).*

It was observed that following the unrestrained NPT equilibration, the position of the ligand CP55940 (6) changed in the system, as shown in Figure 5.3. Unlike the orientation seen in Figure 5.1, CP55940 (6) forms hydrogen bonds with backbone oxygen

of Tyr25(N-term) and sidechain oxygen of Ser90(2.60). However, it still retains the slanted geometry of the docked ligand.

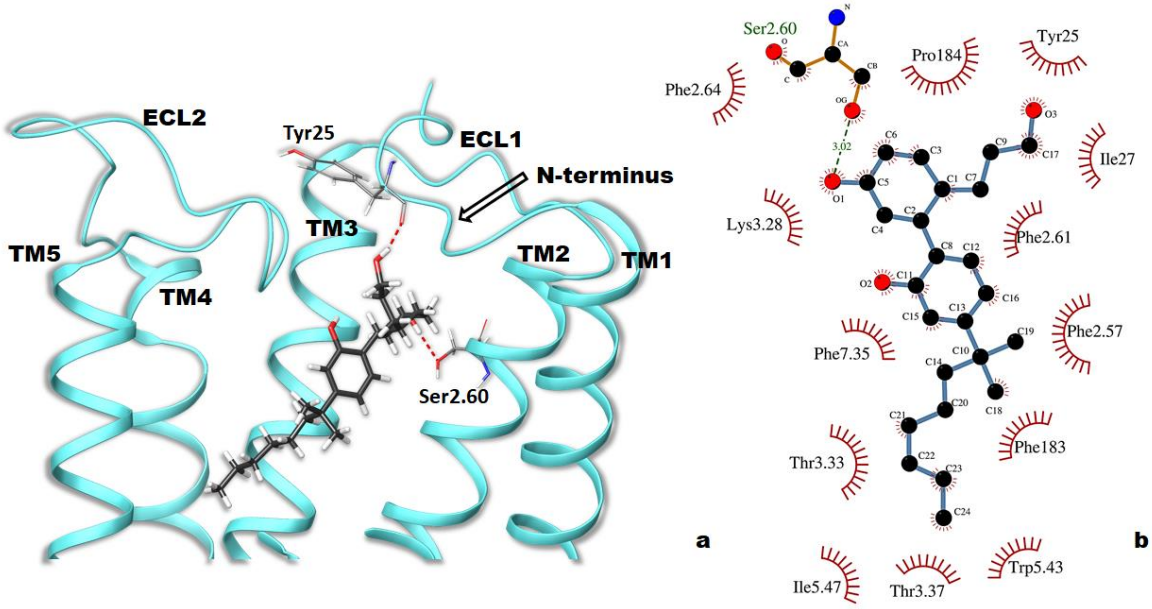

Figure 5.3 (a)Position of ligand post equilibration of CB2-CP55940 system. *CP55940 (6) is shown in grey. Residues are shown as thin tubes in grey. Red dotted lines indicate hydrogen bond interactions. TM6 and TM7 were removed for purposes of image clarity.* ***(b) 2D Ligand interaction diagram of CP55940 (6) with CB2*** *– residues within 3.9 Å displayed. Image generated using LigPlot*[270]*. The green line indicates a hydrogen bond. Hydrogen bond with backbone oxygen of Tyr25 not displayed by LigPlot.*

The conformation of the toggle switch residue Trp258(6.48) also changed from its crystal structure orientation. In the CB2-Apo system, Trp6.48 shows a change in χ1 angle of about -20° from that observed in the crystal structure. This shifts the residue orientation from being horizontal to the binding pocket (and perpendicular to TM6) to face the binding pocket, similar to that seen in CB1 active structures (Figures 1.15 and 1.16). In the CB2-CP55940 system, though there is no change in χ1 angle, the aromatic rings vertically rise by about 45°; this results in the tryptophan to assume a conformation vertical to the binding

pocket along the axis of TM6. This post equilibration state before productions runs is referred to as the initial conformation or initial state in the current chapter.

5.4.2 RMSF Analysis

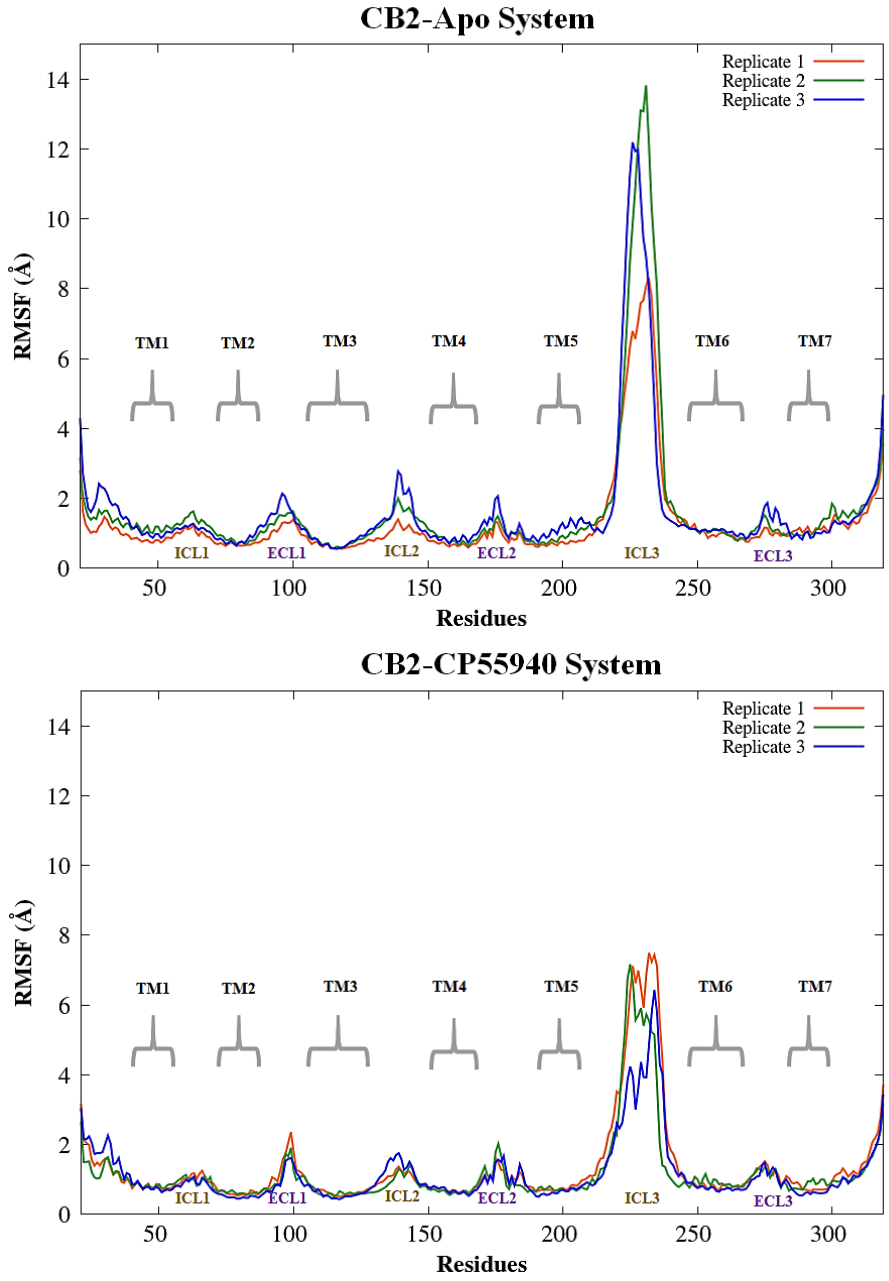

Figure 5.4 RMSF plots of CB2-Apo and CB2-CP55940 systems. Replicates 1, 2, and 3 of each system are represented by colours orange, green, and blue*. Curly braces represent the TM regions. ECL and ICL regions are marked under the respective plot areas.*

The RMSF value for both CB2-Apo and CB2-CP55940 systems was calculated as explained in Section 3.4.2 using the initial conformation (i.e. the conformation at the start of the simulation post-NPT equilibration) as reference.

As in the case of the CB1 systems, loop regions show more fluctuations compared to transmembrane regions. From the plots shown in Figure 5.4, it can be seen that the ICL3 of CB2-Apo exhibits more flexibility as compared to that of the agonist bound system. Replicate 3 of CB2-Apo system shows more fluctuations in loop regions in general, though replicate 2 shows the highest fluctuation of ICL3. In the CB2-CP55940 system, all three replicates show a comparable level of flexibility with no dominance in RMSF values. ICL2 shows the second-highest fluctuation among loops in the CB2-Apo system; the CB2-CP55940 system has ECL1, ICL2, and ECL2 showing an almost equal magnitude of fluctuation.

5.4.3 RMSD of the Protein Structures

The plot of RMSD of CB2 TM-BB atoms against that of the crystal structure (5ZTY) for both CB2-Apo and CB2-CP55940 systems is given in Figure 5.5. From the RMSD plots, it is evident that the protein in both CB2-Apo and CB2-CP55940 systems show minimal deviation from the initial structure from the range of 1 – 2 Å. A faint rise in RMSD is seen in the replicates 1 and 2 of the CB2-Apo system; however, the extent of change in RMSD is far less compared to the change in the CB1-Apo system seen in Chapter 3 (Figure 3.4).

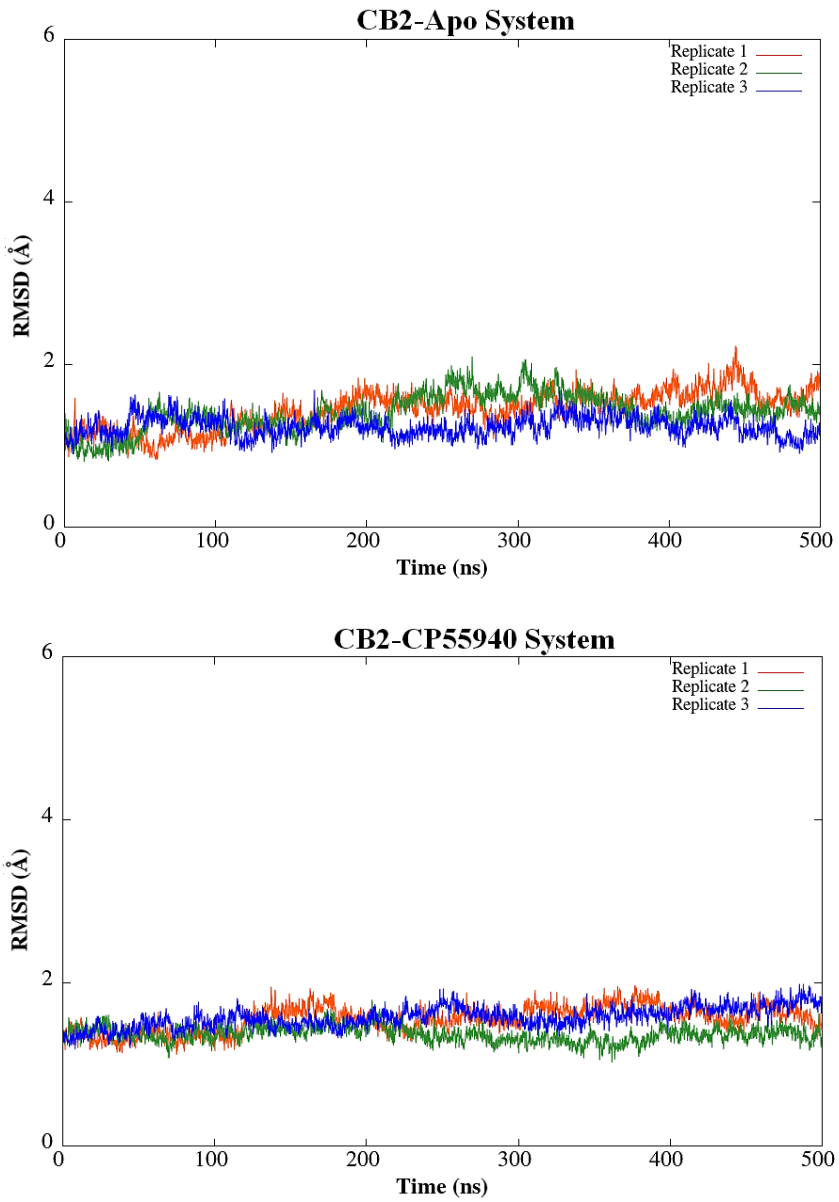

Figure 5.5 RMSD values of CB2-Apo and CB2-CP55940 systems against the crystal structure 5ZTY. *Replicates 1, 2, and 3 are represented by colours orange, green, and blue.*

5.4.4 Ligand RMSD

The RMSD for ligand molecule against its initial position (i.e. orientation post equilibration) is shown in Figure 5.6.

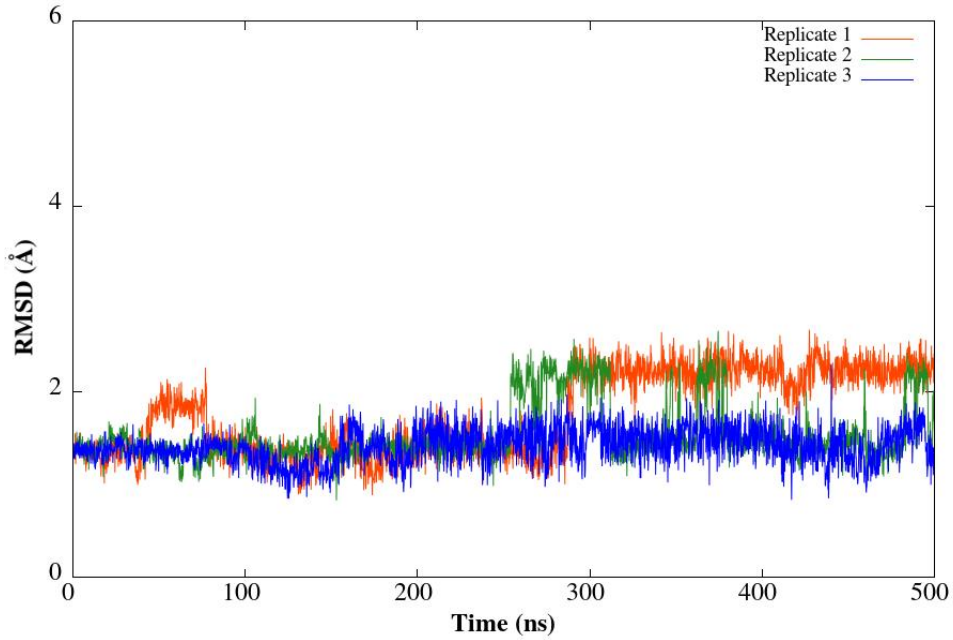

Figure 5.6 RMSD values of CP55940 (6) against its initial position throughout the trajectory of CB2-CP55940 system. *Replicates 1, 2, and 3 are represented by colours orange, green, and blue.*

It can be seen from the plot that the RMSD of ligand for replicate 3 stays well under 2 Å throughout the trajectory. For replicate 1, however, the RMSD shows sharp changes at two junctures. Firstly, there is a rise in RMSD between 50 – 100 ns to 2 Å, beyond which it subsides. Another sharp change in ligand RMSD is seen close to 300 ns, whereby the value rises to 2.6 Å from its observed range. The value then remains in the range of 2.4 – 2.6 Å till the end of the run. Inspecting the trajectories at the mentioned time intervals (Figure 5.7), it was found that around 45 ns the ligand slowly changes its orientation with the A ring facing ECL2 as in the docked model (Figure 5.1) and the aliphatic tail bending (green and blue). At about 77.54 ns the ligand assumes an orientation seen initially (in yellow), thus explaining the drop in RMSD. At about 150 ns, the conformation remains almost the same with the exception that the A ring is facing the ECL2 once again. At 287.19

ns, the aliphatic tail of the ligand bends upwards, almost perpendicular to the aromatic groups. This conformation is observed until the end of the trajectory, with a low unquantifiable variation as seen in Figure 5.7 (in orange). It is similar to that observed by Li *et al*[127] in their study with crystal CB2, as well as the agonist conformation seen in CB1 crystal structures[103].

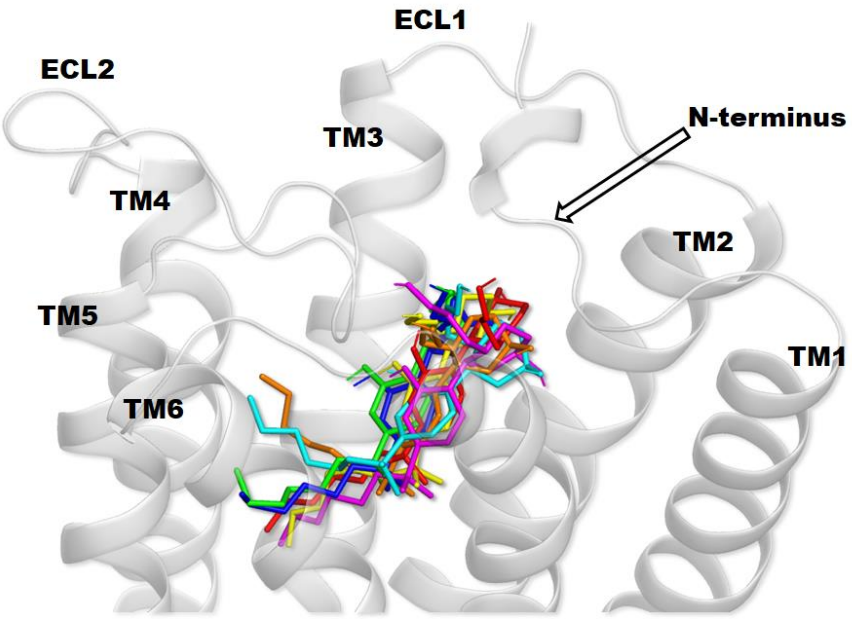

Figure 5.7 Changes in ligand position through replicate 1 of CB2-CP55940 system. *The colours representing the time points are: Red – initial position; Green – 45.39ns; Blue – 45.42ns; Yellow – 77.54 ns; Pink – 150ns; Cyan -287.19ns; Orange – 500ns (final position). Only polar hydrogens are shown in the ligands.*

In the case of replicate 2, the ligand RMSD value appears to remain under 2 Å for the majority of the run. However, in the intervals between 250-300 ns, 350-390 ns, and the final 20 ns of the run, fluctuations in the RMSD are observed. Looking at the changes in the ligand positions in those time intervals (Figure 5.8), at 200 ns, the ligand tail moves downward from its original position; at 255 ns (in blue), the tail bends behind the A ring changing the conformation of the ligand completely. At 295 ns (in yellow), the aliphatic

chain extends once again; however, the ligand is much more linear compared to the initial position (in red). At 318.10 ns (in pink), the ligand once again resembles its initial position. At the end of the simulation, the orientation of the ligand is quite similar to the one seen at 200 ns. Through the trajectory, the A ring is faced towards TM7 and moves to and from in proximity to the helix. No significant change is observed in the position of the C ring.

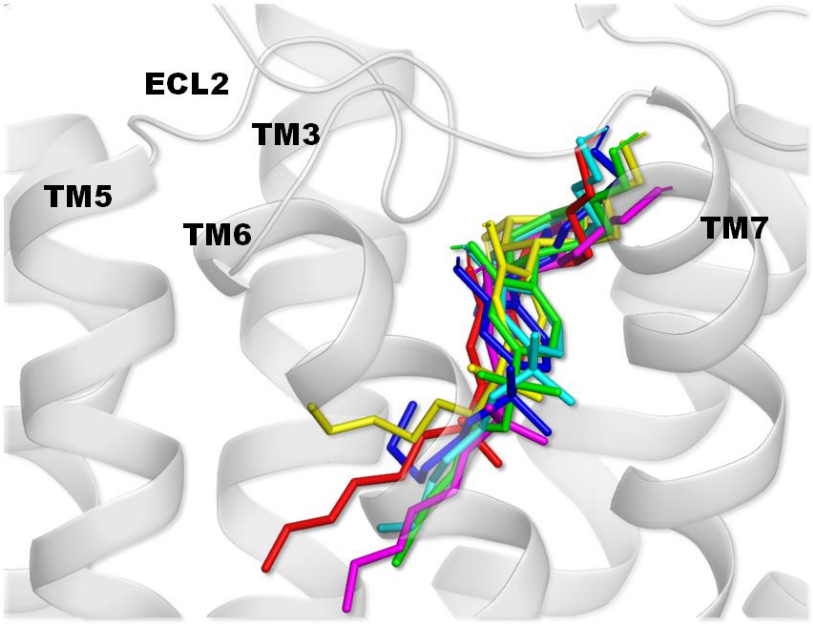

Figure 5.8 Changes in ligand position through replicate 2 of CB2-CP55940 system. *The colours representing the time points are: Red – initial position; Green – 200ns; Blue – 255ns; Yellow – 295 ns; Pink – 318.10ns; Cyan - 500ns (final position). Only polar hydrogens are shown in the ligands.*

5.4.5 Principal Component Analysis (PCA)

As mentioned in Section 1.5.3.1, PCA reduces the number of dimensions required to describe the dynamics of a protein and helps identify essential motions in a trajectory. In this regard, PCA on TM-BB atoms of the CB2 model in both systems was performed in the same manner as mentioned in Section 3.4.5 for CB1 models. The projection of

eigenvector 1 on eigenvector 2 for all three replicates of a system plotted onto a common subspace is shown in Figure 5.9. Comparing the area spanned by each replicate in the plots in Figure 5.9, it can be said that helices of the CB2-Apo system explore more conformations than those of the agonist bound system, as expected. In the CB2-Apo system, the final positions of all three replicates are far off from each other as well as the initial position. While each replicate also occupies a unique area of the subspace, it also shows considerable overlap with the other replicates. In the case of the CB2-CP55940 system, replicate 1 overlaps with replicate 3, while replicate 2 occupies a different area of the subspace, indicating differential motions. The final position of replicates 1 and 2 also coincide with each other.

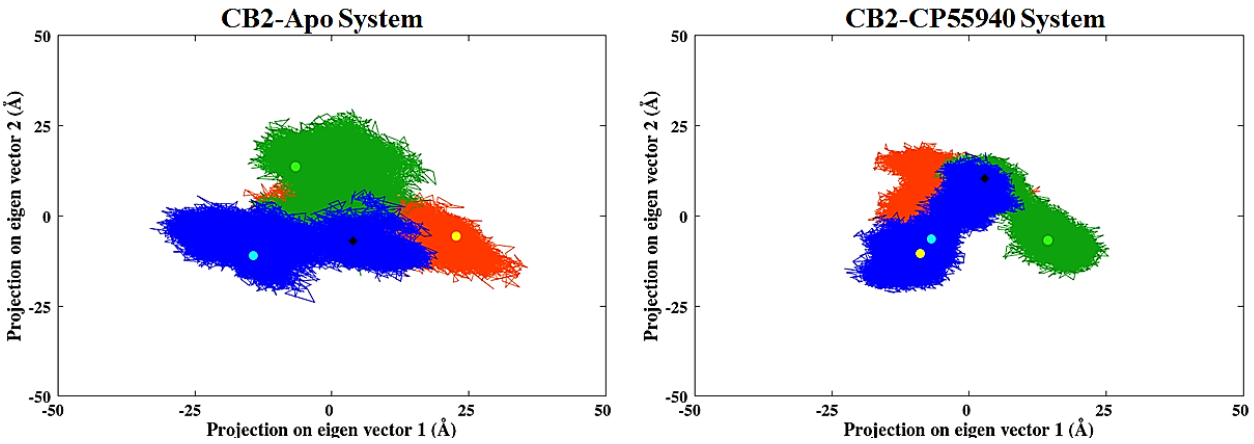

Figure 5.9 PCA plots of principal component 1 and 2 for transmembrane backbone atoms of CB2-Apo and CB2-CP55940 systems. *The replicates 1, 2, and 3 are represented by colours orange, green, and blue respectively. Black diamond denotes the initial position of the protein. The yellow, green, and cyan dots represent the final position of the proteins in replicates 1, 2, and 3 respectively.*

To identify which part of helix shows the most movement and the direction of that movement, porcupine plots for PC1 of the TM-BB atoms of each replicate in each system were generated using PyMol[276]. The plots for each system along PC1 are given in Figures

5.10 and 5.11. A guide for the terms used to describe the motions has already been provided in Figure 3.8.

5.4.5.1 CB2-Apo System

In replicate 1, the lower portion (IC) (i.e. that half of the helix near the intracellular region) of TM1 bends towards TM7, while the upper portion (EC) (i.e. that half of the helix near the extracellular region) rotates downward in an anticlockwise direction. In replicate2, both EC and IC ends of TM1 bend away from the binding pocket, though in different directions. In replicate 3, the EC end tilts towards the pocket while the IC end tilts away from it.

In the case of TM2, replicate 1 shows the bending of the EC end towards TM1 while replicate 2 shows rotation (anticlockwise) of the EC end towards the same helix. In contrast, the IC end of replicate 1 bends towards the pocket and in replicate 2, it bends away from the pocket. In replicate 3, the EC end bends away from the pocket in an upward direction resembling helix elongation while the IC end bends slightly away from the pocket.

In replicate 1, the EC end of TM3 bends away from the pocket while the IC end bends towards TM5. In contrast, replicate 2 shows the EC end tilting towards the binding pocket while the IC end tilts away from the binding pocket. In replicate 3, the EC end rotates downwards in the anticlockwise direction and IC end tilts away from the binding pocket.

The descriptions of PC1 motions for TM4 and TM5 are given in Appendix 5.

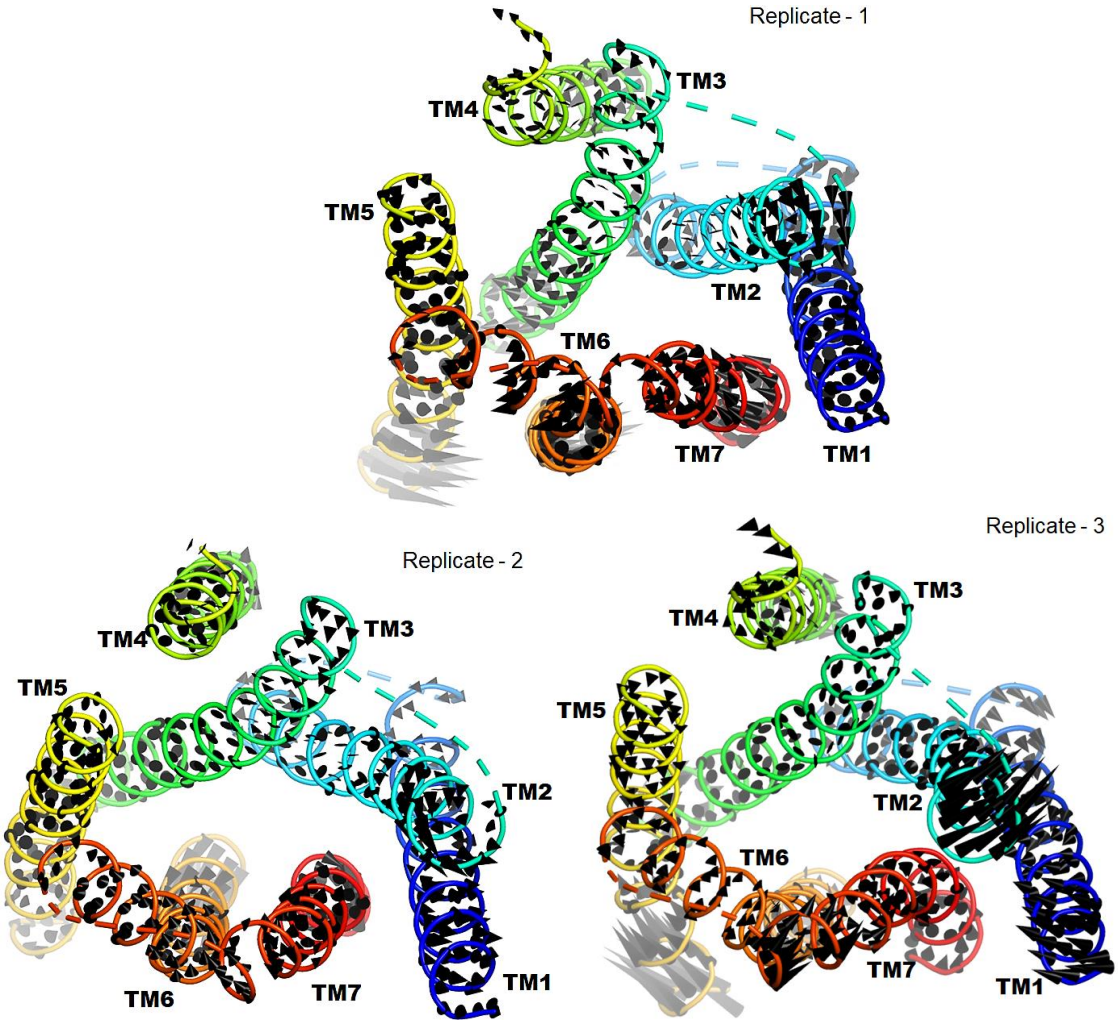

Figure 5.10 Porcupine plots for PC1 of CB2-Apo system. The transmembrane regions are coloured in the direction of blue to red from TM1 to TM7. *Black arrows denote the direction of movement.*

High flexibility with respect to TM movement is exhibited by TM6 and 7. For TM6, the Pro kink serves as a divide between EC and IC of the helix TM. In replicate 1, the EC end of TM6 bends towards TM5 while the IC end tilts towards TM7. In replicate 2, the EC end shows minimal movement in an upward direction; the IC end shows bending in a direction away from the binding pocket. In replicate 3, the EC end bends away from the

binding pocket towards TM7 and the IC end bends towards TM5. The extent of movement, however, is lesser than that seen in replicate 1.

TM7, in replicate 1 shows a movement of the entire helix in an upward direction with its N-terminus near ECL3 bending in the direction of TM1. A similar kind of upward movement is also observed in replicate 2. However, in the NPXXY region, helix unwinding in an anticlockwise direction is observed. In replicate 3, by contrast, the helix moves downward, while the N-terminus region bends away from TM6 in an upward direction resembling helix straightening.

5.4.5.2 CB2-CP55940 System

In all three replicates, the IC end of TM3 shows a movement in the direction of the binding pocket either by bending (Replicate 1 and 3) or by tilting (Replicate 2). The EC end, however, shows differential motions - in replicate 1 it bends towards TM4, in replicate 2 it bends in the direction of the binding pocket away from TM4, and in TM3 bends away from the binding pocket.

TM6 in replicate 1 shows a downward movement of the helix with the N-terminal near ICL3 bending towards TM7. In replicate 2, an upward movement of the whole helix is observed. In replicate 3, the EC end of TM6 bends towards TM7 and IC bends towards TM5.

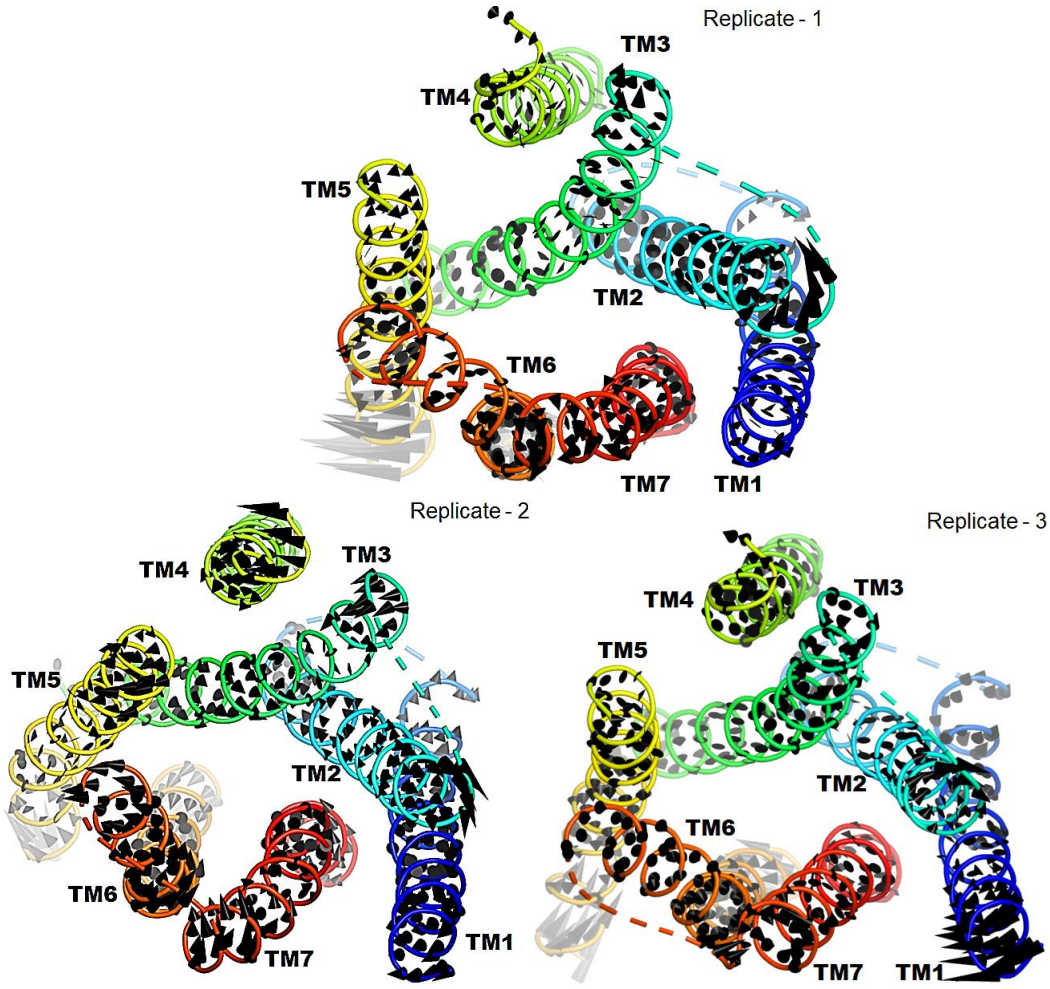

Figure 5.11 Porcupine plots for PC1 of CB2-CP55940 system. *The transmembrane regions are coloured in the direction of blue to red from TM1 to TM7. Black arrows denote the direction of movement.*

The motions seen in replicate 1 for TM7 can be described by dividing the helix into three parts – N-terminus near the ECL3 shows clockwise rotation away from the binding pocket, the mid-portion of the helix bends into the binding pocket and the C-terminus near H8 bends away from the binding pocket. TM7 in replicate 2 also shows such differential motions along the helix. The N-terminus bends in the direction of the binding pocket. The mid-portion, however, shows a downward movement which is countered by the C-terminus whereby the helix unwinds around the NPXXY motif. Replicate 3 also exhibits complex

motions – the N terminus bends towards TM1 and the three-helix turns that immediately follow the N-terminus rotate in an anticlockwise fashion. This rotation is counteracted by the remainder of the helix which shows a clockwise rotation. The C-terminus binds into the binding pocket. The descriptions of PC1 motions for TM1. TM2, TM4 and TM5 are given in Appendix 5.

5.4.6 Conformation of Conserved Residues

5.4.6.1 Twin Toggle Switch

As seen in Sections 1.1.3 and 1.3, the rotameric change and a break in the interaction between Phe200(3.36) and Trp6.48(356) is essential in the transition from inactive to active structures of cannabinoid receptors. Similar to CB1 simulations (Section 3.4.6.1), the distance between the centre of mass (COM) of the carbon atoms comprising the aromatic rings of Phe117(3.36) and Trp258(6.48) was calculated (Figure 5.12) as a means of analysing the proximity between the two residues.

In all the three replicates of the CB2-Apo system, an increase in the distance between Phe117(3.36) and Trp258(6.48) is observed within the first 20ns. After 20ns, the value drops and shows minor fluctuations for the rest of the simulation. In the crystal structure of 5ZTY, the aromatic stacking interaction between Phe117(3.36) and Trp258(6.48) is interjected by the cognate ligand, AM10257 (23) and their rotamers are constrained. In the absence of a ligand, the rotamers of both residues undergo a swift change.

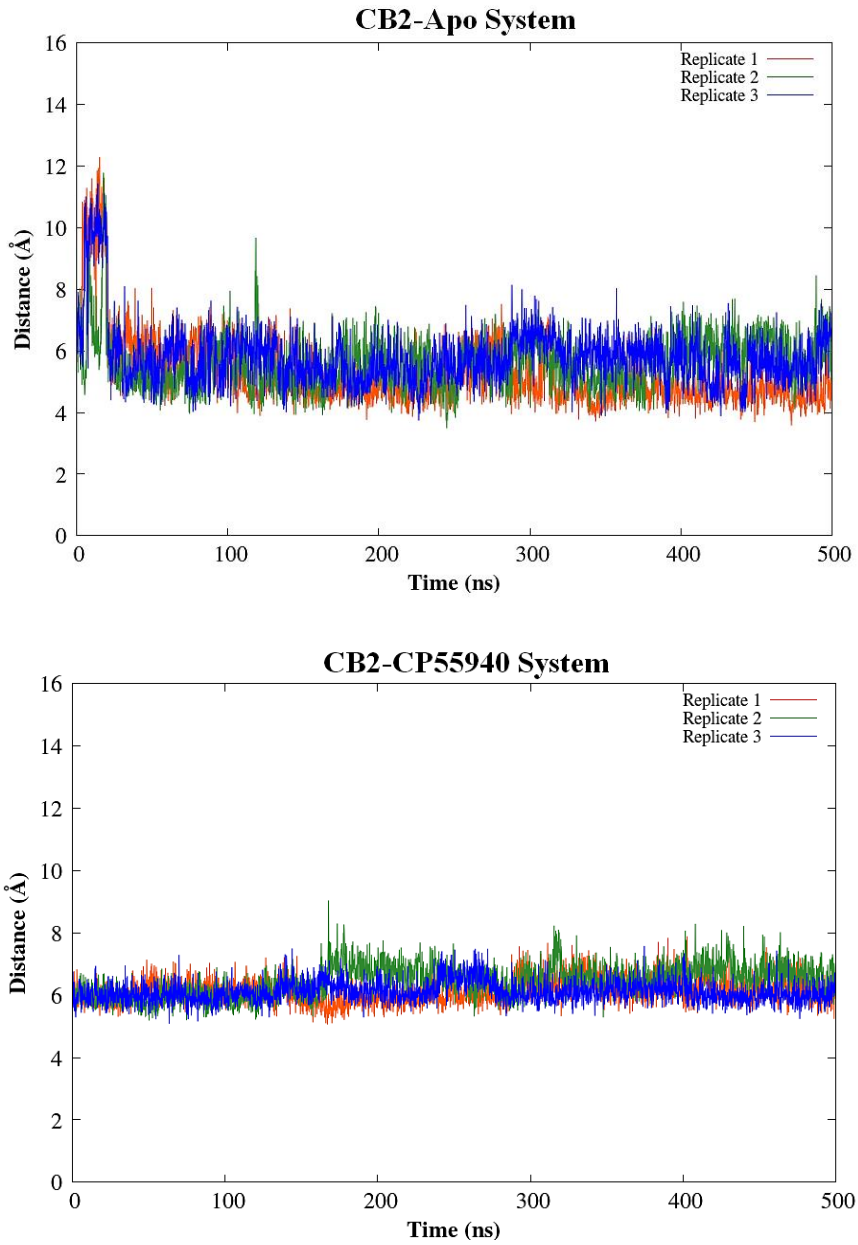

Figure 5.12 Distance between the COM of carbon atoms comprising the aromatic rings of Phe117(3.36) and Trp258(6.48) in CB2-Apo and CB2-CP55940 system. *Replicates 1,2, and 3 of each system are represented by colours orange, green, and blue respectively.*

Conformational change starts with Trp5.48 changing its orientation from pointing into the binding pocket to pointing away from it and towards TM5. Following this, Phe3.36 which initially pointed in the direction of the ligand undergoes a change in its rotamer and

bends down into the pocket. At this stage, the Phe117(3.36) residue is under the Trp258(6.48) residue. The stacking interaction either re-forms or breaks depending on the rotamer of the residues as, beyond 20 ns, the rotamer angles fluctuate. The changes in the conformation of the toggle switch residues in replicate 3 have been shown in Figure 5.13 for example. The conformation of Trp258(6.48) changes from its initial position at 4 ns (in green) by about 30°. At 5 ns, another change in angle by 66.5° occurs (in blue). The conformation of Phe3.36 remains the same in this time. At 20.62 ns, the conformation of Phe3.36 changes from its initial position (in yellow) by 69.3°. During this period the conformation of Trp258(6.48) stays the same. Post 100 ns time, fluctuations in the residue conformers are seen (as shown in Figure 5.13(b)) which influences the distance between the COM of residues as calculated in Figure 5.12.

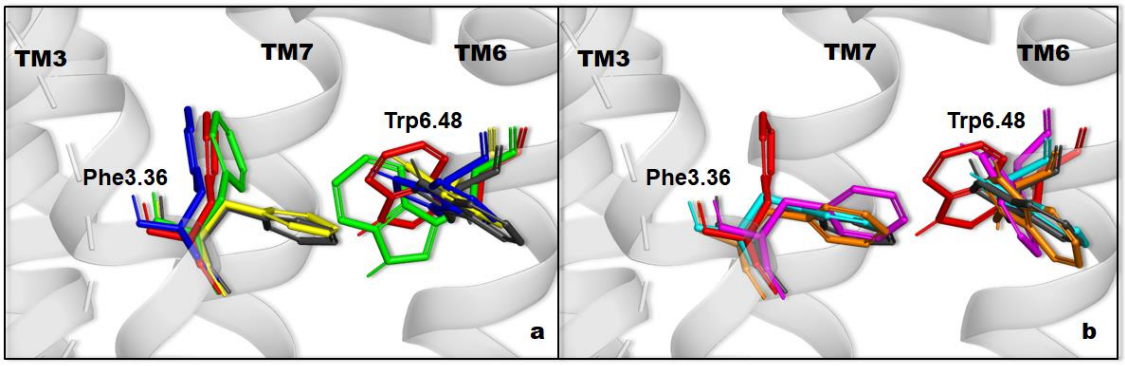

Figure 5.13 Changes in rotameric states of Phe117(3.36) and Trp258(6.48) in the replicate 3 of the CB2-Apo system. *Residues are represented as sticks – initial position is in red and the final position is in grey in both images. (a) Residue conformations within first 100ns of the trajectory. Green – 4ns; Blue – 5ns; Yellow – 20.62 ns. (b) Residue conformations beyond 100ns of the trajectory. Magenta – 167.43 ns; Cyan – 301.70ns; Orange – 316.09ns.*

In the case of the CB2-CP55940 system, the distance between COM of both residues is stable throughout the trajectory. The χ1 angle of both residues range from -40° to -120° throughout the trajectory and no significant change in rotamer angle or distance between the residues is observed.

5.4.6.2 Arginine Cage Ionic Lock

As in the case of CB1 simulations (Section 3.4.6.2), the distance between side chains of residue pairs of Arg131(3.50)-Asp130(3.49) and Arg131(3.50)-Asp240(6.30) was monitored throughout the trajectory, as breakage in the ionic lock between these two residue pairs is indicative of transition into an active state (Section 1.1.3 and 1.3). As aspartic acid has a carboxylic side chain capable of switching the extra pair of electrons via resonance (as explained in Section 3.4.6.2), instead of measuring the distance between basic nitrogen to acidic OH the distance between the immediately preceding carbon atoms in either residue was calculated. In Arg131(3.50) this corresponds to the Cζ atom and in both aspartic acid residues, this corresponds to the Cγ atom. The distances are shown in Figures 5.14 and 5.16.

The distance between side chains Arg131(3.50)-Asp240(6.30) in replicate 1 of the CB2-Apo system shows high fluctuation (Figure 5.14). The same replicate shows a stable value for the distance between the side chains of Arg131(3.50)-Asp130(3.49) implying that the fluctuation in distance between Arg131(3.50)-Asp240(6.30) could be due the increase in separation between TM6 and TM3 than any conformational change in Arg131(3.50). This was confirmed upon visualising the trajectories (Figure 5.15(a)).

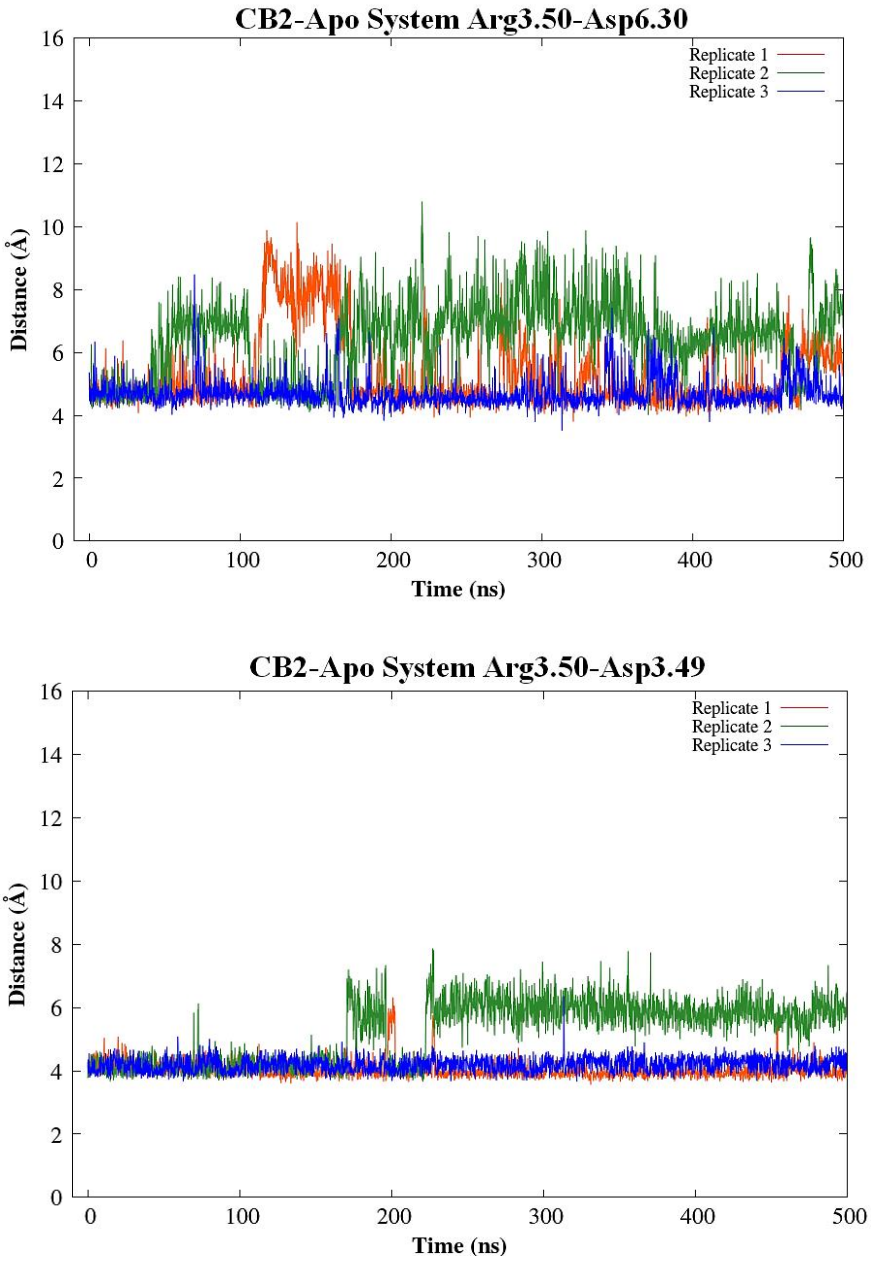

Figure 5.14 Distance between Cζ and Cγ atoms of Arg131(3.50)-Asp240(6.30) and Arg131(3.50)-Asp130(3.49) of the CB2-Apo system. *Replicates 1,2, and 3 of each system are represented by colours orange, green, and blue respectively.*

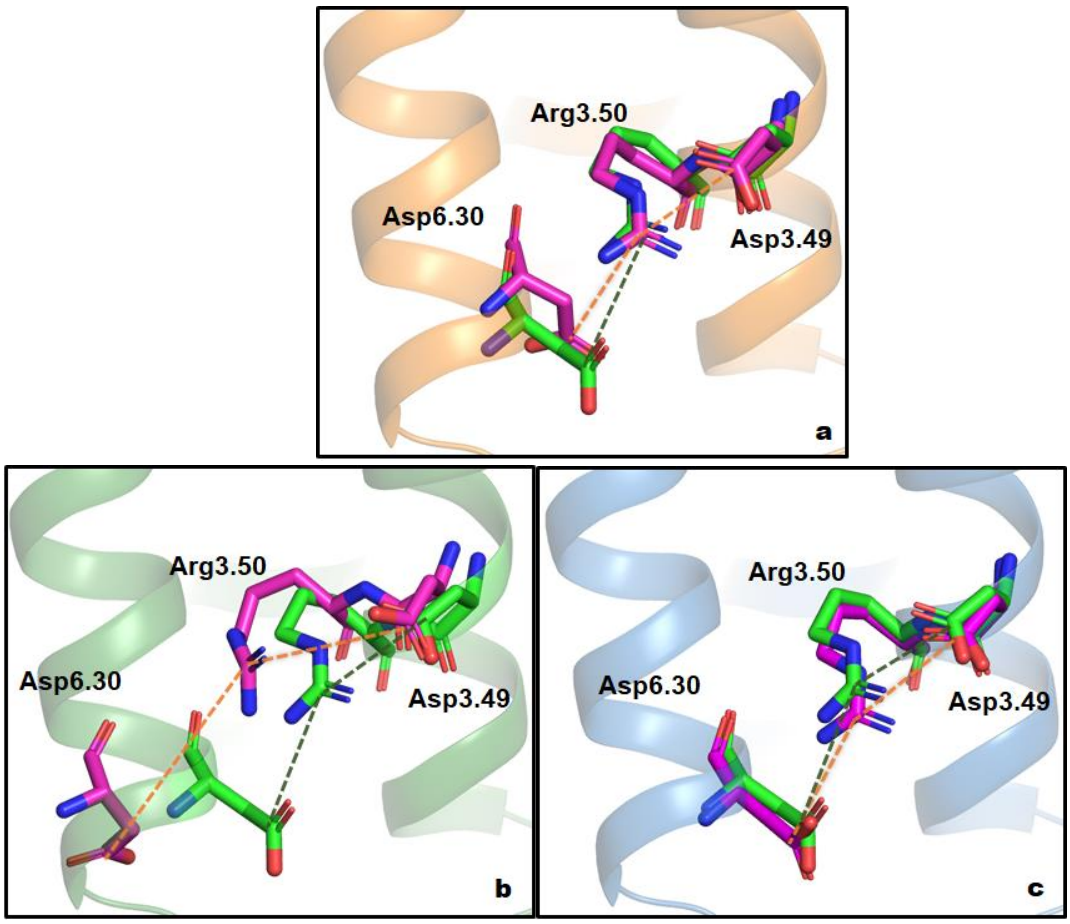

Figure 5.15 Initial (green) and final (pink) conformations of residues involved in the 'ionic lock' in the CB2-Apo system. *(a) Replicate 1 (b) Replicate 2 (c) Replicate 3. Dotted lines link the carbon atoms of residues between which the distances were measured (green – initial state; orange - final state). The cartoon representation depicts the initial state of the receptor.*

In the case of replicate 2, distance between Arg131(3.50)-Asp240(6.30) side chain shows fluctuations as seen in replicate 1. However, unlike replicate 1, the distance between side chains of Arg131(3.50)-Asp130(3.49) shows a minor fluctuation around 200 ns and a sharp increase after 220 ns. This value then stays stable through the rest of the trajectory. This implies that the conformation of Arg131(3.50) also changes after 220 ns aside from the movement of TM6 separating Arg131(3.50) from Asp240(6.30). This was also

confirmed upon visualising the trajectories (Figure 5.15(b)). In replicate 3, both distances between side chains of Arg131(3.50)-Asp240(6.30) and Arg131(3.50)-Asp130(3.49) stay stable throughout the run (Figure 5.15(c)).

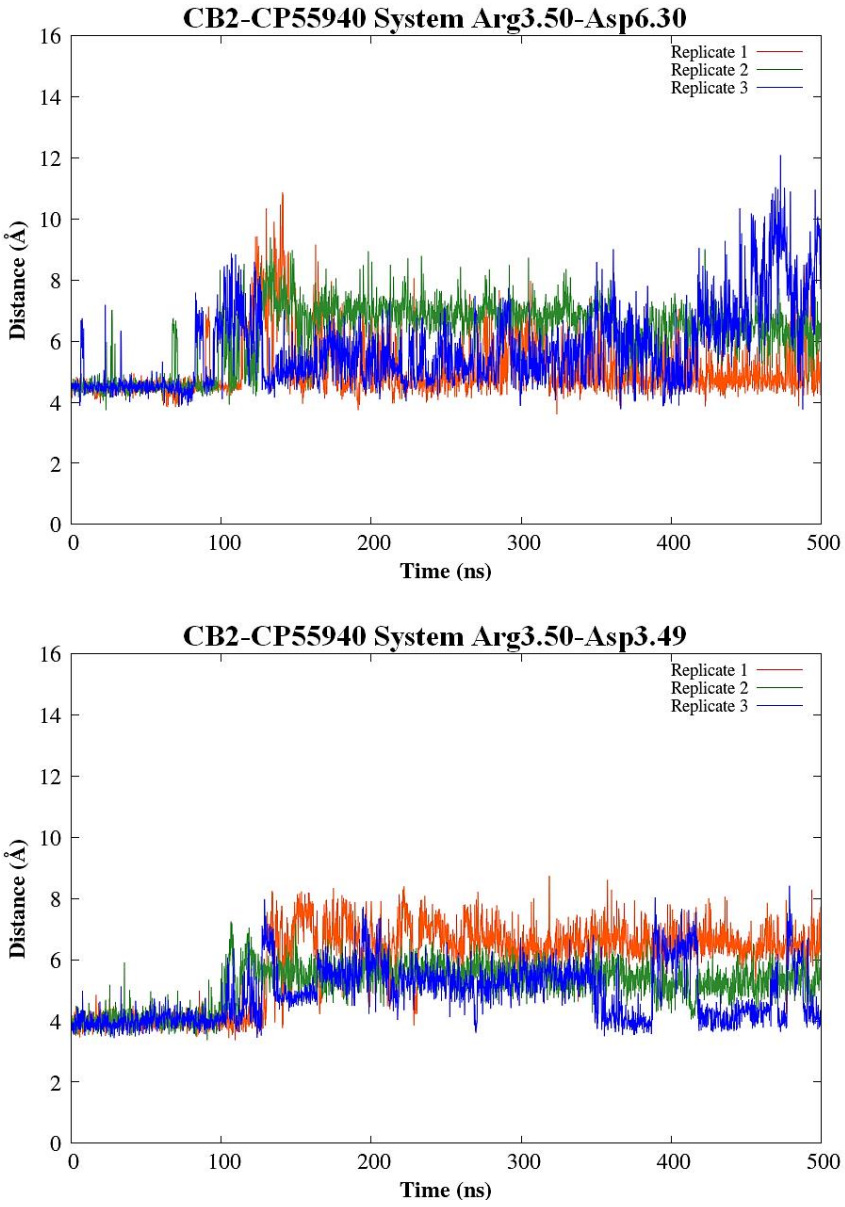

Figure 5.16 Distance between Cζ and Cγ atoms of Arg131(3.50)-Asp240(6.30) and Arg131(3.50)-Asp130(3.49) of the CB2-CP55940 system. *Replicates 1,2, and 3 of each system are represented by colours orange, green, and blue respectively.*

In the case of the CB2-CP55940 system, the distance between either pair of residues is stable until 90 ns in all three replicates (Figure 5.16). Beyond 100 ns varying levels of fluctuation in residue-residue proximity is seen. In replicate 1, the Arg131(3.50)-Asp240(6.30) side chain distance reaches its high around 150 ns after which it subsides to its initial value, but with sporadic fluctuations. In contrast, the distance between side chains of Arg131(3.50)-Asp130(3.49), instantly increases from 4 Å to about 8 Å around 120 ns and is maintained between a 6-8 Å range till the end of the trajectory (Figure 5.17). Replicate 2 shows an increase in distance between Arg131(3.50)-Asp240(6.30) to about 8 Å around 100 ns which gradually decreases as the simulation progresses. However, the increase in the distance between the side chains of Arg131(3.50)-Asp130(3.49) at 120 ns is maintained through the rest of the simulation as in the case of replicate 1. Replicate 3 shows high fluctuation in the side chain distance of Arg131(3.50)-Asp240(6.30), which reaches its maximum towards the end of the trajectory. The distance between side chains of Arg131(3.50)-Asp130(3.49) increases sharply at the same instance as that seen in replicate 1 and replicate 2 and stays stable until 350 ns. After 350 ns, a drop to the initial value is observed. An increase in value is seen around 400 ns – the same time interval around which a drop in the distance between Arg131(3.50)-Asp240(6.30) is seen. The drop and increase in value are seen again towards the close of the simulation, the inverse of which is seen in the distance between Arg131(3.50)-Asp240(6.30). In replicates 1 and 3, an approximately inverse relationship is seen with respect to the proximity of Arg131(3.50) side chain to that of the either Asp residues. This indicates that in both replicates, the conformation of Arg131(3.50) along with the movement of TM6 both play a role in maintaining salt bridge interaction if any is formed.

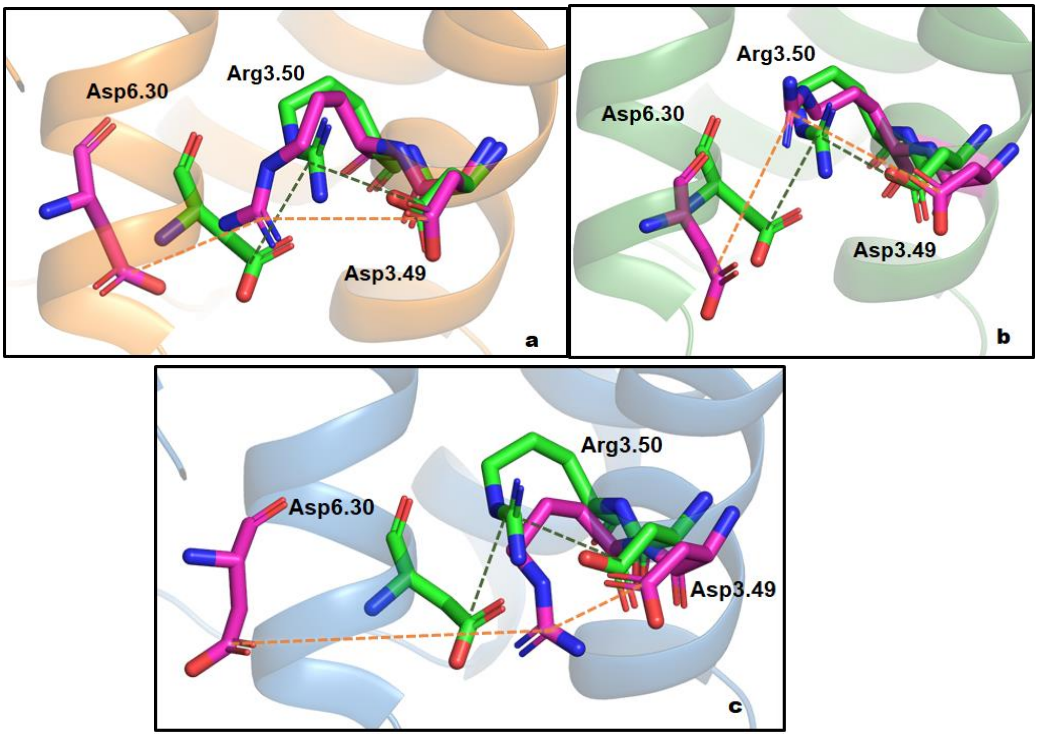

Figure 5.17 Initial (green) and final (pink) conformations of residues involved in the 'ionic lock' in the CB2-CP55940 system. *(a) Replicate 1 (b) Replicate 2 (c) Replicate 3. Dotted lines link the carbon atoms of residues between which the distances were measured (green – initial state; orange - final state). The cartoon representation depicts the initial state of the receptor.*

5.4.7 Formation of Potential Lipid Access Channels

In the CB2-Apo system, two very small circular openings of the order of a few angstroms radius were discovered between TM2 and TM3 after unrestricted equilibration (Figure 5.18). These 'gaps' lead into the orthosteric binding pocket. These openings are not as wide as the access channels seen in the crystal structures of lipid binding receptors (Section 1.3), hence the term 'gaps' has been used to label them. During production simulations, it was noted that transient gaps of a similar size form and disappear predominantly between the EC of TM2-3 and TM1-7. In replicate 2, such a gap was found between TM6-7 midway of their helix length which quickly disappeared in the next 5 ns.

The opening observed between TM1-7 at the end of the simulation in replicate 3 (Figure 5.19), however, slightly resembles an access channel (as seen in crystal structures) – in this conformation, entry via the aqueous layer appears to be blocked.

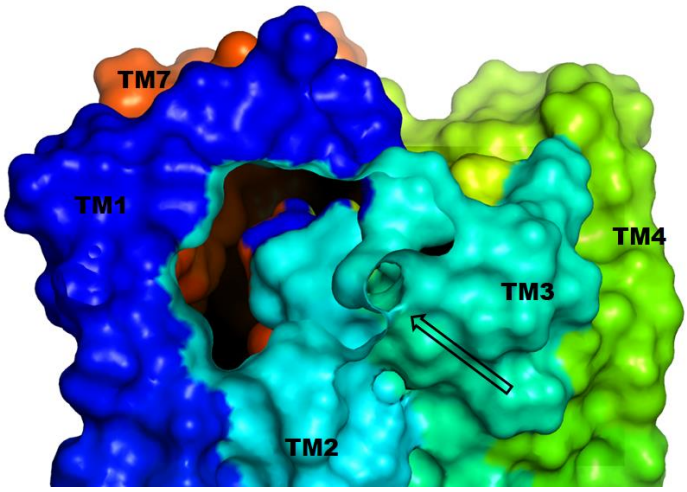

Figure 5.18 CB2-Apo model post equilibration - the 'gap' is marked by the arrow. *TM helices are represented by colours blue through red. Gaps detected using PyMol*[276] *surface view with 1.4 Å as probe radius. TM2 has been partially removed to show the binding pocket*

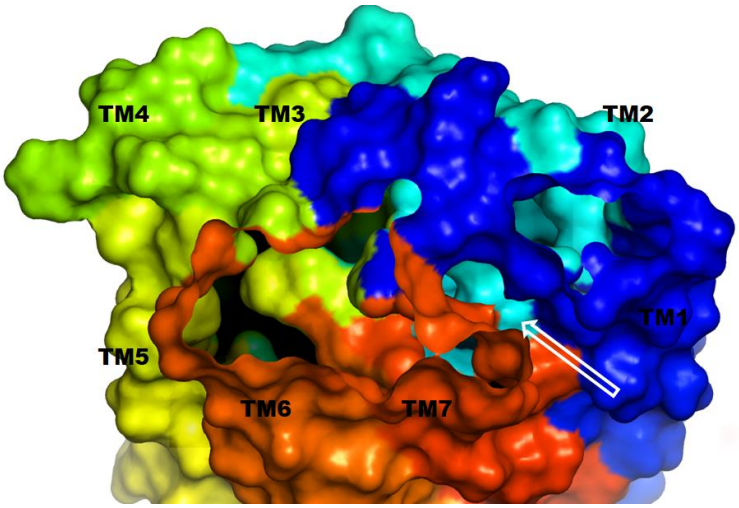

Figure 5.19 CB2-Apo model of replicate 3 after 500 ns simulation - the 'gap' is marked by the arrow. *TM helices are represented by colours blue through red. Gaps detected using PyMol*[276] *surface view with 1.4 Å as probe radius. TM6 and TM7 have been partially removed to show the binding pocket.*

5.5 Discussion

From the RMSF calculations, the most fluctuating regions were identified. Quite similar to the MD simulations of CB1, the ICL3 loops showed the most fluctuation in both the CB2-Apo and ligand-bound. However, the fluctuation shown by the ICL3 of CB2-Apo system is almost twice as that of the one in the agonist system in replicates 2 and 3 (Figure 5.4). From the subsequent RMSD calculations on the TM-BB atoms, it was identified that the helix arrangement did not vary to a significant extent from that observed in the crystal structure.

Considering the essential motions analysed using PC1, it could be observed that TM4 does not exhibit much movement as in the case of CB1 simulations. It is possible that similar to CB1, the TM4 of CB2 aids in forming dimers (Section 3.5); that line of investigation, however, is beyond the scope of the present study. TM1, in the apo system, shows movement towards and away from the binding pocket; however, it is not as far off the helical bundle as seen in CB1 (this could be attributed to the helical arrangement in the crystal structures). This movement seems to be quite important in opening up pathways between transmembrane helices in CB2-Apo structures (Section 5.4.7). In the case of TM2, C-terminal shows much flexibility in movements compared to the rest of the helix; in CB2-Apo the EC end of TM2 moves towards TM1, a movement which also influences potential openings to the orthosteric binding pocket. In the ligand complex structure, it changes its direction of movement towards TM3. The TM6 of CB2 is much less flexible than that of CB1. As seen earlier (Section 1.2.2), the presence of two aromatic residues next to each other in the CWFP motif largely restricts the bending of TM6. Instead, the upward or downward movement of the helix is observed, predominantly. TM7 is the most

flexible helix amongst all, similar to that of CB1. PC1 analysis revealed that TM7 shows significant helix unwinding around the NPXXY motif. In the CB2-Apo system, TM6 and TM7 show synergy in their PC1 motions; in the ligand-bound structure, however, TM7 shows differential motions along its helix length.

Upon inspecting the aromatic toggle switches, it can be seen that the residues in the CB2-Apo system assume conformations that vary greatly compared to that of the ligand-bound system. In the ligand-bound system, the conformation of the two residues after unrestricted equilibration (as observed in Section 5.4.1.1) remains stable throughout the production simulation. Aromatic interaction, if any formed, between the rings of Phe117(3.36) and Trp258(6.48) would be edge-face due to their perpendicular arrangement. In CB2-Apo system, despite the apparent rigidity of TM6 backbone, unrestrained equilibration led Trp258(6.48) side chain to assume a conformation similar to that observed in active CB1 structures (Section 5.4.1.1 and Figure 5.13). Owing to the flexible nature of the system, the rotameric angles were observed to change rapidly after the first few changes (as detailed in Section 5.4.6.1). Phe200(3.36) does not exhibit a significant change in conformation after bending down into the binding pocket. Interestingly, this conformation of Phe3.36 is quite similar to the one seen in inactive CB1 crystal structures. On the contrary, the inactive CB2 crystal structure has the Phe117(3.36) facing towards the ligand akin to that seen in the active CB1 crystal structure (Section 1.3). In the case of CB2-CP55940, much like CB1-AM841 simulations, no significant changes in the conformation of toggle switch residues were observed.

Considering the residues involved in the ‘ionic lock’ between TM3 and TM6, the change in conformation of Arg131(3.50) is a differentiating factor between the CB2-Apo

and CB2-CP55940 systems. In the former, Arg131(3.50) remains in close contact with Asp130(3.49) throughout the trajectory in 2 out of 3 replicates; the fluctuations in the distance between Arg131(3.50) and Asp240(6.30) is due to the increase in distance between the IC regions of TM3 and TM6 (as seen in PC1 motions). In the agonist bound system, Arg131(3.50) elongates from the folded conformation in 2 out of 3 replicates, as evident from the increase in distance between Arg131(3.50) and Asp130(3.49). In addition, the distance between the IC of TM3 and TM6 also increases accompanied by fluctuations as evident from Figure 5.15 (a) – leading to a separation of Arg131(3.50) and Asp240(6.30). The conformational change in Arg131(3.50) is comparable, if not exactly akin to, the one seen in active CB1 crystal structures. In all three active CB1 structures known till date, Arg214(3.50) extends out into the binding pocket and is proximal to neither Asp213(3.49) or Asp338(6.50) (Section 1.3). In 6N4B, where the active CB1 is co-crystallised with $G_{\alpha i}$ protein, Arg214(3.50) extends into the G protein binding region and is proximal to the C-terminal of α5 helix of the $G_{\alpha i}$[104]. Though an exact replication of such a conformation is not seen in the results reported, it can be suggested from the changes in distance between the residue side chains that Arg131(3.50) might be heading towards such a conformation.

Analysing the ionic lock and twin toggle residues for the CB2-Apo model, trends similar to that seen in CB1-Apo simulations emerge. While the distance between Arg131(3.50)-Asp240(6.30) shows fluctuations reaching a maximum of 10 Å, the distance between Arg131(3.50)-Asp130(3.49) stays constant except in replicate 2 where an increment of 2 Å was observed. Recalling Section 3.4.6.2, CB1-Apo showed similar trends with separation of Arg131(3.50)-Asp240(6.30) and retaining the proximity between

Arg131(3.50)-Asp130(3.49). β2AR and M2 have also been reported to show fluctuations breaking and reforming the ionic lock[280,281]. Furthermore, CB2-Apo simulations also exhibit diversity in the conformation of toggle switch residues similar to apo simulations of M2, A2AR, and S1P1[277,280,282]. Despite, the fact that protein backbone shows a minimal change from crystal structure through the trajectory, changes in the side chain conformations of conserved residues imply that CB2 might also assume a conformation unlike an inactive or an active one, much like CB1 and other receptors mentioned herein. However, an active CB2 structure is necessary to confirm the hypothesis.

The orientation of Tyr299(7.53) was also monitored by visualising the trajectories. The residue assumes two major conformations : (a) pointing up into the binding pocket and (b) pointing towards TM5. The inactive crystal structure had the tyrosine pointing towards TM5, yet another feature that was seen in active CB1 crystal structures (Section 1.3). As seen in Section 1.1.3, (a) represents an intermediate conformation, and is also seen in CB1 inactive crystal structures. However, in both conformations, Tyr299(7.53) was fully engaged in a hydrophobic residue network as mentioned in the same section in Chapter 1. Given the seemingly inverse relationship between CB1 and CB2 inactive structures, more analysis and further study is required on the conformation of Tyr7.53 in a fully active CB2 structure (or model).

Concerning the changes in ligand conformation, three different kinds were observed in the course of the production run. The initial binding conformation, as stated earlier is close to that seen in the docking of CP55940 (6) by Li *et al*. into the crystal 5ZTY[127]. The major difference is that the aliphatic tail in the initial docking reported here is rather perpendicular to the pocket down into the pocket. Li *et al.* observed a V-shaped

docking orientation which is much closer to the agonist conformations seen in the active CB1 crystal structures. The authors also reported after 200 ns of MD simulation, the observed ligand conformation was stable. Such a conformation was also observed by Diaz *et al.* in an MD study of CP55940 (6) bound to inactive CB1 model in a POPC bilayer and a 1,2-dioleoyl-sn-glycero-3-phosphoglycerol bilayer[235]. The CB1 model in the complex exhibited features of activation such as the separation of the ionic lock and the turn of the of TM6 helix away from the binding pocket thus breaking the aromatic stacking between toggle switch residues. From the findings reported in this chapter, replicate 1 exhibited such a conformation about halfway through the trajectory (Figure 5.7), which did not change through the rest of the trajectory. This conformation was also suggested by NMR experiments to be stable and most energetically favoured[291]. In replicate 2, the ligand assumed a different folded conformation whereby the aliphatic tail faced down vertically between TM3 and TM6 with the A and C rings still being perpendicular to the pocket (Figure 5.8). The ligand, however, returned back to its original conformation after about 50 ns. A similar conformation was also observed in the MD study with CB1 by Diaz *et al.*[235]; the authors, however, suggested that such a conformation may not be necessary to trigger activation and could be a "consequence of inherent system flexibility". In replicate 3, the ligand remained in the vertical position (observed in the initial docking (Figure 5.1)), occupying the pocket between TM2-3-6-7 for the entire simulation period. No significant positional changes of the ligand were seen in the trajectory either. This conformation of the ligand was observed by Feng *et al.* in a 50 ns MD simulation study of CP55940 (6) docked to CB2 model generated using β1AR crystal structure (PDB ID 2Y00) as template[126]. In the study by Feng *et al.*, CP55940 (6) docked perpendicular to the binding

pocket in the region between TM3-6-7; at the end of 50 ns, it had moved to the region between TM5-6-7 adopting a rather slanted conformation as seen in the docking conformation reported in the current study.

Throughout the trajectory, the ligand in both replicates 1 and 2 forms hydrogen bonds with Ser90(2.60), Tyr25(N-term), His95(2.65), and residues from ECL2 such as Leu182 and Phe183. It also forms hydrophobic interactions with Phe87(2.57), Phe91(2.61), Phe94(2.64), Ile110(3.30), Val113(3.32), Thr114(3.33), Phe117(3.36), Tyr190(5.56), Trp194(5.43), Trp258(6.48), Val261(6.51), and Cys288(7.42). Most of the ligand-protein hydrophobic contacts and hydrogen bonds observed in the work reported here agree with previous modelling studies by Diaz *et al.* and Feng *et al.*[126,235]. However, a hydrogen bond with Ser285(7.39), suggested to be important for CP55940 (6) binding with CB2[126], was not observed. In the current study, the oxygen atom-containing groups in A and C rings of the ligand interact with residues of ECL2, N-terminus and TM2 but are not in the vicinity of Ser285(7.39) in all three replicates.

5.6 Conclusion

In this chapter, the possible conformations of both CB2-Apo and CB2-CP5540 systems were explored. While an overall change in RMSD with respect to transmembrane helix backbone was not observed in either model, significant changes were observed in conserved residue motifs. CB2-Apo models in all three replicates developed transient gap-like openings into the orthosteric binding pocket between TM2-3 and TM1-7 at varying times. The effect of lipids on the protein structure could be an influencing factor for the formation of such 'channels'[104]; that is, however, warrants further exploration. Three different types of ligand orientations – two folded and one linear - were observed in the

simulation of the CB2-CP55940 complex. While the conformation of the ligand is in accordance with the available literature, a hydrogen bond with Ser7.39 was not seen in any replicates. It could be suggested that the absence of such a hydrogen bond hindered the protein from transforming into a fully active state. However, the inactive CB2 sharing structural commonalities with active CB1 structures opens up questions regarding the active conformation of CB2. Longer simulation times of inactive CB2 bound to different agonists might hence help in identifying a potentially active state for CB2.

6 Repurposing Non-Cannabinoid Ligands for Use at Cannabinoid Receptors

6.1 Introduction

Aside from endo-, phyto- and synthetic cannabinoids, ligands of other chemical classes have been reported to act on cannabinoid receptors (as seen in Section 1.5). These ligands, hence, possess the potential to be repurposed to treat physiological conditions mediated by CB1 and CB2 (Section 1.2.5). Repurposing is the process of identifying novel usages for existing drugs outside the scope of their original medical indication[292]. Drug repurposing has two major benefits - (a) the risk of failure is low for repurposed drugs as they have already passed the necessary clinical tests and have been proven to be functional at a certain dosage in humans, and (b) the time taken to repurpose a drug would be shorter than to develop a drug *de novo*. In this regard, the interaction of selected non-cannabinoid ligands at CB1 and CB2 will be investigated. This chapter has two parts: the first part reports the testing of a selection of non-cannabinoid drugs against human CB1 and CB2 receptors for agonist activity using [^{35}S]GTPγS binding assay. The tested compounds currently used for various indications were selected from the World Health Organisation (WHO) Essential Medicines database [293].

Aside from experimental techniques, *in silico* docking has also been suggested to be one of the approaches in drug repurposing[294]. Indeed, it was via high-throughput screening that the anti-parasitic drug mebendazole was found to structurally inhibit vascular endothelial growth factor 2, which is an angiogenesis mediator; experimental data later confirmed the inhibitory activity[295]. In a similar direction, a set of non-cannabinoid

ligands that have been reported to show activity at CB1 and CB2 were docked to models of the same to identify their binding mode. This forms the second part of the chapter. Some of these ligands, such as the SERMs, were described in Section 1.4. Four of five classes of SERMs seen in Section 1.4 with varying affinities at CB1 and CB2 receptors and one novel SERM (Ridaifen-B (41)) were chosen for the study. In addition to the SERMs, AM404 (33) and fenofibrate (38) (Table 6.2) were also considered for docking studies. AM404 (33), a metabolite of acetaminophen, acts as an agonist at CB1 and CB2[296]. Post deacetylation, acetaminophen forms 4-aminophenol that conjugates with arachidonic acid in the central nervous system to form AM404 (33)[296]. Similarly, fenofibrate (38)- a peroxisome proliferator-activated receptor-α agonist has been reported to act as an agonist at CB2 and as a NAM at CB1[297]. Molecular docking was performed on three models – inactive CB1 (CB1), active CB1 (CB1*), and inactive CB2 (CB2). The variations in the interaction of each set of ligands with CB1 and CB2 were identified and compared across the receptors. As explained in Section 1.4, the overlapping properties of SERMs and cannabinoids have led to the proposal to develop novel cannabinoids based on tamoxifen[208]. In that direction, the screening (or) docking work reported here can potentially lead to the development of new scaffolds in the area of cannabinoid drug design.

6.2 Aims

1. To screen for agonist activity of selected drugs against CB1 and CB2.
2. To perform docking studies on non-cannabinoid ligands that show activity at CB1 and CB2 and analyse interactions.

6.3 Testing non-cannabinoid ligands at cannabinoid receptors

6.3.1 Selection of ligands to test

Table 6.1 gives a list of the ligands from the WHO essential medicines drug database. Further details regarding the ligands and their usage are given in Table VI-1, Appendix 6.

Ligands	Structure
Carbenoxolone (26)	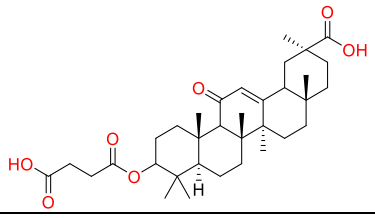
Dexamethasone (27)	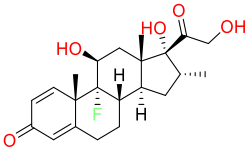
Haloperidol (28)	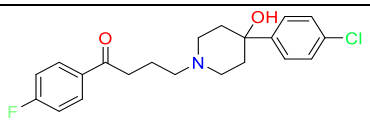
Metoclopramide (29)	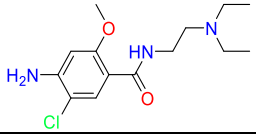
Prednisolone (30)	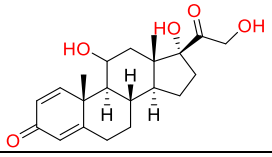
Prednisolone hemisuccinate (31)	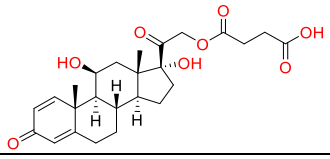
Pregnenolone acetate (32)	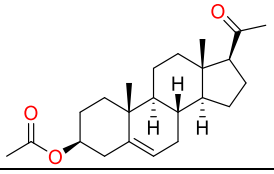

Table 6.1 Ligands tested against cannabinoid receptors

The criteria for selecting the ligands to be screened were that they should be

1. Primarily exhibiting activity at a receptor/enzyme other than those in the ECS :
2. Possessing structural similarity with cholesterol (or) reported to indirectly influence the ECS.

As seen in Section 1.2.1, cannabinoids are lipophilic in nature. Cholesterol helps in the membrane insertion of anandamide, and its transport to other receptors[298]. Cholesterol also regulates the activity of those receptors such as serotonin 5HT-3 receptor, vanilloid receptor subtype 1, and L-type Ca^{2+} channels[298]. Thus, a structural similarity with cholesterol was considered as a criterion. In Section 1.4, it was mentioned that there are drugs which influence the ECS in an indirect manner; such compounds were also tested for activity at CB1 and CB2 as the pharmacological effects of such an interaction (if present) are already known.

6.3.2 Working Mechanism of [^{35}S]GTPγS assay

The [^{35}S]GTPγS binding assay is commonly used to compare agonist potency and efficacy of ligands at GPCRs. It was first employed with a purified receptor and G protein systems in phospholipid vesicles using β-adrenergic receptors[299]. The working principle of the assay can be best described using Figure 6.1.

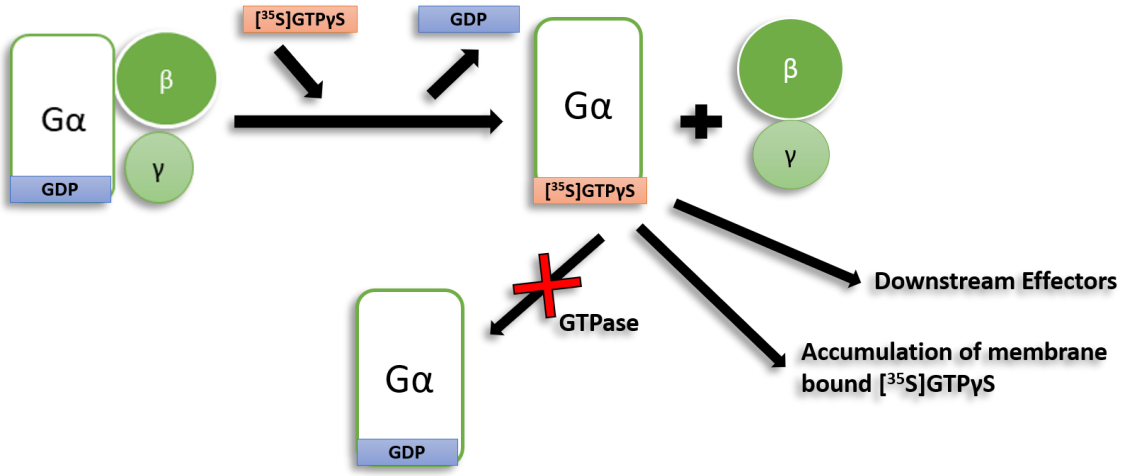

Figure 6.1 Principle of [35S]GTPγS Assay. *In the presence of [^{35}S]GTPγS, exchange of [^{35}S]GTPγS for GDP occurs, but the GTPase activity on the G_a subunit is unable to hydrolyse G_a-bound [^{35}S]GTPγS, which accumulates during the assay period.*

This assay measures the level of G protein activation following agonist occupation of a GPCR. As described in Section 1.1.4, during G protein activation, GDP is released from the Gα subunit and is replaced by GTP. The Gα-GTP complex then separates from Gβγ and initiates a cascade of downstream signalling. Signalling is terminated by GTPase action that hydrolyses GTP to GDP, thus reforming the G protein heterotrimer complex. In this assay, [^{35}S]GTPγS replaces the endogenous GTP to form [^{35}S]GTPγS-Gα species. The γ-thiophosphate bond is resistant to hydrolysis by GTPase and hence prohibits the restoration of the heterotrimer. This accumulated [^{35}S]GTPγS-Gα can be measured by counting the amount of [^{35}S]-label incorporated. These data can be converted to an amount of [^{35}S]GTPγS bound/mg membrane protein, or as fold/percentage increase over basal binding or a percentage of the effect produced by a known high efficacy agonist[129]. The assay is suggested to suit $G_{\alpha i/o}$ coupled receptors as $G_{\alpha i/o}$ has a higher rate of nucleotide exchange and is more abundant compared to other G proteins; this registers a higher signal

to noise ratio[129]. Hence, this assay is suited to test for agonist activity at CB1 and CB2, since both signal predominantly via $G_{\alpha i}/_{o}$ receptors (Sections 1.2.2 and 1.2.3).

6.3.3 Materials and Methods

6.3.3.1 Ligand preparation

All the ligands used in the study were purchased from Sigma Aldrich (St. Louis, MO, USA) (Carbenoxolone (26): C4790, Dexamethasone (27): BP811, Haloperidol (28): H1512, Metoclopramide (29): M0763, Prednisolone (30): P6004, Prednisolone hemisuccinate.sodium salt (31): P4153, Pregnenolone acetate (32): P49902). A stock solution of 10 mM of each was prepared using 100% ethanol. Bovine Serum Albumin (BSA), Tris-HCl, GTPγS tetralithium salt, and GDP sodium salt were also purchased from Sigma Aldrich. NaCl and $MgCl_2.6H_2O$ were purchased from Fisher Scientific (Loughborough, Leicester, UK). CP55940 (6) purchased from Tocris Bioscience (Bristol, UK) was used as the control drug. [^{35}S]GTPγS (250 µCi) and UltimaGold^{TM} XR aqueous scintillation cocktail were purchased from PerkinElmer (Boston, USA).

6.3.3.2 Binding Assay

Ligand stock solutions were diluted using drug buffer to get a concentration of 10^{-4} M; the drug buffer was made up of 2.5 mg/ml BSA in Tris-NaCl buffer at pH 7.4 at 30 ℃. Aliquots of [^{35}S]GTPγS initially prepared by diluting stock [^{35}S]GTPγS 100-fold with an aliquoting buffer (10 mM Tricine and 10 mM dithiothreitol at pH 7.6) were provided by Dr Wafa Hourani from the School of Pharmacy, University of Nottingham, United Kingdom. The [^{35}S]GTPγS solution was diluted to ~0.2 nM using assay buffer. The assay buffer was made of 50 mM Tris, 10 mM $MgCl_2.6H_2O$, 100 mM NaCl, and 0.2 mg/ml BSA at pH 7.4 at 30 ℃. Membrane fractions of Chinese Hamster Ovary (CHO) cells stably

expressing CB1 (CHO-CB1) and CB2 (CHO-CB2) used in the assay were also prepared by Dr Hourani. The membrane fractions were diluted to a concentration of 250 μg/ml in assay buffer. The membrane fraction was incubated with 500 μM GDP at 30℃ for 20 min (with gentle shaking) to allow pre-coupling of GDP with Gα. Meanwhile, a reaction mixture was set up with 700 μl of assay buffer, 100 μl of the ligand dilution, and 100 μl of [^{35}S]GTPγS solution. Non-specific binding was determined using 10^{-5} M unlabelled GTPγS (diluted with drug buffer). The total (basal) binding was determined using 100 μl drug buffer only. To both tubes measuring total and non-specific binding, 700 μl assay buffer and 100 μl [^{35}S]GTPγS solution were also added. After 20 min incubation at 30 ℃, 100 μl of the membrane fraction was added to all the samples; this brought the final volume of the reaction mixture to 1 ml. The final concentration of the membrane was 25 μg/ml and that of the ligands was 10^{-5} M. All test tubes were vortexed and again incubated at 30℃ for 120 min. The reaction was terminated by rapid filtration through a Whatman GF/B filter paper under vacuum (using a Brandel M24R Cell Harvester) and washed three times with cold distilled water. The radioactivity of the filters was detected in UltimaGold™ XR aqueous scintillation cocktail with Packard Tricarb 2100TR liquid scintillation counter. A 5 min counting period was applied and values in counts per minute (CPM) were obtained. The binding assays were performed in triplicate and repeated at least five times per ligand.

6.3.4 Data Analysis

GraphPad Prism version 8.2.0 for Windows was used to analyse the results from binding assay[300]. The CPM values hence obtained for each ligand (i.e. control and test ligands) were normalised against that of the total binding. A one way ANOVA test was then performed with a 95% confidence interval. Dunnett's multiple comparison test was

used to identify those ligands that show a significant activity from the results of the ANOVA.

6.3.5 Results

From the results obtained after the one way ANOVA test (Figure 6.2), it can be seen that none of the test ligands showed significant activity at both CB1 and CB2, in comparison to the positive control (as indicated by the **** symbol).

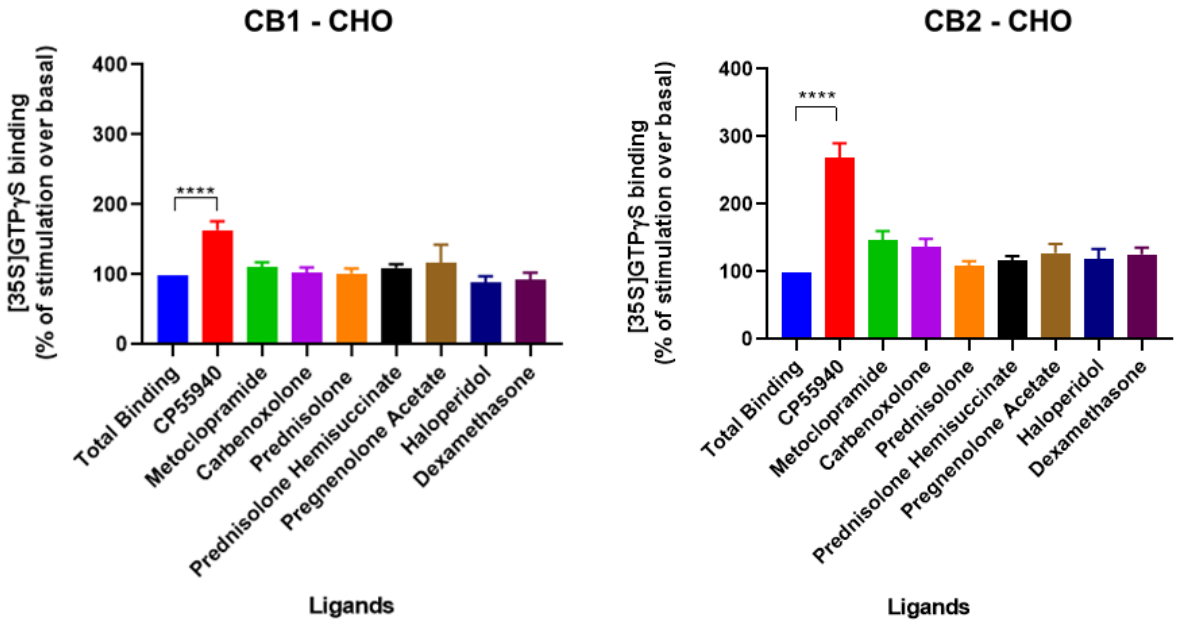

Figure 6.2 Effect of selected ligands (Table 6.1) on [35S]GTPγS binding in CHO-CB1 and CHO-CB2 membranes. *Data are mean ± SEM of five to eight individual experiments performed in triplicates expressed as a percentage of binding stimulation over GDP levels. ****$P \leq 0.0001$ *compared to the corresponding basal binding using one-way ANOVA followed by Dunnett's multiple comparisons test with a confidence level of 95%. Plot generated using GraphPad Prism*[300].

6.3.6 Discussion

The results of the [^{35}S]GTPγS assay reveal that none of the chosen ligands shows significant agonist activity at either CB1 or CB2 receptors. Carbenoxolone (26), prednisolone (30) and prednisolone hemisuccinate (31) have not been reported for any interaction, either directly or indirectly, with the cannabinoid receptors; they were chosen for their structural similarity with cholesterol. Hence, it can be said that for a ligand to show agonist activity at cannabinoid receptors structural analogy with cholesterol is not a critical factor. Other ligands have been reported to have an indirect influence on the ECS. Dexamethasone (27), a corticosteroid, helps treat motion sickness by acting on glucocorticoid receptors. These receptors regulate the transcription and translational process for CB1, which in turn regulates emesis (Section 1.2.5)[301]. Haloperidol (28), too, influences the ECS indirectly. Subchronic administration of haloperidol (28) was shown to increase CB1 density in rat brains[302]. In the case of dexamethasone (27) and haloperidol (28), it is now clear that an alternative pathway is responsible for their influence on ECS. Metoclopramide (29) (acts mainly at dopamine D2 receptors), which have been demonstrated to form heterodimers with CB1[303]. Whether metoclopramide (29) interaction with the D2 receptor influences the formation of the heterodimer goes beyond the scope of this study. But it's inactivity at CB1 eliminates the possibility of metoclopramide (29) acting on two different receptors at the same instance. Pregnenolone (32) has been shown to act as a NAM in a probe-dependent manner at CB1[304]; accordingly, no agonist activity was found for pregnenolone acetate (32) at CB1. Absence of agonist activity of pregnenolone acetate (32) at CB2 suggests the possibility of it acting as an endogenous

antagonist or as an allosteric modulator. This, however, has to be confirmed via further detailed experimentation.

6.4 *In silico* docking studies of ligands that interact with CB1 and CB2

6.4.1 Materials and Methods

Ligands used for docking studies were selected after a literature search for non-cannabinoid compounds that show activity at CB1 and CB2. They are given in Table 6.2. The nature of activity and K_i values of the ligands at CB1 and CB2 receptors are given in Appendix 6 (Table VI.2). The selected ligands were downloaded from the PubChem database[250] and subjected to preparation using LigPrep[305] as explained in Section 2.4.2.1. Possible protonation states and tautomeric states at pH 7.0+/-2.0 were generated using Epik[306]. The state with the least ionisation penalty was used for docking.

The protein models generated from 5TGZ (CB1), 5XR8 (CB1*), and 5ZTY(CB2) (as seen in Section 2.4.1) were used for docking. Grid generation and ligand docking were performed as mentioned in Section 2.4.2.1. The tools used for docking were from the Schrodinger Suite (version 2018.2 for CB1 and version 2019.1 for CB2). Ligands were docked onto the prepared models in Standard Precision mode. 20 poses per ligand were produced and the top-scoring pose in terms of GlideScore was selected for analysis. As fenofibrate (38) acts as a NAM at CB1 receptors at higher concentrations, it was docked only to CB2 model[297].

Ligands	Structure	Ligands	Structure
AM404 (33)	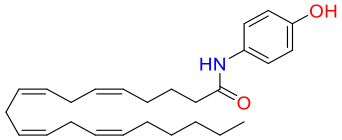	Lasofoxifene (39) [c]	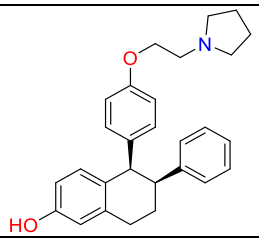
Bazedoxifene (34) [a]	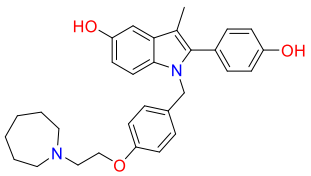	Raloxifene (40) [d]	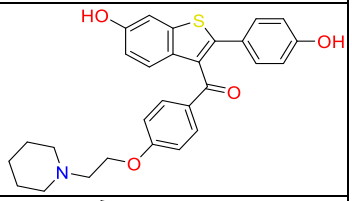
E-4-OH-tamoxifen (35) [b]	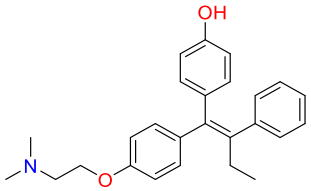	Ridaifen-B (41)	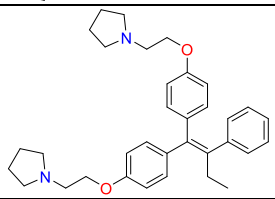
E-endoxifen (36) [b]	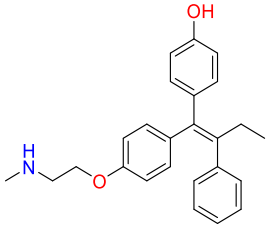	Z-4-OH-tamoxifen (42) [b]	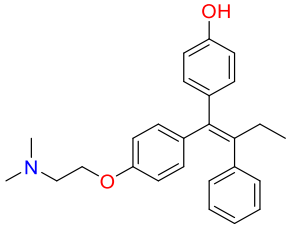
E-tamoxifen (37) [b]	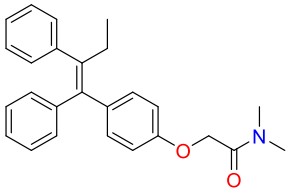	Z-endoxifen (43) [b]	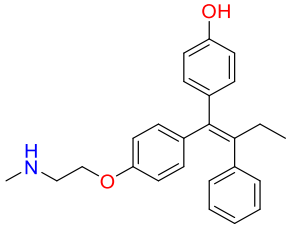
Fenofibrate (38)	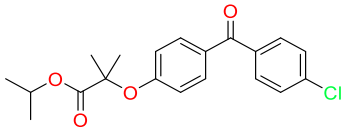	Z-tamoxifen (44) [b]	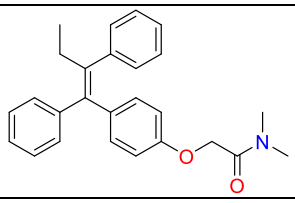

Table 6.2 Compounds with reported ability to bind to CB1 and CB2. *Selected classes of SERM include: [a]indole, [b]triphenylethylene, [c]tetrahydronaphthalene, and [d]benzothiaphene.*

6.4.2 Results

The criteria and cut-off distances for interactions reported herein are based on the visualisation tool Maestro (version 2019.2) from Schrodinger Suite[307]. As discussed previously (Section 1.3), cannabinoid receptors are lipid-binding receptors and commonly form hydrophobic interactions and van der Waals interaction with their ligands. Since van der Waals interactions are often transient and comparatively weak, those interactions other than van der Waals were analysed and have been reported in the forthcoming sections. The terms HBA and HBD have been used to represent hydrogen bond acceptors and hydrogen-bond donors, respectively. For ease of analysis, SERMs have been split into three groups: E-tamoxifen (E-Tam) (37) and metabolites [E-4-OH-tamoxifen (35) (E-4-OH-Tam) and E-endoxifen (36) (E-End)], Z-tamoxifen (Z-Tam) (44) and metabolites [Z-4-OH-tamoxifen (Z-4-OH) (42) and Z-endoxifen (Z-End) (43)], and bulky SERMs (i.e. those with a molecular weight greater than tamoxifen).

6.4.2.1 Binding modes of non-cannabinoid ligands docked into CB1 and CB2 receptors

6.4.2.1.1 CB1 model

1. **SERMs**

In the inactive model, most of the bulky SERMS (bazedoxifene (34), lasofoxifene (39), raloxifene (40), and ridaifen-B (41)) exhibited a horizontal binding pose (Figure 6.3(a)). The aromatic groups face TM1 and are arranged in a vertical fashion with the piperidine group facing TM5. All the four ligands do not interfere with the stacking between the toggle switch residues Phe200(3.36) and Trp356(6.48) but form an aromatic hydrogen bond with Trp356(6.48) (HBD). Bazedoxifene (34), lasofoxifene (39), and

raloxifene (40) also form an aromatic hydrogen bond with backbone oxygen of Ser383(7.39) (HBA) and Gly166(2.53) (HBA). Bazedoxifene (34), lasofoxifene (39), and ridaifen-B (41) form a π-cation interaction with Trp279(5.43) with the nitrogen atom of their piperidine moiety.

Considering the E-isomer of tamoxifen (E-Tam) (37) and its metabolites, a vertical orientation is observed with the aromatic benzene pointing down into the binding pocket (Figure 6.3(b)). All three ligands form edge-face π-π stacking interactions with Phe102(N-terminus (N-term)) and Phe170(2.57), and an aromatic hydrogen bond with backbone oxygen of Ser383(7.39) (HBA). The protonated nitrogen at the piperidine moiety forms hydrogen bonds and (or) or ionic interactions with Ile267 (E-4-OH-Tam (35) and E-Tam (37)) or Asp104 (E-End (36)). The OH of the phenyl group in E-4-OH-Tam (35) and E-End (36) (HBA) form aromatic hydrogen bonds with Trp356(6.48). The aminoalkyl group of E-4-OH-Tam (35) and E-Tam (37) form a hydrogen bond with backbone oxygen of Ile267(ECL2)(HBA).

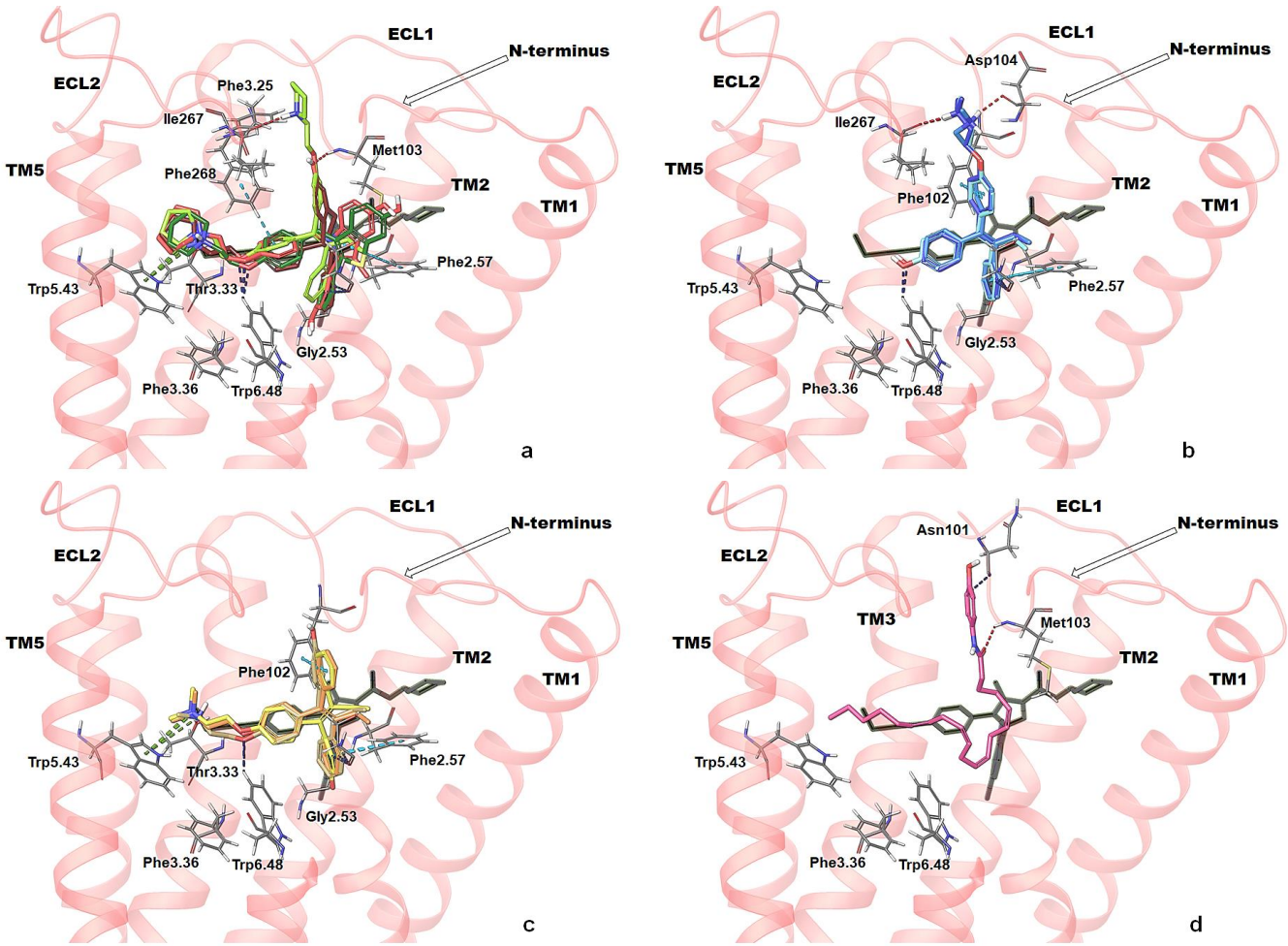

Figure 6.3 Binding modes of ligands docked to an inactive CB1 model. (a) Bulky SERMs*: Red - Bazedoxifene (34), Brown – Lasofoxifene (39), Lime - Ridaifen-B (41), and Dark green - Raloxifene (40)* **(b) E-tamoxifen and isomers**: *Light blue – E-4-OH-tamoxifen (35), Blue – E-endoxifen (36), and Deep blue – E-tamoxifen (37)* **(c) Z-Tamoxifen and metabolites**: *Yellow – Z-4-OH-tamoxifen (42), Gold – Z-endoxifen (43), and Orange – Z-tamoxifen (44)* **(d) AM404 (33)**. *In each figure, the cognate ligand AM6538 (18) is depicted in black tracing. Residues are depicted as thin sticks. TM 6 and 7 have been truncated for purposes of picture clarity. Blue, green, red, and black dotted lines represent π-π, π-cation, hydrogen bond and aromatic hydrogen bonds, respectively.*

The Z-isomer of tamoxifen (Z-Tam) (44) and its metabolites show a horizontal orientation upon docking as opposed to their E-counterparts (Figure 6.3(c)). Similar to the bulky SERMs, the aromatic groups arranged in a vertical fashion facing TM1 while the

aminoalkyl group points to TM5. All three ligands show almost the same binding interactions: edge-face π-π stacking with Phe102(N-term) and Phe170(2.57), π-cation interaction with Trp356(6.48), hydrogen bond with the side-chain oxygen atom of Thr197(3.33) (HBA) via its protonated nitrogen at the aminoalkyl moiety and aromatic hydrogen bond with the backbone oxygen atom of Ser383(7.39)(HBA) via hydrogen atom of its phenol group. Z-Tam (42) and Z-End (43) also form aromatic hydrogen bonds with Trp356(6.48). The phenol group of E-4-OH-Tam (35) faces down into the pocket and the benzene is pointed towards the N-terminus while their positions are inversed in the docking of Z-End (43).

2. AM404

As depicted in Figure 6.3(d), AM404 (33) adopts an L-shaped pose with the aromatic portion of the ligand facing TM1 and the aliphatic chain orientated towards the gap between TM4 and TM5. The oxygen atom in the aromatic portion of the molecule forms a hydrogen bond with backbone nitrogen of Met103(N-term) (HBD).

6.4.2.1.2 CB1* model

1. SERMs

The bulky SERMs all exhibit a folded conformation in the CB1* model (Figure 6.4(a)) as opposed to the horizontally extended conformation seen in the CB1 model poses (Figure 6.3(a)). Bazedoxifene (34), raloxifene (40) and ridaifen-B (41) all show edge-face π-π stacking interaction with Phe268(ECL2) via the central benzene group and π-cation interaction with Trp279(5.43) via the nitrogen atom of piperidine group. They also form edge-face π-π interactions with aromatic residues from TM2 such as Phe170(2.57), Phe174(2.61), and His178(2.65). Although interacting with different groups on different

bulky SERMs, the backbone oxygen of Phe108(N-term) (HBA) forms a hydrogen bond with bazedoxifene (34) and ridaifen-B (41) (HBD). Lasofoxifene (39) adopts a binding orientation quite different from the other bulky SERMS. It forms predominantly edge-face π-π interactions Phe177(2.64), His178(2.65), Phe189(3.25), and Phe379(7.34), and a π-cation interaction with Phe200(3.36).

As seen in the CB1 model, the E-isomers of tamoxifen and metabolites dock vertically, albeit in a slightly folded manner (Figure 6.4(b)). All three ligands form an edge-face π-π stacking interaction with Phe200(3.36) and an aromatic hydrogen bond interaction with Ile267(ECL2) (HBA). E-4-OH-Tam (35) and E-End (36) form an aromatic hydrogen bond with backbone oxygen of Val196(3.32)(HBA) with the phenyl that forms stacking with Phe200(3.36); E-Tam (37), however, forms an aromatic hydrogen bond with Thr197(3.33) (HBA) with the same phenyl group due to slight variations in docking orientation. E-4-OH-Tam (35) and E-End (36) also form a hydrogen bond with backbone oxygen of Phe108(N-term)(HBA) via their aminoalkyl arm (HBD).

The Z-isomers of tamoxifen and metabolites are docked in an orientation inverse to the E-isomers (Figure 6.4(c)). The aromatic groups face TM1 and the aminoalkyl arm point towards the orthosteric binding pocket. All three ligands form an edge-face π-π interaction with His178(2.65) and an aromatic hydrogen bond with the sidechain oxygen atom of Ser383(7.39) (HBA). The oxygen atom of the phenol group in Z-4-OH-Tam (42) and Z-End (43) form hydrogen bonds with Phe103(N-term)(HBA). While Phe268(ECL2) forms an edge-face stacking interaction with Z-End (43) and Z-Tam (44), a slight change in docking orientation causes the phenyl group of Z-4-OH-Tam (42) to form an edge-face π-π interaction with Phe170(2.57) instead.

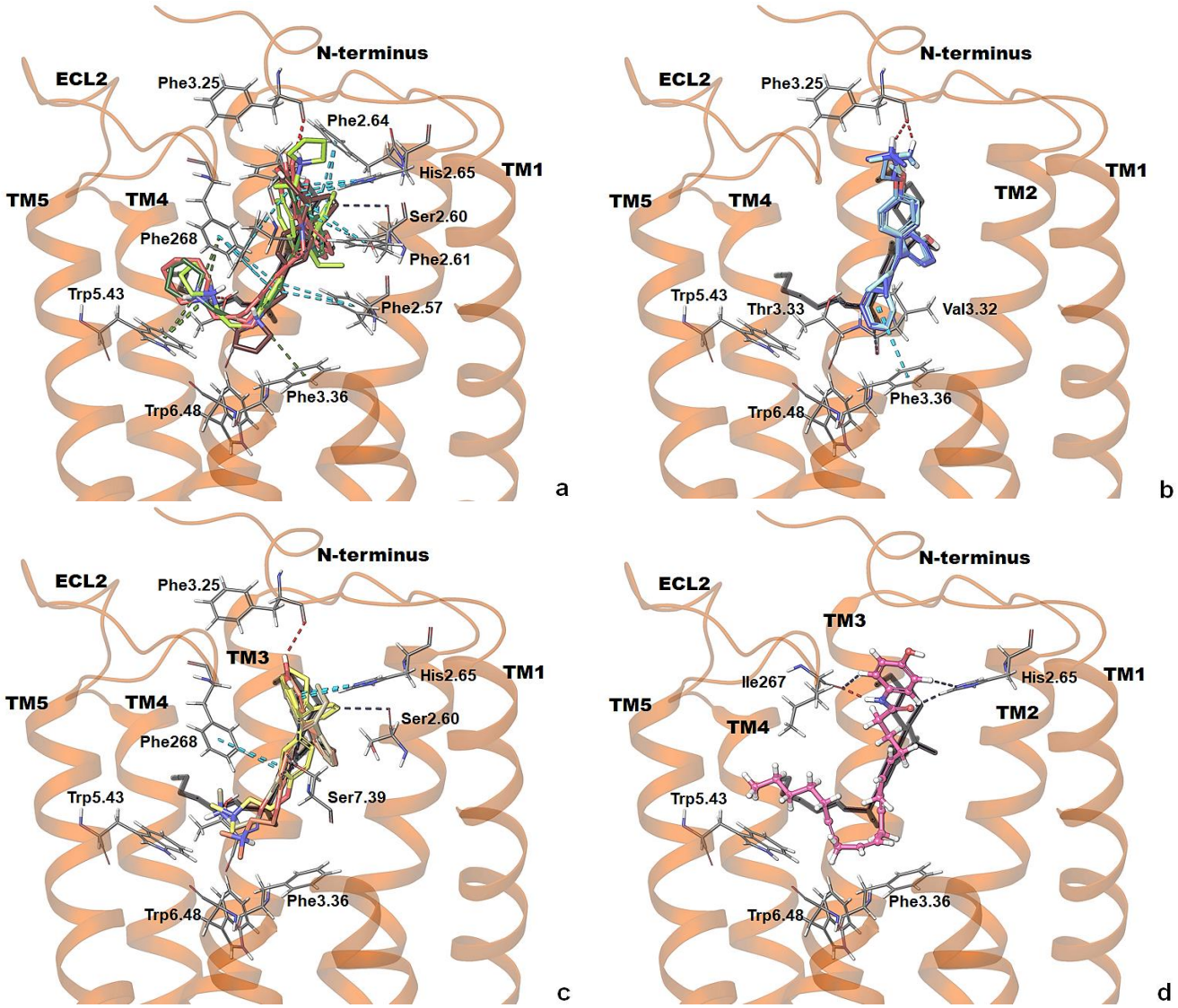

Figure 6.4 Binding modes of ligands docked to CB1* model (a) Bulky SERMS : *Red - Bazedoxifene (34), Brown – Lasofoxifene (39), Lime - Ridaifen-B (41), and Dark green – Raloxifene (40)* ***(b) E-tamoxifen and metabolites****: Light blue – E-4-OH-tamoxifen (35), Blue – E-endoxifen (36), and Deep blue – E-tamoxifen (37)* ***(c) Z-tamoxifen and metabolites****: Yellow – Z-4-OH-tamoxifen (42), Gold – Z-endoxifen (43), and Orange – Z-tamoxifen (44)* ***(d) AM404 (33).*** *In each figure, the cognate ligand AM841(21) is depicted in black tracing. Residues are depicted as thin sticks. TM6 and 7 have been truncated for purposes of picture clarity. Blue, green, red, and black dotted lines represent π-π, π-cation, hydrogen bond and aromatic hydrogen bonds respectively.*

2. AM404

AM404 (33) binds in a U-shape to the active structure with the aromatic head groups facing TM1 and TM2 (Figure 6.4(d)). It forms aromatic hydrogen bonds with His178(2.65) (two bonds: one as a donor and other as acceptor) and Ile267(ECL2) (HBA). It also forms a hydrogen bond with backbone oxygen of Ile267(ECL2) (HBA) via nitrogen atom (HBD) in the aromatic portion of the ligand.

6.4.2.1.3 CB2 model

1. SERMs

The bulky SERMs (Figure 6.5(a)) all exhibited a folded conformation in a manner similar to that seen in the CB1* model (Figure 6.4(a)). Bazedoxifene (34) and raloxifene (40) form π-cation interaction with Phe117(3.36) and Trp258(6.48) via the piperidine nitrogen atom. Ridaifen-B (41) forms an edge-face π-π stacking interaction with the toggle switch residues via the central benzene moiety. All three ligands formed edge-face π-π interactions with Phe87(2.57) and Phe183(ECL2), with different groups on different bulky SERMs. Bazedoxifene (34) and raloxifene (40) also show edge-face π-π interactions at His95(2.65). Lasofoxifene (39) showed an edge-face π-π interaction with Phe94(2.64) and a π-cation interaction with Trp194(5.43); it did not show any stacking interaction with Phe117(3.36) and Trp258(6.48). The backbone oxygen atom of Ser90(2.60) (HBA) formed aromatic hydrogen bond interactions with these ligands; Thr114(3.33), Leu182(ECL2), Lys278(7.32), and Phe174(2.61) formed either hydrogen bonds or aromatic hydrogen bonds with these ligands.

The E-isomers of tamoxifen and metabolites docked at an angle to the binding pocket (about 45°) (Figure 6.5(b)). The alkyl group points towards TM2 and the benzene

group points down into the pocket. All three ligands form edge-face π-π interactions with Phe183(ECL2) and Trp258(6.48). Phe117(3.36) forms π-π interactions with E-4-OH-Tam (35) and Phe87(2.57) forms edge-faced π-π interactions with E-End (36) and E-Tam (37). E-4-OH-Tam (35) also forms an edge-face π-π interaction with Trp194(5.43).

Z-End (43) and Z-Tam (44) show binding orientations similar to that seen in the CB1 model, albeit slanted by about 30° (Figure 6.5(c)). Both ligands form edge face π-π interactions with Phe87(2.57), Phe183(ECL2), Phe117(3.36), and Trp258(6.48) and π-cation interaction with Trp194(5.43). Z-End (43), in addition, forms a hydrogen bond via the amino group (HBD) with the hydroxyl group of Thr114(3.33) (HBA). Z-4-OH-Tam (42), on the other hand, shows slanted docking similar to the Z-tamoxifen metabolites in active CB1* model. It forms edge-face π-π interactions with Phe117(3.36), and Trp258(6.48), π-cation interactions with Phe87(2.57), His95(2.65), Phe183 (ECL2), and Phe281(7.35), hydrogen bond via phenolic OH (HBD) with backbone oxygen of Lys278(7.32) (HBA) and aromatic hydrogen bonds with sidechain oxygen of Ser90(2.60) (HBA) and backbone oxygen of Leu182(ECL2) (HBA).

2. AM404

AM404 (33) adopted a slightly U-shaped confirmation with the head group facing TM2 and the aliphatic chain in the direction of TM5 (Figure 6.5(d)). The ligand forms a hydrogen bond with the backbone oxygen of Ser90(2.60) (HBA) via phenolic OH (HBD). It also forms aromatic hydrogen bonds with the backbone oxygen Ser90(2.60) (HBA) and sidechain of His2.65 (HBD) via its phenol group and the adjacent oxygen atom respectively.

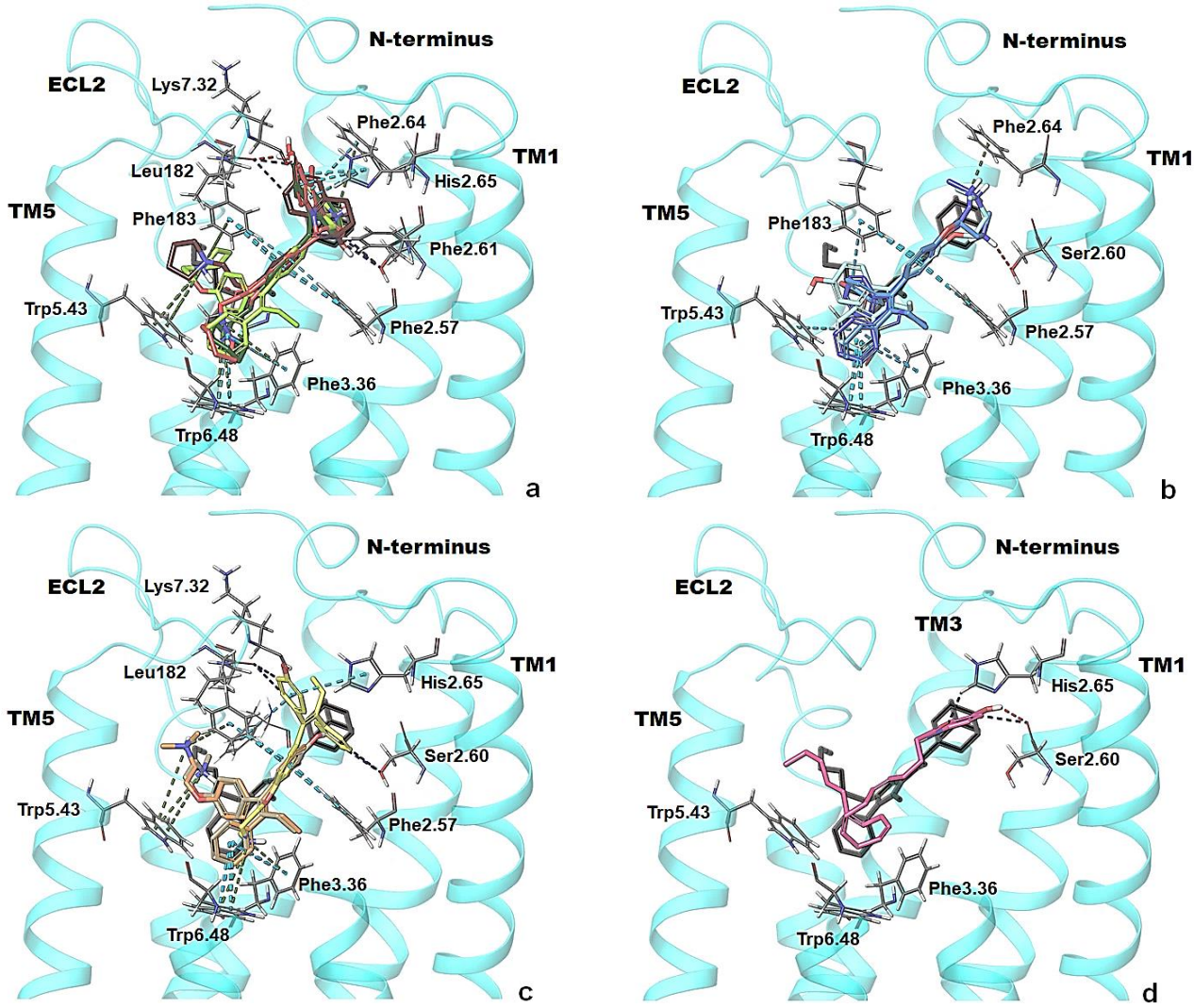

Figure 6.5 Binding modes of ligands docked to CB2 model (a) Bulky SERMS *: Red - Bazedoxifene (34), Brown – Lasofoxifene (39), Lime - Ridaifen-B (41), and Dark green – Raloxifene (40)* ***(b) E-tamoxifen and metabolites****: Light blue – E-4-OH-tamoxifen (35), Blue – E-endoxifen (36), and Deep blue – E-tamoxifen (37)* ***(c) Z-tamoxifen and metabolites****: Yellow – Z-4-OH-tamoxifen (42), Gold – Z-endoxifen (43), and Orange – Z-tamoxifen (44)* ***(d) AM404 (33)****. In each figure, the cognate ligand AM10257 (23) is depicted in black tracing. Residues are depicted as thin sticks. TM6 and 7 have been truncated for purposes of picture clarity. Blue, green, red, and black dotted lines represent π-π, π-cation, hydrogen bond and aromatic hydrogen bonds respectively*

3. Fenofibrate

Fenofibrate (38) docked in a horizontal manner with the chlorophenyl group towards TM5 and the tail group in the TM7-TM2 region (Figure 6.6). It formed edge-face π-π interaction with Trp194(5.43) and aromatic hydrogen bonds with Phe87(2.57) (HBA).

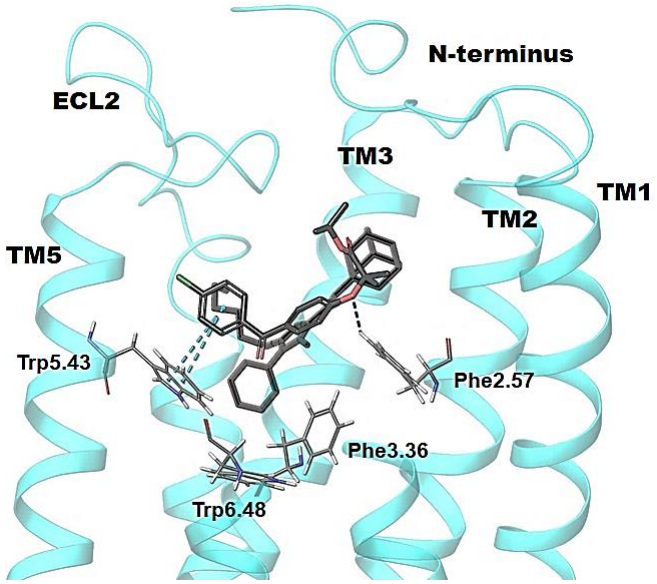

Figure 6.6 Binding modes of fenofibrate (38) docked to the CB2 model. *The cognate ligand AM10257 (23) is depicted in black tracing. Residues are depicted as thin sticks. TM6 and 7 have been truncated for purposes of picture clarity. Blue, green, red, and black dotted lines represent π-π, π-cation, hydrogen bond and aromatic hydrogen bonds respectively.*

6.4.3 Discussion

With the exception of E-4-OH-Tam (35), raloxifene (40), and ridaifen-B (41) at CB1, and lasofoxifene (39) at both CB1 and CB2, the chosen SERMs show inverse agonist activity at both CB1 and CB2 (Table VI.2, Appendix 6)[209,308,309]. By analysing binding modes of the chosen non-cannabinoid ligands into CB1, CB1* and CB2 model, it can be observed that most ligands choose a preferential orientation based on (a) the binding

surface area available, and (b) the shape of the pocket (influenced by the orientation of the cognate ligand in the respective crystal structure template) (Section1.3). In the case of SERMs, the binding mode also appears to be stereomer dependent.

E-Tam (37) and metabolites show a vertical docking irrespective of the type of model they are docked into. CB1 generally allows for an extended docking conformation, while CB1* model predominantly exhibits folded conformation. Tamoxifen and its metabolites show particularly interesting binding in the case of inactive CB1 and CB2. The CB1* model shows a rather folded binding for E-isomers and an almost inverse orientation for Z-isomers in comparison to the binding seen in inactive CB1. The E-isomers and Z-isomers of docked to inactive CB2 model appear to be slanted versions of the orientations of the same ligands seen in inactive CB1. The orientation of AM404 (33) correlates with the preferred U-shaped conformation of anandamide (1), the endocannabinoid with which it shares a structural similarity[105,310,311]. This conformation is observed uniformly across all receptors. Apart from a weak interaction with the toggle switch residues, AM404 (33) does not interfere with the π-π interaction between Phe3.36 and Trp6.48. Fenofibrate (38), which too shows agonist activity at CB2, does not interfere in the stacking. However, unlike the cognate ligand, it assumes a horizontal binding orientation.

6.4.3.1 Interaction with toggle switch residues

The docking results for non-cannabinoid ligands show that most inverse agonists docked to inactive CB2 model form more π-π stacking interaction (or a π-cation interaction, depending on the ligand) with toggle switch residues compared to inactive CB1 model, with the exception of both E and Z-endoxifen. In case of the CB1* model, almost all ligands show π-π stacking interaction with Phe3.36, but only in certain cases with Trp6.48.

The variation in interaction with toggle switch residues observed in the study can be explained on the basis of the arrangement of Phe3.36 and Trp6.48 in the three crystal structures used as templates. As already noted in Section 1.3 (and Figures 1.14 and 1.15), Phe3.36 restrains the rotamer state of Trp6.48 via stacking interactions in 5TGZ(CB1), and neither interact with the cognate ligand; in 5ZTY(CB2) both residues are oriented towards the binding pocket are arranged such that they can interact with the cognate ligand. In an active state crystal structure (CB1*), Trp6.48 moves away from the binding pocket post-activation while Phe3.36 turns towards the binding pocket. Thus, Phe3.36 is available to engage in ligand interaction.

Trp6.48 is a distinctive feature of cannabinoid receptors. The influence of the residue in receptor activation has already been highlighted upon in other chapters. As seen in Sections 2.1 and 2.6.3, the novel ligands MRI2687 and COR170 (25) exhibit inverse agonist activity at CB2; upon docking to CB2 it was observed that both interact with Trp258(6.48) by stacking interactions (docking was performed by Li *et al.* for MRI2687[127]; refer to Figure 2.12, Section 2.6.2 for docking of COR170 (25)). Their analogues (MRI2594 and COR167 (24)), which have an alkyl group instead of the phenyl group that MRI2687 and COR170 (25) possess, did not interact with Trp258(6.48) in docking studies (docking was performed by Li *et al.* for MRI2594[127]; refer to Figure 2.12, Section 2.6.2 for docking of COR167 (24)).

In the case of inactive CB1, no interference by the docked ligands between the toggle switch residues is seen – despite the fact that most of them are inverse agonists at CB1. This is also true for the inactive crystal structures, as seen earlier (Figures 1.15 and 1.16, Section 1.3). It is arguable that a larger binding surface area and close contact between

toggle switch residues lowers the probability of ligand interaction with Trp6.48 in an inactive CB1 model. But it is also to be noted that certain CB2 antagonist (or) inverse agonists have an opposing functional profile at CB1. AM10257 (23), whilst acting as an antagonist (or) inverse agonist at CB2, showed partial agonist activity at CB1[127]. MRI2687 also exhibited partial agonist activity at CB1. 3'-functionalised adamantyl cannabinoid ligands that act as potent agonists at CB1 show either antagonistic or inverse agonist activity at CB2[312]. Examples also include CB2 selective agonists URB447 (peripheral CB1 antagonist), GW405833 (a non-competitive CB1 antagonist) and AM1710 (competitive CB1 antagonist (or) CB1 inverse agonist)[313,314]. Given these examples of opposing functional relations between CB1 and CB2 selective ligands, there is a possibility that compounds that act as inverse agonists at both may exert their activity through varying binding modes.

6.5 Conclusion

In this chapter, the interaction of non-cannabinoid ligands at cannabinoid receptors was studied as a first step towards repurposing them as scaffolds for cannabinoid drug design. In this regard, a set of clinical compounds currently used for the treatment of various indications as mentioned in the WHO essential medicines database were tested for agonist activity against CB1 and CB2 using [^{35}S]GTPγS binding assay. Drugs were selected on the basis they should have either structural analogy with cholesterol, (or) had been reported to indirectly influence the ECS. It was found that none of the selected drugs exhibited agonist activity against either CB1 or CB2. Hence, it can be suggested that structural similarity with cholesterol alone is not a sufficient criterion for a ligand to be a cannabinoid agonist. The ligands which indirectly affect the ECS were also identified not

to have any direct G protein activating agonist activity at the cannabinoid receptors. However, the possibility of the selected ligands acting on CB1 and CB2 receptors either as antagonists or allosteric modulators yet remains.

The binding modes of certain non-cannabinoid receptor ligands that were previously reported to show activity at CB1 and CB2 were also studied. Upon analysing the ligand orientations, significant differences in the binding modes of those ligands were found. Both the binding pocket area and shape were seen to influence the interaction of the selected non-cannabinoids with the receptor. In the case of the SERMs, it can be said that their binding modes at CB1 and CB2 also depend on the ligand stereoisomer. The analysis of interactions of inverse agonist SERMS at the receptors also suggests that a stacking interaction with Trp6.48 could be a critical factor in determining inverse agonist activity of a ligand at CB2.

7 Conclusions and Future Work

7.1 Conclusions

Cannabinoid receptors (CB1 and CB2) are pharmacologically versatile members of GPCRs that have been studied extensively since their discovery. Though the existence of a unique receptor through which cannabinoids act (CB1) was discovered in 1988, it was not until October 2016 that the first inactive structure of CB1 was solved. This was subsequently followed by another inactive and three active structures for CB1 (with one complexed to $G_{\alpha i}$), and one inactive structure for CB2. More recently, another structure of CB1 bound to an agonist (CP55940 (6)) and an allosteric modulator (ORG27569 (16)) has been released (PDB ID 6KQI) (Figure 7.1)[52].

The work reported herein, which was started in early 2016 before the release of the crystal structures, was initially aimed towards modelling cannabinoid receptors. With the release of crystal structures, the need for exploring the structural conformations of CB1 and CB2 was recognised. This is because crystal structures, while providing irrefutable structural information, represent the conformation of a receptor at only one instant of time and under certain thermodynamic conditions. Given the plastic nature of GPCRs, crystal structures relay valuable but incomplete structural information. Hence with crystal structures as the starting point, the aim of work shifted towards exploring conformations of CB1 and CB2 through computational techniques such as molecular docking and molecular dynamics (MD) simulation.

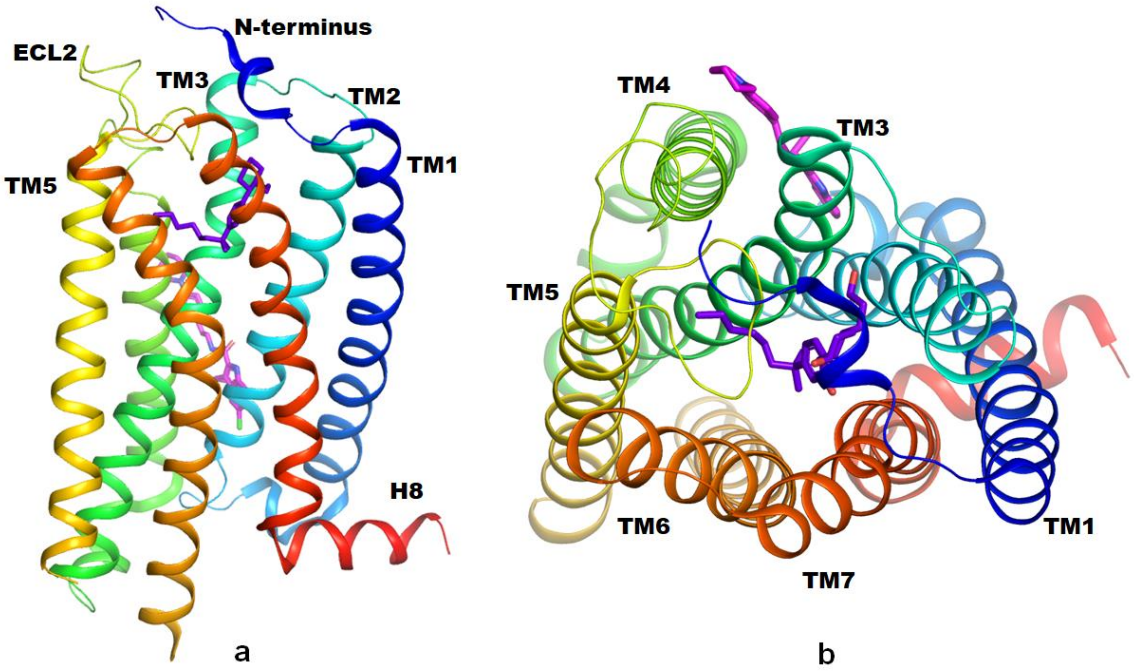

Figure 7.1 Crystal Structure of 6KQI. *(a) Side view (b) Top view. Ligands are shown as sticks. Orthosteric agonist CP55940 (6) (purple) occupies the canonical binding pocket and the allosteric ligand ORG27569 (16) (pink) occupies the extrahelical region between TM2, TM3, and TM4.*

As the first step in this direction, cannabinoid crystal structures were first remodelled so that the analysed receptors are devoid of crystallographic imperfections. MD simulation for CB1 and CB2 were performed under both apo and holo states (Chapter 3 and 5). Through collaborative work with Dr Jason Loo, trajectories of cross-docked active and inactive CB1 receptors, simulated in unbiased conditions were also analysed. From the apo simulations, a marked difference in the flexibility of CB1 and CB2 can be identified from RMSD analysis. While CB1-Apo progressively deviated from an active and an inactive conformation, CB2-Apo did not vary much from its crystal structure state though its simulation time is twice as that of CB1. Since the starting structure is itself a low energy inactive structure, it is possible that CB2 may require more time to break free of its

conformation. Furthermore, the TM6 of CB2 does not exhibit the same level of flexibility as it does in CB1 (Section 5.5), due to the CWFP motif (Sections 1.2.2 and 5.5). Hence, it is possible that even in an apo state, the apparent rigidity of the TM6 of CB2 impedes it from attaining the conformational plasticity that could be seen in an apo CB1 form. While this is true for the protein backbone, conserved residues (such as ionic lock and toggle switch residues) in the apo simulations break from their conformations observed in inactive crystal structures. These residues explore a variety of conformations in both CB1-Apo and CB2-Apo simulations, much like other apo GPCRs simulated (Sections 3.5 and 5.5). As apo structures are regarded as intermediary states[234], this leads to further questions regarding the structural nature of a CB1 (or) CB2 resting state.

An interesting structural feature that was analysed in the apo simulations of CB1 and CB2 is 'lipid access channels'. Both CB1-Apo and CB2-Apo systems simulations showed that TM1 could have a significant role in either forming or maintaining potential access channels. In CB1-Apo, the access pathway between TM1 and TM7 was closed down by the sideways movement of TM1, whereas a pathway to the orthosteric pocket (other than one through the extracellular side) was found towards the end of the simulation in replicate 3 of CB2-Apo. The other entry sites found in Apo-CB2 were not as wide as the access channels seen in the other lipid-binding inactive crystal structures (Section 1.3), yet the possibility of CB2 having an alternate pathway for ligand entry cannot be dismissed.

The common denominator observed in all the ligand-bound simulations analysed herein is that, with an inactive state conformation as the starting structure that is bound to an agonist, the receptor exhibited minimal changes in the structure (as in CB1-AM841 and CB2-CP55940, Chapters 3 and 5) or it explored a different area of the conformational

landscape (as in CB1-AM11542 simulations, Chapter 4). However, with an active starting structure bound to an antagonist, a partial change in receptor towards the intended conformation was seen (as in CB1*-MK0364 simulations, Chapter 4). The study hence demonstrates the influence of the starting structure on conformational exploration by a receptor in an unbiased MD simulation. Another common finding was that TM1, TM6 and TM7 influence the conformational states and structural features of the cannabinoid receptors to a higher extent than other TM helices. Specifically, the results of CB1-AM841 simulations in (Chapter 3) also illustrated that an aromatic headgroup (A, B, C rings (Figure 1.8)) -first entry via the proposed access channel between TM1 and TM7 by a classical cannabinoid, may not be favourable for receptor activation.

It must be noted that in all the unbiased MD simulation studies reported herein, a complete transformation from an observed functional state to the intended state (e.g. inactive state to active state conformation) was not observed, even in the case of microsecond long simulations (Chapter 4). This, however, does not diminish the utility of MD in studying the transition of GPCR functional states. To observe the activation of GPCRs, unbiased simulations of tens of microseconds may be required[315,316]. As an alternative to avoid long timescales, accelerated molecular dynamics and metadynamics (which use a modified energy landscape) have been suggested to enhance the sampling of protein confirmations in MD[316]. Both methods have faster calculation time as opposed to conventional methods. These methods, however, are outside the scope of the reported work and hence have not been discussed. Hamelberg *et al.* [317]and Valsson *et al.*[318] provide further information regarding the usage of accelerated dynamics and metadynamics in the study of protein structures.

In addition to the structural studies of CB1 and CB2 via MD, the interaction of non-cannabinoid ligands at cannabinoid receptors were also studied as a step towards repurposing them as scaffolds for cannabinoid drug design (Chapter 6). In this direction, a set of clinically used compounds that are not classified as cannabinoids were tested on CB1 and CB2 for agonist activity. While the tested compounds returned negative for agonistic action, the study has shown that structural analogy with cholesterol is not a crucial criterion for a ligand to exert activity at the cannabinoid receptors (Section 6.3.6).

Aside from biological assays, *in silico* docking has also been suggested to be a valid approach for drug repurposing studies. Hence, with the aim of deciphering their binding modes, a set of non-cannabinoid ligands which have been proven to show activity at CB1 and CB2 were docked to active and inactive CB1, and inactive CB2 models. The study demonstrated that the area and the shape of the receptor-binding pocket, and the stereoisomer of the ligand (i.e. E and Z forms), influence the binding mode of a ligand and hence, its interaction with cannabinoid receptors.

The docking studies reported for novel quinolone-3-carboxylic acid cannabinoids (Section 2.6) and SERMs (Section 6.4.2) have illustrated that for an inverse agonistic activity at CB2, a stacking interaction between the ligand and the Trp6.48 residue is necessary. Such an interaction was also observed in the inactive CB2 crystal structure (PDB ID 5ZTY) and docking studies by Li *et al.* on a different set of novel cannabinoids[127]. Given that different classes of ligands which act as inverse agonists at CB2 interact with Trp6.48, this aspect of the binding pocket could be acknowledged in the design of future cannabinoids.

7.2 Future Work

In the work presented herein, most of the structural exploration concerning MD simulations as well as molecular docking concentrated more on the inactive structures than the active forms of CB1. The unbiased MD simulations performed and (or) analysed in this work have collectively demonstrated the effect of the starting conformation on the receptor structural exploration. This effect was noticeable in the difference in flexibility of an apo CB1 and apo CB2 simulation, whereby the starting conformation was inactive. In a resting state, receptors are often in an apo condition. In this regard, unbiased apo CB1 simulations with an active structure as the starting conformation would provide vital information as to how an active receptor would approach an apo state upon the dissociation of the agonist. The study would reveal intermediate transitional states of the receptor, which could be used for virtual screening studies as seen in Loo *et al*[240]. Subjecting apo models to MD simulation has helped to identify critical structural information regarding allosteric binding sites, G protein coupling sites, cholesterol-binding regions, and activation pathways in A2AR and muscarinic receptors[280,319–321]. As observed from the MD simulations of inactive apo systems reported here (Sections 3.4.7 and 5.4.7), simulating active structures in an apo state may also provide further information regarding access channels.

In the study for re-purposing non-cannabinoid ligands for activity at cannabinoid receptors, though none of the ligands tested returned positive for agonist action, the possibility of them acting as antagonists or allosteric modulators still exists. Hence, the selected ligands are required to be tested for antagonistic activity and allosterism at CB1 and CB2. [^{35}S]GTPγS binding assay can be used for testing the antagonist activity of a ligand in the presence of an agonist[129]. A decrease in the G protein activation can mean

that the tested ligand is an antagonist. [^{35}S]GTPγS assay can also be used to detect allosteric activity, as allosteric modulators increase or decrease G protein activity according to their nature (Section 1.15). Indeed, [^{35}S]GTPγS has been used to assess the effect of alcuronium at M2 and amilorides at α-adrenergic receptor[129].

Another interesting future direction for the work presented here is the study of SERM interaction at cannabinoid receptors. As mentioned earlier (Section 1.5.3), docking helps to identify the ligand interactions at the active site of a receptor for only one particular conformation of the receptor. To study how the ligand affects the receptor conformation, MD simulations are essential. Subjecting the docked SERM-cannabinoid receptor complexes to MD simulations can help to understand the exact nature of ligand-receptor interaction. Through the results obtained, new arenas in cannabinoid drug design via drug repurposing could be explored.

8 References:

(1) Worth, C. L.; Kleinau, G.; Krause, G. Comparative Sequence and Structural Analyses of G-Protein-Coupled Receptor Crystal Structures and Implications for Molecular Models. *PLoS ONE* **2009**, *4* (9), e7011. https://doi.org/10.1371/journal.pone.0007011.

(2) Alexander, S. P.; Christopoulos, A.; Davenport, A. P.; Kelly, E.; Marrion, N. V.; Peters, J. A.; Faccenda, E.; Harding, S. D.; Pawson, A. J.; Sharman, J. L.; Southan, C.; Davies, J. A.; CGTP Collaborators. The Concise Guide to Pharmacology 2017/18: G Protein-Coupled Receptors. *Br. J. Pharmacol.* **2017**, *174*, S17–S129. https://doi.org/10.1111/bph.13878.

(3) Ngo, T.; Kufareva, I.; Coleman, J. L.; Graham, R. M.; Abagyan, R.; Smith, N. J. Identifying Ligands at Orphan GPCRs: Current Status Using Structure-Based Approaches: Approaches for Identifying Orphan GPCR Ligands. *Br. J. Pharmacol.* **2016**, *173* (20), 2934–2951. https://doi.org/10.1111/bph.13452.

(4) Kolakowski, L. F. GCRDb: A G-Protein-Coupled Receptor Database. *Receptors Channels* **1994**, *2* (1), 1–7.

(5) Fredriksson, R. The G-Protein-Coupled Receptors in the Human Genome Form Five Main Families. Phylogenetic Analysis, Paralogon Groups, and Fingerprints. *Mol. Pharmacol.* **2003**, *63* (6), 1256–1272. https://doi.org/10.1124/mol.63.6.1256.

(6) Kobilka, B. K. G Protein Coupled Receptor Structure and Activation. *Biochim. Biophys. Acta BBA - Biomembr.* **2007**, *1768* (4), 794–807. https://doi.org/10.1016/j.bbamem.2006.10.021.

(7) Berman, H. M.; Westbrook, J.; Feng, Z.; Gilliland, G.; Bhat, T. N.; Weissig, H.; Shindyalov, I. N.; Bourne, P. E. The Protein Data Bank. *Nucleic Acids Res.* **2000**, *28* (1), 235–242. https://doi.org/10.1093/nar/28.1.235.

(8) Munk, C.; Isberg, V.; Mordalski, S.; Harpsøe, K.; Rataj, K.; Hauser, A. S.; Kolb, P.; Bojarski, A. J.; Vriend, G.; Gloriam, D. E. GPCRdb: The G Protein-Coupled Receptor Database - an Introduction: GPCRdb: The GPCR Database. *Br. J. Pharmacol.* **2016**, *173* (14), 2195–2207. https://doi.org/10.1111/bph.13509.

(9) Garland, S. L. Are GPCRs Still a Source of New Targets? *J. Biomol. Screen.* **2013**. https://doi.org/10.1177/1087057113498418.

(10) Wishart, D. S. DrugBank: A Comprehensive Resource for in Silico Drug Discovery and Exploration. *Nucleic Acids Res.* **2006**, *34* (90001), D668–D672. https://doi.org/10.1093/nar/gkj067.

(11) Isberg, V.; de Graaf, C.; Bortolato, A.; Cherezov, V.; Katritch, V.; Marshall, F. H.; Mordalski, S.; Pin, J.-P.; Stevens, R. C.; Vriend, G.; Gloriam, D. E. Generic GPCR Residue Numbers – Aligning Topology Maps While Minding the Gaps. *Trends Pharmacol. Sci.* **2015**, *36* (1), 22–31. https://doi.org/10.1016/j.tips.2014.11.001.

(12) Ballesteros, J. A.; Weinstein, H. [19] Integrated Methods for the Construction of Three-Dimensional Models and Computational Probing of Structure-Function Relations in G Protein-Coupled Receptors. In *Methods in Neurosciences*; Elsevier, 1995; Vol. 25, pp 366–428. https://doi.org/10.1016/S1043-9471(05)80049-7.

(13) Oliveira, L.; Paiva, A. C. M.; Vriend, G. A Common Motif in G-Protein-Coupled Seven Transmembrane Helix Receptors. *J. Comput. Aided Mol. Des.* **1993**, *7* (6), 649–658. https://doi.org/10.1007/BF00125323.

(14) Baldwin, J. M. The Probable Arrangement of the Helices in G Protein-Coupled Receptors. *EMBO J.* **1993**, *12* (4), 1693–1703. https://doi.org/10.1002/j.1460-2075.1993.tb05814.xPa.

(15) Schwartz, T. W. Locating Ligand-Binding Sites in 7tm Receptors by Protein Engineering. *Curr. Opin. Biotechnol.* **1994**, *5* (4), 434–444. https://doi.org/10.1016/0958-1669(94)90054-X.

(16) Wootten, D.; Simms, J.; Miller, L. J.; Christopoulos, A.; Sexton, P. M. Polar Transmembrane Interactions Drive Formation of Ligand-Specific and Signal Pathway-Biased Family B G Protein-Coupled Receptor Conformations. *Proc. Natl. Acad. Sci.* **2013**, *110* (13), 5211–5216. https://doi.org/10.1073/pnas.1221585110.

(17) Pin, J.-P.; Galvez, T.; Prézeau, L. Evolution, Structure, and Activation Mechanism of Family 3/C G-Protein-Coupled Receptors. *Pharmacol. Ther.* **2003**, *98* (3), 325–354. https://doi.org/10.1016/S0163-7258(03)00038-X.

(18) Wang, Z.; Zhao, F.; Peng, J.; Xu, J. Protein 8-Class Secondary Structure Prediction Using Conditional Neural Fields. *PROTEOMICS* **2011**, *11* (19), 3786–3792. https://doi.org/10.1002/pmic.201100196.

(19) Trzaskowski, B.; Latek, D.; Yuan, S.; Ghoshdastider, U.; Debinski, A.; Filipek, S. Action of Molecular Switches in GPCRs--Theoretical and Experimental Studies. *Curr. Med. Chem.* **2012**, *19* (8), 1090–1109. https://doi.org/10.2174/092986712799320556PDB.

(20) Katritch, V.; Cherezov, V.; Stevens, R. C. Structure-Function of the G Protein–Coupled Receptor Superfamily. *Annu. Rev. Pharmacol. Toxicol.* **2013**, *53* (1), 531–556. https://doi.org/10.1146/annurev-pharmtox-032112-135923.

(21) Ballesteros, J.; Kitanovic, S.; Guarnieri, F.; Davies, P.; Fromme, B. J.; Konvicka, K.; Chi, L.; Millar, R. P.; Davidson, J. S.; Weinstein, H.; Sealfon, S. C. Functional Microdomains in G-Protein-Coupled Receptors: The Conserved Arginine-Cage Motif in the Gonadotropin-Releasing Hormone Receptor. *J. Biol. Chem.* **1998**, *273* (17), 10445–10453. https://doi.org/10.1074/jbc.273.17.10445.

(22) Moreira, I. S. Structural Features of the G-Protein/GPCR Interactions. *Biochim. Biophys. Acta BBA - Gen. Subj.* **2014**, *1840* (1), 16–33. https://doi.org/10.1016/j.bbagen.2013.08.027.

(23) Palczewski, K.; Kumasaka, T.; Hori, T.; Behnke, C. A.; Motoshima, H.; Fox, B. A.; Le Trong, I.; Teller, D. C.; Okada, T.; Stenkamp, R. E.; Yamamoto, M.; Miyano, M. Crystal Structure of Rhodopsin: A G Protein-Coupled Receptor. *Science* **2000**, *289* (5480), 739–745. https://doi.org/10.1126/science.289.5480.739.

(24) Visiers, I.; Ballesteros, J. A.; Weinstein, H. Three-Dimensional Representations of G Protein-Coupled Receptor Structures and Mechanisms. In *G Protein Pathways Part A: Ribonucleases*; Iyengar, R., Hildebrandt, J. D., Eds.; Methods in Enzymology; Elsevier, 2002; Vol. 343, pp 329–371. https://doi.org/10.1016/S0076-6879(02)43145-X.

(25) Nygaard, R.; Frimurer, T. M.; Holst, B.; Rosenkilde, M. M.; Schwartz, T. W. Ligand Binding and Micro-Switches in 7TM Receptor Structures. *Trends Pharmacol. Sci.* **2009**, *30* (5), 249–259. https://doi.org/10.1016/j.tips.2009.02.006.

(26) Prioleau, C.; Visiers, I.; Ebersole, B. J.; Weinstein, H.; Sealfon, S. C. Conserved Helix 7 Tyrosine Acts as a Multistate Conformational Switch in the 5HT2C Receptor: Identification of a Novel "Locked-On" Phenotype and Double Revertant Mutations. *J. Biol. Chem.* **2002**, *277* (39), 36577–36584. https://doi.org/10.1074/jbc.M206223200.

(27) Haga, K.; Kruse, A. C.; Asada, H.; Yurugi-Kobayashi, T.; Shiroishi, M.; Zhang, C.; Weis, W. I.; Okada, T.; Kobilka, B. K.; Haga, T.; Kobayashi, T. Structure of the Human M2 Muscarinic Acetylcholine Receptor Bound to an Antagonist. *Nature* **2012**, *482* (7386), 547–551. https://doi.org/10.1038/nature10753.

(28) Kruse, A. C.; Hu, J.; Pan, A. C.; Arlow, D. H.; Rosenbaum, D. M.; Rosemond, E.; Green, H. F.; Liu, T.; Chae, P. S.; Dror, R. O.; Shaw, D. E.; Weis, W. I.; Wess, J.; Kobilka, B. K. Structure and Dynamics of the M3 Muscarinic Acetylcholine Receptor. *Nature* **2012**, *482* (7386), 552–556. https://doi.org/10.1038/nature10867.

(29) Lin, S. W.; Sakmar, T. P. Specific Tryptophan UV-Absorbance Changes Are Probes of the Transition of Rhodopsin to Its Active State †. *Biochemistry* **1996**, *35* (34), 11149–11159. https://doi.org/10.1021/bi960858u.

(30) Lebon, G.; Warne, T.; Edwards, P. C.; Bennett, K.; Langmead, C. J.; Leslie, A. G. W.; Tate, C. G. Agonist-Bound Adenosine A2A Receptor Structures Reveal Common Features of GPCR Activation. *Nature* **2011**, *474* (7352), 521–525. https://doi.org/10.1038/nature10136.

(31) Xu, F.; Wu, H.; Katritch, V.; Han, G. W.; Jacobson, K. A.; Gao, Z.-G.; Cherezov, V.; Stevens, R. C. Structure of an Agonist-Bound Human A2A Adenosine Receptor. *Science* **2011**, *332* (6027), 322–327. https://doi.org/10.1126/science.1202793.

(32) Deupi, X.; Standfuss, J. Structural Insights into Agonist-Induced Activation of G-Protein-Coupled Receptors. *Curr. Opin. Struct. Biol.* **2011**, *21* (4), 541–551. https://doi.org/10.1016/j.sbi.2011.06.002.

(33) García-Nafría, J.; Tate, C. G. Cryo-EM Structures of GPCRs Coupled to Gs, Gi and Go. *Mol. Cell. Endocrinol.* **2019**. https://doi.org/10.1016/j.mce.2019.02.006.

(34) Lundstrom, K. H. Biology of G Protein-Coupled Receptors. In *G protein-coupled receptors in drug discovery*; Lundstrom, K. H., Chiu, M. L., Eds.; Carmen, A., Series Ed.; Drug discovery series; CRC Press, 2006; Vol. 4.

(35) Milligan, G.; Kostenis, E. Heterotrimeric G-Proteins: A Short History. *Br. J. Pharmacol.* **2006**, *147 Suppl 1*, S46-55. https://doi.org/10.1038/sj.bjp.0706405.

(36) Pierce, K. L.; Premont, R. T.; Lefkowitz, R. J. Seven-Transmembrane Receptors. *Nat. Rev. Mol. Cell Biol.* **2002**, *3* (9), 639–650. https://doi.org/10.1038/nrm908.

(37) Rasmussen, S. G. F.; DeVree, B. T.; Zou, Y.; Kruse, A. C.; Chung, K. Y.; Kobilka, T. S.; Thian, F. S.; Chae, P. S.; Pardon, E.; Calinski, D.; Mathiesen, J. M.; Shah, S. T. A.; Lyons, J. A.; Caffrey, M.; Gellman, S. H.; Steyaert, J.; Skiniotis, G.; Weis, W. I.; Sunahara, R. K.; Kobilka, B. K. Crystal Structure of the B2 Adrenergic Receptor–Gs Protein Complex. *Nature* **2011**, *477* (7366), 549–555. https://doi.org/10.1038/nature10361.

(38) Smith, J. S.; Rajagopal, S. The β-Arrestins: Multifunctional Regulators of G Protein-Coupled Receptors. *J. Biol. Chem.* **2016**, *291* (17), 8969–8977. https://doi.org/10.1074/jbc.R115.713313.

(39) DeGraff, J. L.; Gurevich, V. V.; Benovic, J. L. The Third Intracellular Loop of α 2 -Adrenergic Receptors Determines Subtype Specificity of Arrestin Interaction. *J. Biol. Chem.* **2002**, *277* (45), 43247–43252. https://doi.org/10.1074/jbc.M207495200.

(40) Marion, S.; Oakley, R. H.; Kim, K.-M.; Caron, M. G.; Barak, L. S. A β-Arrestin Binding Determinant Common to the Second Intracellular Loops of Rhodopsin Family G Protein-Coupled Receptors. *J. Biol. Chem.* **2006**, *281* (5), 2932–2938. https://doi.org/10.1074/jbc.M508074200.

(41) Ferguson, S. S.; Downey, W. E.; Colapietro, A. M.; Barak, L. S.; Ménard, L.; Caron, M. G. Role of Beta-Arrestin in Mediating Agonist-Promoted G Protein-Coupled Receptor Internalization. *Science* **1996**, *271* (5247), 363–366. https://doi.org/10.1126/science.271.5247.363.

(42) Benovic, J. L.; Kuhn, H.; Weyand, I.; Codina, J.; Caron, M. G.; Lefkowitz, R. J. Functional Desensitization of the Isolated Beta-Adrenergic Receptor by the Beta-Adrenergic Receptor Kinase: Potential Role of an Analog of the Retinal Protein Arrestin (48-KDa Protein). *Proc. Natl. Acad. Sci.* **1987**, *84* (24), 8879–8882. https://doi.org/10.1073/pnas.84.24.8879.

(43) Kenakin, T. Functional Selectivity of Drugs for Seven Transmembrane Receptors: Biased Agonism and Antagonism. In *G protein-coupled receptors: From structure to function*; RSC drug discovery series; RSC Publishing, 2011; Vol. 8, pp 429–445.

(44) Ikeda, Y.; Kumagai, H.; Motozawa, Y.; Suzuki, J.; Komuro, I. Biased Agonism of the Angiotensin II Type I Receptor: A Potential Strategy for the Treatment of Acute Heart Failure. *Int. Heart. J.* **2015**, *56* (5), 485–488. https://doi.org/10.1536/ihj.15-256.

(45) Ahn, S.; Shenoy, S. K.; Wei, H.; Lefkowitz, R. J. Differential Kinetic and Spatial Patterns of β-Arrestin and G Protein-Mediated ERK Activation by the Angiotensin II Receptor. *J. Biol. Chem.* **2004**, *279* (34), 35518–35525. https://doi.org/10.1074/jbc.M405878200.

(46) Bologna, Z.; Teoh, J.; Bayoumi, A. S.; Tang, Y.; Kim, I. Biased G Protein-Coupled Receptor Signaling: New Player in Modulating Physiology and Pathology. *Biomol. Ther.* **2017**, *25* (1), 12–25. https://doi.org/10.4062/biomolther.2016.165.

(47) Tan, L.; Yan, W.; McCorvy, J. D.; Cheng, J. Biased Ligands of G Protein-Coupled Receptors (GPCRs): Structure − Functional Selectivity Relationships (SFSRs) and Therapeutic Potential. *J. Med. Chem.* **2018**, *61* (22), 9841–9878. https://doi.org/10.1021/acs.jmedchem.8b00435.

(48) *Rang and Dale's Pharmacology*, 7. ed.; Rang, H. P., Dale, M. M., Ritter, J. M., Flower, R. J., Henderson, G., Eds.; Student consult; Elsevier, Churchill Livingstone: Edinburgh, 2012.

(49) Cawston, E. E.; Hunter, M. R.; Glass, M. Allosteric Modulation of the Cannabinoid CB1 Receptor. In *Handbook of Cannabis and Related Pathologies*; Preedy, V., Ed.; 2017; pp 573–583.

(50) Christopoulos, A.; Kenakin, T. G Protein-Coupled Receptor Allosterism and Complexing. *Pharmacol. Rev.* **2002**, *54* (2), 323–374. https://doi.org/10.1124/pr.54.2.323.

(51) Congreve, M.; Murray, C. W.; Blundell, T. L. Keynote Review: Structural Biology and Drug Discovery. *Drug Discov. Today* **2005**, *10* (13), 895–907. https://doi.org/10.1016/S1359-6446(05)03484-7.

(52) Shao, Z. H.; Yan, W.; Chapman, K.; Ramesh, K.; Ferrell, A.; Yin, J.; Wang, X.; Xu, Q.; Rosenbaum, D. M. Structure of an Allosteric Modulator Bound to the CB1 Cannabinoid Receptor. *Nat.Chem.Biol.* **2019**. https://doi.org/10.2210/PDB6KQI/PDB.

(53) Katritch, V.; Fenalti, G.; Abola, E. E.; Roth, B. L.; Cherezov, V.; Stevens, R. C. Allosteric Sodium in Class A GPCR Signaling. *Trends Biochem. Sci.* **2014**, *39* (5), 233–244. https://doi.org/10.1016/j.tibs.2014.03.002.

(54) Granier, S.; Kobilka, B. A New Era of GPCR Structural and Chemical Biology. *Nat. Chem. Biol.* **2012**, *8* (8), 670–673. https://doi.org/10.1038/nchembio.1025.

(55) Du, Y.; Duc, N. M.; Rasmussen, S. G. F.; Hilger, D.; Kubiak, X.; Wang, L.; Bohon, J.; Kim, H. R.; Wegrecki, M.; Asuru, A.; Jeong, K. M.; Lee, J.; Chance, M. R.; Lodowski, D. T.; Kobilka, B. K.; Chung, K. Y. Assembly of a GPCR-G Protein Complex. *Cell* **2019**, *177* (5), 1232-1242.e11. https://doi.org/10.1016/j.cell.2019.04.022.

(56) Liu, X.; Xu, X.; Hilger, D.; Aschauer, P.; Tiemann, J. K. S.; Du, Y.; Liu, H.; Hirata, K.; Sun, X.; Guixà-González, R.; Mathiesen, J. M.; Hildebrand, P. W.; Kobilka, B. K. Structural Insights into the Process of GPCR-G Protein Complex Formation. *Cell* **2019**, *177* (5), 1243-1251.e12. https://doi.org/10.1016/j.cell.2019.04.021.

(57) Borroto-Escuela, D. O.; Rodriguez, D.; Romero-Fernandez, W.; Kapla, J.; Jaiteh, M.; Ranganathan, A.; Lazarova, T.; Fuxe, K.; Carlsson, J. Mapping the Interface of a GPCR Dimer: A Structural Model of the A2A Adenosine and D2 Dopamine Receptor Heteromer. *Front. Pharmacol.* **2018**, *9*, 829. https://doi.org/10.3389/fphar.2018.00829.

(58) Salon, J. A.; Lodowski, D. T.; Palczewski, K. The Significance of G Protein-Coupled Receptor Crystallography for Drug Discovery. *Pharmacol. Rev.* **2011**, *63* (4), 901–937. https://doi.org/10.1124/pr.110.003350.

(59) Henderson, R.; Baldwin, J. M.; Ceskat, T. A.; Zemlin, F.; Beckmann, E.; Downing, K. H. Model for the Structure of Bacteriorhodopsin Based on High-Resolution Electron Cryo-Microscopy. 31.

(60) Kühne, W. Chemical Processes in the Retina. *Vision Res.* **1977**, *17* (11–12), 1269–1316. https://doi.org/10.1016/0042-6989(77)90114-6.

(61) Errey, J. C.; Marshall, F. H. New Techniques to Express and Crystallize G Protein Coupled Receptors. In *GPCR Molecular Pharmacology and Drug Targeting : Shifting Paradigms and New Directions*; Gilchrist, A., Ed.; Wiley, 2010.

(62) Rosenbaum, D. M.; Cherezov, V.; Hanson, M. A.; Rasmussen, S. G. F.; Thian, F. S.; Kobilka, T. S.; Choi, H.-J.; Yao, X.-J.; Weis, W. I.; Stevens, R. C.; Kobilka, B. K. GPCR Engineering Yields High-Resolution Structural Insights into Beta2-Adrenergic Receptor Function. *Science* **2007**, *318* (5854), 1266–1273. https://doi.org/10.1126/science.1150609.

(63) Rosenbaum, D. M.; Rasmussen, S. G. F.; Kobilka, B. K. The Structure and Function of G-Protein-Coupled Receptors. *Nature* **2009**, *459* (7245), 356–363. https://doi.org/10.1038/nature08144.

(64) Jaakola, V.-P.; Griffith, M. T.; Hanson, M. A.; Cherezov, V.; Chien, E. Y. T.; Lane, J. R.; Ijzerman, A. P.; Stevens, R. C. The 2.6 Angstrom Crystal Structure of a Human A2A Adenosine Receptor Bound to an Antagonist. *Science* **2008**, *322* (5905), 1211–1217. https://doi.org/10.1126/science.1164772.

(65) Nehmé, R.; Carpenter, B.; Singhal, A.; Strege, A.; Edwards, P. C.; White, C. F.; Du, H.; Grisshammer, R.; Tate, C. G. Mini-G Proteins: Novel Tools for Studying GPCRs in Their Active Conformation. *PLOS ONE* **2017**, *12* (4), e0175642. https://doi.org/10.1371/journal.pone.0175642.

(66) Popov, P.; Kozlovskii, I.; Katritch, V. Computational Design for Thermostabilization of GPCRs. *Curr. Opin. Struct. Biol.* **2019**, *55*, 25–33. https://doi.org/10.1016/j.sbi.2019.02.010.

(67) Kufareva, I.; Rueda, M.; Katritch, V.; Stevens, R. C.; Abagyan, R. Status of GPCR Modeling and Docking as Reflected by Community-Wide GPCR Dock 2010 Assessment. *Structure* **2011**, *19* (8), 1108–1126. https://doi.org/10.1016/j.str.2011.05.012.

(68) Kufareva, I.; Katritch, V.; Stevens, R. C.; Abagyan, R. Advances in GPCR Modeling Evaluated by the GPCR Dock 2013 Assessment: Meeting New Challenges. *Structure* **2014**, *22* (8), 1120–1139. https://doi.org/10.1016/j.str.2014.06.012.

(69) GPCR Dock 2008 participants; Michino, M.; Abola, E.; Brooks, C. L.; Dixon, J. S.; Moult, J.; Stevens, R. C. Community-Wide Assessment of GPCR Structure Modelling and Ligand Docking: GPCR Dock 2008. *Nat. Rev. Drug Discov.* **2009**, *8* (6), 455–463. https://doi.org/10.1038/nrd2877.

(70) Ryazantsev, M. N.; Nikolaev, D. M.; Struts, A. V.; Brown, M. F. Quantum Mechanical and Molecular Mechanics Modeling of Membrane-Embedded Rhodopsins. *J. Membr. Biol.* **2019**. https://doi.org/10.1007/s00232-019-00095-0.

(71) Lu, H.-C.; Mackie, K. An Introduction to the Endogenous Cannabinoid System. *Biol. Psychiatry* **2016**, *79* (7), 516–525. https://doi.org/10.1016/j.biopsych.2015.07.028.

(72) Lawrence, D. K.; Gill, E. W. The Effects of Delta1-Tetrahydrocannabinol and Other Cannabinoids on Spin-Labeled Liposomes and Their Relationship to Mechanisms of General Anesthesia. *Mol. Pharmacol.* **1975**, *11* (5), 595–602.

(73) Gaoni, Y.; Mechoulam, R. Isolation, Structure, and Partial Synthesis of an Active Constituent of Hashish. *J. Am. Chem. Soc.* **1964**, *86* (8), 1646–1647. https://doi.org/10.1021/ja01062a046.

(74) Hollister, L. E. Structure-Activity Relationships in Man of Cannabis Constituents, and Homologs and Metabolites of Δ^{9}-Tetrahydrocannabinol. *Pharmacology* **1974**, *11* (1), 3–11. https://doi.org/10.1159/000136462.

(75) Devane, W. A.; Dysarz, F. A.; Johnson, M. R.; Melvin, L. S.; Howlett, A. C. Determination and Characterization of a Cannabinoid Receptor in Rat Brain. *Mol. Pharmacol.* **1988**, *34* (5), 605–613.

(76) Busquets-Garcia, A.; Bains, J.; Marsicano, G. CB1 Receptor Signaling in the Brain: Extracting Specificity from Ubiquity. *Neuropsychopharmacology* **2018**, *43* (1), 4–20. https://doi.org/10.1038/npp.2017.206.

(77) Elphick, M. R.; Egertova, M. Cannabinoid Receptor Genetics and Evolution. In *The Cannabinoid Receptors*; Reggio, P. H., Ed.; The receptors; Humana Press, 2009; pp 123–149.

(78) Glass, M.; Faull, R. L. M.; Dragunow, M. Loss of Cannabinoid Receptors in the Substantia Nigra in Huntington's Disease. *Neuroscience* **1993**, *56* (3), 523–527. https://doi.org/10.1016/0306-4522(93)90352-g.

(79) Mackie, K. Cannabinoid Receptor Homo- and Heterodimerization. *Life Sci.* **2005**, *77* (14), 1667–1673. https://doi.org/10.1016/j.lfs.2005.05.011.

(80) Sansuk, K.; Deupi, X.; Torrecillas, I. R.; Jongejan, A.; Nijmeijer, S.; Bakker, R. A.; Pardo, L.; Leurs, R. A Structural Insight into the Reorientation of Transmembrane Domains 3 and 5 during Family A G Protein-Coupled Receptor Activation. *Mol. Pharmacol.* **2011**, *79* (2), 262–269. https://doi.org/10.1124/mol.110.066068.

(81) Deupi, X. Relevance of Rhodopsin Studies for GPCR Activation. *Biochim. Biophys. Acta BBA - Bioenerg.* **2014**, *1837* (5), 674–682. https://doi.org/10.1016/j.bbabio.2013.09.002.

(82) Zhou, D.; Song, Z. H. CB1 Cannabinoid Receptor-Mediated Tyrosine Phosphorylation of Focal Adhesion Kinase-Related Non-Kinase. *FEBS Lett.* **2002**, *525* (1–3), 164–168. https://doi.org/10.1016/S0014-5793(02)03091-0.

(83) Bramblett, R. D.; Panu, A. M.; Ballesteros, J. A.; Reggio, P. H. Construction of a 3D Model of the Cannabinoid CB1 Receptor: Determination of Helix Ends and Helix Orientation. *Life Sci.* **1995**, *56* (23–24), 1971–1982. https://doi.org/10.1016/0024-3205(95)00178-9.

(84) Howlett, A. C.; Barth, F.; Bonner, T. I.; Cabral, G.; Casellas, P.; Devane, W. A.; Felder, C. C.; Herkenham, M.; Mackie, K.; Martin, B. R.; Mechoulam, R.; Pertwee, R. G. International Union of Pharmacology. XXVII. Classification of Cannabinoid Receptors. *Pharmacol. Rev.* **2002**, *54* (2), 161–202.

(85) Glass, M.; Northup, J. K. Agonist Selective Regulation of G Proteins by Cannabinoid CB(1) and CB(2) Receptors. *Mol. Pharmacol.* **1999**, *56* (6), 1362–1369. https://doi.org/10.1124/mol.56.6.1362.

(86) Finlay, D. B.; Cawston, E. E.; Grimsey, N. L.; Hunter, M. R.; Korde, A.; Vemuri, V. K.; Makriyannis, A.; Glass, M. $G\alpha_s$ Signalling of the CB_1 Receptor and the Influence of Receptor Number: CB_1 Receptor $G\alpha_s$ Signalling. *Br. J. Pharmacol.* **2017**, *174* (15), 2545–2562. https://doi.org/10.1111/bph.13866.

(87) Ibsen, M. S.; Connor, M.; Glass, M. Cannabinoid CB_1 and CB_2 Receptor Signaling and Bias. *Cannabis Cannabinoid Res.* **2017**, *2* (1), 48–60. https://doi.org/10.1089/can.2016.0037.

(88) Lauckner, J. E.; Hille, B.; Mackie, K. The Cannabinoid Agonist WIN55,212-2 Increases Intracellular Calcium via CB1 Receptor Coupling to Gq/11 G Proteins. *Proc. Natl. Acad. Sci.* **2005**, *102* (52), 19144–19149. https://doi.org/10.1073/pnas.0509588102.

(89) Redmond, W. J.; Cawston, E. E.; Grimsey, N. L.; Stuart, J.; Edington, A. R.; Glass, M.; Connor, M. Identification of *N* -Arachidonoyl Dopamine as a Highly Biased Ligand at Cannabinoid CB_1 Receptors: NADA Elevates Intracellular Calcium. *Br. J. Pharmacol.* **2016**, *173* (1), 115–127. https://doi.org/10.1111/bph.13341.

(90) Mukhopadhyay, S. Chemically Distinct Ligands Promote Differential CB1 Cannabinoid Receptor-Gi Protein Interactions. *Mol. Pharmacol.* **2005**, *67* (6), 2016–2024. https://doi.org/10.1124/mol.104.003558.

(91) Mahmoudian, M. The Cannabinoid Receptor: Computer-Aided Molecular Modeling and Docking of Ligand. *J. Mol. Graph. Model.* **1997**, *15* (3), 149–153. https://doi.org/10.1016/S1093-3263(97)00098-3.

(92) Shim, J.-Y.; Welsh, W. J.; Howlett, A. C. Homology Model of the CB1 Cannabinoid Receptor: Sites Critical for Nonclassical Cannabinoid Agonist Interaction. *Biopolymers* **2003**, *71* (2), 169–189. https://doi.org/10.1002/bip.10424.

(93) Singh, R.; Hurst, D. P.; Barnett-Norris, J.; Lynch, D. L.; Reggio, P. H.; Guarnieri, F. Activation of the Cannabinoid CB1 Receptor May Involve a W6 48/F3 36 Rotamer Toggle Switch. *J. Pept. Res. Off. J. Am. Pept. Soc.* **2002**, *60* (6), 357–370. https://doi.org/10.1034/j.1399-3011.2002.21065.x.

(94) McAllister, S. D.; Hurst, D. P.; Barnett-Norris, J.; Lynch, D.; Reggio, P. H.; Abood, M. E. Structural Mimicry in Class A G Protein-Coupled Receptor Rotamer Toggle Switches: THE IMPORTANCE OF THE F3.36(201)/W6.48(357) INTERACTION IN CANNABINOID CB $_1$ RECEPTOR ACTIVATION. *J. Biol. Chem.* **2004**, *279* (46), 48024–48037. https://doi.org/10.1074/jbc.M406648200.

(95) McAllister, S. D.; Rizvi, G.; Anavi-Goffer, S.; Hurst, D. P.; Barnett-Norris, J.; Lynch, D. L.; Reggio, P. H.; Abood, M. E. An Aromatic Microdomain at the Cannabinoid CB $_1$ Receptor Constitutes an Agonist/Inverse Agonist Binding Region. *J. Med. Chem.* **2003**, *46* (24), 5139–5152. https://doi.org/10.1021/jm0302647.

(96) McAllister, S. D.; Tao, Q.; Barnett-Norris, J.; Buehner, K.; Hurst, D. P.; Guarnieri, F.; Reggio, P. H.; Nowell Harmon, K. W.; Cabral, G. A.; Abood, M. E. A Critical Role for a Tyrosine Residue in the Cannabinoid Receptors for Ligand Recognition. *Biochem. Pharmacol.* **2002**, *63* (12), 2121–2136. https://doi.org/10.1016/s0006-2952(02)01031-6.

(97) Song, Z. H.; Slowey, C. A.; Hurst, D. P.; Reggio, P. H. The Difference between the CB(1) and CB(2) Cannabinoid Receptors at Position 5.46 Is Crucial for the Selectivity of WIN55212-2 for CB(2). *Mol. Pharmacol.* **1999**, *56* (4), 834–840.

(98) Murphy, J. W.; Kendall, D. A. Integrity of Extracellular Loop 1 of the Human Cannabinoid Receptor 1 Is Critical for High-Affinity Binding of the Ligand CP 55,940 but Not SR 141716A. *Biochem. Pharmacol.* **2003**, *65* (10), 1623–1631. https://doi.org/10.1016/S0006-2952(03)00155-2.

(99) Shim, J.-Y.; Rudd, J.; Ding, T. T. Distinct Second Extracellular Loop Structures of the Brain Cannabinoid CB1 Receptor: Implication in Ligand Binding and Receptor Function. *Proteins Struct. Funct. Bioinforma.* **2011**, *79* (2), 581–597. https://doi.org/10.1002/prot.22907.

(100) Kapur, A.; Hurst, D. P.; Fleischer, D.; Whitnell, R.; Thakur, G. A.; Makriyannis, A.; Reggio, P. H.; Abood, M. E. Mutation Studies of Ser7.39 and Ser2.60 in the Human CB1 Cannabinoid Receptor: Evidence for a Serine-Induced Bend in CB1 Transmembrane Helix 7. *Mol. Pharmacol.* **2007**, *71* (6), 1512–1524. https://doi.org/10.1124/mol.107.034645.

(101) Ahn, K. H.; Scott, C. E.; Abrol, R.; Goddard, W. A.; Kendall, D. A. Computationally-Predicted CB1 Cannabinoid Receptor Mutants Show Distinct

Patterns of Salt-Bridges That Correlate with Their Level of Constitutive Activity Reflected in G Protein Coupling Levels, Thermal Stability, and Ligand Binding: Constitutive Activity of CB1 Receptors. *Proteins Struct. Funct. Bioinforma.* **2013**, *81* (8), 1304–1317. https://doi.org/10.1002/prot.24264.

(102) Hua, T.; Vemuri, K.; Pu, M.; Qu, L.; Han, G. W.; Wu, Y.; Zhao, S.; Shui, W.; Li, S.; Korde, A.; Laprairie, R. B.; Stahl, E. L.; Ho, J.-H.; Zvonok, N.; Zhou, H.; Kufareva, I.; Wu, B.; Zhao, Q.; Hanson, M. A.; Bohn, L. M.; Makriyannis, A.; Stevens, R. C.; Liu, Z.-J. Crystal Structure of the Human Cannabinoid Receptor CB1. *Cell* **2016**, *167* (3), 750-762.e14. https://doi.org/10.1016/j.cell.2016.10.004.

(103) Hua, T.; Vemuri, K.; Nikas, S. P.; Laprairie, R. B.; Wu, Y.; Qu, L.; Pu, M.; Korde, A.; Jiang, S.; Ho, J.-H.; Han, G. W.; Ding, K.; Li, X.; Liu, H.; Hanson, M. A.; Zhao, S.; Bohn, L. M.; Makriyannis, A.; Stevens, R. C.; Liu, Z.-J. Crystal Structures of Agonist-Bound Human Cannabinoid Receptor CB1. *Nature* **2017**, *547* (7664), 468–471. https://doi.org/10.1038/nature23272.

(104) Krishna Kumar, K.; Shalev-Benami, M.; Robertson, M. J.; Hu, H.; Banister, S. D.; Hollingsworth, S. A.; Latorraca, N. R.; Kato, H. E.; Hilger, D.; Maeda, S.; Weis, W. I.; Farrens, D. L.; Dror, R. O.; Malhotra, S. V.; Kobilka, B. K.; Skiniotis, G. Structure of a Signaling Cannabinoid Receptor 1-G Protein Complex. *Cell* **2019**, *176* (3), 448-458.e12. https://doi.org/10.1016/j.cell.2018.11.040.

(105) Shao, Z.; Yin, J.; Chapman, K.; Grzemska, M.; Clark, L.; Wang, J.; Rosenbaum, D. M. High-Resolution Crystal Structure of the Human CB1 Cannabinoid Receptor. *Nature* **2016**, *540* (7634), 602–606. https://doi.org/10.1038/nature20613.

(106) Munro, S.; Thomas, K. L.; Abu-Shaar, M. Molecular Characterization of a Peripheral Receptor for Cannabinoids. *Nature* **1993**, *365* (6441), 61–65. https://doi.org/10.1038/365061a0.

(107) Whiteside, G. T.; Lee, G. P.; Valenzano, K. J. The Role of the Cannabinoid CB2 Receptor in Pain Transmission and Therapeutic Potential of Small Molecule CB2 Receptor Agonists. *Curr. Med. Chem.* **2007**, *14* (8), 917–936. https://doi.org/10.2174/092986707780363023.

(108) Gong, J.-P.; Onaivi, E. S.; Ishiguro, H.; Liu, Q.-R.; Tagliaferro, P. A.; Brusco, A.; Uhl, G. R. Cannabinoid CB2 Receptors: Immunohistochemical Localization in Rat Brain. *Brain Res.* **2006**, *1071* (1), 10–23. https://doi.org/10.1016/j.brainres.2005.11.035.

(109) Van Sickle, M. D. Identification and Functional Characterization of Brainstem Cannabinoid CB2 Receptors. *Science* **2005**, *310* (5746), 329–332. https://doi.org/10.1126/science.1115740.

(110) Malfitano, A. M.; Basu, S.; Maresz, K.; Bifulco, M.; Dittel, B. N. What We Know and Do Not Know about the Cannabinoid Receptor 2 (CB2). *Semin. Immunol.* **2014**, *26* (5), 369–379. https://doi.org/10.1016/j.smim.2014.04.002.

(111) Dhopeshwarkar, A.; Mackie, K. CB2 Cannabinoid Receptors as a Therapeutic Target-What Does the Future Hold? *Mol. Pharmacol.* **2014**, *86* (4), 430–437. https://doi.org/10.1124/mol.114.094649.

(112) Hurst, D. P.; Reggio, P. H. Models of Cannabinoid Inverse Agonism, Neutral Antagonism, and Agonism: Tools for Rational Drug Design. In *The Cannabinoid Receptors*; Reggio, P. H., Ed.; Neve, K. A., Series Ed.; The Receptors; Humana Press, 2009; pp 235–278.

(113) Shoemaker, J. L. Agonist-Directed Trafficking of Response by Endocannabinoids Acting at CB2 Receptors. *J. Pharmacol. Exp. Ther.* **2005**, *315* (2), 828–838. https://doi.org/10.1124/jpet.105.089474.

(114) Atwood, B. K.; Wager-Miller, J.; Haskins, C.; Straiker, A.; Mackie, K. Functional Selectivity in CB(2) Cannabinoid Receptor Signaling and Regulation: Implications for the Therapeutic Potential of CB(2) Ligands. *Mol. Pharmacol.* **2012**, *81* (2), 250–263. https://doi.org/10.1124/mol.111.074013.

(115) Schuehly, W.; Paredes, J. M. V.; Kleyer, J.; Huefner, A.; Anavi-Goffer, S.; Raduner, S.; Altmann, K.-H.; Gertsch, J. Mechanisms of Osteoclastogenesis Inhibition by a Novel Class of Biphenyl-Type Cannabinoid CB(2) Receptor Inverse Agonists. *Chem. Biol.* **2011**, *18* (8), 1053–1064. https://doi.org/10.1016/j.chembiol.2011.05.012.

(116) Soethoudt, M.; Grether, U.; Fingerle, J.; Grim, T. W.; Fezza, F.; de Petrocellis, L.; Ullmer, C.; Rothenhäusler, B.; Perret, C.; van Gils, N.; Finlay, D.; MacDonald, C.; Chicca, A.; Gens, M. D.; Stuart, J.; de Vries, H.; Mastrangelo, N.; Xia, L.; Alachouzos, G.; Baggelaar, M. P.; Martella, A.; Mock, E. D.; Deng, H.; Heitman, L. H.; Connor, M.; Di Marzo, V.; Gertsch, J.; Lichtman, A. H.; Maccarrone, M.; Pacher, P.; Glass, M.; van der Stelt, M. Cannabinoid CB2 Receptor Ligand Profiling Reveals Biased Signalling and Off-Target Activity. *Nat. Commun.* **2017**, *8*, 13958. https://doi.org/10.1038/ncomms13958.

(117) Gouldson, P.; Calandra, B.; Legoux, P.; Kernéis, A.; Rinaldi-Carmona, M.; Barth, F.; Le Fur, G.; Ferrara, P.; Shire, D. Mutational Analysis and Molecular Modelling of the Antagonist SR 144528 Binding Site on the Human Cannabinoid CB2 Receptor. *Eur. J. Pharmacol.* **2000**, *401* (1), 17–25. https://doi.org/10.1016/S0014-2999(00)00439-8.

(118) Xie, X.-Q.; Chen, J.-Z.; Billings, E. M. 3D Structural Model of the G-Protein-Coupled Cannabinoid CB2 Receptor. *Proteins* **2003**, *53* (2), 307–319. https://doi.org/10.1002/prot.10511.

(119) Durdagi, S.; Papadopoulos, M. G.; Papahatjis, D. P.; Mavromoustakos, T. Combined 3D QSAR and Molecular Docking Studies to Reveal Novel Cannabinoid Ligands with Optimum Binding Activity. *Bioorg. Med. Chem. Lett.* **2007**, *17* (24), 6754–6763. https://doi.org/10.1016/j.bmcl.2007.10.044.

(120) Montero, C.; Campillo, N. E.; Goya, P.; Páez, J. A. Homology Models of the Cannabinoid CB1 and CB2 Receptors. A Docking Analysis Study. *Eur. J. Med. Chem.* **2005**, *40* (1), 75–83. https://doi.org/10.1016/j.ejmech.2004.10.002.

(121) Pei, Y.; Mercier, R. W.; Anday, J. K.; Thakur, G. A.; Zvonok, A. M.; Hurst, D.; Reggio, P. H.; Janero, D. R.; Makriyannis, A. Ligand-Binding Architecture of Human CB2 Cannabinoid Receptor: Evidence for Receptor Subtype-Specific Binding Motif and Modeling GPCR Activation. *Chem. Biol.* **2008**, *15* (11), 1207–1219. https://doi.org/10.1016/j.chembiol.2008.10.011.

(122) Salo, O. M. H.; Raitio, K. H.; Savinainen, J. R.; Nevalainen, T.; Lahtela-Kakkonen, M.; Laitinen, J. T.; Järvinen, T.; Poso, A. Virtual Screening of Novel CB2 Ligands Using a Comparative Model of the Human Cannabinoid CB2 Receptor. *J. Med. Chem.* **2005**, *48* (23), 7166–7171. https://doi.org/10.1021/jm050565b.

(123) Tuccinardi, T.; Ferrarini, P. L.; Manera, C.; Ortore, G.; Saccomanni, G.; Martinelli, A. Cannabinoid CB2/CB1 Selectivity. Receptor Modeling and Automated Docking

Analysis. *J. Med. Chem.* **2006**, *49* (3), 984–994. https://doi.org/10.1021/jm050875u.

(124) Cichero, E.; Menozzi, G.; Guariento, S.; Fossa, P. Ligand-Based Homology Modelling of the Human CB $_2$ Receptor SR144528 Antagonist Binding Site: A Computational Approach to Explore the 1,5-Diaryl Pyrazole Scaffold. *MedChemComm* **2015**, *6* (11), 1978–1986. https://doi.org/10.1039/C5MD00333D.

(125) Durdagi, S.; Papadopoulos, M. G.; Zoumpoulakis, P. G.; Koukoulitsa, C.; Mavromoustakos, T. A Computational Study on Cannabinoid Receptors and Potent Bioactive Cannabinoid Ligands: Homology Modeling, Docking, de Novo Drug Design and Molecular Dynamics Analysis. *Mol. Divers.* **2010**, *14* (2), 257–276. https://doi.org/10.1007/s11030-009-9166-4.

(126) Feng, Z.; Alqarni, M. H.; Yang, P.; Tong, Q.; Chowdhury, A.; Wang, L.; Xie, X.-Q. Modeling, Molecular Dynamics Simulation, and Mutation Validation for Structure of Cannabinoid Receptor 2 Based on Known Crystal Structures of GPCRs. *J. Chem. Inf. Model.* **2014**, *54* (9), 2483–2499. https://doi.org/10.1021/ci5002718.

(127) Li, X.; Hua, T.; Vemuri, K.; Ho, J.-H.; Wu, Y.; Wu, L.; Popov, P.; Benchama, O.; Zvonok, N.; Locke, K.; Qu, L.; Han, G. W.; Iyer, M. R.; Cinar, R.; Coffey, N. J.; Wang, J.; Wu, M.; Katritch, V.; Zhao, S.; Kunos, G.; Bohn, L. M.; Makriyannis, A.; Stevens, R. C.; Liu, Z.-J. Crystal Structure of the Human Cannabinoid Receptor CB2. *Cell* **2019**, *176* (3), 459-467.e13. https://doi.org/10.1016/j.cell.2018.12.011.

(128) Tate, C. G. A Crystal Clear Solution for Determining G-Protein-Coupled Receptor Structures. *Trends Biochem. Sci.* **2012**, *37* (9), 343–352. https://doi.org/10.1016/j.tibs.2012.06.003.

(129) Harrison, C.; Traynor, J. R. The [35S]GTPγS Binding Assay: Approaches and Applications in Pharmacology. *Life Sci.* **2003**, *74* (4), 489–508. https://doi.org/10.1016/j.lfs.2003.07.005.

(130) Devane, W.; Hanus, L.; Breuer, A.; Pertwee, R.; Stevenson, L.; Griffin, G.; Gibson, D.; Mandelbaum, A.; Etinger, A.; Mechoulam, R. Isolation and Structure of a Brain Constituent That Binds to the Cannabinoid Receptor. *Science* **1992**, *258* (5090), 1946–1949. https://doi.org/10.1126/science.1470919.

(131) Hanus, L.; Abu-Lafi, S.; Fride, E.; Breuer, A.; Vogel, Z.; Shalev, D. E.; Kustanovich, I.; Mechoulam, R. 2-Arachidonyl Glyceryl Ether, an Endogenous Agonist of the Cannabinoid CB1 Receptor. *Proc. Natl. Acad. Sci.* **2001**, *98* (7), 3662–3665. https://doi.org/10.1073/pnas.061029898.

(132) Hanus, L.; Gopher, A.; Almog, S.; Mechoulam, R. Two New Unsaturated Fatty Acid Ethanolamides in Brain That Bind to the Cannabinoid Receptor. *J. Med. Chem.* **1993**, *36* (20), 3032–3034. https://doi.org/10.1021/jm00072a026.

(133) Mechoulam, R.; Ben-Shabat, S.; Hanus, L.; Ligumsky, M.; Kaminski, N. E.; Schatz, A. R.; Gopher, A.; Almog, S.; Martin, B. R.; Compton, D. R. Identification of an Endogenous 2-Monoglyceride, Present in Canine Gut, That Binds to Cannabinoid Receptors. *Biochem. Pharmacol.* **1995**, *50* (1), 83–90.

(134) Okamoto, Y.; Wang, J.; Morishita, J.; Ueda, N. Biosynthetic Pathways of the Endocannabinoid Anandamide. *Chem. Biodivers.* **2007**, *4* (8), 1842–1857. https://doi.org/10.1002/cbdv.200790155.

(135) Ueda, N.; Tsuboi, K.; Uyama, T.; Ohnishi, T. Biosynthesis and Degradation of the Endocannabinoid 2-Arachidonoylglycerol. *BioFactors* **2011**, *37* (1), 1–7. https://doi.org/10.1002/biof.131.

(136) Felder, C. C.; Joyce, K. E.; Briley, E. M.; Mansouri, J.; Mackie, K.; Blond, O.; Lai, Y.; Ma, A. L.; Mitchell, R. L. Comparison of the Pharmacology and Signal Transduction of the Human Cannabinoid CB1 and CB2 Receptors. *Mol. Pharmacol.* **1995**, *48* (3), 443–450.

(137) Gareau, Y.; Dufresne, C.; Gallant, M.; Rochette, C.; Sawyer, N.; Slipetz, D. M.; Tremblay, N.; Weech, P. K.; Metters, K. M.; Labelle, M. Structure Activity Relationships of Tetrahydrocannabinol Analogues on Human Cannabinoid Receptors. *Bioorg. Med. Chem. Lett.* **1996**, *6* (2), 189–194. https://doi.org/10.1016/0960-894X(95)00573-C.

(138) Hanus, L.; Breuer, A.; Tchilibon, S.; Shiloah, S.; Goldenberg, D.; Horowitz, M.; Pertwee, R. G.; Ross, R. A.; Mechoulam, R.; Fride, E. HU-308: A Specific Agonist for CB2, a Peripheral Cannabinoid Receptor. *Proc. Natl. Acad. Sci.* **1999**, *96* (25), 14228–14233. https://doi.org/10.1073/pnas.96.25.14228.

(139) Melvin, L. S.; Johnson, M. R.; Harbert, C. A.; Milne, G. M.; Weissman, A. A Cannabinoid Derived Prototypical Analgesic. *J. Med. Chem.* **1984**, *27* (1), 67–71. https://doi.org/10.1021/jm00367a013.

(140) Johnson, M. R.; Melvin, L. S. The Discovery of Nonclassical Cannabinoid Analgesics. In *Cannabinoids as Therapeutic Agents*; Mechoulam, R., Ed.; CRC Press: Boca Raton, Fla., 1986; pp 121–145.

(141) Little, P. J.; Compton, D. R.; Johnson, M. R.; Melvin, L. S.; Martin, B. R. Pharmacology and Stereoselectivity of Structurally Novel Cannabinoids in Mice. *J. Pharmacol. Exp. Ther.* **1988**, *247* (3), 1046–1051.

(142) Pacheco, M. A.; Ward, S. J.; Childers, S. R. Identification of Cannabinoid Receptors in Cultures of Rat Cerebellar Granule Cells. *Brain Res.* **1993**, *603* (1), 102–110. https://doi.org/10.1016/0006-8993(93)91304-b.

(143) Bell, M. R.; D'Ambra, T. E.; Kumar, V.; Eissenstat, M. A.; Herrmann, J. L.; Wetzel, J. R.; Rosi, D.; Philion, R. E.; Daum, S. J.; Hlasta, D. J. Antinociceptive (Aminoalkyl)Indoles. *J. Med. Chem.* **1991**, *34* (3), 1099–1110. https://doi.org/10.1021/jm00107a034.

(144) D'Ambra, T. E.; Estep, K. G.; Bell, M. R.; Eissenstat, M. A.; Josef, K. A.; Ward, S. J.; Haycock, D. A.; Baizman, E. R.; Casiano, F. M.; Beglin, N. C. Conformationally Restrained Analogues of Pravadoline: Nanomolar Potent, Enantioselective, (Aminoalkyl)Indole Agonists of the Cannabinoid Receptor. *J. Med. Chem.* **1992**, *35* (1), 124–135. https://doi.org/10.1021/jm00079a016.

(145) Bouaboula, M.; Perrachon, S.; Milligan, L.; Canat, X.; Rinaldi-Carmona, M.; Portier, M.; Barth, F.; Calandra, B.; Pecceu, F.; Lupker, J.; Maffrand, J. P.; Le Fur, G.; Casellas, P. A Selective Inverse Agonist for Central Cannabinoid Receptor Inhibits Mitogen-Activated Protein Kinase Activation Stimulated by Insulin or Insulin-like Growth Factor 1. Evidence for a New Model of Receptor/Ligand Interactions. *J. Biol. Chem.* **1997**, *272* (35), 22330–22339. https://doi.org/10.1074/jbc.272.35.22330.

(146) Jansen, E. M.; Haycock, D. A.; Ward, S. J.; Seybold, V. S. Distribution of Cannabinoid Receptors in Rat Brain Determined with Aminoalkylindoles. *Brain Res.* **1992**, *575* (1), 93–102. https://doi.org/10.1016/0006-8993(92)90428-c.

(147) Kuster, J. E.; Stevenson, J. I.; Ward, S. J.; D'Ambra, T. E.; Haycock, D. A. Aminoalkylindole Binding in Rat Cerebellum: Selective Displacement by Natural and Synthetic Cannabinoids. *J. Pharmacol. Exp. Ther.* **1993**, *264* (3), 1352–1363.

(148) Savinainen, J. R.; Kokkola, T.; Salo, O. M. H.; Poso, A.; Järvinen, T.; Laitinen, J. T. Identification of WIN55212-3 as a Competitive Neutral Antagonist of the Human Cannabinoid CB2 Receptor. *Br. J. Pharmacol.* **2005**, *145* (5), 636–645. https://doi.org/10.1038/sj.bjp.0706230.

(149) Aung, M. M.; Griffin, G.; Huffman, J. W.; Wu, M.; Keel, C.; Yang, B.; Showalter, V. M.; Abood, M. E.; Martin, B. R. Influence of the N-1 Alkyl Chain Length of Cannabimimetic Indoles upon CB(1) and CB(2) Receptor Binding. *Drug Alcohol Depend.* **2000**, *60* (2), 133–140. https://doi.org/10.1016/s0376-8716(99)00152-0.

(150) Mauler, F.; Mittendorf, J.; Horváth, E.; De Vry, J. Characterization of the Diarylether Sulfonylester (-)-(R)-3-(2-Hydroxymethylindanyl-4-Oxy)Phenyl-4,4,4-Trifluoro-1-Sulfonate (BAY 38-7271) as a Potent Cannabinoid Receptor Agonist with Neuroprotective Properties. *J. Pharmacol. Exp. Ther.* **2002**, *302* (1), 359–368. https://doi.org/10.1124/jpet.302.1.359.

(151) Yao, B. B.; Hsieh, G. C.; Frost, J. M.; Fan, Y.; Garrison, T. R.; Daza, A. V.; Grayson, G. K.; Zhu, C. Z.; Pai, M.; Chandran, P.; Salyers, A. K.; Wensink, E. J.; Honore, P.; Sullivan, J. P.; Dart, M. J.; Meyer, M. D. In Vitro and in Vivo Characterization of A-796260: A Selective Cannabinoid CB2 Receptor Agonist Exhibiting Analgesic Activity in Rodent Pain Models. *Br. J. Pharmacol.* **2008**, *153* (2), 390–401. https://doi.org/10.1038/sj.bjp.0707568.

(152) Rinaldi-Carmona, M.; Barth, F.; Héaulme, M.; Shire, D.; Calandra, B.; Congy, C.; Martinez, S.; Maruani, J.; Néliat, G.; Caput, D. SR141716A, a Potent and Selective Antagonist of the Brain Cannabinoid Receptor. *FEBS Lett.* **1994**, *350* (2–3), 240–244. https://doi.org/10.1016/0014-5793(94)00773-x.

(153) Rinaldi-Carmona, M.; Barth, F.; Millan, J.; Derocq, J. M.; Casellas, P.; Congy, C.; Oustric, D.; Sarran, M.; Bouaboula, M.; Calandra, B.; Portier, M.; Shire, D.; Brelière, J. C.; Le Fur, G. L. SR 144528, the First Potent and Selective Antagonist of the CB2 Cannabinoid Receptor. *J. Pharmacol. Exp. Ther.* **1998**, *284* (2), 644–650.

(154) Pertwee, R. G. Pharmacology of Cannabinoid Receptor Ligands. *Curr. Med. Chem.* **1999**, *6* (8), 635–664.

(155) Sim-Selley, L. J.; Brunk, L. K.; Selley, D. E. Inhibitory Effects of SR141716A on G-Protein Activation in Rat Brain. *Eur. J. Pharmacol.* **2001**, *414* (2–3), 135–143. https://doi.org/10.1016/S0014-2999(01)00784-1.

(156) Christensen, R.; Kristensen, P. K.; Bartels, E. M.; Bliddal, H.; Astrup, A. Efficacy and Safety of the Weight-Loss Drug Rimonabant: A Meta-Analysis of Randomised Trials. *Lancet Lond. Engl.* **2007**, *370* (9600), 1706–1713. https://doi.org/10.1016/S0140-6736(07)61721-8.

(157) Lan, R.; Lu, Q.; Fan, P.; Gatley, J.; Volkow, N. D.; Fernando, S. R.; Pertwee, R.; Makriyannis, A. Design and Synthesis of the CB1 Selective Cannabinoid

Antagonist AM281: A Potential Human SPECT Ligand. *AAPS PharmSci* **1999**, *1* (2), 39–45. https://doi.org/10.1208/ps010204.

(158) Felder, C. C.; Joyce, K. E.; Briley, E. M.; Glass, M.; Mackie, K. P.; Fahey, K. J.; Cullinan, G. J.; Hunden, D. C.; Johnson, D. W.; Chaney, M. O.; Koppel, G. A.; Brownstein, M. LY320135, a Novel Cannabinoid CB1 Receptor Antagonist, Unmasks Coupling of the CB1 Receptor to Stimulation of CAMP Accumulation. *J. Pharmacol. Exp. Ther.* **1998**, *284* (1), 291–297.

(159) Ross, R. A.; Brockie, H. C.; Stevenson, L. A.; Murphy, V. L.; Templeton, F.; Makriyannis, A.; Pertwee, R. G. Agonist-Inverse Agonist Characterization at CB1 and CB2 Cannabinoid Receptors of L759633, L759656, and AM630. *Br. J. Pharmacol.* **1999**, *126* (3), 665–672. https://doi.org/10.1038/sj.bjp.0702351.

(160) Hosohata, K.; Quock, R. M.; Hosohata, Y.; Burkey, T. H.; Makriyannis, A.; Consroe, P.; Roeske, W. R.; Yamamura, H. I. AM630 Is a Competitive Cannabinoid Receptor Antagonist in the Guinea Pig Brain. *Life Sci.* **1997**, *61* (9), PL115-118. https://doi.org/10.1016/s0024-3205(97)00596-1.

(161) Hosohata, Y.; Quock, R. M.; Hosohata, K.; Makriyannis, A.; Consroe, P.; Roeske, W. R.; Yamamura, H. I. AM630 Antagonism of Cannabinoid-Stimulated [35S]GTP Gamma S Binding in the Mouse Brain. *Eur. J. Pharmacol.* **1997**, *321* (1), R1-3. https://doi.org/10.1016/s0014-2999(97)00047-2.

(162) Iwamura, H.; Suzuki, H.; Ueda, Y.; Kaya, T.; Inaba, T. In Vitro and in Vivo Pharmacological Characterization of JTE- 907, a Novel Selective Ligand for Cannabinoid CB2 Receptor. **2000**, 6.

(163) Price, M. R.; Baillie, G. L.; Thomas, A.; Stevenson, L. A.; Easson, M.; Goodwin, R.; McLean, A.; McIntosh, L.; Goodwin, G.; Walker, G.; Westwood, P.; Marrs, J.; Thomson, F.; Cowley, P.; Christopoulos, A.; Pertwee, R. G.; Ross, R. A. Allosteric Modulation of the Cannabinoid CB1 Receptor. *Mol. Pharmacol.* **2005**, *68* (5), 1484–1495. https://doi.org/10.1124/mol.105.016162.

(164) Petrucci, V.; Chicca, A.; Glasmacher, S.; Paloczi, J.; Cao, Z.; Pacher, P.; Gertsch, J. Pepcan-12 (RVD-Hemopressin) Is a CB2 Receptor Positive Allosteric Modulator Constitutively Secreted by Adrenals and in Liver upon Tissue Damage. *Sci. Rep.* **2017**, *7* (1), 9560. https://doi.org/10.1038/s41598-017-09808-8.

(165) Gado, F.; Di Cesare Mannelli, L.; Lucarini, E.; Bertini, S.; Cappelli, E.; Digiacomo, M.; Stevenson, L. A.; Macchia, M.; Tuccinardi, T.; Ghelardini, C.; Pertwee, R. G.; Manera, C. Identification of the First Synthetic Allosteric Modulator of the CB_2 Receptors and Evidence of Its Efficacy for Neuropathic Pain Relief. *J. Med. Chem.* **2018**. https://doi.org/10.1021/acs.jmedchem.8b00368.

(166) Blankman, J. L.; Simon, G. M.; Cravatt, B. F. A Comprehensive Profile of Brain Enzymes That Hydrolyze the Endocannabinoid 2-Arachidonoylglycerol. *Chem. Biol.* **2007**, *14* (12), 1347–1356. https://doi.org/10.1016/j.chembiol.2007.11.006.

(167) Pertwee, R. G. The Therapeutic Potential of Drugs That Target Cannabinoid Receptors or Modulate the Tissue Levels or Actions of Endocannabinoids. In *Drug addiction from basic research to therapy*; Rapaka, R., Sadee, W., Eds.; Springer, 2008; pp 637–686.

(168) *Class 3.4–6 Hydrolases, Lyases, Isomerases, Ligases*; Schomburg, D., Schomburg, I., Eds.; Springer Berlin Heidelberg: Berlin, Heidelberg, 2013. https://doi.org/10.1007/978-3-642-36260-6.

(169) Pertwee, R. G.; Howlett, A. C.; Abood, M. E.; Alexander, S. P. H.; Di Marzo, V.; Elphick, M. R.; Greasley, P. J.; Hansen, H. S.; Kunos, G.; Mackie, K.; Mechoulam, R.; Ross, R. A. International Union of Basic and Clinical Pharmacology. LXXIX. Cannabinoid Receptors and Their Ligands: Beyond CB1 and CB2. *Pharmacol. Rev.* **2010**, *62* (4), 588–631. https://doi.org/10.1124/pr.110.003004.

(170) Pacher, P. The Endocannabinoid System as an Emerging Target of Pharmacotherapy. *Pharmacol. Rev.* **2006**, *58* (3), 389–462. https://doi.org/10.1124/pr.58.3.2.

(171) Fraguas-Sánchez, A. I.; Torres-Suárez, A. I. Medical Use of Cannabinoids. *Drugs* **2018**. https://doi.org/10.1007/s40265-018-0996-1.

(172) West, M. E. Cannabis and Night Vision. *Nature* **1991**, *351* (6329), 703–704. https://doi.org/10.1038/351703b0.

(173) *Cannabinoids as Therapeutics*; Mechoulam, R., Ed.; Milestones in drug therapy; Birkhäuser: Basel, 2005.

(174) Herkenham, M.; Lynn, A. B.; Little, M. D.; Johnson, M. R.; Melvin, L. S.; de Costa, B. R.; Rice, K. C. Cannabinoid Receptor Localization in Brain. *Proc. Natl. Acad. Sci. U. S. A.* **1990**, *87* (5), 1932–1936. https://doi.org/10.1073/pnas.87.5.1932.

(175) Pérez-Gómez, E.; Andradas, C.; Blasco-Benito, S.; Caffarel, M. M.; García-Taboada, E.; Villa-Morales, M.; Moreno, E.; Hamann, S.; Martín-Villar, E.; Flores, J. M.; Wenners, A.; Alkatout, I.; Klapper, W.; Röcken, C.; Bronsert, P.; Stickeler, E.; Staebler, A.; Bauer, M.; Arnold, N.; Soriano, J.; Pérez-Martínez, M.; Megías, D.; Moreno-Bueno, G.; Ortega-Gutiérrez, S.; Artola, M.; Vázquez-Villa, H.; Quintanilla, M.; Fernández-Piqueras, J.; Canela, E. I.; McCormick, P. J.; Guzmán, M.; Sánchez, C. Role of Cannabinoid Receptor CB2 in HER2 Pro-Oncogenic Signaling in Breast Cancer. *JNCI J. Natl. Cancer Inst.* **2015**, *107* (6). https://doi.org/10.1093/jnci/djv077.

(176) Marcu, J. P.; Christian, R. T.; Lau, D.; Zielinski, A. J.; Horowitz, M. P.; Lee, J.; Pakdel, A.; Allison, J.; Limbad, C.; Moore, D. H.; Yount, G. L.; Desprez, P.-Y.; McAllister, S. D. Cannabidiol Enhances the Inhibitory Effects of Delta9-Tetrahydrocannabinol on Human Glioblastoma Cell Proliferation and Survival. *Mol. Cancer Ther.* **2010**, *9* (1), 180–189. https://doi.org/10.1158/1535-7163.MCT-09-0407.

(177) Massi, P.; Solinas, M.; Cinquina, V.; Parolaro, D. Cannabidiol as Potential Anticancer Drug: Cannabidiol and Cancer. *Br. J. Clin. Pharmacol.* **2013**, *75* (2), 303–312. https://doi.org/10.1111/j.1365-2125.2012.04298.x.

(178) Vara, D.; Salazar, M.; Olea-Herrero, N.; Guzmán, M.; Velasco, G.; Díaz-Laviada, I. Anti-Tumoral Action of Cannabinoids on Hepatocellular Carcinoma: Role of AMPK-Dependent Activation of Autophagy. *Cell Death Differ.* **2011**, *18* (7), 1099–1111. https://doi.org/10.1038/cdd.2011.32.

(179) Grimaldi, C.; Pisanti, S.; Laezza, C.; Malfitano, A. M.; Santoro, A.; Vitale, M.; Caruso, M. G.; Notarnicola, M.; Iacuzzo, I.; Portella, G.; Di Marzo, V.; Bifulco, M. Anandamide Inhibits Adhesion and Migration of Breast Cancer Cells. *Exp. Cell Res.* **2006**, *312* (4), 363–373. https://doi.org/10.1016/j.yexcr.2005.10.024.

(180) Ligresti, A.; Moriello, A. S.; Starowicz, K.; Matias, I.; Pisanti, S.; De Petrocellis, L.; Laezza, C.; Portella, G.; Bifulco, M.; Di Marzo, V. Antitumor Activity of Plant Cannabinoids with Emphasis on the Effect of Cannabidiol on Human Breast

Carcinoma. *J. Pharmacol. Exp. Ther.* **2006**, *318* (3), 1375–1387. https://doi.org/10.1124/jpet.106.105247.

(181) Qamri, Z.; Preet, A.; Nasser, M. W.; Bass, C. E.; Leone, G.; Barsky, S. H.; Ganju, R. K. Synthetic Cannabinoid Receptor Agonists Inhibit Tumor Growth and Metastasis of Breast Cancer. *Mol. Cancer Ther.* **2009**, *8* (11), 3117–3129. https://doi.org/10.1158/1535-7163.MCT-09-0448.

(182) Blasco-Benito, S.; Seijo-Vila, M.; Caro-Villalobos, M.; Tundidor, I.; Andradas, C.; García-Taboada, E.; Wade, J.; Smith, S.; Guzmán, M.; Pérez-Gómez, E.; Gordon, M.; Sánchez, C. Appraising the "Entourage Effect": Antitumor Action of a Pure Cannabinoid versus a Botanical Drug Preparation in Preclinical Models of Breast Cancer. *Biochem. Pharmacol.* **2018**, *157*, 285–293. https://doi.org/10.1016/j.bcp.2018.06.025.

(183) Osei-Hyiaman, D.; DePetrillo, M.; Pacher, P.; Liu, J.; Radaeva, S.; Bátkai, S.; Harvey-White, J.; Mackie, K.; Offertáler, L.; Wang, L.; Kunos, G. Endocannabinoid Activation at Hepatic CB1 Receptors Stimulates Fatty Acid Synthesis and Contributes to Diet-Induced Obesity. *J. Clin. Invest.* **2005**, *115* (5), 1298–1305. https://doi.org/10.1172/JCI200523057.

(184) Piazza, P. V.; Cota, D.; Marsicano, G. The CB1 Receptor as the Cornerstone of Exostasis. *Neuron* **2017**, *93* (6), 1252–1274. https://doi.org/10.1016/j.neuron.2017.02.002.

(185) Quarta, C.; Bellocchio, L.; Mancini, G.; Mazza, R.; Cervino, C.; Braulke, L. J.; Fekete, C.; Latorre, R.; Nanni, C.; Bucci, M.; Clemens, L. E.; Heldmaier, G.; Watanabe, M.; Leste-Lassere, T.; Maitre, M.; Tedesco, L.; Fanelli, F.; Reuss, S.; Klaus, S.; Srivastava, R. K.; Monory, K.; Valerio, A.; Grandis, A.; De Giorgio, R.; Pasquali, R.; Nisoli, E.; Cota, D.; Lutz, B.; Marsicano, G.; Pagotto, U. CB1 Signaling in Forebrain and Sympathetic Neurons Is a Key Determinant of Endocannabinoid Actions on Energy Balance. *Cell Metab.* **2010**, *11* (4), 273–285. https://doi.org/10.1016/j.cmet.2010.02.015.

(186) Bajzer, M.; Olivieri, M.; Haas, M. K.; Pfluger, P. T.; Magrisso, I. J.; Foster, M. T.; Tschöp, M. H.; Krawczewski-Carhuatanta, K. A.; Cota, D.; Obici, S. Cannabinoid Receptor 1 (CB1) Antagonism Enhances Glucose Utilisation and Activates Brown Adipose Tissue in Diet-Induced Obese Mice. *Diabetologia* **2011**, *54* (12), 3121–3131. https://doi.org/10.1007/s00125-011-2302-6.

(187) Hall, W.; Christie, M.; Currow, D. Cannabinoids and Cancer: Causation, Remediation, and Palliation. *Lancet Oncol.* **2005**, *6* (1), 35–42. https://doi.org/10.1016/S1470-2045(04)01711-5.

(188) Martin, B. R.; Wiley, J. L. Mechanism of Action of Cannabinoids: How It May Lead to Treatment of Cachexia, Emesis, and Pain. *J. Support. Oncol.* **2004**, *2* (4), 305–316.

(189) Benito, C.; Núñez, E.; Tolón, R. M.; Carrier, E. J.; Rábano, A.; Hillard, C. J.; Romero, J. Cannabinoid CB2 Receptors and Fatty Acid Amide Hydrolase Are Selectively Overexpressed in Neuritic Plaque-Associated Glia in Alzheimer's Disease Brains. *J. Neurosci. Off. J. Soc. Neurosci.* **2003**, *23* (35), 11136–11141. https://doi.org/10.1523/JNEUROSCI.23-35-11136.2003.

(190) Marsicano, G. CB1 Cannabinoid Receptors and On-Demand Defense Against Excitotoxicity. *Science* **2003**, *302* (5642), 84–88. https://doi.org/10.1126/science.1088208.

(191) Shirzadian, A.; Ostadhadi, S.; Hassanipour, M.; Shafaroodi, H.; Khoshnoodi, M.; Haj-Mirzaian, A.; Sharifzadeh, M.; Amiri, S.; Ghasemi, M.; Dehpour, A. R. Acute Foot-Shock Stress Decreased Seizure Susceptibility against Pentylenetetrazole-Induced Seizures in Mice: Interaction between Endogenous Opioids and Cannabinoids. *Epilepsy Behav. EB* **2018**, *87*, 25–31. https://doi.org/10.1016/j.yebeh.2018.06.035.

(192) Wallace, M. J.; Blair, R. E.; Falenski, K. W.; Martin, B. R.; DeLorenzo, R. J. The Endogenous Cannabinoid System Regulates Seizure Frequency and Duration in a Model of Temporal Lobe Epilepsy. *J. Pharmacol. Exp. Ther.* **2003**, *307* (1), 129–137. https://doi.org/10.1124/jpet.103.051920.

(193) Basavarajappa, B. S.; Shivakumar, M.; Joshi, V.; Subbanna, S. Endocannabinoid System in Neurodegenerative Disorders. *J. Neurochem.* **2017**, *142* (5), 624–648. https://doi.org/10.1111/jnc.14098.

(194) Hurley, M. J.; Mash, D. C.; Jenner, P. Expression of Cannabinoid CB1 Receptor MRNA in Basal Ganglia of Normal and Parkinsonian Human Brain. *J. Neural Transm. Vienna Austria 1996* **2003**, *110* (11), 1279–1288. https://doi.org/10.1007/s00702-003-0033-7.

(195) Gonçalves, E. D.; Dutra, R. C. Cannabinoid Receptors as Therapeutic Targets for Autoimmune Diseases: Where Do We Stand? *Drug Discov. Today* **2019**, S1359644618304847. https://doi.org/10.1016/j.drudis.2019.05.023.

(196) Borgan, F.; Beck, K.; Butler, E.; McCutcheon, R.; Veronese, M.; Vernon, A.; Howes, O. D. The Effects of Cannabinoid 1 Receptor Compounds on Memory: A Meta-Analysis and Systematic Review across Species. *Psychopharmacology (Berl.)* **2019**. https://doi.org/10.1007/s00213-019-05283-3.

(197) Evren, C. Cannabis Use and Cognitive Function. In *Handbook of Cannabis and Related Pathologies*; Elsevier, 2017; pp 70–78. https://doi.org/10.1016/B978-0-12-800756-3.00009-0.

(198) Chun, J.; Goetzl, E. J.; Hla, T.; Igarashi, Y.; Lynch, K. R.; Moolenaar, W.; Pyne, S.; Tigyi, G. International Union of Pharmacology. XXXIV. Lysophospholipid Receptor Nomenclature. *Pharmacol. Rev.* **2002**, *54* (2), 265–269. https://doi.org/10.1124/pr.110.003111.

(199) Halgren, T. A. Identifying and Characterizing Binding Sites and Assessing Druggability. *J. Chem. Inf. Model.* **2009**, *49* (2), 377–389. https://doi.org/10.1021/ci800324m.

(200) Chrencik, J. E.; Roth, C. B.; Terakado, M.; Kurata, H.; Omi, R.; Kihara, Y.; Warshaviak, D.; Nakade, S.; Asmar-Rovira, G.; Mileni, M.; Mizuno, H.; Griffith, M. T.; Rodgers, C.; Han, G. W.; Velasquez, J.; Chun, J.; Stevens, R. C.; Hanson, M. A. Crystal Structure of Antagonist Bound Human Lysophosphatidic Acid Receptor 1. *Cell* **2015**, *161* (7), 1633–1643. https://doi.org/10.1016/j.cell.2015.06.002.

(201) Hanson, M. A.; Roth, C. B.; Jo, E.; Griffith, M. T.; Scott, F. L.; Reinhart, G.; Desale, H.; Clemons, B.; Cahalan, S. M.; Schuerer, S. C.; Sanna, M. G.; Han, G. W.; Kuhn, P.; Rosen, H.; Stevens, R. C. Crystal Structure of a Lipid G Protein-

Coupled Receptor. *Science* **2012**, *335* (6070), 851–855. https://doi.org/10.1126/science.1215904.

(202) Al-Zoubi, R.; P. Hurst, D.; H. Reggio, P. Structural Insights from Recent CB1 X-Ray Crystal Structures. In *Recent Advances in Cannabinoid Research*; Costain, W. J., Ed.; IntechOpen, 2018. https://doi.org/10.5772/intechopen.73801.

(203) Patel, S.; Wohlfeil, E. R.; Rademacher, D. J.; Carrier, E. J.; Perry, L. J.; Kundu, A.; Falck, J. R.; Nithipatikom, K.; Campbell, W. B.; Hillard, C. J. The General Anesthetic Propofol Increases Brain N-Arachidonylethanolamine (Anandamide) Content and Inhibits Fatty Acid Amide Hydrolase. *Br. J. Pharmacol.* **2003**, *139* (5), 1005–1013. https://doi.org/10.1038/sj.bjp.0705334.

(204) Păunescu, H.; Coman, O. A.; Coman, L.; Ghiţă, I.; Georgescu, S. R.; Drăghia, F.; Fulga, I. Cannabinoid System and Cyclooxygenases Inhibitors. *J. Med. Life* **2011**, *4* (1), 11–20.

(205) Schelling, G.; Hauer, D.; Azad, S. C.; Schmoelz, M.; Chouker, A.; Schmidt, M.; Hornuss, C.; Rippberger, M.; Briegel, J.; Thiel, M.; Vogeser, M. Effects of General Anesthesia on Anandamide Blood Levels in Humans. *Anesthesiology* **2006**, *104* (2), 273–277. https://doi.org/10.1097/00000542-200602000-00012.

(206) Sanchez-Marin, L.; Pavon, F. J.; Decara, J.; Suarez, J.; Gavito, A.; Castilla-Ortega, E.; Rodriguez de Fonseca, F.; Serrano, A. Effects of Intermittent Alcohol Exposure on Emotion and Cognition: A Potential Role for the Endogenous Cannabinoid System and Neuroinflammation. *Front. Behav. Neurosci.* **2017**, *11*, 15. https://doi.org/10.3389/fnbeh.2017.00015.

(207) Dutertre, M.; Smith, C. L. Molecular Mechanisms of Selective Estrogen Receptor Modulator (SERM) Action. *J. Pharmacol. Exp. Ther.* **2000**, *295* (2), 431–437.

(208) Franks, L. N.; Ford, B. M.; Prather, P. L. Selective Estrogen Receptor Modulators: Cannabinoid Receptor Inverse Agonists with Differential CB1 and CB2 Selectivity. *Front. Pharmacol.* **2016**, *7*. https://doi.org/10.3389/fphar.2016.00503.

(209) Ford, B. M.; Franks, L. N.; Radominska-Pandya, A.; Prather, P. L. Tamoxifen Isomers and Metabolites Exhibit Distinct Affinity and Activity at Cannabinoid Receptors: Potential Scaffold for Drug Development. *PLOS ONE* **2016**, *11* (12), e0167240. https://doi.org/10.1371/journal.pone.0167240.

(210) Krieger, E.; Nabuurs, S.; Vriend, G. Homology Modeling. In *Structural Bioinformatics*; Bourne, P. E., Weissig, H., Eds.; Methods of Biochemical Analyses; Wiley-Liss, 2003; Vol. 44.

(211) Leach, A. R. *Molecular Modelling: Principles and Applications*, 2. ed.,.; Pearson/Prentice Hall: Harlow, 2009.

(212) Xiang, Z. Advances in Homology Protein Structure Modeling. *Curr. Protein Pept. Sci.* **2006**, *7* (3), 217–227. https://doi.org/10.2174/138920306777452312.

(213) Laskowski, R. A.; MacArthur, M. W.; Thornton, J. M. PROCHECK: Validation of Protein Structure Coordinates. *Int. Tables Crystallogr. Vol F Crystallogr. Biol. Macromol.* **2001**, 722–725. https://doi.org/10.1107/97809553602060000882.

(214) Ramachandran, G. N.; Sasisekharan, V. Conformation of Polypeptides and Proteins. *Adv. Protein Chem.* **1968**, *23*, 283–438. https://doi.org/10.1016/S0065-3233(08)60402-7.

(215) Jacobson, M. P.; Pincus, D. L.; Rapp, C. S.; Day, T. J. F.; Honig, B.; Shaw, D. E.; Friesner, R. A. A Hierarchical Approach to All-Atom Protein Loop Prediction.

Proteins Struct. Funct. Bioinforma. **2004**, *55* (2), 351–367. https://doi.org/10.1002/prot.10613.

(216) Nayeem, A. A Comparative Study of Available Software for High-Accuracy Homology Modeling: From Sequence Alignments to Structural Models. *Protein Sci.* **2006**, *15* (4), 808–824. https://doi.org/10.1110/ps.051892906.

(217) Krumrine, J.; Raubacher, F.; Brooijmans, N.; Kuntz, I. Principles and Methods of Docking and Ligand Design. In *Structural Bioinformatics*; Weissig, H., Bourne, P. E., Eds.; Methods of Biochemical Analyses; Wiley-Liss, 2003; Vol. 44.

(218) Meng, X.-Y.; Zhang, H.-X.; Mezei, M.; Cui, M. Molecular Docking: A Powerful Approach for Structure-Based Drug Discovery. *Curr. Comput. Aided Drug Des.* **2011**, *7* (2), 146–157. https://doi.org/10.2174/157340911795677602.

(219) Zhang, S. Computer-Aided Drug Discovery and Development. In *Drug Design and Discovery*; Satyanarayanajois, S. D., Ed.; Walker, J. M., Series Ed.; Methods in molecular biology; Humana Press, 2011; Vol. 716.

(220) Friesner, R. A.; Banks, J. L.; Murphy, R. B.; Halgren, T. A.; Klicic, J. J.; Mainz, D. T.; Repasky, M. P.; Knoll, E. H.; Shelley, M.; Perry, J. K.; Shaw, D. E.; Francis, P.; Shenkin, P. S. Glide: A New Approach for Rapid, Accurate Docking and Scoring. 1. Method and Assessment of Docking Accuracy. *J. Med. Chem.* **2004**, *47* (7), 1739–1749. https://doi.org/10.1021/jm0306430.

(221) Pagadala, N. S.; Syed, K.; Tuszynski, J. Software for Molecular Docking: A Review. *Biophys. Rev.* **2017**, *9* (2), 91–102. https://doi.org/10.1007/s12551-016-0247-1.

(222) Castro-Alvarez, A.; Costa, A. M.; Vilarrasa, J. The Performance of Several Docking Programs at Reproducing Protein-Macrolide-Like Crystal Structures. *Mol. Basel Switz.* **2017**, *22* (1). https://doi.org/10.3390/molecules22010136.

(223) Cross, J. B.; Thompson, D. C.; Rai, B. K.; Baber, J. C.; Fan, K. Y.; Hu, Y.; Humblet, C. Comparison of Several Molecular Docking Programs: Pose Prediction and Virtual Screening Accuracy. *J. Chem. Inf. Model.* **2009**, *49* (6), 1455–1474. https://doi.org/10.1021/ci900056c.

(224) Sherman, W.; Day, T.; Jacobson, M. P.; Friesner, R. A.; Farid, R. Novel Procedure for Modeling Ligand/Receptor Induced Fit Effects. *J. Med. Chem.* **2006**, *49* (2), 534–553. https://doi.org/10.1021/jm050540c.

(225) Durrant, J. D.; McCammon, J. A. Molecular Dynamics Simulations and Drug Discovery. *BMC Biol.* **2011**, *9* (1), 1. https://doi.org/10.1186/1741-7007-9-71.

(226) Hollingsworth, S. A.; Dror, R. O. Molecular Dynamics Simulation for All. *Neuron* **2018**, *99* (6), 1129–1143. https://doi.org/10.1016/j.neuron.2018.08.011.

(227) Ganesan, A.; Coote, M. L.; Barakat, K. Molecular Dynamics-Driven Drug Discovery: Leaping Forward with Confidence. *Drug Discov. Today* **2017**, *22* (2), 249–269. https://doi.org/10.1016/j.drudis.2016.11.001.

(228) Anwar, J.; Zahn, D. Polymorphic Phase Transitions: Macroscopic Theory and Molecular Simulation. *Adv. Drug Deliv. Rev.* **2017**, *117*, 47–70. https://doi.org/10.1016/j.addr.2017.09.017.

(229) Christen, M.; Hünenberger, P. H.; Bakowies, D.; Baron, R.; Bürgi, R.; Geerke, D. P.; Heinz, T. N.; Kastenholz, M. A.; Kräutler, V.; Oostenbrink, C.; Peter, C.; Trzesniak, D.; van Gunsteren, W. F. The GROMOS Software for Biomolecular

Simulation: GROMOS05. *J. Comput. Chem.* **2005**, *26* (16), 1719–1751. https://doi.org/10.1002/jcc.20303.

(230) Huang, J.; MacKerell, A. D. CHARMM36 All-Atom Additive Protein Force Field: Validation Based on Comparison to NMR Data. *J. Comput. Chem.* **2013**, *34* (25), 2135–2145. https://doi.org/10.1002/jcc.23354.

(231) Ponder, J. W.; Case, D. A. Force Fields for Protein Simulations. *Adv. Protein Chem.* **2003**, *66*, 27–85. https://doi.org/10.1016/S0065-3233(03)66002-X.

(232) David, C. C.; Jacobs, D. J. Principal Component Analysis: A Method for Determining the Essential Dynamics of Proteins. In *Protein Dynamics*; Livesay, D. R., Ed.; Humana Press: Totowa, NJ, 2014; Vol. 1084, pp 193–226. https://doi.org/10.1007/978-1-62703-658-0_11.

(233) Amadei, A.; Linssen, A. B. M.; Berendsen, H. J. C. Essential Dynamics of Proteins. *Proteins Struct. Funct. Genet.* **1993**, *17* (4), 412–425. https://doi.org/10.1002/prot.340170408.

(234) Fleetwood, O.; Matricon, P.; Carlsson, J.; Delemotte, L. *Energy Landscapes Reveal Agonist Control of GPCR Activation via Microswitches*; preprint; Biophysics, 2019. https://doi.org/10.1101/627026.

(235) Díaz, Ó.; Dalton, J. A. R.; Giraldo, J. Revealing the Mechanism of Agonist-Mediated Cannabinoid Receptor 1 (CB1) Activation and Phospholipid-Mediated Allosteric Modulation. *J. Med. Chem.* **2019**, *62* (11), 5638–5654. https://doi.org/10.1021/acs.jmedchem.9b00612.

(236) Jung, S. W.; Cho, A. E.; Yu, W. Exploring the Ligand Efficacy of Cannabinoid Receptor 1 (CB1) Using Molecular Dynamics Simulations. *Sci. Rep.* **2018**, *8* (1), 13787. https://doi.org/10.1038/s41598-018-31749-z.

(237) Liu, Q.-R.; Huang, N. S.; Qu, H.; O'Connell, J. F.; Gonzalez-Mariscal, I.; Santa-Cruz-Calvo, S.; Doyle, M. E.; Xi, Z.-Xiong.; Wang, Y.; Onaivi, Emmanuel. S.; Egan, J. M. Identification of Novel Mouse and Rat CB1R Isoforms and In Silico Modeling of Human CB1R for Peripheral Cannabinoid Therapeutics. *Acta Pharmacol. Sin.* **2019**, *40* (3), 387–397. https://doi.org/10.1038/s41401-018-0152-1.

(238) Syed Haneef, S. A.; Ranganathan, S. Structural Bioinformatics Analysis of Variants on GPCR Function. *Curr. Opin. Struct. Biol.* **2019**, *55*, 161–177. https://doi.org/10.1016/j.sbi.2019.04.007.

(239) Sapundzhi, F. I.; Dzimbova, T. A.; Pencheva, N. S.; Milanov, P. B. Molecular Docking Experiments of Cannabinoid Receptor. *Belg. Chem. Commun.* **2017**, *50* (Special Issue B), 44–48.

(240) Loo, J. S. E.; Emtage, A. L.; Murali, L.; Lee, S. S.; Kueh, A. L. W.; Alexander, S. P. H. Ligand Discrimination during Virtual Screening of the CB1 Cannabinoid Receptor Crystal Structures Following Cross-Docking and Microsecond Molecular Dynamics Simulations. *RSC Adv.* **2019**, *9* (28), 15949–15956. https://doi.org/10.1039/C9RA01095E.

(241) Contartese, A.; Valoti, M.; Corelli, F.; Pasquini, S.; Mugnaini, C.; Pessina, F.; Aldinucci, C.; Sgaragli, G.; Frosini, M. A Novel CB2 Agonist, COR167, Potently Protects Rat Brain Cortical Slices against OGD and Reperfusion Injury. *Pharmacol. Res.* **2012**, *66* (6), 555–563. https://doi.org/10.1016/j.phrs.2012.08.003.

(242) Pasquini, S.; Ligresti, A.; Mugnaini, C.; Semeraro, T.; Cicione, L.; De Rosa, M.; Guida, F.; Luongo, L.; De Chiaro, M.; Cascio, M. G.; Bolognini, D.; Marini, P.; Pertwee, R.; Maione, S.; Marzo, V. D.; Corelli, F. Investigations on the 4-Quinolone-3-Carboxylic Acid Motif. 3. Synthesis, Structure−Affinity Relationships, and Pharmacological Characterization of 6-Substituted 4-Quinolone-3-Carboxamides as Highly Selective Cannabinoid-2 Receptor Ligands. *J. Med. Chem.* **2010**, *53* (16), 5915–5928. https://doi.org/10.1021/jm100123x.

(243) Cascio, M. G.; Bolognini, D.; Pertwee, R. G.; Palazzo, E.; Corelli, F.; Pasquini, S.; Di Marzo, V.; Maione, S. In Vitro and in Vivo Pharmacological Characterization of Two Novel Selective Cannabinoid CB(2) Receptor Inverse Agonists. *Pharmacol. Res.* **2010**, *61* (4), 349–354. https://doi.org/10.1016/j.phrs.2009.11.011.

(244) The UniProt Consortium. UniProt: A Worldwide Hub of Protein Knowledge. *Nucleic Acids Res.* **2019**, *47* (D1), D506–D515. https://doi.org/10.1093/nar/gky1049.

(245) Altschul, S. F.; Gish, W.; Miller, W.; Myers, E. W.; Lipman, D. J. Basic Local Alignment Search Tool. *J. Mol. Biol.* **1990**, *215* (3), 403–410. https://doi.org/10.1016/S0022-2836(05)80360-2.

(246) Rice, P.; Longden, I.; Bleasby, A. EMBOSS: The European Molecular Biology Open Software Suite. *Trends Genet. TIG* **2000**, *16* (6), 276–277. https://doi.org/10.1016/S0168-9525(00)02024-2.

(247) Ahn, K. H.; Bertalovitz, A. C.; Mierke, D. F.; Kendall, D. A. Dual Role of the Second Extracellular Loop of the Cannabinoid Receptor 1: Ligand Binding and Receptor Localization. *Mol. Pharmacol.* **2009**, *76* (4), 833–842. https://doi.org/10.1124/mol.109.057356.

(248) Fredriksson, R.; Höglund, P. J.; Gloriam, D. E. I.; Lagerström, M. C.; Schiöth, H. B. Seven Evolutionarily Conserved Human Rhodopsin G Protein-Coupled Receptors Lacking Close Relatives. *FEBS Lett.* **2003**, *554* (3), 381–388. https://doi.org/10.1016/s0014-5793(03)01196-7.

(249) Sastry, G. M.; Adzhigirey, M.; Day, T.; Annabhimoju, R.; Sherman, W. Protein and Ligand Preparation: Parameters, Protocols, and Influence on Virtual Screening Enrichments. *J. Comput. Aided Mol. Des.* **2013**, *27* (3), 221–234. https://doi.org/10.1007/s10822-013-9644-8.

(250) Kim, S.; Chen, J.; Cheng, T.; Gindulyte, A.; He, J.; He, S.; Li, Q.; Shoemaker, B. A.; Thiessen, P. A.; Yu, B.; Zaslavsky, L.; Zhang, J.; Bolton, E. E. PubChem 2019 Update: Improved Access to Chemical Data. *Nucleic Acids Res.* **2019**, *47* (D1), D1102–D1109. https://doi.org/10.1093/nar/gky1033.

(251) *Maestro*; Schrodinger Release 2016-3; Schrödinger, LLC: New York, NY, 2016.

(252) *LigPrep*; Schrodinger Release 2016-3; Schrödinger, LLC: New York, NY, 2016.

(253) Wang, Z.; Sun, H.; Yao, X.; Li, D.; Xu, L.; Li, Y.; Tian, S.; Hou, T. Comprehensive Evaluation of Ten Docking Programs on a Diverse Set of Protein-Ligand Complexes: The Prediction Accuracy of Sampling Power and Scoring Power. *Phys. Chem. Chem. Phys. PCCP* **2016**, *18* (18), 12964–12975. https://doi.org/10.1039/c6cp01555g.

(254) Tian, S.; Sun, H.; Pan, P.; Li, D.; Zhen, X.; Li, Y.; Hou, T. Assessing an Ensemble Docking-Based Virtual Screening Strategy for Kinase Targets by Considering

Protein Flexibility. *J. Chem. Inf. Model.* **2014**, *54* (10), 2664–2679. https://doi.org/10.1021/ci500414b.

(255) Halgren, T. A.; Murphy, R. B.; Friesner, R. A.; Beard, H. S.; Frye, L. L.; Pollard, W. T.; Banks, J. L. Glide: A New Approach for Rapid, Accurate Docking and Scoring. 2. Enrichment Factors in Database Screening. *J. Med. Chem.* **2004**, *47* (7), 1750–1759. https://doi.org/10.1021/jm030644s.

(256) Keenan, C. M.; Storr, M. A.; Thakur, G. A.; Wood, J. T.; Wager-Miller, J.; Straiker, A.; Eno, M. R.; Nikas, S. P.; Bashashati, M.; Hu, H.; Mackie, K.; Makriyannis, A.; Sharkey, K. A. AM841, a Covalent Cannabinoid Ligand, Powerfully Slows Gastrointestinal Motility in Normal and Stressed Mice in a Peripherally Restricted Manner. *Br. J. Pharmacol.* **2015**, *172* (9), 2406–2418. https://doi.org/10.1111/bph.13069.

(257) Halgren, T. A.; Murphy, R. B.; Friesner, R. A.; Beard, H. S.; Frye, L. L.; Pollard, W. T.; Banks, J. L. Glide: A New Approach for Rapid, Accurate Docking and Scoring. 2. Enrichment Factors in Database Screening. *J. Med. Chem.* **2004**, *47* (7), 1750–1759. https://doi.org/10.1021/jm030644s.

(258) Wu, E. L.; Cheng, X.; Jo, S.; Rui, H.; Song, K. C.; Dávila-Contreras, E. M.; Qi, Y.; Lee, J.; Monje-Galvan, V.; Venable, R. M.; Klauda, J. B.; Im, W. CHARMM-GUI Membrane Builder toward Realistic Biological Membrane Simulations. *J. Comput. Chem.* **2014**, *35* (27), 1997–2004. https://doi.org/10.1002/jcc.23702.

(259) Lomize, M. A.; Pogozheva, I. D.; Joo, H.; Mosberg, H. I.; Lomize, A. L. OPM Database and PPM Web Server: Resources for Positioning of Proteins in Membranes. *Nucleic Acids Res.* **2012**, *40* (D1), D370–D376. https://doi.org/10.1093/nar/gkr703.

(260) Jorgensen, W. L.; Chandrasekhar, J.; Madura, J. D.; Impey, R. W.; Klein, M. L. Comparison of Simple Potential Functions for Simulating Liquid Water. *J. Chem. Phys.* **1983**, *79* (2), 926–935. https://doi.org/10.1063/1.445869.

(261) Vanommeslaeghe, K.; Hatcher, E.; Acharya, C.; Kundu, S.; Zhong, S.; Shim, J.; Darian, E.; Guvench, O.; Lopes, P.; Vorobyov, I.; Mackerell, A. D. CHARMM General Force Field: A Force Field for Drug-like Molecules Compatible with the CHARMM All-Atom Additive Biological Force Fields. *J. Comput. Chem.* **2009**, NA-NA. https://doi.org/10.1002/jcc.21367.

(262) Hoover, W. G. Canonical Dynamics: Equilibrium Phase-Space Distributions. *Phys. Rev. A* **1985**, *31* (3), 1695–1697. https://doi.org/10.1103/PhysRevA.31.1695.

(263) Parrinello, M.; Rahman, A. Polymorphic Transitions in Single Crystals: A New Molecular Dynamics Method. *J. Appl. Phys.* **1981**, *52* (12), 7182–7190. https://doi.org/10.1063/1.328693.

(264) Bussi, G.; Donadio, D.; Parrinello, M. Canonical Sampling through Velocity Rescaling. *J. Chem. Phys.* **2007**, *126* (1), 014101. https://doi.org/10.1063/1.2408420.

(265) Hess, B.; Bekker, H.; Berendsen, H. J. C.; Fraaije, J. G. E. M. LINCS: A Linear Constraint Solver for Molecular Simulations. *J. Comput. Chem.* **1993**, *18* (12), 1463–1472. https://doi.org/10.1002/(SICI)1096-987X(199709)18:12<1463::AID-JCC4>3.0.CO;2-H.

(266) Essmann, U.; Perera, L.; Berkowitz, M. L. A Smooth Particle Mesh Ewald Method. *J. Chem. Phys.* **1995**, *103* (19). https://doi.org/10.1063/1.470117.

(267) Shkurti, A.; Goni, R.; Andrio, P.; Breitmoser, E.; Bethune, I.; Orozco, M.; Laughton, C. A. PyPcazip: A PCA-Based Toolkit for Compression and Analysis of Molecular Simulation Data. *SoftwareX* **2016**, *5*, 44–50. https://doi.org/10.1016/j.softx.2016.04.002.

(268) Humphrey, W.; Dalke, A.; Schulten, K. VMD: Visual Molecular Dynamics. *J. Mol. Graph.* **1996**, *14* (1), 33–38. https://doi.org/10.1016/0263-7855(96)00018-5.

(269) Racine, J. Gnuplot 4.0: A Portable Interactive Plotting Utility. *J. Appl. Econom.* **2006**, *21* (1), 133–141. https://doi.org/10.1002/jae.885.

(270) Laskowski, R. A.; Swindells, M. B. LigPlot+: Multiple Ligand-Protein Interaction Diagrams for Drug Discovery. *J. Chem. Inf. Model.* **2011**, *51* (10), 2778–2786. https://doi.org/10.1021/ci200227u.

(271) Picone, R. P. AM841, A High-Affinity Electrophilic Ligand Interacts Covalently with a Cysteine in Helix Six and Activates the CB1 Cannabinoid Receptor. *Mol. Pharmacol.* **2005**. https://doi.org/10.1124/mol.105.014407.

(272) Hurst, D. P.; Grossfield, A.; Lynch, D. L.; Feller, S.; Romo, T. D.; Gawrisch, K.; Pitman, M. C.; Reggio, P. H. A Lipid Pathway for Ligand Binding Is Necessary for a Cannabinoid G Protein-Coupled Receptor. *J. Biol. Chem.* **2010**, *285* (23), 17954–17964. https://doi.org/10.1074/jbc.M109.041590.

(273) Makriyannis, A.; Tian, X.; Guo, J. How Lipophilic Cannabinergic Ligands Reach Their Receptor Sites. *Prostaglandins Other Lipid Mediat.* **2005**, *77* (1–4), 210–218. https://doi.org/10.1016/j.prostaglandins.2004.01.010.

(274) Ng, H. W.; Laughton, C. A.; Doughty, S. W. Molecular Dynamics Simulations of the Adenosine A2a Receptor: Structural Stability, Sampling, and Convergence. *J. Chem. Inf. Model.* **2013**, *53* (5), 1168–1178. https://doi.org/10.1021/ci300610w.

(275) Stein, S. A. M.; Loccisano, A. E.; Firestine, S. M.; Evanseck, J. D. Chapter 13 Principal Components Analysis: A Review of Its Application on Molecular Dynamics Data. In *Annual Reports in Computational Chemistry*; Elsevier, 2006; Vol. 2, pp 233–261. https://doi.org/10.1016/S1574-1400(06)02013-5.

(276) *The PyMOL Molecular Graphics System*; Schrödinger, LLC.

(277) Caliman, A. D.; Miao, Y.; McCammon, J. A. Activation Mechanisms of the First Sphingosine-1-Phosphate Receptor: Activation Mechanisms of the S1PR1. *Protein Sci.* **2017**, *26* (6), 1150–1160. https://doi.org/10.1002/pro.3165.

(278) Jakowiecki, J.; Filipek, S. Hydrophobic Ligand Entry and Exit Pathways of the CB1 Cannabinoid Receptor. *J. Chem. Inf. Model.* **2016**, *56* (12), 2457–2466. https://doi.org/10.1021/acs.jcim.6b00499.

(279) Milligan, G. G Protein-Coupled Receptor Hetero-Dimerization: Contribution to Pharmacology and Function. *Br. J. Pharmacol.* **2009**, *158* (1), 5–14. https://doi.org/10.1111/j.1476-5381.2009.00169.x.

(280) Miao, Y.; Nichols, S. E.; McCammon, J. A. Free Energy Landscape of G-Protein Coupled Receptors, Explored by Accelerated Molecular Dynamics. *Phys. Chem. Chem. Phys.* **2014**, *16* (14), 6398. https://doi.org/10.1039/c3cp53962h.

(281) Romo, T. D.; Grossfield, A.; Pitman, M. C. Concerted Interconversion between Ionic Lock Substates of the B2 Adrenergic Receptor Revealed by Microsecond Timescale Molecular Dynamics. *Biophys. J.* **2010**, *98* (1), 76–84. https://doi.org/10.1016/j.bpj.2009.09.046.

(282) Li, J.; Jonsson, A. L.; Beuming, T.; Shelley, J. C.; Voth, G. A. Ligand-Dependent Activation and Deactivation of the Human Adenosine A $_{2A}$ Receptor. *J. Am. Chem. Soc.* **2013**, *135* (23), 8749–8759. https://doi.org/10.1021/ja404391q.

(283) Abraham, M. J.; Murtola, T.; Schulz, R.; Páll, S.; Smith, J. C.; Hess, B.; Lindahl, E. GROMACS: High Performance Molecular Simulations through Multi-Level Parallelism from Laptops to Supercomputers. *SoftwareX* **2015**, *1–2*, 19–25. https://doi.org/10.1016/j.softx.2015.06.001.

(284) Jämbeck, J. P. M.; Lyubartsev, A. P. Derivation and Systematic Validation of a Refined All-Atom Force Field for Phosphatidylcholine Lipids. *J. Phys. Chem. B* **2012**, *116* (10), 3164–3179. https://doi.org/10.1021/jp212503e.

(285) Lindorff-Larsen, K.; Piana, S.; Palmo, K.; Maragakis, P.; Klepeis, J. L.; Dror, R. O.; Shaw, D. E. Improved Side-Chain Torsion Potentials for the Amber Ff99SB Protein Force Field. *Proteins* **2010**, *78* (8), 1950–1958. https://doi.org/10.1002/prot.22711.

(286) Wang, J.; Wolf, R. M.; Caldwell, J. W.; Kollman, P. A.; Case, D. A. Development and Testing of a General Amber Force Field. *J. Comput. Chem.* **2004**, *25* (9), 1157–1174. https://doi.org/10.1002/jcc.20035.

(287) Sousa da Silva, A. W.; Vranken, W. F. ACPYPE - AnteChamber PYthon Parser InterfacE. *BMC Res. Notes* **2012**, *5*, 367. https://doi.org/10.1186/1756-0500-5-367.

(288) Berendsen, H. J. C.; Postma, J. P. M.; van Gunsteren, W. F.; DiNola, A.; Haak, J. R. Molecular Dynamics with Coupling to an External Bath. *J. Chem. Phys.* **1984**, *81* (8), 3684–3690. https://doi.org/10.1063/1.448118.

(289) Halgren, T. New Method for Fast and Accurate Binding-Site Identification and Analysis. *Chem. Biol. Drug Des.* **2007**, *69* (2), 146–148. https://doi.org/10.1111/j.1747-0285.2007.00483.x.

(290) Lindahl; Abraham; Hess; Spoel, V. D. *GROMACS 2019.2 Source Code*; Zenodo, 2019. https://doi.org/10.5281/zenodo.2636382.

(291) Xie, X. Q.; Melvin, L. S.; Makriyannis, A. The Conformational Properties of the Highly Selective Cannabinoid Receptor Ligand CP-55,940. *J. Biol. Chem.* **1996**, *271* (18), 10640–10647. https://doi.org/10.1074/jbc.271.18.10640.

(292) Ashburn, T. T.; Thor, K. B. Drug Repositioning: Identifying and Developing New Uses for Existing Drugs. *Nat. Rev. Drug Discov.* **2004**, *3* (8), 673–683. https://doi.org/10.1038/nrd1468.

(293) *20th WHO Essential Medicines List*; WHO Essential Medicines List; World Health Organization, 2017.

(294) Pushpakom, S.; Iorio, F.; Eyers, P. A.; Escott, K. J.; Hopper, S.; Wells, A.; Doig, A.; Guilliams, T.; Latimer, J.; McNamee, C.; Norris, A.; Sanseau, P.; Cavalla, D.; Pirmohamed, M. Drug Repurposing: Progress, Challenges and Recommendations. *Nat. Rev. Drug Discov.* **2019**, *18* (1), 41–58. https://doi.org/10.1038/nrd.2018.168.

(295) Dakshanamurthy, S.; Issa, N. T.; Assefnia, S.; Seshasayee, A.; Peters, O. J.; Madhavan, S.; Uren, A.; Brown, M. L.; Byers, S. W. Predicting New Indications for Approved Drugs Using a Proteochemometric Method. *J. Med. Chem.* **2012**, *55* (15), 6832–6848. https://doi.org/10.1021/jm300576q.

(296) Sinning, C.; Watzer, B.; Coste, O.; Nüsing, R. M.; Ott, I.; Ligresti, A.; Di Marzo, V.; Imming, P. New Analgesics Synthetically Derived from the Paracetamol Metabolite N-(4-Hydroxyphenyl)-(5Z,8Z,11Z,14Z)-Icosatetra-5,8,11,14-

Enamide. *J. Med. Chem.* **2008**, *51* (24), 7800–7805. https://doi.org/10.1021/jm800807k.

(297) Priestley, R. S.; Nickolls, S. A.; Alexander, S. P. H.; Kendall, D. A. A Potential Role for Cannabinoid Receptors in the Therapeutic Action of Fenofibrate. *FASEB J.* **2015**, *29* (4), 1446–1455. https://doi.org/10.1096/fj.14-263053.

(298) Scala, C.; Fantini, J.; Yahi, N.; Barrantes, F.; Chahinian, H. Anandamide Revisited: How Cholesterol and Ceramides Control Receptor-Dependent and Receptor-Independent Signal Transmission Pathways of a Lipid Neurotransmitter. *Biomolecules* **2018**, *8* (2), 31. https://doi.org/10.3390/biom8020031.

(299) Asano, T.; Pedersen, S. E.; Scott, C. W.; Ross, E. Reconstitution of Catecholamine-Stimulated Binding of Guanosine 5'-O-(3-Thiotriphosphate) to the Stimulatory GTP-Binding Protein of Adenylate Cyclase. *Biochemistry* **1984**, *23* (23), 5460–5467. https://doi.org/10.1021/bi00318a013.

(300) *GraphPad Prism*; GraphPad Software, Inc.: San Diego, California, USA, 2019.

(301) Zheng, Y.; Wang, X.-L.; Mo, F.-F.; Li, M. Dexamethasone Alleviates Motion Sickness in Rats in Part by Enhancing the Endocannabinoid System. *Eur. J. Pharmacol.* **2014**, *727*, 99–105. https://doi.org/10.1016/j.ejphar.2014.01.047.

(302) McPartland, J. M.; Guy, G. W.; Di Marzo, V. Care and Feeding of the Endocannabinoid System: A Systematic Review of Potential Clinical Interventions That Upregulate the Endocannabinoid System. *PLoS ONE* **2014**, *9* (3), e89566. https://doi.org/10.1371/journal.pone.0089566.

(303) Kearn, C. S.; Blake-Palmer, K.; Daniel, E.; Mackie, K.; Glass, M. Concurrent Stimulation of Cannabinoid CB1 and Dopamine D2 Receptors Enhances Heterodimer Formation: A Mechanism for Receptor Cross-Talk? *Mol. Pharmacol.* **2005**, *67* (5), 1697–1704. https://doi.org/10.1124/mol.104.006882.

(304) Morales, P.; Goya, P.; Jagerovic, N.; Hernandez-Folgado, L. Allosteric Modulators of the CB $_1$ Cannabinoid Receptor: A Structural Update Review. *Cannabis Cannabinoid Res.* **2016**, *1* (1), 22–30. https://doi.org/10.1089/can.2015.0005.

(305) *LigPrep*; Schrodinger Release 2018-1; Schrödinger, LLC: New York, NY, 2018.

(306) Greenwood, J. R.; Calkins, D.; Sullivan, A. P.; Shelley, J. C. Towards the Comprehensive, Rapid, and Accurate Prediction of the Favorable Tautomeric States of Drug-like Molecules in Aqueous Solution. *J. Comput. Aided Mol. Des.* **2010**, *24* (6–7), 591–604. https://doi.org/10.1007/s10822-010-9349-1.

(307) *Maestro*; Schrodinger Release 2019-2; Schrödinger, LLC: New York, NY, 2019.

(308) Franks, L. N.; Ford, B. M.; Prather, P. L. Selective Estrogen Receptor Modulators: Cannabinoid Receptor Inverse Agonists with Differential CB1 and CB2 Selectivity. *Front. Pharmacol.* **2016**, *7*, 503. https://doi.org/10.3389/fphar.2016.00503.

(309) Franks, L. N.; Ford, B. M.; Fujiwara, T.; Zhao, H.; Prather, P. L. The Tamoxifen Derivative Ridaifen-B Is a High Affinity Selective CB 2 Receptor Inverse Agonist Exhibiting Anti-Inflammatory and Anti-Osteoclastogenic Effects. *Toxicol. Appl. Pharmacol.* **2018**, *353*, 31–42. https://doi.org/10.1016/j.taap.2018.06.009.

(310) Reggio, P. H.; Traore, H. Conformational Requirements for Endocannabinoid Interaction with the Cannabinoid Receptors, the Anandamide Transporter and Fatty Acid Amidohydrolase. *Chem. Phys. Lipids* **2000**, *108* (1–2), 15–35. https://doi.org/10.1016/S0009-3084(00)00185-7.

(311) Salo, O. M. H.; Lahtela-Kakkonen, M.; Gynther, J.; Järvinen, T.; Poso, A. Development of a 3D Model for the Human Cannabinoid CB1 Receptor. *J. Med. Chem.* **2004**, *47* (12), 3048–3057. https://doi.org/10.1021/jm031052c.

(312) Ogawa, G.; Tius, M. A.; Zhou, H.; Nikas, S. P.; Halikhedkar, A.; Mallipeddi, S.; Makriyannis, A. 3'-Functionalized Adamantyl Cannabinoid Receptor Probes. *J. Med. Chem.* **2015**, *58* (7), 3104–3116. https://doi.org/10.1021/jm501960u.

(313) Dhopeshwarkar, A.; Murataeva, N.; Makriyannis, A.; Straiker, A.; Mackie, K. Two Janus Cannabinoids That Are Both CB_2 Agonists and CB_1 Antagonists. *J. Pharmacol. Exp. Ther.* **2017**, *360* (2), 300–311. https://doi.org/10.1124/jpet.116.236539.

(314) LoVerme, J.; Duranti, A.; Tontini, A.; Spadoni, G.; Mor, M.; Rivara, S.; Stella, N.; Xu, C.; Tarzia, G.; Piomelli, D. Synthesis and Characterization of a Peripherally Restricted CB1 Cannabinoid Antagonist, URB447, That Reduces Feeding and Body-Weight Gain in Mice. *Bioorg. Med. Chem. Lett.* **2009**, *19* (3), 639–643. https://doi.org/10.1016/j.bmcl.2008.12.059.

(315) Heyden, M.; Jardon-Valadez, H. E.; Bondar, A.-N.; Tobias, D. J. GPCR Activation on the Microsecond Timescale in MD Simulations. *Biophys. J.* **2013**, *104* (2), 115a. https://doi.org/10.1016/j.bpj.2012.11.666.

(316) Zou, Y.; Ewalt, J.; Ng, H.-L. Recent Insights from Molecular Dynamics Simulations for G Protein-Coupled Receptor Drug Discovery. *Int. J. Mol. Sci.* **2019**, *20* (17). https://doi.org/10.3390/ijms20174237.

(317) Hamelberg, D.; Mongan, J.; McCammon, J. A. Accelerated Molecular Dynamics: A Promising and Efficient Simulation Method for Biomolecules. *J. Chem. Phys.* **2004**, *120* (24), 11919–11929. https://doi.org/10.1063/1.1755656.

(318) Valsson, O.; Tiwary, P.; Parrinello, M. Enhancing Important Fluctuations: Rare Events and Metadynamics from a Conceptual Viewpoint. *Annu. Rev. Phys. Chem.* **2016**, *67* (1), 159–184. https://doi.org/10.1146/annurev-physchem-040215-112229.

(319) Lovera, S.; Cuzzolin, A.; Kelm, S.; De Fabritiis, G.; Sands, Z. A. Reconstruction of Apo A2A Receptor Activation Pathways Reveal Ligand-Competent Intermediates and State-Dependent Cholesterol Hotspots. *Sci. Rep.* **2019**, *9* (1), 14199. https://doi.org/10.1038/s41598-019-50752-6.

(320) Martínez-Archundia, M.; Correa-Basurto, J.; Montaño, S.; Rosas-Trigueros, J. L. Studying the Collective Motions of the Adenosine A2A Receptor as a Result of Ligand Binding Using Principal Component Analysis. *J. Biomol. Struct. Dyn.* **2019**, *37* (18), 4685–4700. https://doi.org/10.1080/07391102.2018.1564700.

(321) Miao, Y.; Nichols, S. E.; Gasper, P. M.; Metzger, V. T.; McCammon, J. A. Activation and Dynamic Network of the M2 Muscarinic Receptor. *Proc. Natl. Acad. Sci.* **2013**, *110* (27), 10982–10987. https://doi.org/10.1073/pnas.1309755110.

(322) Frost, J. M.; Dart, M. J.; Tietje, K. R.; Garrison, T. R.; Grayson, G. K.; Daza, A. V.; El-Kouhen, O. F.; Miller, L. N.; Li, L.; Yao, B. B.; Hsieh, G. C.; Pai, M.; Zhu, C. Z.; Chandran, P.; Meyer, M. D. Indol-3-Yl-Tetramethylcyclopropyl Ketones: Effects of Indole Ring Substitution on CB2 Cannabinoid Receptor Activity. *J. Med. Chem.* **2008**, *51* (6), 1904–1912. https://doi.org/10.1021/jm7011613.

(323) Khanolkar, A. D.; Lu, D.; Ibrahim, M.; Duclos, R. I.; Thakur, G. A.; Malan, T. P.; Porreca, F.; Veerappan, V.; Tian, X.; George, C.; Parrish, D. A.; Papahatjis, D. P.; Makriyannis, A. Cannabilactones: A Novel Class of CB2 Selective Agonists with Peripheral Analgesic Activity. *J. Med. Chem.* **2007**, *50* (26), 6493–6500. https://doi.org/10.1021/jm070441u.

(324) Järbe, T. U. C.; DiPatrizio, N. V.; Lu, D.; Makriyannis, A. (-)-Adamantyl-Delta8-Tetrahydrocannabinol (AM-411), a Selective Cannabinoid CB1 Receptor Agonist: Effects on Open-Field Behaviors and Antagonism by SR-141716 in Rats. *Behav. Pharmacol.* **2004**, *15* (7), 517–521. https://doi.org/10.1097/00008877-200411000-00008.

(325) Showalter, V. M.; Compton, D. R.; Martin, B. R.; Abood, M. E. Evaluation of Binding in a Transfected Cell Line Expressing a Peripheral Cannabinoid Receptor (CB2): Identification of Cannabinoid Receptor Subtype Selective Ligands. *J. Pharmacol. Exp. Ther.* **1996**, *278* (3), 989–999.

(326) López-Rodríguez, M. L.; Viso, A.; Ortega-Gutiérrez, S.; Lastres-Becker, I.; González, S.; Fernández-Ruiz, J.; Ramos, J. A. Design, Synthesis and Biological Evaluation of Novel Arachidonic Acid Derivatives as Highly Potent and Selective Endocannabinoid Transporter Inhibitors. *J. Med. Chem.* **2001**, *44* (26), 4505–4508. https://doi.org/10.1021/jm015545y.

(327) Huffman, J. W.; Zengin, G.; Wu, M.-J.; Lu, J.; Hynd, G.; Bushell, K.; Thompson, A. L. S.; Bushell, S.; Tartal, C.; Hurst, D. P.; Reggio, P. H.; Selley, D. E.; Cassidy, M. P.; Wiley, J. L.; Martin, B. R. Structure-Activity Relationships for 1-Alkyl-3-(1-Naphthoyl)Indoles at the Cannabinoid CB(1) and CB(2) Receptors: Steric and Electronic Effects of Naphthoyl Substituents. New Highly Selective CB(2) Receptor Agonists. *Bioorg. Med. Chem.* **2005**, *13* (1), 89–112. https://doi.org/10.1016/j.bmc.2004.09.050.

(328) Martin, B. R. Pharmacological Characterization of Novel Water-Soluble Cannabinoids. *J. Pharmacol. Exp. Ther.* **2006**, *318* (3), 1230–1239. https://doi.org/10.1124/jpet.106.104109.

(329) Meng, T.; Wang, J.; Peng, H.; Fang, G.; Li, M.; Xiong, B.; Xie, X.; Zhang, Y.; Wang, X.; Shen, J. Discovery of Benzhydrylpiperazine Derivatives as CB1 Receptor Inverse Agonists via Privileged Structure-Based Approach. *Eur. J. Med. Chem.* **2010**, *45* (3), 1133–1139. https://doi.org/10.1016/j.ejmech.2009.12.018.

(330) Meschler, J. P.; Kraichely, D. M.; Wilken, G. H.; Howlett, A. C. Inverse Agonist Properties of N-(Piperidin-1-Yl)-5-(4-Chlorophenyl)-1-(2,4-Dichlorophenyl)-4-Methyl-1H-Pyrazole-3-Carboxamide HCl (SR141716A) and 1-(2-Chlorophenyl)-4-Cyano-5-(4-Methoxyphenyl)-1H-Pyrazole-3-Carboxylic Acid Phenylamide (CP-272871) for the CB1 Cannabinoid Receptor. *Biochem. Pharmacol.* **2000**, *60* (9), 1315–1323. https://doi.org/10.1016/S0006-2952(00)00447-0.

(331) Kanyonyo, M.; Govaerts, S. J.; Hermans, E.; Poupaert, J. H.; Lambert, D. M. 3-Alkyl-(5,5′-Diphenyl)Imidazolidinediones as New Cannabinoid Receptor Ligands. *Bioorg. Med. Chem. Lett.* **1999**, *9* (15), 2233–2236. https://doi.org/10.1016/S0960-894X(99)00353-4.

(332) Lin, L. S.; Lanza, T. J.; Jewell, J. P.; Liu, P.; Shah, S. K.; Qi, H.; Tong, X.; Wang, J.; Xu, S. S.; Fong, T. M.; Shen, C.-P.; Lao, J.; Xiao, J. C.; Shearman, L. P.; Stribling, D. S.; Rosko, K.; Strack, A.; Marsh, D. J.; Feng, Y.; Kumar, S.; Samuel,

K.; Yin, W.; Van der Ploeg, L. H. T.; Goulet, M. T.; Hagmann, W. K. Discovery of N-[(1S,2S)-3-(4-Chlorophenyl)-2- (3-Cyanophenyl)-1-Methylpropyl]-2-Methyl-2- {[5-(Trifluoromethyl)Pyridin-2-Yl]Oxy}propanamide (MK-0364), a Novel, Acyclic Cannabinoid-1 Receptor Inverse Agonist for the Treatment of Obesity. *J. Med. Chem.* **2006**, *49* (26), 7584–7587. https://doi.org/10.1021/jm060996+.

(333) Ruiu, S. Synthesis and Characterization of NESS 0327: A Novel Putative Antagonist of the CB1 Cannabinoid Receptor. *J. Pharmacol. Exp. Ther.* **2003**, *306* (1), 363–370. https://doi.org/10.1124/jpet.103.049924.

(334) Katoch-Rouse, R.; Pavlova, O. A.; Caulder, T.; Hoffman, A. F.; Mukhin, A. G.; Horti, A. G. Synthesis, Structure−Activity Relationship, and Evaluation of SR141716 Analogues: Development of Central Cannabinoid Receptor Ligands with Lower Lipophilicity. *J. Med. Chem.* **2003**, *46* (4), 642–645. https://doi.org/10.1021/jm020157x.

(335) Wiley, J. L.; Jefferson, R. G.; Grier, M. C.; Mahadevan, A.; Razdan, R. K.; Martin, B. R. Novel Pyrazole Cannabinoids: Insights into CB(1) Receptor Recognition and Activation. *J. Pharmacol. Exp. Ther.* **2001**, *296* (3), 1013–1022.

(336) Lange, J. H. M.; Coolen, H. K. A. C.; van Stuivenberg, H. H.; Dijksman, J. A. R.; Herremans, A. H. J.; Ronken, E.; Keizer, H. G.; Tipker, K.; McCreary, A. C.; Veerman, W.; Wals, H. C.; Stork, B.; Verveer, P. C.; den Hartog, A. P.; de Jong, N. M. J.; Adolfs, T. J. P.; Hoogendoorn, J.; Kruse, C. G. Synthesis, Biological Properties, and Molecular Modeling Investigations of Novel 3,4-Diarylpyrazolines as Potent and Selective CB $_1$ Cannabinoid Receptor Antagonists. *J. Med. Chem.* **2004**, *47* (3), 627–643. https://doi.org/10.1021/jm031019q.

(337) Rinaldi-Carmona, M. SR147778 [5-(4-Bromophenyl)-1-(2,4-Dichlorophenyl)-4-Ethyl-N-(1-Piperidinyl)-1H-Pyrazole-3-Carboxamide], a New Potent and Selective Antagonist of the CB1 Cannabinoid Receptor: Biochemical and Pharmacological Characterization. *J. Pharmacol. Exp. Ther.* **2004**, *310* (3), 905–914. https://doi.org/10.1124/jpet.104.067884.

I Appendix 1

Figure I.1 Sequences of CB1 and CB2 Receptors

Cannabinoid Receptor 1

```
        10         20         30         40         50
MKSILDGLAD TTFRTITTDL LYVGSNDIQY EDIKGDMASK LGYFPQKFPL
        60         70         80         90        100
TSFRGSPFQE KMTAGDNPQL VPADQVNITE FYNKSLSSFK ENEENIQCGE
       110        120        130        140        150
NFMDIECFMV LNPSQQLAIA VLSLTLGTFT VLENLLVLCV ILHSRSLRCR
       160        170        180        190        200
PSYHFIGSLA VADLLGSVIF VYSFIDFHVF HRKDSRNVFL FKLGGVTASF
       210        220        230        240        250
TASVGSLFLT AIDRYISIHR PLAYKRIVTR PKAVVAFCLM WTIAIVIAVL
       260        270        280        290        300
PLLGWNCEKL QSVCSDIFPH IDETYLMFWI GVTSVLLLFI VYAYMYILWK
       310        320        330        340        350
AHSHAVRMIQ RGTQKSIIIH TSEDGKVQVT RPDQARMDIR LAKTLVLILV
       360        370        380        390        400
VLIICWGPLL AIMVYDVFGK MNKLIKTVFA FCSMLCLLNS TVNPIIYALR
       410        420        430        440        450
SKDLRHAFRS MFPSCEGTAQ PLDNSMGDSD CLHKHANNAA SVHRAAESCI
       460        470
KSTVKIAKVT MSVSTDTSAE AL
```

Cannabinoid Receptor 2

```
        10         20         30         40         50
MEECWVTEIA NGSKDGLDSN PMKDYMILSG PQKTAVAVLC TLLGLLSALE
        60         70         80         90        100
NVAVLYLILS SHQLRRKPSY LFIGSLAGAD FLASVVFACS FVNFHVFHGV
       110        120        130        140        150
DSKAVFLLKI GSVTMTFTAS VGSLLLTAID RYLCLRYPPS YKALLTRGRA
       160        170        180        190        200
LVTLGIMWVL SALVSYLPLM GWTCCPRPCS ELFPLIPNDY LLSWLLFIAF
       210        220        230        240        250
LFSGIIYTYG HVLWKAHQHV ASLSGHQDRQ VPGMARMRLD VRLAKTLGLV
       260        270        280        290        300
LAVLLICWFP VLALMAHSLA TTLSDQVKKA FAFCSMLCLI NSMVNPVIYA
       310        320        330        340        350
LRSGEIRSSA HHCLAHWKKC VRGLGSEAKE EAPRSSVTET EADGKITPWP
       360
DSRDLDLSDC
```

Table I.1 Percentage identity and similarity of lipid binding GPCRs against CB1

Receptor	%Identity	%Similarity
S1P1 receptor	30	53
LPA1 receptor	30	51
Prostanoid EP4 receptor	17	40
Leukotriene BLT1 receptor	18	35
Prostanoid EP3 receptor	18	35
Platelet-activating factor receptor	14	33
Leukotriene TP receptor	16	33
GPR55	11	27

Table I.2 Percentage identity and similarity of lipid binding GPCRs against CB1

Receptor	%Identity	%Similarity
LPA1 receptor	26	47
S1P1 receptor	28	47
Prostanoid EP4 receptor	14	35
Leukotriene BLT1 receptor	17	33
Platelet-activating factor receptor	15	32
Prostanoid EP3 receptor	16	32
LeukotrieneTP receptor	15	31
GPR55	13	29

II Appendix 2

Figure II.1 Ramachandran plots for re-engineered CB1 and CB2 models. *Complete models of (a) 5U09 based CB1 (b) 5ZTY based CB2. Truncated models of (c) 5TGZ based CB1 (d) 5XR8 based CB1*

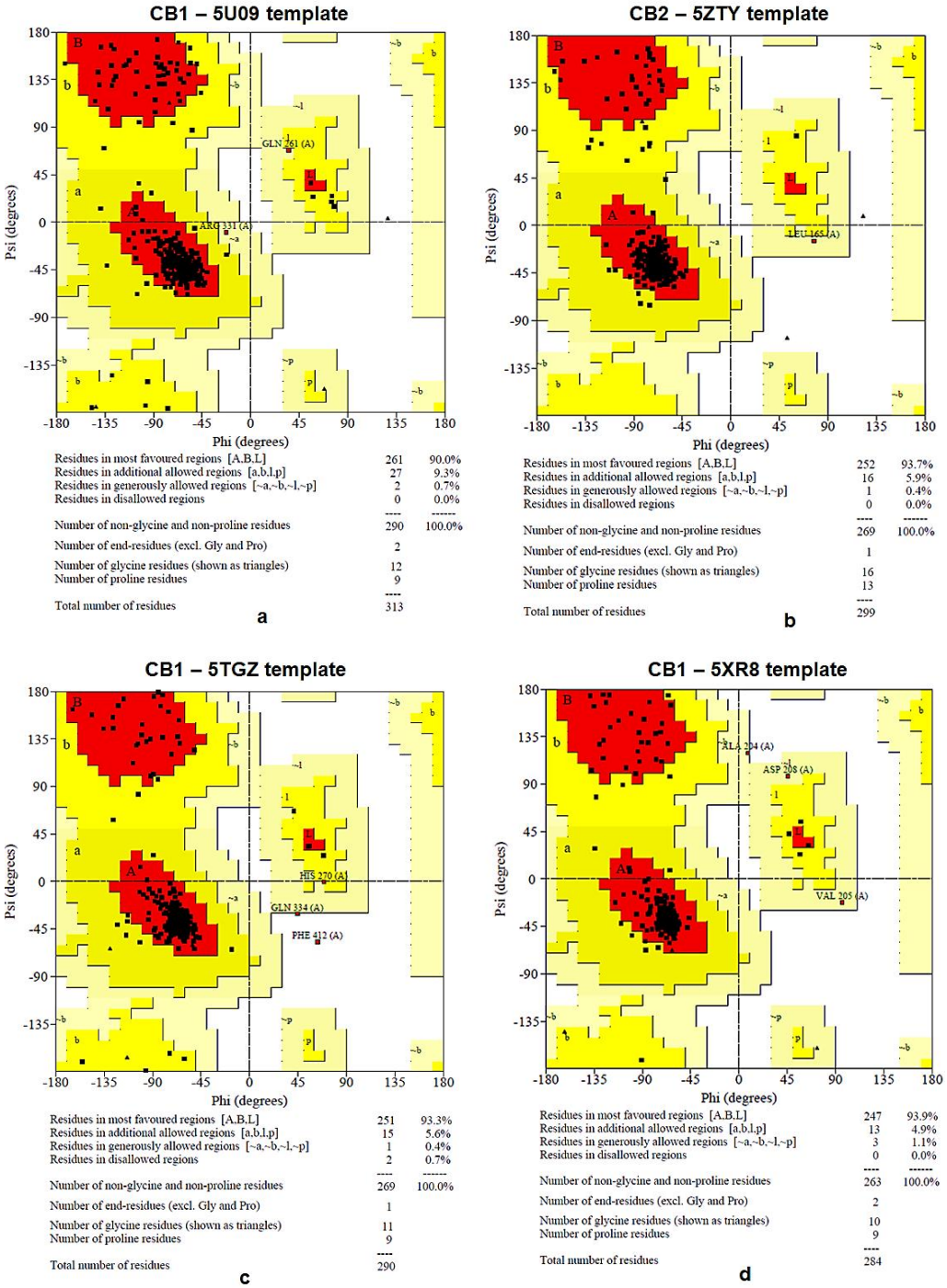

Table II.1 Agonists used in docking evaluation of CB1 receptor homology model

S.No.	Compound	Experimental pK_i	Reference
1	2-AG (2)	6.3	133
2	A796260	6.1	322
3	AM1714	6.4	323
4	AM411	8.2	324
5	Anandamide (1)	6.6	130
6	BAY387271	8.7	150
7	Cannabinol	6.5	325
8	CP55940 (6)	9.2	326
9	HU210 (4)	10.2	136
10	JWH-015 (9)	6.4	149
11	JWH-133 (5)	6.2	327
12	O-2545	8.9	328
13	Δ^9-THC (3)	7.3	73
14	WIN55,212-2 (8)	8.7	325

Table II.2 Antagonists used in docking evaluation of CB1 receptor homology model

S.No.	Compound	Experimental pK_i	Reference
1	AM281 (12)	7.9	329
2	AM630 (14)	5.3	159
3	CP27281	8.5	330
4	DML23	7.0	331
5	JTE907 (15)	5.6	162
6	LY320135 (13)	6.9	158
7	MK0364 (19)	9.5	332
8	NESS0327	12.5	333
9	NIDA41020	8.4	334
10	NIDA41109	8.9	334
11	O-1270	7.3	335
12	O-2050	8.6	169
13	SLV319	8.1	336
14	SR141716 (10)	9.1	152
15	SR147778	8.5	337

Table II.3 Binding pocket contact residues interacting with COR167 (24) and COR170 (25) docked to the inactive CB2 model and the predominant interaction type observed.

Residues	Predominant interaction type observed in inactive CB2
Phe87(2.57)	Aromatic hydrogen bond
Phe91(2.61)	van der Waals
Ile110(3.29)	van der Waals
Val113(3.32)	van der Waals
Thr114(3.33)	van der Waals
Phe117(3.36)	Aromatic stacking (COR170 (25))
Leu182(ECL2)	van der Waals
Phe183(ECL2)	Aromatic stacking
Trp258(6.48)	Aromatic stacking (COR170 (25))
Val261(6.51)	van der Waals
Ser285(7.39)	van der Waals
Cys288(7.41)	van der Waals

III Appendix 3

Table III.1 Motions of individual helices observed in PC1 analysis of CB1-Apo, CB1-AM841 and CB1-AM6538 systems.

TM Helix	CB1-Apo System	CB1-AM841 System	CB1-AM6538 System
1	Refer to the main text in Section 3.4.5.1	Refer to the main text in Section 3.4.5.2	In replicates 1 and 3 EC end tilts towards TM7. In replicate 2 bends away from TM7.
2	The EC end of TM2 in replicate 1 moves into the binding pocket by an anticlockwise rotation. In replicates 2 and 3 it moves out of the pocket by tilting.	The IC end exhibits minimal bending motions towards the binding pocket, away from binding pocket and towards TM1 in replicates 1, 2, and 3 respectively.	Minimal movement. Replicates 1 and - clockwise upward rotation. Replicate 2 – EC end bends toward the binding pocket.
3	Refer to the main text in Section 3.4.5.1	Refer to the main text in Section 3.4.5.2	Refer to the main text in Section 3.4.5.3
4	In all replicates, primary motion is helix tilting sideways (with respect to the binding pocket).	In all replicates, primary motion is the lateral tilting (with respect to the binding pocket).	No significant movement in replicates 1 and 2. In replicate 3 an anticlockwise rotation is observed.
5	Replicate 1 - the EC end bends towards TM3 while the IC end bends towards TM6. Replicate 2, IC end bends away from TM6 and the EC end rotates in upward in an anticlockwise direction. Replicate 3, the EC end bends towards TM6 while IC end moves away from it.	The movement of the IC end is converse to that of TM3. Replicate 1 - IC end bends towards TM3. Replicates 2 and 3 - IC end bends away from TM3 The EC end bends in a direction opposed to that of IC end in all three replicates.	Replicate 1 - EC end bends towards TM3 and IC end tilts away from it. Replicate 2 - EC end slightly bends away from TM3 and IC end moves away from TM6. Replicate 3 - IC end bends towards TM6.
6	Refer to the main text in Section 3.4.5.1	Refer to the main text in Section 3.4.5.2	Refer to the main text in Section 3.4.5.3
7	Refer to the main text in Section 3.4.5.1	Refer to the main text in Section 3.4.5.2	Refer to the main text in Section 3.4.5.3

IV Appendix 4

Table IV.1 Motions of individual helices observed in PC1 analysis of CB1-AM11542 and CB1*-MK0364 systems

TM Helix	CB1-AM11542 System	CB1*-MK0364 System
1	Replicate 1 - tilting motion lateral to the binding pocket. Replicate 2 - tilting motion towards TM7. Replicate 3 - minimal motion with a slight bending motion towards TM7	(refer to the main text in Section 4.4.2.2)
2	Shows minimal movement in all three replicates; in all three replicates, the N-terminal connected to ICL1 bends towards TM3. Replicate 1 shows downward helix movement	Replicate 1 - a downward movement of the helix. Replicate 2 - minimal movement, slight tilting motion towards TM3. Replicate 3 - C-terminal near ECL1 bends towards TM1, while the rest of the helix bends towards the binding pocket.
3	(refer to the main text in Section 4.4.2.1)	Replicate 1 – upward movement of the helix. Replicate 2 - the N-terminus near ECL1 bending away from TM4 and the IC end tilting toward TM5. Replicate 3 - EC end bends in the direction of the binding pocket and the IC end bends away from TM5
4	Replicate 1-tilting towards TM5 in the IC end region. Replicates 2 and 3 - moves away from the helical bundle by rotation and tilting respectively	Replicate1 - upward movement of the helix; no significant motion in replicates 2 and 3
5	(refer to the main text in Section 4.4.2.1)	(refer to the main text in Section 4.4.2.2)
6	(refer to the main text in Section 4.4.2.1)	(refer to the main text in Section 4.4.2.2)
7	(refer to the main text in Section 4.4.2.1)	(refer to the main text in Section 4.4.2.2)

V Appendix 5

Table V.1 Motions of individual helices observed in PC1 analysis of CB2-Apo Systems and CB2-CP55940 systems.

TM Helix	CB2-Apo System	CB2-CP55940 System
1	Refer to the main text in Section 5.4.5.1	Replicate 1 – minimal movement. Replicate 2 – EC end and IC end bend in opposite directions, lateral to the binding pocket. Replicate 3 - EC end tilts towards the TM7, IC end bends in the opposite direction.
2	Refer to the main text in Section 5.4.5.1	Minimal movement in all three replicates. Notable motions are: Replicates 1 and 3 - C-terminus near ECL1 bends towards TM3. Replicate 2 - the C-terminus bends away from TM3.
3	Refer to the main text in Section 5.4.5.1	Refer to the main text in Section 5.4.5.2
4	Only IC end shows notable bending movements: replicate 1 – towards TM5, replicate 2 – towards the binding pocket, replicate 3 – away from TM5	Replicate 1 – minimal movement. Replicates 2 and 3 - Slight tilting of EC end towards TM5 in all replicates.
5	Replicate 1 – upward clockwise by EC end; IC end bends towards TM6. Replicate 2 - EC end tilting away from TM6. Replicate 3 - EC end rotates away from TM4 towards TM6; IC end bends away from TM6	Replicate 1 – EC end tilts slightly towards TM6 and the binding pocket, IC end bends away from the binding pocket. Replicate 2 - EC end tilts away from the pocket while the IC end shows a clockwise rotation. Replicate 3 - can be described by dividing the helix into three parts - N-terminus near the ECL2 shows a mild rotation in an anticlockwise fashion; the mid-portion of the helix bends in a direction away from TM4 and the C-terminus near ICL3 moves towards TM3.
6	Refer to the main text in Section 5.4.5.1	Refer to the main text in Section 5.4.5.2
7	Refer to the main text in Section 5.4.5.1	Refer to the main text in Section 5.4.5.2

VI Appendix 6

Table VI.1 Details of ligands tested on CB1 and CB2 using [^{35}S]GTPγS

Ligands	Receptor where it shows activity	Currently used as (or) for
Carbenoxolone (26)	Connexins	Peptic, oesophageal and oral ulceration and inflammation
Dexamethasone (27)	Glucocorticoid receptors	Anti-inflammatory action
Haloperidol (28)	Serotonin and dopamine receptors	Anti-psychotic
Metoclopramide (29)	Primarily dopamine D2 receptor	Anti-emetic
Prednisolone (30)	Glucocorticoid receptors	Anti-inflammatory (or) immunosuppressive agent
Prednisolone hemisuccinate (31)	Glucocorticoid receptors	Anti-inflammatory (or) immunosuppressive agent
Pregnenolone acetate (32)		Precursor of sterols

Table VI.2 Details of ligands selected for binding mode analysis by molecular docking

Compound	K_i at CB1	Type of Ligand	K_i at CB2	Type of Ligand	Source
AM404	1.5+/-0.09 μM	Agonist	1.3+/-0.08 μM	Agonist	296
Bazedoxifene	826nM	Full inverse agonist.	254nM	Full inverse agonist.	308
E-4-OH-Tamoxifen	1242nM	Neutral antagonist	957nM	Full inverse agonist	209
E-Endoxifen	1393nM	Full inverse agonist	2355nM	Full inverse agonist	209
E-Tamoxifen	1510nM	Full inverse agonist	847nM	Full inverse agonist	209
Fenofibrate	501nM	Partial agonist. NAM at high concentrations.	19nM	Full agonist	297
Lasofoxifene	NA	Weak binding	NA	Partial inverse agonist	308
Raloxifene	210nM	Partial inverse agonist	240nM	Full inverse agonist	308
Ridaifen - B	732+/-168nM	Weak binding	43.7+/-14.6nM	Inverse agonist	309
Z-4-OH-Tamoxifen	681nM	Full inverse agonist	495nM	Full inverse agonist	209
Z-Endoxifen	1161nM	Full inverse agonist	2393nM	Full inverse agonist	209
Z-Tamoxifen	1574nM	Full inverse agonist	798nM	Full inverse agonist	209

Table VI.3 Binding pocket contact residues interacting with non-cannabinoids docked to the inactive CB1 model and the predominant interaction type observed.

Residues	**Predominant interaction type observed**	
	SERMs	**AM404 (33)**
Asn101(N-term)		Aromatic hydrogen bond
Phe102(N-term)	Aromatic stacking	
Met103(N-term)		Hydrogen bond
Ile105(N-term)	van der Waals	van der Waals
Gly 166(2.53)	Aromatic hydrogen bond	
Phe 170 (2.57)	Aromatic stacking	van der Waals
Phe 174 (2.61)		
His 178 (2.65)		
Phe 189 (3.25)	van der Waals	van der Waals
Val 196 (3.32)	van der Waals	van der Waals
Thr 197 (3.33)	Hydrogen bond/ Van der Waals	van der Waals
Ile 267 (ECL2)	van der Waals	van der Waals
Phe 268 (ECL2)	Aromatic stacking	van der Waals
Pro 269 (ECL2)		van der Waals
Trp 279 (5.43)	π-cation	van der Waals
Trp 356 (6.48)	Aromatic hydrogen bond	van der Waals
Phe 379 (7.34)	van der Waals	van der Waals
Ala 380 (7.35)	van der Waals	
Ser 383 (7.39)	Aromatic hydrogen bond	van der Waals
Cys 386 (7.41)		van der Waals

Table VI.4 Binding pocket contact residues interacting with non-cannabinoids docked to the active CB1 model and the predominant interaction type observed.

Residues	Predominant interaction type observed	
	SERMs	**AM404 (33)**
Phe 108 (N-term)	Hydrogen bond	
Phe 170 (2.57)	Aromatic stacking	van der Waals
Phe 174 (2.61)	van der Waals	van der Waals
Phe 177 (2.64)	Aromatic stacking	
His 178 (2.65)	Aromatic stacking	Aromatic hydrogen bond
Phe 189 (3.25)	Hydrogen bond	
Phe 191 (3.27)	van der Waals	
Val 196 (3.32)	van der Waals	van der Waals
Thr 197 (3.33)	van der Waals/Hydrogen bonds	
Phe 200 (3.36)	Aromatic stacking/ π -cation	van der Waals
Ile 267 (ECL2)	van der Waals	Hydrogen bond/ Aromatic hydrogen bond
Phe 268 (ECL2)	Aromatic stacking	van der Waals
Trp 279 (5.43)	van der Waals	van der Waals
Trp 356 (6.48)		van der Waals
Leu 359 (6.51)	van der Waals	
Met 363 (6.55)	van der Waals	
Phe 379 (7.34)	van der Waals	van der Waals
Ser 383 (7.39)	Aromatic hydrogen bond	van der Waals
Cys 386 (7.41)	van der Waals	van der Waals

Table VI.5 Binding pocket contact residues interacting with non-cannabinoids docked to the inactive CB2 model and the predominant interaction type observed.

Residues	Predominant interaction type observed		
	SERMs	**AM404 (33)**	**Fenofibrate (38)**
Phe 87 (2.57)	Aromatic stacking	van der Waals	Aromatic hydrogen bond
Ser 90 (2.60)	Aromatic hydrogen bond	Hydrogen bond/Aromatic hydrogen bond	van der Waals
Phe 91 (2.61)	Aromatic stacking	van der Waals	van der Waals
Phe 94 (2.64)	Aromatic stacking	van der Waals	van der Waals
His 95 (2.65)	Aromatic stacking	Aromatic hydrogen bond	van der Waals
Ile 110 (3.29)	van der Waals	van der Waals	van der Waals
Val 113 (3.32)	van der Waals	van der Waals	van der Waals
Thr 114 (3.33)	Hydrogen bonding	van der Waals	van der Waals
Phe 117 (3.36)	Aromatic stacking/ π -cation interaction	van der Waals	van der Waals
Leu182 (ECL2)		van der Waals	van der Waals
Phe 183 (ECL2)	Aromatic stacking	van der Waals	
Leu 191 (5.40)	van der Waals	van der Waals	
Trp 194 (5.43)	Aromatic stacking/ π -cation interaction	van der Waals	Aromatic stacking
Trp 258 (6.48)	Aromatic stacking/ π -cation interaction		
Val 261 (6.51)	van der Waals	van der Waals	
Met 265 (6.55)		van der Waals	
Lys 279 (7.32)	Hydrogen bond		
Ser 285 (7.39)	van der Waals	van der Waals	
Cys 288 (7.41)	van der Waals	van der Waals	